UNIVERSITA' DEGLI STUDI DI NAPOLI
"FEDERICO II"

DIPARTIMENTO DI FARMACIA

DOTTORATO DI RICERCA IN SCIENZA DEL FARMACO

XXVII CICLO

Anti-Cripto Monoclonal Antibodies and their fragments: Structural and Functional Studies

TUTORS	DOTTORANDA
CH. MO PROF. PAOLO GRIECO	DR. GIUSEPPINA FOCA'
CH.MO DR. MENOTTI RUVO	

COORDINATORE
PROF.SSA MARIA VALERIA D'AURIA

INDEX

ABSTRACT

Human Cripto-1 (CR-1) is the founding member of the epidermal growth factors (EGF-CFC) superfamily, composed of structurally related protein members.

CR-1 is involved in many biological functions. Among the others, it is a key regulator of the embryogenesis, promoting the differentiation of embryonic stem cells and the organogenesis of brain and heart. Interestingly, CR-1 also promotes tumorigenesis, regulating cell proliferation, migration, epithelial-mesenchimal transition, survival and angiogenesis. The functional part of CR-1 protein consists of two central Cysteine Rich Domains, EGF-like and CFC, that independently interact with several partners. The increasing interest on CR-1 as a novel diagnostic and therapeutic target is derived from the evidence that it is highly expressed in many human solid tumors, while it is barely present or totally absent in normal adult tissues. CR-1 can promote tumorigenesis by activation of several pathways; we have focused our attention on the CR-1/ALK4 interaction which triggers the Smads cascade, leading to the activation of gene transcription encoding tumor-related factors (Nodal, Lefty).

Thus, the aim of this study was the generation and development of smart and highly selective biomolecules such as mAbs and their fragments that target the CFC domain of CR-1, directly involved in the CR-1/ALK4 as well as in the CR-1/ GRP78 interactions.

For this purpose, as starting point, a set of monoclonal antibodies was generated by the hybridoma technique, using as antigen the synthetic and correctly folded human CFC [112-150] domain.

A screening was performed to identify the mAbs with the highest affinity toward the full-length recombinant human CR-1 protein (*rh*CR-1) and with the highest specificity toward the two “hot spots” residues (H120 and W123) of the CFC domain. We thus identified two mAbs, named 10D1 and 1B4. 10D1 and 1B4 interacted very strongly with CR-1, as they were characterized by K_D of 70 pM and 200 pM, respectively.

A subsequent comparative epitope study, combining a computational and a biochemical approach, confirmed that both mAbs recognized the region of the CFC domain containing the H120 and W123, suggesting that these molecules may act as potential blocking antibodies and/or at least be the starting point to develop potential therapeutic tools to be employed on cancer cells over-expressing CR-1. In addition, preliminary *in vitro* assays suggested that the 1B4 mAb had such properties, as it promoted cell death on GEO cancer cell lines.

The second phase of this study was focused on the generation of functional antibody fragments of the 1B4 mAb. A first proteolytic approach was unsuccessful, leading to a partially inactive Fab fragment. We thus next moved to generate an engineered recombinant chimeric Fab fragment of the same mAb (1B4 *r*Fab) that only retained a partial binding activity (K_D 6 nM) toward the target protein. Using this recombinant fragment as template, a new innovative dimeric format (1B4 *r*Fab_2) was created exploiting an elegant conjugation strategy based on the use of the M-TGase enzyme. This dimeric 1B4 *r*Fab_2 protein displayed to *rh*CR1 a binding affinity comparable to that one of the whole 1B4 antibody. Finally, with the aim of increasing the cell killing potential of the 1B4 *r*Fab and to exploit its CR-1 specificity in *tumor homing* approaches, we designed and realized a strategy to generate an ADC (Antibody Drug Conjugate), arming the 1B4 *r*Fab with a payload consisting of the cytotoxic agent Doxorubicin.

CHAPTER I

INTRODUCTION

I.1 THE EGF-CFC SUPERFAMILY

The epidermal growth factor (EGF)-Cripto-1/Fibroblast Growth factor related ligand (FRL-1)/Cryptic (CFC) gene family encodes a group of structurally related proteins, found only in vertebrates **[1]**, whose human Cripto-1, also known as teratocarcinoma derived growth factor (TDGF-1), is the founding member.

Human Cripto-1 was initially isolated for the first time from NTERA-2 human embryonal carcinoma cells **[2]** and orthologs of human Cripto-1 were secondly identified in mouse (Cripto-1/cfc2 and Cryptic/cfc1), zebrafish (one-eyed pinhead/oep), *Xenopus* (XCR1/FRL-1, XCR2, and XCR3), chicken and monkey **[3,4]**. The EGF-CFC members display several functions depending on the organism in which they are expressed, mainly related to embryogenesis.

Human Cripto-1 acts predominantly both as a regulator of gastrulation during embryogenesis and of mammary morphogenesis **[1]**.

In mouse, cripto-1 is involved in several processes, including mesoderm and endoderm formation, and cardiomycites development **[5]**.

FRL-1 and Oep exert similar functions, such as mesoderm and neuroectoderm formation **[6,7]**.

The core of the EGF-CFC proteins is made up of around 180-200 amino acid residues. Mouse and human Cripto proteins have a molecular weight of 24, 28 and 36 kDa by virtue of differential glycosylation status at N- and O-linked Asn and Ser residues **[8-13]**. With regard to the other members, cryptic protein exists as 20, 21.8 and 23 kDa isoforms, while oep protein as 18 and 20 kDa forms **[11-13]**.

All the members of the EGF-CFC family exhibit a highly shared structure consisting of a NH_2-terminal signal sequence, a modified epidermal growth factor (EGF)-like motif, a conserved cysteine-rich motif (CFC region) and a short hydrophobic COOH-terminal region which in some cases contains additional consensus sequences for potential glycosylphosphatidylinositol (GPI) cleavage and attachment **[2,14,15]**. An overall sequence identity of 22–32% is found among mouse and human Cripto, mouse cryptic, human criptin, *Xenopus* FRL-1 and zebrafish oep. More precisely, the EGF-like domain exhibits a sequence similarity of 60-70%, whereas the CFC region shows a similarity of 35-48% **[13]**.

I.2 HUMAN CRIPTO-1

2.1 Structure

Human Cripto-1 gene (2 kb mRNA) is localized on chromosome 3p21.3 **[16]** and consistists of six exons and five introns, in which exon 4 encodes the EGF-like motif, while the exon 5 encodes the CFC motif. Moreover, a truncated form was found to be expressed in some cancers encoded by a 1.7 kb mRNA, that lacks exons 1 and 2 **[5,16]**.

The human Cipto-1 protein is composed of 188 amino acids, showing a structure correlated to the other members of the EGF-CFC family. Thus, the structure of human Cripto-1 contains:

- a signal sequence at the N-terminus
- two Cysteine-Rich Domains (CRDs): the EGF-like and the CFC
- a hydrophobic region at the C-terminus

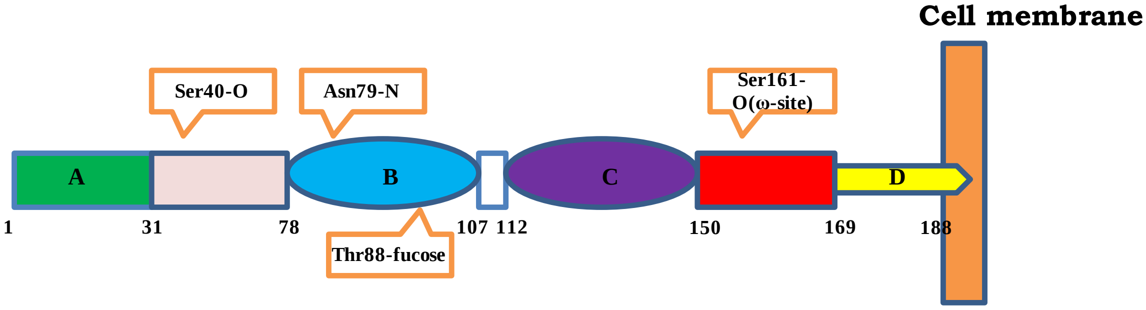

A. N-terminal Signal sequence
B. EGF-like domain
C. CFC domain
D. C-terminal hydrophobic region

Figure 1.1: Schematic structure of human CR-1 protein, in which the glycosylation sites are reported.

The signal sequence (Met1-Gly30) at the N-terminal region allows the secretion of CR-1 from the endoplasmic reticulum (ER) into the Golgi body, where the protein is processed and undergoes post-translational modifications, mainly glycosylation.

The core of the protein is mainly represented by the EGF-CFC region, of ~20 kDa but glycosylation and further post-translational modifications give a provide an increased molecular weight (28-36 kDa). The EGF-CFC domain has been demonstrated to be sufficient to CR-1 to exert its biological functions **[8,13]**.

The EGF-like domain (Leu78-Glu107), a region of approximately 40 amino acids, contains six Cysteine residues that form three intramolecular disulfide bonds. While in the canonical EGF motif there are three loops (A, B and C), the EGF-CFC proteins are characterized by a EGF-like motif variant, that lacks the A loop, possesses a truncated B loop and has a C loop completely different compared to the other members in the EGF superfamily **[17].**

Like the EGF-like domain, also the CFC domain (Lys112-Asp150) is composed of 40 amino acid residues and contains six Cysteine residues. The disulfide bonds pattern has been experimentally determined, showing that the six Cysteines are linked following the C1-C4, C3-C5, C2-C6 scheme **[18].** Moreover, the 3D model of CFC domain, proposed by Foley *et al.* **[18]**, showed a hydrophobic patch consisting of Trp134, Leu138, Phe141 and Pro142. Leu138 and homologues of Trp134 and Phe141 have been reported to be highly conserved throughout the Cripto family and are clustered on the side of the CFC domain opposite to residues His120 and Trp123 that are involved in binding of Cripto-1 to ALK4.The hydrophobic residues presumably exert a structural role, affecting the folding of CR-1 by interacting with the EGF-like domain, or they may represent the interaction site with other signaling partners.

Furthermore, the interaction between the CFC domain and the ALK4 receptor has been elucidated by docking studies performed using the NMR structure of the synthetic human CFC and ALK4-ECD structure obtained by homology modelling. In particular, a close fitting was found between the His120 and Trp123 of CFC domain and the Phe55 and Tyr56 of ALK4-ECD, that form a pocket in which the two residues of hCFC perfectly match. In addition, a contribution is even given by favorable electrostatic and hydrophobic interactions. This docking study was supported by SPR binding assays on synthetic hCFC on *rh*ALK4 by which a K_D value of ~13 µM was extrapolated for the ligand-receptor complex **[19]**.

Furthermore, docking studies, carried out by Calvanese *et al.* **[20]** to investigate the ternary complex ALK4/CR-1/Nodal, showed that the EGF-like domain of CR-1 forms a polar groove, which perfectly allows the interaction with Tyr58 of Nodal helix. Also Glu49 and Glu50, embedded on the pre-helix loop of Nodal, were found as crucial residues for the interaction between Nodal and the EGF-like domain of CR-1, establishing favorable electrostatic interactions.

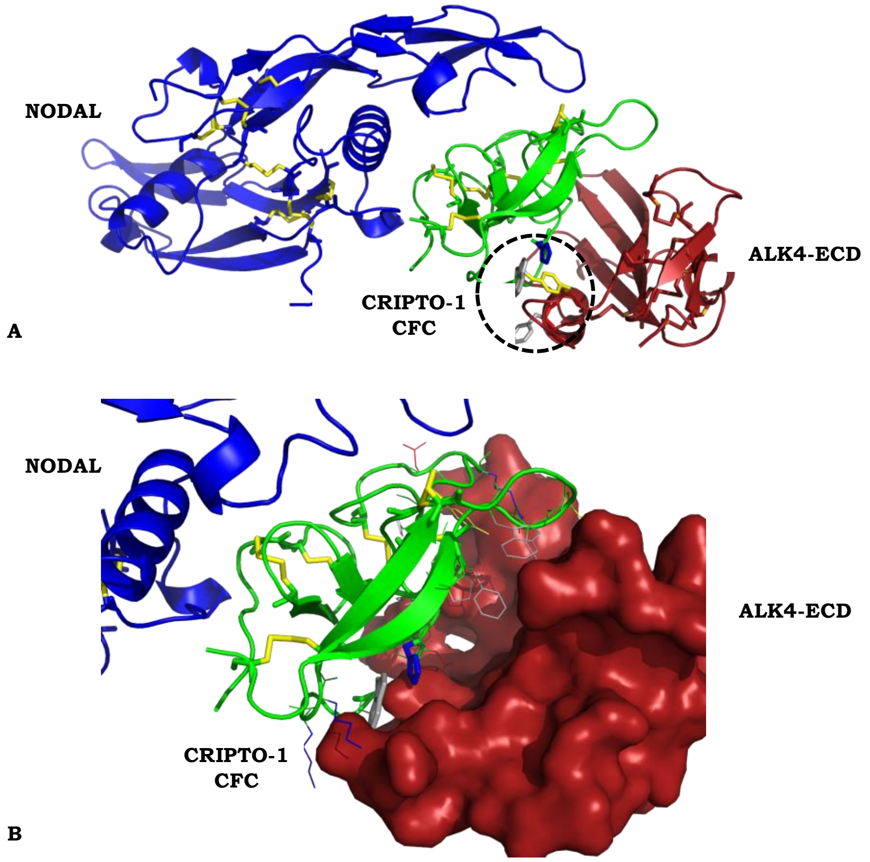

Figure 1.2: Ribbon representation of the proposed model for the ternary complex composed of Nodal (blue), CR-1 (green) and ALK4-ECD (red) (**A**). The relevant residues at the binding interface between hCFC and ALK-ECD are highlighted. Zoom representation of the contact region between hCFC (stick model) and the hydrophobic pocket of ALK4-ECD (Connolly surface area in red) (**B**).

Many studies have shown that the EGF-like domain is involved in binding to several partners: in addition to the morphogen Nodal [21], even with Glypican-1 [22], Activins [23] and in cross-talk with ErbB4 [1]. By contrast, the CFC domain is principally involved in binding to ALK4 receptor [18, 24-26] and GRP78 co-receptor [27].

Cripto-1, as a GPI membrane-anchored protein, undergoes enzymatic cleavage from the cell membrane by GPI-phospholipease D (GPI-PLD) so as to be released into the cell media.

Since the presence of the GPI anchoring, Cripto-1 can act as a membrane-anchored protein within lipid rafts microdomains and in addition, it can function as Nodal co-receptor [24,28,29]. Thus, Cripto-1 can act both as a co-receptor in cis (autocrine/cell-autonomous) and as ligand in trans (paracrine/cell-nonautonomous) conformation **[30]**.

Cripto-1 glycosylation sites include O-linked glycosylation at Ser40 and Ser61 (ω-site for GPI-anchoring), N-linked glycosylation at Asn79 and O-linked fucosylation at Thr88 (See Fig. 1.1). Moreover, experiments using O-fucosylation mutants have demonstrated that the Thr88 residue but not the fucosylation is crucial for activation of Nodal/Cripto-1 dependent signaling pathways **[28, 31]**.

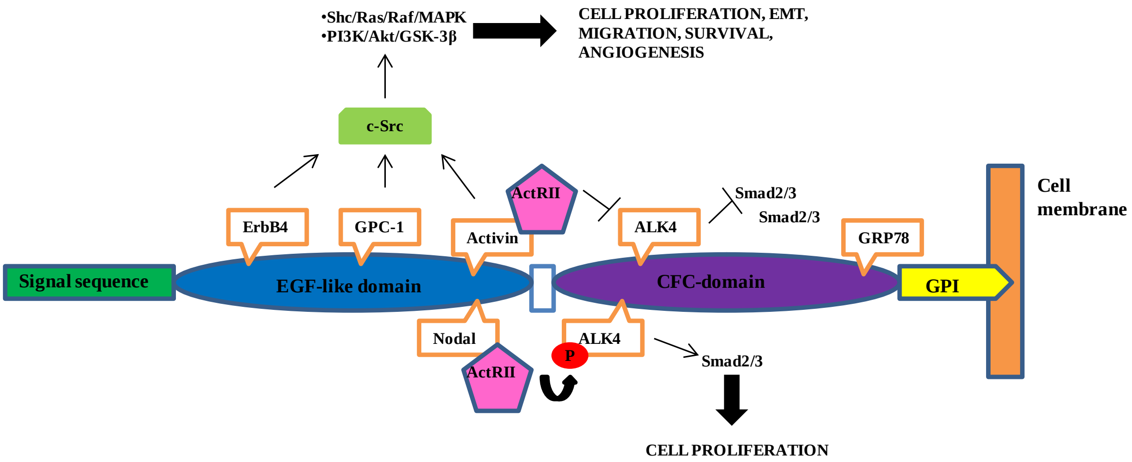

Figure 1.3: Representation of the Cripto-1 domains and domain-dependent signalling.

2.2 Functions

CR-1 is a multifunctional protein involved in various physiological and pathological processes, resulting from the interaction between its extracellular form and the intracellular signal transduction pathways activated by several partners, ultimately leading to cell proliferation, transformation, survival and cancer cells metastatis **[32]**.

CR-1, as well as other EGF-CFC family members, performs regulatory cell functions and tissue patterning during embryogenesis whereby it plays a crucial role in the specification of the posterior-anterior and left-right axis and in the formation of several organs (organogenesis) such as heart and brain development. It acts as a co-receptor for the TGF-β ligands (Nodal, GDF1 and GDF3) during gastrulation while together with Apelin and APJ regulates cardiac specification of ES cells **[4,33,34]**.

The emerging role of CR-1 to maintain the pluripotential capacity and self-renewal of human and mouse embryonic stem cells, makes it an innovative and attractive stem cell marker **[35]**.

Furthermore, since CR-1 belongs to "developmental oncoprotein family", it represents a typical example of a gene associated with early embryogenesis and re-expressed in human tumors in a dis-regulated manner. It is well-established that CR-1 expression is very low in normal differentiated adult tissues, while it is highly expressed in 50% to 80% of different types of primary human carcinomas, including breast, colon, lung, ovary, cervix, testis **[32].**

Several *in vitro* experiments have demonstrated its oncogenic activity by enhancing proliferation, migration, invasion, epithelial-mesenchymal transition, branching morphogenesis of several mouse and human epithelial cell lines and, finally it can also promote tumor angiogenesis **[35]**.

Interestingly, CR-1 was found to be heterogeneously expressed in human embryonal carcinoma (EC) cells, grouped into two different subpopulations (reported as CR-1^{High} and CR-1^{Low}), on the basis of the protein expression levels **[36]**. Comparing the two subpopulations, the first one exhibits hallmarks of stem cells with a higher degree of tumorigenicity than the latter. Thus, the EC cells, like the ES cells, can spontaneously differentiate into various types of cells and maintain the pluripotency through a transcriptional self-regulatory circuit regulated by transcriptional factors such as Oct4 and Nanog **[36].**

In addition, expression of CR-1 is also reported in other human tumor species, including cutaneous melanoma, in particular in a subpopulation of aggressive melanoma cells exhibiting stem cell-like characteristics (C8161 and ROS184) **[37,38]** and in EGFR-mutant non-small cell lung cancer (NSLC) [**39]**.

Recently, Pilgaard *et al.* **[40]** have investigated and demonstrated, for the first time, the presence of Cripto-1 in glioblastoma multiforme (GBM) tissues and its correlation with the disease outcome. In GBM tissues, CR-1 positive cells were found bordering glomeruloid blood vessels (localized in the microvasculature) in the regions of vascular genesis caused by hypoxia and in areas of rapid tumor growth, characterized by higher proliferation. These evidences suggest that CR-1 may be involved in GBM progression.

2.3 Signaling pathways activated by Cripto-1

a) TGF-β dependent signaling pathways

During embryogenesis, cell-membrane anchored CR-1 functions as a co-receptor with the type I Activin serine-threonine kinase receptors (ALK4 or ALK7) for the transforming growth factor β (TGF-β)-related proteins , Nodal and Growth and Differentiation factor 1 and 3 (GDF1 and GDF3).

CR-1 is able to bind directly to both Nodal (via EGF-like domain) and ALK4 (via CFC domain) to help Nodal signaling through the phosphorylation of Smad-2/Smad-3, which in turn bind to Smad-4, that then translocate into the nucleus enhancing the transcription - with other activators - of specific target genes **[24,25,30]**. So far, it has been reported that the presence of CR-1 represents a pre-requisite for CR-1/Nodal dependent signaling pathway to support the binding of Nodal to ALK4 during the formation of a biologically active ternary complex (CR-1/Nodal/ALK4). However, recent biochemical binding assays have revealed that Nodal is able to bind physically to ALK4 without the presence of CR-1 **[41]**; these new findings need to be better understood and validated in cellular systems.

In addition to ALK4, CR-1 hab been shown to significantly potentiate the responsiveness of the ALK7/ActRIIB complex to Nodal, indicating that both ALK7 and ALK4 cooperate with CR-1 in modulating Nodal signaling **[42]**.

CR-1 can facilitate Nodal signaling during embryogenesis also interacting with antagonists of Nodal, including Tomoregulin-1 and Lefty or acting as inhibitor of Activin B (via CFC domain), Activin A, and TGF-β1 (via EGF-like domain) signaling **[33, 35]**.

Moreover, the inhibitory effects of CR-1 on TGF-β1 and Activin signaling can be enhanced by the 78-kDa heat shock protein glucose-regulated protein (GRP78), which has been found in human carcinoma cells. CR-1, through the CFC domain, binds the N-terminus region of GRP78, forming a complex able to inhibits TGF-β1 signaling and its anti-proliferative effects. Thus, the modulation of these factors by Cripto-1 has been proposed as a possible mechanism by which Cripto-1 promotes cell proliferation and tumorigenesis **[27,43]**.

Finally, CR-1 oncogenic activity is related also to Notch signaling pathway, necessary to maintain the normal development and stem cell fate in several tissues

[44]. In particular, Notch4 has been demonstrated to regulate the expression of Nodal in malignant melanoma cells, suggesting a potential cross-talk between the Nodal/CR-1 and Notch signaling pathways during tumorigenesis **[45]**.

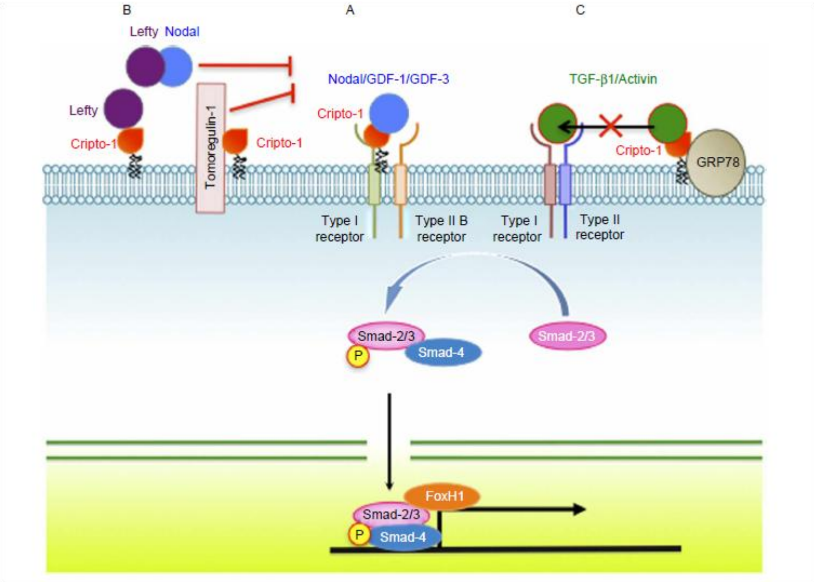

Figure 1.4: Cripto-1 modulation of TGF-β dependent signaling pathways. Cripto-1 functions as co-receptor for Nodal, GDF-1, and GDF-3 leading to the activation of a Smad-2/3 intracellular signaling pathway (**A**). Cripro-1 binds to Tomoregulin-1 and Lefty that normally antagonize Nodal signaling (**B**). Cripto-1 and GRP78 antagonize Activin and TGF-β1 signaling (**C**) **[46]**.

b) TGF-β -independent signaling pathways

In addition to its function as a co-receptor of TGF-β members (Nodal/GDF1/GDF3), CR-1 can induce the signaling of further molecules independently of Nodal and ALK4.

CR-1 can also function as a ligand for Glypican-1, a GPI-anchored heparan sulphate proteoglycan (HSPG), linked to the plasma membrane in lipid rafts, leading to a phosphorylation of the cytoplasmic tyrosine kinase c-src which, in turn, activates mitogen-activated protein kinase (MAPK) phosphatidylinositol 3’-kinase (PI3K)/Akt signaling pathways, involved in the regulation of cell proliferation, motility and survival **[22]**. The MAPK and AKT pathways are also involved in epithelial to mesenchymal transition (EMT) through a canonical Wnt/β-catenin signaling pathway, by inhibition of glycogen synthase kinase (GSK)-3β activity leading ultimately to the stabilization of β-catenin and Snail **[47]**. Also GRP78 has been demonstrated to be essential for CR-1 activation of the MAPK/AKT signaling pathway.

Furthermore, several studies have demonstrated a potential interaction between CR-1 and the Wnt/β-catenin signaling pathway during embryonic development and in colon carcinoma cells **[48]**. The canonical Wnt/β-catenin/Tcf signaling pathway performs several functions including the regulation of proliferation and cell lineage specification during embryonic development, the maintenance of the undifferentiated state of ES cells and the development of different types of carcinomas (skin, intestine, liver and brain) **[49]**.

An interesting cross-talk between Cripto-1 and ErbB4 receptor has been found. It is well known that Cripto-1 cannot bind directly to the ErbB type I tyrosine kinase receptors family, including Epidermal Growth Factor Receptor (EGFR), ErbB2, ErbB3 and ErbB4, because of its modified EGF-like domain **[4]**. However, Cripto-1 has been reported to can indirectly enhance the tyrosine phosphorylation of ErbB4 in breast cancer cells, by a Tomoregulin-related mechanism **[50]**.

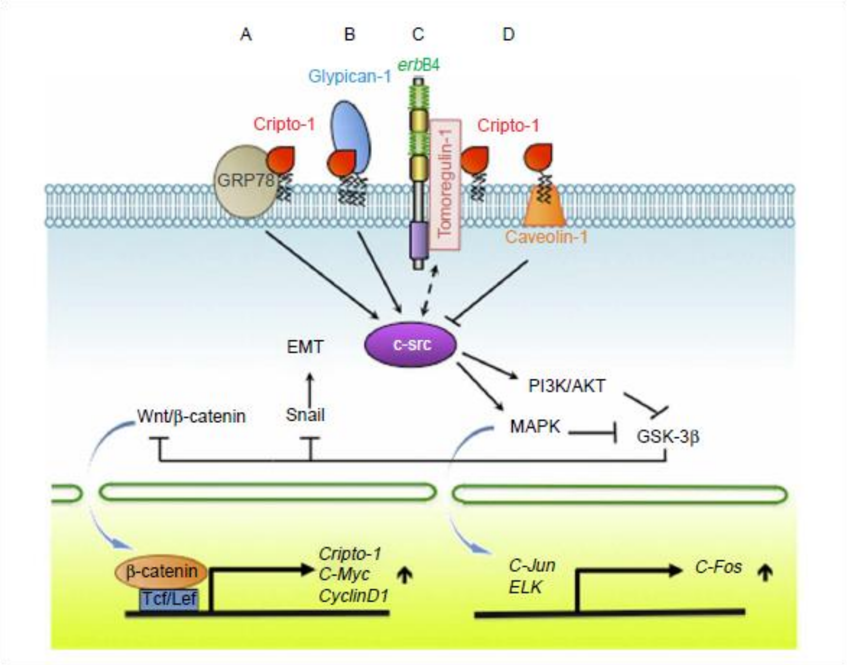

Figure 1.5: Cripto-1 activation TGF-β independent signaling pathways. Cripto-1 binding to GRP78 induces the MAPK/AKT activation (**A**). Cripto-1 interaction with Glypican-1 (**B**). The MAPK/AKT pathway can also inhibit GSK-3b. Cripto-1 and Tomoregulin-1 induce the phosphorylation of ErbB4 (**C**). Cav-1 binds to Cripto-1 and inhibits the capacity of Cripto-1 to activate a c-src/MAPK/AKT signaling pathway (**D**) **[46]**.

I.3 TARGETING CRIPTO-1 IN CANCER THERAPY

The high expression levels of CR-1 in a variety of human tumors and its low expression or the fully absence in healthy tissues, make CR-1 a novel intriguing target in cancer therapy.

Several studies reported the detection of higher levels of CR-1 in plasma of patients with breast and colon cancer and, more recently, in the less common GBM, compared with levels in the plasma of healthy volunteers, also validating the role of CR-1 as a new useful serologic marker correlated to the tumor progression in some cancers. Moreover, CR-1 is known to be expressed in cancer stem-like cells that exhibit peculiar stem-like hallmarks such as the ability of self-renewal, as well as resistance to chemotherapy and radiotherapy.

Considering the relevant role of cancer stem-like cells in the tumor growth and progression and drug resistance, the presence of CR-1 both in tumor tissues and in cancer stem-like cells strengthens the validation of Cripto-1 as a potential cancer target.

Despite the numerous breakthroughs in anti-cancer therapy, the research of specific and efficient anti-tumoral therapeutic agents is still a big challenge. In this context, the identification of specific neutralizing molecules (monoclonal antibodies, antibody fragments or peptide fragments) against CR-1 could represent a promising strategy in cancer therapy to treat human solid tumors in which this protein is over-expressed. The use of these biotherapeutic agents should preserve the healthy tissues and minimize the common side effects related to the use of broad ranging anti-tumoral therapeutics.

For instance, anti-CR-1 antibodies can be classified in four classes: N-terminal tip, N-terminal, EGF-like domain and CFC domain. mAbs targeting either the EGF or the CFC domains of CR-1 were able to inhibit tumor growth *in vivo*; by contrast, the anti- N-terminal mAbs showed no significant effects on the tumor growth of NCCIT or GEO xenografts, indicating that monoclonal antibodies targeting the N-terminal region of CR-1 act as simple binding antibodies without any blocking action **[21,51,52].**

Interestingly, Biogen-Idec has developed a N-terminal binding antibody conjugated to the DM4 cytotoxin to target CR-1 in human tumors. Upon internalization by cells expressing CR-1, the DM4 moiety binds to tubulin, disrupting microtubule structures and leading to inhibition of cell division. This DM4-conjugated humanized mAb was tested on NCCIT human embryonal carcinoma and CLAU-6 lung cancer xenografts to assess its capability of allowing tumor regression and a strong inhibitory effect on tumor growth was detected (Biogen-Idec: Cripto binding molecules. US0008906. 2010).

In addition, the emerging role of GRP78 in the modulation of CR-1 oncogenic signaling strengthens the importance to develop anti-CR-1 antibodies.

However, since the pharmacological therapy based on the simple use of monoclonal antibodies is often not sufficient to eradicate a solid tumor, despite a robust anti-tumoral effectiveness *in vitro* and *in vivo*, a more robust approach could be represented by the combination of the specificity of a monoclonal antibody and the toxicity of a cytotoxic drug able to potentiate the therapeutic efficacy **[53]**.

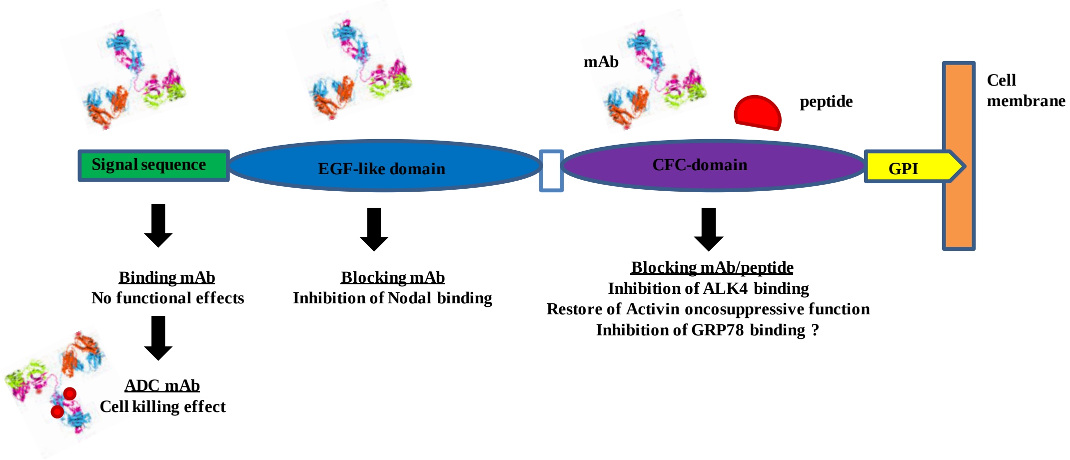

Figure 1.6: Schematic illustration of antibody/molecules useful in targeting CR-1 in tumor tissues

.

I.4 MONOCLONAL ANTIBODIES IN ONCOLOGY

4.1 Anatomy of antibody molecule

Antibodies are glycosylated proteins, characterized by a typical "Y" shape. The structure of antibodies, with complete amino acid content and disulfide bond pairing, was elucidated by G. Edelman and R. Porter in the early 1960s.

The Ig monomer is composed of two identical heavy chains (HC) and two identical light chains (LC) linked by inter-chain disulfide bonds.

On the basis of the constant region of the heavy chain, immunoglobulines are classified into five classes, IgA (α), IgD (δ), IgE (ε), IgG (γ) and IgM (μ); on the other hand, the light chain exists only as two different forms, κ and λ. The IgG and IgA classes in turn are classified into further sub-classes by virtue of their abundancy in serum, the IgG into four (IgG1, IgG2, IgG3 and IgG4) while the IgA only into two (IgA_1 and IgA_2) respectively.

defining a structure composed of three main portions: two identical Fabs and the Fc. The Fabs are linked to the Fc by the hinge region, which varies in length and flexibility in the different antibody classes and isotypes. The antigen-binding sites (paratopes) are localized at the N-terminal tips of the Fabs. Specific studies on antibody structure **[54-57]** have demonstrated that all antibody domains, variable and constant (defined Immunoglobulin domains), are made up of 70–110 amino acids and form a compact globular structure with a characteristic β-barrel fold.

Each domain consists of a stable arrangement of hydrogen-bonded, anti-parallel β-strands which form a bilayer structure, stabilized by a disulfide bond between the two layers **[58]** .

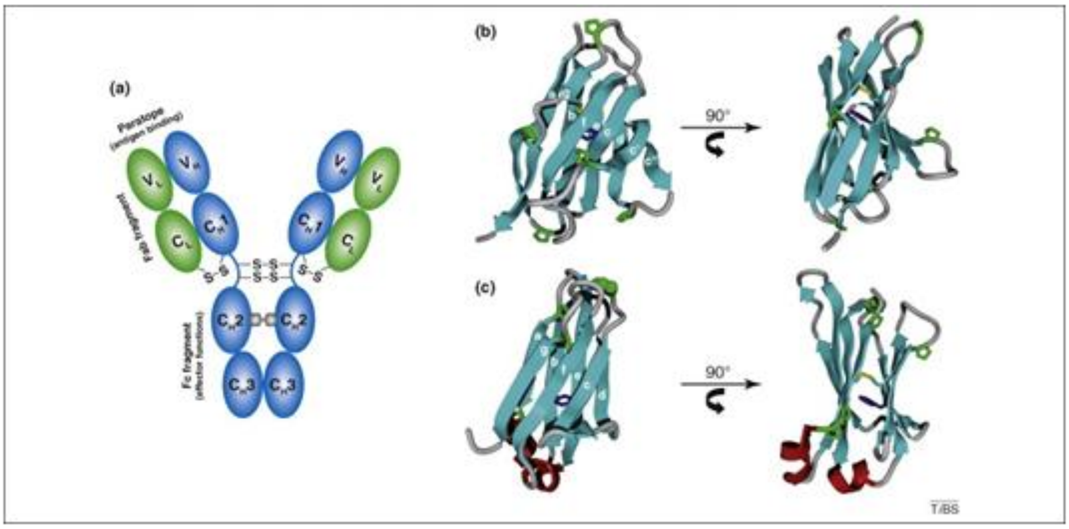

Figure 1.7: Overall structure and domain architecture of antibodies. Domain arrangement of an IgG antibody molecule. The light chains are shown in green, the heavy chains in blue (**a**). Domain architecture of the light chain variable (VL) **(b)** and constant (CL) domains **(c)** **[58]**.

The antibody structure is characterized by two variable domains, one belonging to the heavy chain and the other one to the light chain (V_H and V_L domains respectively), and four constant domains: the C_L of the light chain and the C_H1 of the heavy chain constituting the C-terminal region of Fab, and the C_H2 and the C_H3 domains constituting the Fc. At the N-terminal tip, the Fv of the Fab fragment contains the complementarity determining regions (CDRs) which are strictly involved in the interaction with the antigen, displaying a surface equated with the counterpart of the antibody, represented by the paratope **[59]**.

The CDRs, also known as hypervariable regions, are three on each variable domain: L1, L2 and L3 on the V_L domain, and H1, H2 and H3 on the V_H domain. The CDR regions are connected by the non-hypervariable or framework regions (FRs), four on each domain, that differ in length and composition among all the antibodies and that are crucial to stabilize the whole structure of the Fab fragment. The CDR loops differ for extent and conformation depending on the nature and number of amino acids in the segment, allowing a high variability in the topography of the CDR surface, that is characterized by depressions and protrusions and may contain a deep pocket or cleft or a protuberance. The plasticity of the combining site allows the IgG molecule to assume different conformations, in an “induced fit” manner. Instead, the flexibility of IgG molecule is provided by the hinge region between the Fabs and the Fc and the switch regions within each fragment, allowing rotation movements **[60-62]**.

The intra-chain disulfides of the HC and LC domains for the four IgG isotypes are similar while the inter-chain disulfide bridges arrangements are different, on the basis of the different amino acid composition of the hinge region and the number and position of the Cysteine residues. Both IgG1 and IgG4 have two disulfide linkages between their HC, whereas, IgG2 and IgG3 have four and eleven, respectively. The inter-chain linkage between the HC and the LC of IgG1 is established between the C-terminal Cysteine belonging to the LC and the first Cysteine of the hinge region, whereas, IgG2, IgG3 and IgG4 possess this linkage between the terminal Cysteine of the LC and the Cysteine in the Fab region (N-terminal of the C_H1 domain). The variation in hinge length and amino acid sequence in the different heavy chain classes and isotypes affect the different rotational adaptability, resulting in different spacing and orientations of antigenic determinants by the immune system **[63-67]**.

The IgGs represent the preferred class to be developed as therapeutics, on the basis of their more favourable features compared with the other classes, although the IgG3 are not used as therapeutic candidates because of their shorter half-life and their long hinge region, that is easily accessible to proteases and allotypic polymorphism **[68]**.

4.2 monoclonal antibodies: development as therapeutic tools

a) From murine to human monoclonal antibody

The most common method to generate murine monoclonal antibodies is the hybridoma technology, developed by Köhler and Milstein in 1975 **[69]**. This procedure is based on the fusion of myeloma cells with B cells from mice spleen, generating cell hybrids, capable to ensure a continuous production of fully-murine antibodies. 11 years after, Muromonab-CD3 was approved by FDA as the first monoclonal antibody in treatment of transplantation rejection (DB00075). Next, to reduce the murine portion, "chimeric antibodies" were generated in mammalian cell lines, exploiting the technique of cloning out murine V_H and V_L genes, by PCR technique, leading to antibodies composed of murine V_H and V_L chains fused with human constant regions **[70]**. Rituximab is an example of the first chimeric anti-CD20 monoclonal antibody approved in 1994 for the treatment of lymphoma **[71]**. However, chimeric antibodies, because of their one-third murine portion, did not completely avoid the enhanced immunogenicity. Thus, to overcome this limitation the next step was grafting the CDR regions from a murine antibody into the closely related human framework, to obtain the so-called “humanized antibody” **[72]**. Daclizumab (anti-CD25) was the first humanized mAb introduced in 1997 as biotherapeutic agent to suppress rejection after transplantation. The generation of “fully human antibodies” was the final step to completely remove murine sequences, performed predominantly by the phage display technique, described for the first time by Smith in 1985 and by transgenic human mice **[73]**. Adalimumab, introduced in clinic in 2002, was the first fully human antibody generated by phage display technology, while Panitumumab, marked in 2006, represented the first fully human mAb generated in engineered mice.

b) Pharmacokinetic and Pharmacodynamic properties of IgGs

Antibody uptake by the tumor depends on a subtle balance between efficient penetration and retention in the targeted tissue, and mAbs properties, including molecular size, shape, affinity and valency **[74]**.

As well known, mAbs are large molecules characterized by very long serum half-life, since they exceed the renal clearance cut-off (~70 kDa), preventing their elimination through the kidney glomeruli. Another factor that affects the mAbs serum half-life is the interaction of Fc portion with the neonatal Fc receptor (FcRn) expressed at the surface of several cell types, including vascular endothelium cells, monocytes and macrophages as well as at sites with barrier such as the blood–brain interface, the glomerular filter in the kidneys and the intestinal epithelium **[74]**.

Firstly, IgGs bind to FcRn at low pH, secondly the complex is carried back to the cell surface, where upon it dissociates at neutral pH. FcRn therefore functions as a protective carrier that shuttles IgG molecules away from the lysosome and back into the serum, ensuring a longer serum half-life. Although these pharmacokinetic advantages, even some restrictions may be related to the large size and Fc portion of mAbs **[75]** .

Furthermore, generally mAbs used in cancer therapy are required to exhibit high tissue and extracellular matrix penetration -excluding the case of hematological malignancies and diseases- to ensure high efficiency of the treatment. However, other important issues to be considered are represented by tumor heterogeneous and tortuous vasculature, high interstitial fluid pressure and high viscosity of the tumor blood. Thus, to penetrate tumors, mAb molecules need to fight against the high pressure gradient generated by the tumor environment **[76].**

The diffusion speed through the tumors is mainly affected by the mAbs size, thus, since the rate of diffusion is inversely proportional to their molecular weight, they generally exhibit poor tumor penetration. In addition to the size, another relevant factor is the '*binding site barrier effect'* which can further decrease their tumor penetration **[77]**. This effect is due to the fact that antibodies endowed with high affinity toward the proper antigen, strongly bind it at the first encounter, thus they cannot penetrate deeper inside the tumor until all antigen molecules are saturated in the periphery. Thus, antibodies possessing a moderate binding affinity to the antigen are more suitable because they can be released from the first encounter and penetrate deeper into the tumor, allowing uniform distribution through the tumor mass and higher tumor uptake. In addition to these parameters, uptake and retention of the mAbs by the tumor depend even on further factor, such as antigen density, internalization, association and dissociation rates **[78].**

Furthermore, employing of antibodies as therapeutic tools even requires a suitable half-life in the human body, regulated by the combination of several processes, including absorption, distribution, metabolism and excretion. However, the hal-life property is not universally shared by all the IgGs, since it is a function of their different affinity to the neonatal Fc-receptor (because of their different glycosylation status), which in turn depends on their isotype: IgG1, IgG2 and IgG4 exhibit a half-life of approximately 21 days, while for IgG3 is only 7 days.

Moreover, the half-lives of therapeutic mAbs generally increase with the degree of humanization: murine mAbs exhibit a hal-life of 1.5 days, while for the chimeric mAbs is 10 days, finally humanized and fully human share a comparable half-life of about 15-20 days **[79].** The shorter half-life of murine mAbs derived by the combination of two factors: the leak of the binding to human neonatal Fc-receptor and the generation of human anti-mouse antibodies (HAMA).

Thus, the elimination of mAbs is a complex multi-factorial process regulated by protein catabolism, interaction with neonatal Fc-receptor, target-mediated elimination, immunogenicity, proteolytic degradation and glycosylation **[79, 80]**.

With regard to the pharmacodynamic properties, although mAbs can exhibit a certain mode of action when tested *in vitro,* the exact mode of action in patients is not always clear.

The simplest mechanism is the binding of the antibody to its antigen, interfering with its activity and/or interaction with binding partners. For instance, the most commonly targeted antigens can be represented by soluble ligands (TNF-α, VEGF) or a receptor exposed at the cell surface (EGFR, HER1, HER2).

Moreover, the *tumour cell killing effect* of monoclonal antibodies can be exerted through a variety of mechanisms, some of them are reported below **[81]**:

1. Direct effect: the antibody activity is elicited through receptor agonist or antagonist activity, resulting in perturbation of signal transduction.

The direct effect is the mode of action of Cetuximab **[82]** and Trastuzumab **[83]**, which are directed against receptor targets, EGFR and HER2 respectively.

2. Immune-mediated tumour activity: this effect is mediated by CDC and ADCC mechanisms, even correlated to the induction of phagocytosis and the immune modulation of T cell function.

The CDC effect (complement-dependent cytotoxicity) is achieved by the interaction of the IgG Fc portion to C1q, recruiting the complement cascade, ultimately leading to the formation of pores in the targeted cell membrane, or recruiting effector cells through interaction with the C4b/C2b/C3b complex bound to the target cell surface and the receptor CR1 (complement receptor) **[80]**.

On the other hand, the ADCC effect (antibody dependent cell-mediated cytotoxicity) is exerted through the binding of Fc portion to the Fcγ receptors. The glycosylation status of IgG1 molecules is a key modulator of the Fc-affinity for FcγRIIIa, related to the *in vivo* efficacy of antibodies **[79]**. Moreover, a relevant restriction is represented by the fact that therapeutic antibodies have to compete with a high concentration of patient's IgGs for binding to FcγRIIIa, requiring high doses to reach a sufficiently high serum concentration. Finally, the therapeutic antibodies may also bind inhibitor Fc receptors such as FcγRIIb, expressed by B-cells, macrophages, dendritic cells and neutrophils that negatively regulate their effector functions **[78]**.

Examples of mAbs currently used in clinical, that exhibit this type of mode of action are represented by Rituximab (anti-CD20) **[84]**, that exerts its effector function mainly through ADCC and Ipilimumab (anti- CTLA-4) **[85]** that induces immune modulation of T cell function.

3. Specific effects on tumor vasculature and stroma: vascular and stromal cell ablation can be induced by vasculature receptor antagonism or ligand trapping; stromal cell inhibition; delivery of a toxin to stromal cells and to the vasculature **[81]**.

Finally, beyond the nature of the target antigen also the safety and efficacy of therapeutic mAbs are important to successfully develop a useful product in oncology. Ideally, the target antigen should be abundant and accessible and should be expressed homogeneously, consistently and exclusively on the surface of cancer cells. Antigen secretion should be minimal, since secreted antigens can bind the antibody in the circulation, preventing antibody from sufficiently binding to the tumor. If the desired mechanism of action is ADCC or CDC, the antigen–mAb complex should not be rapidly internalized so as to provide the maximal availability of the Fc portion to immune effector cells and complement proteins. By contrast, good internalization is required for antibodies or proteins that deliver toxins into the cancer cell (in the case of ADCs) and for antibodies whose mechanism of action is primarily based on the down-regulation of cell surface receptors. Although most of the antibodies that have been successfully used in the clinic are intact IgG molecules, new approaches for antibody engineering and for the delivery of conjugated cytotoxic drugs are widely being proposed **[86]**. The main mAbs approved by FDA in clinical use are listed in Table 1 **[81]**.

Table 1. FDA-approved therapeutic antibodies and Fab fragments

Brand Name	Antibody	Target	Source	Year	Indication
Orthoclone®	Muromonab-CD3	CD3	All rodent	1986	Transplantation rejection
ReoPro™	Abiciximab	GPIIb, IIIa	Chimeric	1994	High-risk angioplasty
Rituxan™	Rituximab	CD20	Chimeric	1994	Non-Hodgkin's lymphoma Rheumatoid arthritis
Zenapax®	Daclizumab	CD25	Humanized	1997	Transplantation rejection
REMICADE®	Inflixinmab	TNF-a	Chimeric	1998	Crohn's disease
Simulect®	Basiliximab	CD25	Chimeric	1998	Transplantation rejection
Synagis™	Palivizumab	RSV F protein	Humanized	1998	RSV infection
Herceptin®	Trastuzumab	HER2	Humanized	1998	Breast cancer
Mylotarg™	Gemtuzumab	CD33	Humanized	2000	Acute myeloid leukemia
Campath®	Alemtuzumab	CD52	Humanized	2001	Chronic lymphoticleucemia T-cell lynphoma
Zevalin®	Ibritumomab tiuxetan	CD20	Murine with yttrium-90 or indium-111	2002	Non-Hodgkin's lymphoma
HUMIRA™	Adalimumab	TNF-a	Human	2002	Inflammatory diseases Autoimmune disorders
Bexxar®	Tositumomab	CD20	Murine with iodine-131	2003	Non-Hodgkin's lymphoma
Xolair®	Omalizumab	IgE	Humanized	2003	Severe allergic asthma
Avastin™	Bevacizumab	VEGF	Humanized	2004	Metastatic colorectal cancer NSCLC Metastatic breast cancer Glioblastoma
TYSABRI®	Natalizumab	α4 subunit of α4β1	Humanized	2004	Multiple sclerosis Chron's disease
Erbitux™	Cetuximab	EGFR	Chimeric	2004	Colorectal cancer Head and neck cancer
Vectibix™	Panitumumab	EGFR	Human	2006	Metastatic colorectal carcinoma
LUCENTIS™	Ranibizumab	VEGF-A	Humanized Fab	2006	Wet macular degeneration
Soliris®	Eculizumab	CD59	Humanized	2007	Paroxysmal nocturnal hemoglobinuria
CIMZIA®	Certolizumab pegol	TNF-a	Humanized Fab	2008	Chron's disease Rheumatoid arthritis
Simponi™	Golimumab	TNF-a	Human	2009	Rheumatoid and psoriatic arhtritis Active ankylosing spondylitis
Yervoy®	Ipilimumab	CTLA-4	Human	2011	Metastatic melanoma
Perjeta®	Pertuzumab	HER2	Humanized	2012	Breast cancer
Kadcyla®	Trastuzumab emtansine	HER2	Humanized ADC	2013	Breast cancer

d) Antibody humanization *iter*

Humanization plays a fundamental role in the development of antibodies as therapeutic agents. Monoclonal antibodies humanization is an essential engineering step required to reduce the immunogenicity derived from non-human sources. The original technique initially developed to humanize antibodies was the ‘‘ *CDRs grafting*’’ of murine CDRs onto human antibody frameworks **[87]**. However, two main issues were generally related to this methodology: defects at the CDR/framework interface and consequently decread affinity of the antibody toward the antigen, thus suggesting that residues non belonging to the CDRs are crucial in maintaining optimal antibody/antigen interface. These residues important for maintaining CDR structures was named ‘‘canonical residues’’**[88].** The next generation approach explored to achieve antibody humanization was the ‘‘*back mutation method*”, based on retaining both mouse CDRs and canonical residues in antibody framework **[89].** For this purpose a three-dimensional structure of the mature donor (non-human) antibody, alone or in complex with the target antigen is required to successfully perform the humanization process. In order to produce a humanized antibody with good stability and/or with target affinity comparable to the mature donor antibody, it may be necessary the design and synthesis of some versions of the humanized antibody, each with a few mutations chosen to resolve any clashes or mismatch between the CDRs and the framework regions **[90].** The traditional way to resolve such mismatches is the so-called “*framework redesign*” method, in which the mature donor CDRs alone is left intact, performing mutations only at some human acceptor framework residues in proximity of the CDRs to the amino acids, located at the corresponding positions in the mature donor framework. Thus, the regions surrounding the CDRs are made more like the mature donor antibody as a scaffold to preserve its CDR structure. A recent alternative method to resolve such mismatches, is the ‘‘*CDR redesign*’’ **[91]** consisting in leaving the human framework intact, while redesigning positions on the backside of the mature donor CDRs to the amino acids found at the corresponding positions in the CDR backsides of the human sequences from which the human acceptor frameworks were taken, or to other amino acids determined by *de novo* design. Thus, the result could be a completely human antibody excepted its mature CDRs.

However, humanized antibodies in some patients can evoke anti-idiotypic (anti-Id) responses, due to their xenogenic CDRs. Thus, a new technique, “*SDR grafting*”, was developed starting from the evidence that only 20–33% of CDR residues are critical in the antigen–antibody interaction **[92].** These residues, located in the regions of high variability and most likely to be unique to each antibody, are called SDRs (specificity determining residues) **[93].** Thus, this strategy consists in grafting only the SDRs of a xenogenic antibody onto the human antibody frameworks **[94,95]**, instead of the entire CDRs.

Once the non-human antibody regions targeted for grafting onto the human FRs (framework regions) have been defined, the second step in a humanization process is to identify the more suitable source of human FR donors. The most common strategies are two: the first, named “*the fixed FR method*”, is based on the use of FRs belonging to human antibodies with known structure, regardless their homology to the non-human antibody **[91]**; the second one, termed “*the best fit method* “, is based on the use of human sequences with the highest homology to the non-human antibody **[96]**.

In general, to achieve an antibody humanization, the interaction of the CDRs to each other and with the rest of the variable region must be preserved, maintaining both framework residues involved in V_L–V_H contact and those affecting the overall domain structure. Both the SDR and CDR grafting procedures require selection of the most appropriate human frameworks to be used as templates, and identification of the framework residues that are critical to the preservation of the structure of the antigen-binding site. When comparing the sequences of the frameworks of the target and the template antibodies, if any of the crucial residues of the target antibody is found to be different from their corresponding residues in the human template, the crucial residues of the target antibody are incorporated in the frameworks of the templates for the final design of the humanized antibody.

With regard to the method chosen to select the human FRs, two sources of human sequences can be used: mature and germline sequences. Mature sequences, which are products of immune system, carry somatic mutations generated by random processes and are not under species selection, resulting in potential immunogenic residues. Thus, to avoid immunogenic residues, human germline genes have increasingly been preferred as source of FR donors.

An alternative method to the CDR grafting is the "*Resurfacing*" **[96]** allows to retain the non-exposed residues of non-human antibody. Only surface residues in non-human antibody are changed to human residues. Since resurfacing does not change the residues in the core of V domains, the expectation is to eliminate potential B-cell epitope, while minimizing the perturbation of residues determining the specificity of antibody.

Finally, following an empirical approach, Dall'Acqua et al. have described a new humanization method called ''*framework shuffling*''**[97],** based on the in which the synthesis of a combinatorial library. This library, constituted by six CDRs (three in the light chain, L1, L2, and L3 and three in the heavy chain, H1, H2, and H3), fused in frame to a pool of individual human germline frameworks, are screened for binding to the antigen of interest. This approach allows the selection of the most favorable combinations of fully human frameworks retaining the binding activity of the parental antibody. Finally, the overall execution of this methodology is highly facilitated since it does not require previous antibody structural studies including CDR analysis or framework design.

d) Development of monoclonal antibodies as biotherapeutics: an overwiew

The successful development of candidate antibodies for the clinic involves a complex process of scientific and preclinical evaluations, informed by deep understanding of cancer biology and the properties of antibodies *in vivo*. Essential preclinical characterization includes: identification of the physical and chemical properties of the antibody; detailed specificity analysis of antigen expression using panels of normal and malignant tissues; study of the immune effector functions and signalling pathway effects of the antibody; analysis of *in vivo* antibody localization and distribution in transplanted or syngeneic tumour systems; antibody chimerization and humanization and evaluation of the *in vivo* therapeutic activity of the antibody either alone or conjugated with radioactive isotopes or other toxic agents **[98, 99]**.

However, one of the most essential steps in the clinical evaluation of a potential therapeutic antibody is the *in vivo* specificity determining the bio-distribution of an antibody (often radiolabelled) in patients to assess the ratio of antibody uptake in the tumor versus normal tissues. This information is essential for the rational design of antibody therapy, for which knowledge about the targeting of normal tissues is crucial for predicting toxicity **[100]**.

Normal tissue distribution can be quantitated, thus allowing the relationship of the loading dose to tumor concentration to be accurately assessed, rather than relying on plasma concentration and clearance rates to establish an optimal dose. In conjunction with other pharmacodynamic studies, including computerized tomography with magnetic resonance imaging, positron emission tomography, plasma-based protein, cell and genomic analyses, and tumour biopsies, the effect of antibody abrogation of a signaling pathway function can also be determined **[101]**.

I.5 ANTIBODY FRAGMENTS PRODUCTION: ADVANTAGES AND LIMITATIONS

Considering the limitations and disadvantages due to a full-size antibody molecule, such as high molecular weight, poor tissue penetration and immunogenicity, many attempts have been performed in the last past decades to generate antibody fragments so as to improve the efficiency of these molecules as diagnostic and therapeutic tools **[101]**. Two different approaches can be used to obtain fragments from the parental antibody: through proteolytic fragmentation by specific enzymes or through DNA recombinant technology.

The most common types of antibody fragments generated by enzymatic procedures are Fab, (Fab')$_2$ and Fab'**[102]**. However, the enzymatic approach is commonly used when the final aim is a biochemical characterization of the final product, including the structural study of the distinct regions of an immunoglobulin, crystallization study of the Fab-antigen complex and in some cases use of a cognate Fab to help the crystallization of proteins **[103]**. On the other hand, the recombinant approach is universally used to develop functional fragments as therapeutic tools instead of whole immunoglobulines.

Since antibody genes can now be cloned, the recombinant DNA technology is became an useful tool to express a wide variety of genetically engineered antibody formats, including Fab fragments, Fv fragments and so-called scFv. The most common expression systems are host organisms, including prokaryotic and eukaryotic organisms as well as trangenic organisms.

Among the prokaryotic organisms, ***Escherichia coli***, a Gram negative bacterium, is the most common system for expression of recombinant proteins, ensuring very high volumetric yields **[104,105]**. The major challenges in bacterial Fab fragment expression are the correct assembly of the functional heterodimer and formation of all the disulfide bonds. The key to success was the secretion of both polypeptide chains, light chain and Fd fragment (N-terminal half of the heavy chain) into the periplasmic space of *E. coli* where the oxidizing environment allows the correct formation of disulfide bonds and the assembly to a functional fragment **[106]**. For this purpose bicistronic vectors with the first cistron encoding the light chain and the second cistron encoding the Fd fragment are optimal **[107]**.

Also **Gram-positive bacteria (***Bacillus brevis, Bacillus subtilis* and *Bacillus megaterium)* have already successfully used for the production of different antibody fragments. These bacteria directly secrete proteins into the medium since they lack an outer membrane which could facilitate production of antibody fragments **[108-110].**

On the other hand, eukaryotic cells have developed an advanced folding, post-translational and secretion apparatus which enhance the secretory production of antibody molecules, including full immunoglobulins compared to bacteria.

Pichia pistoris represents the major yeast strain used for recombinant antibody production **[111]**. Also, insect cells represent a very versatile eukaryotic expression system. Insect cell lines (e.g. Sf-9 and Sf-21 of *Spodoptera frugiperda)* can be efficiently transfected with insect-specific viruses from the family of *Baculoviridae*, that are highly species-specific and are considered as safe for humans, mammalian and plants **[112]**.

Today, 60-70% of all recombinant protein pharmaceuticals and 95% of the currently approved therapeutic antibodies are produced in mammalian system despite relatively high production costs and difficulty in handling. However, the advanced mammalian folding, secretion and post-translational apparatus garantee the production of antibodies and their fragments indistinguishable from those in the human body, avoiding immunogenic response.

However, *Chinese hamster ovary (CHO)* cells represent the most common cell line employed in the commercial production of biopharmaceuticals as well as *Baby hamster kidney (BHK)* cells and *Human embryonic kidney cell line HEK293* **[113]**. Although glycosylation patterns of mammalian glycoproteins are very similar to those in humans, even small differences can affect pharmacokinetics and effector functions of antibodies [114]. Finally, the development of transgenic plants for the expression of recombinant antibodies is becoming interesting especially when high amounts are required. Although this expression system exhibits some advantages (higly easily up-scaling of the antibodies production process and lower costs compared to the expression in hybridoma cells), the glycosylation pattern still represents the main obstacle in developing therapeutic antibodie and derivative fragments, compared with the mammalian cells [115].

I.6 NEXT GENERATION ANTIBODY FORMATS

As already mentioned, because of their limited tumor penetration and long serum half-life, antibodies are not suitable for applications such as radioimmunotherapy or imaging. Antibody fragments exhibiting monovalency and limited size can represent a valid alternative so as they are not retained for long time by the antigen and they can be even rapidly cleared by kidneys.

Thus, antibody engineering approach, widely used to produce chimeric or humanized mAbs, has been adapted in order to produce recombinant innovative antibody formats, beyond the most traditional Fab fragment, to retain the binding activity of the intact molecule, but to be more suitable in certain specific applications [116].

The first innovative format, early designed, was the monovalent *scFv* (single-chain variable fragment), consisting of only the variable domains of the heavy and light chains (Fv) linked by a flexible linker [117]. However, because of its very short half-life in serum (~2 h) related to the MW of about 28 kDa, this fragment is not very powerful to be used alone but it has been normally used as a binding element incorporated in more complex molecules.

Thus, an alternative new format has been create, the *Diabodies*, with positive properties, such as bivalency and compact and medium-size (60 kDa). The right compromise between the medium molecular weight and the bivalency provides many advantages, including rapid tissue penetration, high target retention and rapid blood clearance. Given these parameters, diabodies represent promising tools in radioimmunotherapy when labelled with radioisotopes (^{123}I or ^{111}In), or for imaging purposes when labelled with positron emitters (^{64}Cu or ^{124}I) **[118]**.

Furthermore, a new intriguing antibody format is represented by the *single-domain antibodies* (sdAbs) also named "nanobodies" **[119]**, that possess a single variable domain which generates high affinity towards multiple antigens. These molecules consist of small domains (13 kDa) naturally endowed with very powerful characteristics, such as very high stability and the possibility of binding strongly to epitopes not accessible to conventional antibodies such as enzyme active sites. Furthermore, *bispecific antibodies* (bsAb) have been created to generate a format possessing strong and specific binding capability simultaneously to two different antigens **[120]**.

Another interesting next generation antibody format is represented by *intrabodies*, that have been designed to be expressed intracellularly by the incorporation of intracellular peptidic trafficking signals. This allows the antibody to penetrate a cellular compartment (cytosol, nucleus, endoplasmic reticulum (ER), mitochondria) **[121]**, which is normally not enter, where it can interact specifically with the target antigen. Depending on their mechanism, intrabodies can be classified into two categories. The mechanism of the first category is based on the binding to the target within the ER lumen, thus avoiding the target molecule to leave the ER and ultimately to be expressed on the cell surface **[122]**. Moreover, the redox conditions of the ER environment helps the correct formation of disulphide bridges of these intrabodies. By contrast, the second category comprises antibodies expressed on cytoplasmic polysomes and released into the cytoplasm of the cell, thus they need a self-folding ability to correctly fold in the reducing environment of the cytoplasm **[123]**.

As explained previously, the limited size of antibody fragments provides a more rapid and efficient tumor penetration than whole IgG, but this benefit is counterbalanced by a very short serum half-life. A most common strategy exploited to improve the half-life of antibody fragments is the chemical addition of polyethylene glycol (PEG) molecules which notably increase their size and simultaneously provide further advantages, such as longer half-life, stability and decreased immunogenicity. An example of PEGylated fragment is Certolizumab pegol, a FDA- approved anti-TNF-α PEGylated Fab fragment **[124]**. However, since this chemical modifications may lead to partial inactivation or decreased affinity of the fragment, a recently employed alternative approach is represented by the fusion of recombinant antibody fragments to human serum albumin (HSA) to increase the serum half-life without affecting the binding and activity of the fragments **[125]**.

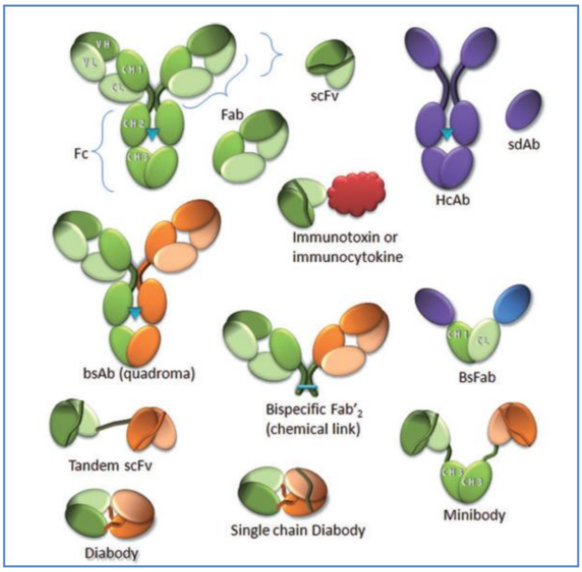

Figure 1.8: Antibody fragments with therapeutic potential. A conventional antibody is illustrated in green. The orange colour symbolizes a different specificity. The red molecule represents a cytokine or a toxin. bsAb, bispecific antibodies; bsFab, bispecific Fab fragment; HcAb, heavy chain only antibodies **[126].**

I.7 ANTIBODY-DRUG CONJUGATES (ADCs)

As said, monoclonal antibodies are an important class of biotherapeutic agents. There are at least 25 antibody-based medicines approved for human therapy and more than 240 antibodies that are being evaluated clinically. Currently also a small number of antibody Fab fragments are used in clinical (Ranibizumab, Certolizumab pegol) and some classes of engineered antibody fragments (scFv, diabodies) are also in development **[127]**.

Although monoclonal antibodies are known to be very useful in cancer treatment, their therapeutic potential is often limited. Thus, the idea of "arming naked" mAbs with bioactive payloads (drugs, cytokines, radionuclides) was realized so as to create the so-called antibody–drug conjugates (ADCs) **[128]**. The ADCs represent an innovative therapeutic approach that combines the high specificity of the mAb portion towards a specific target antigen, with the cell killing activity of cytotoxic drugs, to minimize the systemic toxicity and at the same time to enhance the therapeutic efficiency for patients, leading simultaneously to the gain of a drug-delivery system as well as a *tumor-homing* effect.

The architecture of a typical ADC comprises three elements (Fig. 1.8):

1. a mAb or mAb fragment specific for a target tumor antigen

2. a highly potent cytotoxic agent as payload

3. a linker that enables covalent attachment of the cytotoxin to the mAb.

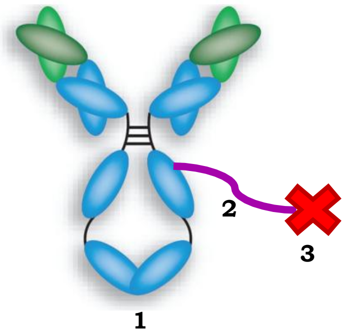

1. **Selectivity**
2. **Connection to antibody portion, polarity, self-immolative spacer**
3. **Citotoxicity**

Figure 1.8: Architecture of an antibody-drug conjugate (ADC).

Critical parameters to the clinical efficacy of an ADC are the target site-specificity and binding properties of the antibody, the *in vitro* and *in vivo* stability of the linker and drug species, the potency of the drug, and both the distribution and average number of drug species on the antibody **[128]**.

The most potent cytotoxic drugs currently used for ADC application, are calicheamicins **[129]**, maytansinoids **[130]** and auristatins **[131]**. One of the critical hallmarks of an ADC is the average number of drugs conjugated because this is highly determinant the amount of "payload" that can be delivered to the tumor cell and can directly affect both safety and efficacy.

The assembly of the ADC from the components is a key step in determining the therapeutic potential of the final product. The conjugation should not alter the integrity of the antibody, the binding of the antibody to the antigen or the biological activity of the drug upon reaching the target cells. Usually, three common methods are reported for conjugation of mAbs to the drug: alkylation of reduced interchain disulfide bridges, acylation of Lysines, and alkylation of genetically engineered Cysteines. The first of two mentioned strategies generate heterogeneous products, with variations in the number of molecules of drug per antibody and in the sites of attachment. The third strategy, instead, allows the specific insertion of Cysteines into the mAb backbone by recombinant methodology, so as to obtain uniform conjugated mAbs **[132]**.

An innovative and very intriguing strategy is the conjugation via enzymatic reaction performed by the TGase (protein glutamine γ-glutamyltransferase, EC 2.3.2.13). This enzyme catalyzes acyltransfer reactions between the γ-carboxamide group of Glutamine (chemically inert under physiological conditions) and the primary ε-amino group of Lysine, to form catabolically stable isopeptide bonds, leading to a highly efficient site-specific and stoichiometric functionalization of antibody molecules **[133]**. The usefulness of this enzyme is the versatility of the reaction because it may be exploited in ADC generation as well as to create new antibody formats, for instance a bivalent fragment when two Fabs from the same antibody are linked or a bispecific fragment when two Fabs from two different antibodies are connected.

Furthermore, the choice of suitable linkers is determinant for the performance of ADC product, since it affects the release of the drug upon reaching the target cells.

Thus, the linker must be extremely stable in systemic circulation, avoiding nonspecific cell killing and toxicity effects due to the premature release of the cytotoxic payload before reaching the target. However, the linker must be labile enough to allow efficient release of the cytotoxic drug in its active form inside the targeted tumor cells, achieving the cell killing **[134,135]**.

The linkers currently used are grouped into two categories: cleavable and noncleavable linkers. More exactly, the cleavable ones are in turn classified into three sub-groups, depending on their cleavage mechanism: i) acid labile hydrazone linkers, ii) disulfide-based linkers, iii) linkers based on p-amino benzoic acid (PBA), a molecular moiety that, following cleavage of a peptide bond by cathepsins, undergoes a rearrangement that expulses the entire linker. This technology is patented by Seattle Genetics and licensed to companies that want to make use it (http://www.seattlegenetics.com/adc_technology).

Two different approaches can be used to target tumor tissues via ADC products. When the tumor-associated antigens are expressed on the surface of cancer cells – in the case of receptors- the ADCs typically require internalizing mAbs, uptaken by cells via receptor-mediated endocytosis and subsequently by different chemical mechanisms, the drug is released **[136]**. However, targeting antigens on tumor cells exhibit physical and kinetic barriers correlated to large solid tumors, and to the potential down-regulation of tumor-associated antigens targeted by the immunoconjugate. Thus, to overcome this limitation, an alternative approach has been developed, targeting markers expressed on tumor neo-vasculature, more easily accessible, requiring non-internalizing antibodies. Remarkably, since angiogenesis is a common feature of all malignancies and tumors express common markers of angiogenesis, a single agent should be exploited in a wide range of tumors **[137, 138]**.

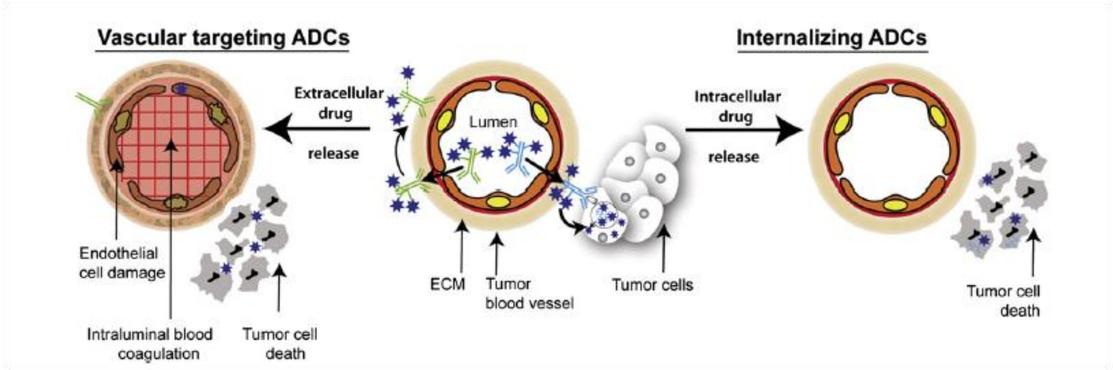

Figure 1.9: Illustration of the two possible strategies used for the delivery of the ADCs and their effect on the tumor cells. (Left) ADCs specific to markers of angiogenesis expressed on the endothelial extracellular matrix (green).(Right) ADCs containing internalizing mAbs (blue) **[135]**.

A further important aspect to be considered is the pharmacology of the ADCs. Ideally, an ADC acts as an inactive pro-drug when in the bloodstream and only upon internalization into target cells or localization to the tumor becomes an active released drug. However, only a small amount of the ADC effectively reach the target cells, thus a highly potent drug is desired. The remaining drug undergoes catabolic processing in normal tissues, causing exposure to the released drug. Thus, an optimal drug for ADCs should not exhibit a long residence time after releasing in normal tissues, while maintain a high concentration in the tumor for an extended time.

Finally, the size of the ADC delivery vehicle also plays an important role in how effectively drug is delivered to tumors **[139, 140]**. A successfully developed ADC is Trastuzumab emtansine **[141]**, the first ADC approved by FDA in treatment of HER2 positive metastatic breast cancer, which consists of the full antibody conjugated to DM-1 toxin.

More recently, the development of a Fab ADC, composed of an anti-c-Met Fab conjugated to Doxorubicin, has been reported, as a promising therapeutic tool in hepatocellular carcinoma (HCC) **[142]**.

I.8 AIM OF THE RESEARCH PROJECT

The main aim of this research project is the development of functional monoclonal antibodies and their fragments, to be employed as powerful diagnostic and therapeutic tools to target human CR-1 protein, which is over-expressed in a broad range of human solid tumors. The specific target pathway involves the interaction of CR-1 with its trans-membrane receptor ALK4, which triggers a series of downstream events that ultimately lead to tumor growth and progression.

Thus, blocking molecules are required to possess high selectivity and affinity toward the CFC domain of CR-1, which is directly involved in the binding to the receptor. Moreover, these molecules need to specifically recognize H120 and W123, known to be "hot spots" for the CR-1/ALK4 interaction. The molecules will be initially tested on cancer cell lines to evaluate their potential as effective anti-tumour agents. We will reach this goal by generating monoclonal antibodies against the CFC domain of human CR-1 and characterizing them for their affinity and selectivity toward the protein. We will also undertake structural and functional studies using the antibodies and their fragments to gain insights into the interacting surfaces and to improve selectivity and affinity.

We will also proceed with a step of partial humanization of the antibody to obtain a molecule with the potential of being used in humans. We will also investigate the feasibility of generating Antibody Drug Conjugates (ADCs), a new powerful approach in oncology, to overcome the limitations of monotherapies which are generally not sufficient for a cell killing effect on tumor cells. This will be achieved by arming the "naked" mAb with a potent cytotoxic agent, linked selectively to the antibody on specific sites.

This goal will be achieved by an innovative conjugation strategy via the M-TGase enzyme. These functionalized antibody or fragments will be used to increase specificity by exploiting the "tumor homing" effect driven by the antibody, providing the drug selectively into tumor cells over-expressing human CR-1, so as to minimize the cross-reactivity with healthy tissues.

CHAPTER II

MATERIALS AND METHODS

II.1 MATERIALS AND CHEMICALS

Protected amino acids for peptide synthesis and coupling agents were purchased from GL-Biochem (Shanghai, PRC), and IRIS Biotech GmbH (Marktrewitz, DE). The RINK amide resin was from Novabiochem (Darmstadt, DE). Solvents, including CH_3CN, DMF and CH_3OH were from ROMIL (Dublin, IRL). The instruments used throughout the peptide generation and characterization were Syro system (MultiSynTech, DE), LC8 Shimadzu HPLC system (Shimadzu Corporation, Milan, IT) and Waters e2695 (Alliance HPLC). For analytical HPLCs an Agilent 1100 system was used. DTT, DMSO, BSA and KLH were provided by Sigma-Aldrich (Milan, IT). Nunc MaxiSorp 96 multi-well plates were purchased from Thermo Scientific (DK). All chemicals used for ELISA assays were provided by Sigma-Aldrich. Microplate plate washer and reader were supplied by BioTek (Winooski, VT, USA).

All the chromatographic columns and AKTA FPLC system were provided by GE Healthcare Life Sciences (Milan, IT). All certified reagents used to perform SPR analyses and Biacore3000 instrument were supplied by GE Heatlhcare Life Sciences. All the chemicals used for electrophoresis and western blot analyses were supplied by Bio-rad (Milan, IT), thereby APS and TEMED were provided by Sigma-Aldrich. Recombinant proteins were purchased from R&D Systems (Minneapolis, MN, USA).Transcriptor High Fidelity cDNA Synthesis Kit (Roche, CH) was used to perform RT-PCR reaction.

All the enzymes used to treat the 1B4 antibody and all the reagents used throughout the digestion reaction were supplied by Sigma-Aldrich.The synthetic gene was purchased from MWG Eurofins, the pET-26b(+) vector was supplied by Novagen and the restriction enzymes, *BlpI* and *KpnI* were provided by New England biolabs.

II.2 METHODS

2.1 CHEMICAL SYNTHESIS, PURIFICATION, CHARACTERIZATION AND REFOLDING OF HUMAN CFC DOMAIN AND ITS MUTANTS

a) Solid-phase peptide synthesis and purification

All peptides were synthesized by using an automatic Syro system. The wild-type human CFC domain, denoted as hCFC[112-150], and its three variants were prepared by step-wise solid phase synthesis as C-terminally amidated derivatives following standard Fmoc chemistry protocol. A Rink-amide MBHA resin (substitution 0.53 mmol/g) and amino acid derivatives with standard protections were used in the synthesis. Each synthesis was performed starting under canonical conditions of peptide synthesis (HATU/DIEA pre-activation, 5-fold excess of Fmoc-protected amino acids). Coupling and deprotection cycles were kept at 25 and 15 min, respectively. Standard side-chain protection groups for Fmoc chemistry were used for all residues; the Cysteines were introduced as trityl (Trt) derivatives, thus generating after cleavage free thiol groups.

Finally, acetylation was performed using acetic anhydride at 0.5 M in DMF with 5% DIEA, 20 min at rt. The cleavage of peptides from the solid support was performed by treatment with a TFA/TIS/water (90:5:5, v/v/v) mixture for 2h at rt, affording the crude peptides after precipitation in cold diethyl-ether. The precipitates were dissolved in water and were finally lyophilized. Products were opportunely reduced with DTT and then purified to homogeneity by RP-HPLC using an ONYX monolithic C18 column (100 x 10 mm ID) applying a linear gradient of 0.05% TFA in CH_3CN from 10% to 60% over 20 min (flow rate at 20 mL/min) using a LC8 Shimadzu HPLC system.

b) Refolding procedure

Refolding reactions were carried out using each polypeptide opportunely reduced and purified, to avoid peptide aggregation and to increase the yield of the final product. Peptide refolding was achieved at the concentration of 0.05 mg/mL under slightly basic conditions, using 10 mM bicarbonate buffer, pH 9.0. For each peptide, refolding was complete at least in 3h as monitored by RP-HPLC using an ONYX monolithic C18 column (50 x 2 mm ID) applying a linear gradient of

0.05% TFA in CH_3CN from 5% to 70% over 10 min (flow rate 0.6 mL/min) using a Waters e2695 instrument provided of a 2998 PDA detector.

The reaction was stopped by acidification. After lyophilization, each refolded polypeptide was purified again as described in the previous section. For each polypeptide, purity and identity were confirmed by LC-ESI-TOF-MS analysis.

c) Peptides identification by LC- ESI-TOF-MS analysis

Mass spectrometry analyses were performed with an Agilent 1290 Infinity LC System coupled to an Agilent 6230 TOF. The liquid chromatographic Agilent 1290 LC module was coupled with a PDA detector and a 6230 time-of-flight MS detector, along with a binary solvent pump degasser, column heater and autosampler. Based on manufacturer’s recommendations, the pump was connected to a gradient binary solvent system: A, 0.01% TFA/H_2O (v/v) and B, 0.01% TFA/CH_3CN (v/v). The mobile phase was programmed consecutively in linear gradients over the different samples. Chromatographic analyses of hCFC domains were performed using an Agilent Extend Zorbax reverse phase C18 column applying a linear gradient of CH3CN, 0.01% TFA from 5% to 70% in 10 min or 20 min. The column flow rate was kept at 0.2 mL/min with the heater at a constant 20 °C. UV spectra were monitored in the range of 200 nm and 400 nm. Injection volume was 1 μL for each sample, followed by needle wash. The mass analyzer Agilent 6230 TOF-MS was set to operate in positive ion scan mode with mass scanning from 100 to 3200 m/z. The ion source was upgraded from the original Agilent Jet Stream (AJS) source to the dual-sprayer version for improved reference mass delivery. Nitrogen was used as the drying and nebulizer gas. The instrument acquired data using the following parameters: drying gas temperature, 325 °C; drying gas flow, 10 L/min; nebulizer, 20 psi; sheath gas temperature, 400 °C; sheath gas flow, 11 L/min; VCap. 3.500 V; nozzle, 0 V; fragmentor, 200 V; skimmer, 65 V; and octapole RF Vpp was 750. The instrument state was set up to extended dynamic range mode (2 GHz). Tuning and calibration were performed before sample running. Data collection and integration were performed using the MassHunter workstation software (version B.05.00). Data were stored in both centroid and profile formats during acquisition. A constant flow of Agilent TOF reference solution through the reference nebulizer allowed the system to continuously correct for any mass drift by using two independent reference lock-mass ions, purine (*m/z* 119.03632) and HP-922 (*m/z* 922.000725), to ensure mass accuracy and reproducibility. Target compounds were detected and reported from accurate-mass scan data using Agilent MassHunter Qualitative software.

2.2 GENERATION AND PRODUCTION OF ANTI-CFC MONOCLONAL ANTIBODIES

a) Antigen preparation: conjugation of hCFC peptide to KLH and BSA

The conjugation reaction was carried out mixing 1.0 mg of synthetic wild-type hCFC[112-150] N-terminal free polypeptide in 1 mL of 20 mM phosphate buffer, pH 7.0, with 3.0 mg of KLH carrier protein in 1.0 mL of 20 mM phosphate buffer, pH 7.0, and 0.2% v/v glutaraldehyde solution. The mixture was left under stirring for 3h, and then 1.0 mL of 1.0 M Glycine in water was added to block the reaction. The solutions were extensively dialyzed against PBS buffer, pH 7.4 and lyophilized. The amount of peptide-protein conjugate was determined by the Bradford assay, using Bio-rad kit (Bio-rad). The same procedure was used to conjugate the hCFC[112-150] to BSA and to prepare self-conjugated BSA (BSA_2), without adding peptide solution.

b) Mice immunization and hybridoma cell generation

Murine monoclonal antibodies were generated in the laboratory of Prof. Antonio Leonardi at University of Naples “Federico II”, Department of Molecular and Cellular Biology and Pathology. The procedure was in accordance to that one described by Köhler and Milstein **[69]**.

BALB/c mice were housed and handled according to the institutional guidelines.

Four-five weeks old Balb/c mice (Jackson Lab) were immunized with 50 μL of suspension containing about 100 μg of incomplete Freund's adjuvant (TiterMax Gold Adjuvant, Sigma-Aldrich)-emulsified KLH-conjugated synthetic wild-type hCFC[112-150] peptide mixture. Two independent injections were carried out sub-cutaneously with 25 μL of immunogen. Before immunization, 250 μL blood samples were taken from each mouse from the caudal vein and used as the pre-immune control (T_0 samples). Mice were again immunized with the same amount of immunogen at day 30 after the first immunization (T = 30d), at day 40 (T = 40d) and at day 60 (T = 60d). A final antigen boost was administered intravenously 20 days before animals were sacrificed and splenectomised. Blood samples were taken from the caudal vein (250 µL) before every subsequent immunization and tested by ELISA to monitor the increase of antibody titer compared to the pre-immune serum. Mice showing the highest antibody titer were sacrificed and splenectomised.

Three days after the boost, spleen cells were collected by surgery from an immunized mouse sacrificed by CO_2 inhalation and for which all efforts were taken to reduce animal suffering; the spleen cells were then fused with myeloma SP2/0 cells in 50% PEG pH 7.4, the fusion solution to generate hybridomas. The splenocytes were fused at a ratio of 5:1 with the mouse plasmacytoma cell line SP2/0 (ATCC) using RPMI-GM containing PEG 1300-1600 (Hybri-Max, Sigma-Aldrich) and 7.5% DMSO, following the standard procedure described by Köhler (1975). The fused hybridoma cells were re-suspended in 30 mL of selection medium consisting of RPMI–GM medium containing PEG 1300-1600, 10% FCS, 100 U/ml penicillin, 100 µg/mL streptomycin, 100 µM hypoxanthine, 16 µM thymidine and 400 nM aminopterin (RPMI-HAT Sigma-Aldrich). The cell suspension (100 µL) was dispensed into 96-well plates and incubated at 37 °C in a 5% CO_2 atmosphere. After 12h, an additional volume of 100 µL of selection medium was added to each well. After 24h, half the medium from each well was removed, and fresh selection medium was added. Every 2 or 3 days, medium was replaced with fresh selection medium. After 10 days, aminopterin was omitted from the medium. Between the 12th and 14th day, supernatants from the 96-well plates were collected and screened by ELISA assay. Hybridoma clones with strong reactivity versus the hCFC peptide were re-cloned twice by limiting dilution, and their reactivity was re-confirmed by ELISA assays.

c) Antibody production

Sub-cloned hybridoma cells were cultured in OPTI-MEM medium containing 10% FCS, adapted gradually to serum-free cell medium, and then transferred to the Bioreactor (INTEGRA Biosciences AG, CH-7000 Chur) for large scale production.

d) Isotypization

Isotype of selected monoclonal antibodies was determined by using the commercial kit specific for murine antibodies, in accordance to the manufacturer's instructions (Pierce Rapid Mouse antibody Isotyping kit, Thermo scientific).

2.3 ELISA assays

a) Titration of antibodies

To determine the antibody titer in mouse sera, 96-well plates were coated with 100 μL of hCFC[112-150] 0.5 μg/mL (110 nM) in PBS, pH 7.4, and incubated o.n. at 4 °C. The excess of ligand was removed from the wells by applying a three washes cycle with PBS-T (containing 0.05% Tween 20). Non-specific sites of the plate were blocked with 2% BSA and incubated at 37 ºC for 60 min. Wells were then washed 3 times again and ascitic fluid was added to the wells in three fold serial dilutions starting from 1:100 up to 1:100000. The plate was incubated at 37 °C for 1h and washed again with PBS-T. Then, 100 μL of a 1:1000 dilution of HRP-conjugated rabbit anti-mouse Ig (1.0 mg/mL, 170-6516 Bio-rad) were added to the wells and incubation was carried out for 1h at 37 °C. After washing, 100 μL of ABTS substrate solution was added to each well. After 15 min, the reaction was stopped by adding 100 μL of 1% SDS solution in water to each well. OD was measured at 415 nm. Antibody titers were evaluated sufficiently high when the average absorbance values from triplicate wells incubated with immune sera dilutions at 1:10000 were at least thrice than those determined on wells incubated with the pre-immune serum.

b) Hybridoma supernatants screening

After hybridomas generation, supernatants were screened simultaneously using the wild-type antigen peptide, hCFC[112-150] and the hCFC[112-150]W123A variant, in which the Triptophan123 was mutated to Alanine residue (Trp123Ala or W123A). 96 multi-well plates were coated with 100 μL of the antigen peptide solutions at a concentration of 1 μg/mL (220 nM) in PBS, pH 7.4, and incubated o.n. at 4 °C. Hybridoma supernatants, diluted in PBS pH 7.4, were tested at a single concentration of 5 µg/mL (33 nM considering the IgGs fraction). To detect the antigen-antibody interaction, 100 μL/well of GAM-HRP (170-6516 Bio-rad) secondary antibody were added, using a 1:1000 dilution (1 μg/mL). The assay was carried out as described above, except for the detection performed by OPD substrate kit. A peroxidase substrate solution (prepared by dissolving OPD at 0.4 mg/mL in 0.1 M citric acid and 0.2 M Na_2HPO_4 buffer, pH 4.8, and adding 0.2 mL of 30% H_2O_2) was added to each well (100 μL) and when the orange color was sufficiently visible, 2.5 M H_2SO_4 (50 μL) was added to stop the enzymatic reaction, as indicated by the solution turning yellow. The plates were read at 490 nm.

c) Epitope mapping assay

Likewise, epitope mapping was also carried out by ELISA, coating on plates 100 μL/well of the synthetic wild-type hCFC[112-150] and its three variants (hCFC[112-150]H120A;hCFC[112-150]W123A;hCFC[112-150]H120AW123A) at a concentration of 0.5 μg/mL (110 nM) in PBS, pH 7.4, incubating o.n. at 4 °C. Dose-dependent assays were performed using 10D1 and 1B4 mAb solutions (100 μL/well), diluted in PBS, pH 7.4, ranging from 0.07 μg/mL (0.5 nM) up to 2.5 μg/mL (17 nM).

d) Binding assays of 1B4mAb and its recombinant fragments on hCFC[112-150] antigen polypeptide

Dose-response comparative binding assays on the hCFC antigen were conducted with the full-size 1B4 antibody and its recombinant new formats (*r*Fab and *r*Fab_2). Plates were coated with 100 μL/well of synthetic hCFC[112-150] at 0.5 μg/mL (110 nM) leaving in incubation o.n. at 4 °C. The analyte solutions (100 μL/well) were used at increasing concentrations. Both ligand and analyte solutions were prepared in PBS, pH 7.4.

e) Specificity ELISA assays on *rh*CR-1/*rm*Cr-1

This assay was performed to evaluate the cross-reactivity and to assess the specificity of the two selected mAbs, named 10D1 and 1B4, and subsequently of the 1B4 *r*Fb4 and 1B4 *r*Fab_2, towards the human form of Cripto-1. The recombinant human Cripto-1 protein (*rh*CR-1, 145-CR-010/CF R&D Systems) was expressed in baculovirus-derived *Spodoptera frugiperda* Sf21 cells as Leu31-Thr172 & Ser63-Thr172 variants and recombinant mouse Cripto-1 (*rm*Cr-1, 1538-

CR-010/CF, R&D Systems) protein was expressed in the mouse myeloma cell line, NS0 derived, as Arg26-Gln50 and added of a 6 x His tag. Plates were coated with 100 μL of each protein solution in PBS, pH 7.4, at different concentrations (0.12 μg/mL, 0.25 μg/mL, 0.5 μg/mL to 1 μg/mL), corresponding to a total amount of 12 ng, 25 ng, 50 ng and 100 ng respectively, to explore the minimum amount detectable. Full-size antibodies were used at a concentration of 6.7 nM, otherwise the 1B4 *r*Fab was tested at 100 nM and the 1B4 *r*Fab$_2$ at 10 nM.

f) ELISA binding assay of *rh*CR-1 to *rh*ALK4 receptor

This ELISA assay was achieved to determine the affinity constant of *rh*CR-1 towards *rh*ALK4 and to set up optimal binding conditions.

*rh*ALK4 (808-AR, R&D systems), was expressed in the murine NS0-derived myeloma cell line as a Fc chimera (residues Leu32 to Glu126) and with a 6 x His fusion tag. For this assay the usual indirect method was used, coating plates with 100 µL of *rh*ALK4 solution at a concentration of 25 nM (considered as dimeric form). *Rh*CR-1 was used at increasing concentrations (0.37 nM; 0.75 nM; 1.5 nM; 3 nM) to obtain a dose-response signal. To detect the binding of *rh*CR-1 to the receptor, the commercial anti-Cripto polyclonal antibody (T4454, Sigma-Aldrich) was used at a concentration of 5 µg/mL (33 nM). This antibody was choosen since it specifically binds the 41-55 region of Cripto-1, so as to not interfere with the binding of CFC domain to ALK4. As secondary antibody, 1: 1000 dilution (1 µg/mL) of GAR-HRP (166-2408 Bio-rad), was used. All ligands, analytes and antibody solutions were prepared in PBS pH 7.4.

g) Capture ELISA for detection of human CR-1 in biological samples

This direct ELISA assay was performed to determine the lowest quantity of *rh*CR-1 detected by the 1B4 mAb, so as to set up preliminary conditions for future assays for the detection of human Cripto-1 in biological samples, including serum and plasma.

The capture system was assembled using in coating 100 µL/well of the commercial anti-Cripto [41-55] polyclonal antibody at a concentration of 6.7 nM. 100 µL of *rh*CR-1 were added to each well at concentrations ranging between 0.007 µg/mL and 0.06 µg/mL, corresponding to 0.7 ng up to 6 ng. The incubation time period was 1h at rt followed by 1h at 37 °C. Next, to detect *rh*CR-1, 1B4 mab was used at 3 nM and the 1:5000 dilution of GAM-HRP secondary antibody was finally added. All the solutions were prepared as usual in PBS buffer, pH 7.4.

The antigen-antibody complex was detected by using TMB (100 µL/well) as chromogen. After yielding a blue color, the reaction was stopped adding 0.18 M H_2SO_4 (50 µL/well), turning the blue color to yellow. Finally, the absorbance was read at 450 nm.

For all ELISA assays washing cycles were performed using a microplate washer and the Abs measurements were conducted using a multi-well plate reader.

Moreover, the evaluation of all data extrapolated from ELISA assays and the dose-response curves fitting, carried out following a non-linear regression method, were achieved using the GraphPad Prism software, version 5.0.

2.4 PURIFICATION OF ANTI-CFC MONOCLONAL ANTIBODIES

Mouse monoclonal antibodies were efficiently purified from the supernatant of hybridomas by two-step procedure including an affinity chromatography on protein G column and a size-exclusion chromatography by using an AKTA FPLC system.

The supernatant, clarified by centrifugation at 4000 rpm for 20 min at 4 °C and filtering through a 0.45 µm filter to remove cells, debris and other impurities, was loaded on protein G column previously equilibrated in PBS, pH 7.4 (binding buffer); 0.1 M Glycine, pH 2.7 (elution buffer) was used to elute bound proteins. The amount of loaded sample was always about 2 mg to not exceed the binding capacity of the column. All the purification processes were performed at a constant flow rate of 0.6 mL/min. The flowthrough fraction was washed away by the binding buffer until the UV absorbance, monitored at 280 nm, reached the baseline, otherwise the bound fractions, containing the IgGs, eluted with strong acidic elution buffer, were immediately neutralized by adding 2 M Tris-HCl, pH 9.0. Pooled purified fractions were concentrated and at the same time buffer-exchanged into PBS, pH 7.4, using cut-off 50 kDa Vivaspin at 4000 rpm at 4 °C.

The next purification step was performed by SEC on a Superdex 200 (10/300 GL) column, using PBS, pH 7.4, as elution buffer, at a constant flow rate of 0.5 mL/min, with a length of elution of 25 mL, monitoring the absorbance at 280 nm.

After elution, purified IgGs were concentrated, quantified by Bradford assay and analyzed by SDS-PAGE on 10% polyacrylamide gel under non-reducing conditions. Gel staining was achieved by Coomassie Brilliant Blue.

2.5 SPR BINDING ASSAYS

All SPR analyses were performed on a Biacore 3000 instrument from GE Healthcare, using CM5 sensor chips and certified HBS-EP buffer (10 mM HEPES, pH 7.4, 150 mM NaCl, 3 mM EDTA, 0.005% surfactant P20), at 25 °C. The immobilization procedures were carried out following the canonical amino coupling chemistry, operating at a flow rate of 5 µL/min, using the Wizard application. The chip surface was activated by a 50:50 (v/v) EDC/NHS mixture (containing 0.4 M EDC and 0.1 M NHS) with a contact time of 7 min; next, the ligand opportunely diluted in the pre-selected NaAc buffer (through a pH scouting procedure) was coupled until the desired level was reached; the remaining active esters were blocked with 1 M ethanolamine-HCl, pH 8.5.

The optimal immobilization level of each ligand protein, expressed as RU, was calculated on the basis of the following formula:

Rmax = MW analyte/MW ligand x Immobilized amount x Stoichiometric ratio

For each sensor chip, a non-functionalized channel was used as reference line (blank). All analyses were carried out setting up the same parameters: 25 °C temperature, 20 µL/min constant flow rate, 60 µL volume of analyte solutions opportunely diluted in the HBS-EP at different concentrations. HBS-EP was used as running buffer. NaOH was used as regeneration solution at different concentrations, ranging from 5 mM to 20 mM, depending on the strength of the ligand-analyte interaction.

Ligand-analyte interactions, detectable as association curves followed by dissociation curves, were always monitored for a total time period of 500 seconds.

For every single analysis, experimental sensorgrams were aligned, subtracted of blank signal and overlayed. All mathematical manipulations and fitting were performed using the BiaEvaluation software, version 4.1 from GE Healthcare.

The data provided a good fit when processed assuming a 1:1 Langmuir binding model.

a) Screening of mAbs: dose-dependent binding assays

SPR binding affinity and selectivity measurements of monoclonal antibodies toward *rh*CR-1 were performed immobilizing the protein on CM5 sensor chip.

The immobilization process was efficiently performed using *rh*CR-1 at 5.0 µg/mL in 10 mM NaAc, pH 4.5, reaching a low immobilization level (around 600 RU).

Each monoclonal antibody was tested using a series of concentrations, starting from the lowest corresponding to 0.125 nM up to the highest corresponding to 300 nM.

b) Epitope mapping

SPR technique was even used to define the epitope recognized by the mAbs. For this purpose, CM5 sensor chip was functionalized immobilizing 10D1 and 1B4 mAbs at 5 µg/mL in 10 mM NaAc, pH 5.0, reaching a final immobilization level of 5000 RU. *rh*CR-1 was used as positive control to assess whether the mabs were immobilized with the correct orientation, exposing the Fab regions to the analyte. Dose-dependent assays were performed by injection of wild-type hCFC[112-150] and mutants at increasing concentrations.

c) Binding assay of *rh*ALK4 receptor on *rh*CR-1

The conditions used to functionalize CM5 sensor chip with *rh*CR-1 were the same as reported in the section a). The analyte solutions of *rh*ALK4 were prepared in HBS-EP buffer at increasing concentrations (10 nM, 25, nM, 50 nM, 100 nM). Dose-response assays were carried out by injecting each solution at increasing concentrations.

d) Comparative binding study of 1B4 mAb and fragments

SPR binding assays were performed to compare the affinity of antibodies and related fragments: whole 1B4 mAb, the proteolytically derived Fab, the recombinant chimeric 1B4 *r*Fab and the artifical dimeric 1B4 *r*Fab$_2$. The immobilization procedure was carried out as described previously in section a.

Each analyte was passed on the immobilized protein injecting solutions at increasing concentrations.

2.6 SEQUENCING OF THE Fab FRAGMENT OF SELECTED mAbs

a) RNA isolation from hybridoma cells

The total RNA extraction from hybridomas was achieved by the Trizol methodology.

The hybridoma pellet was re-suspended in 1 mL of Trizol, transferred into a sterile eppendorf tube and left for 5 min at rt. Then, 0.2 mL of 100% chloroform were added into the tube, the resulting mix was left for 2-3 min at rt and centrifuged for 15 min, 12.000 rpm at 4 °C. Following centrifugation, the mixture resulted to be separated into lower red, phenolchloroform phase, an interphase, and a colorless upper aqueous phase. RNA was exclusively in the aqueous phase, while the interphase contained DNA and the organic phase contained proteins. The upper aqueous phase was transferred carefully without disturbing the interphase into a fresh tube and the RNA was precipitated from the aqueous phase by mixing with 0.5 ml of isopropyl alcohol. Samples were incubated at rt for 10 min and subsequently centrifuged at 12,000 rpm for 10 min at 4 °C. The supernatant was completely removed and the RNA pellet was washed once with 75% ethanol, adding 1 mlof 75% ethanol. Then, the samples were centrifuged at 7,500 rpm for 5 min at 4°C. The supernatant was completely removed and the RNA pellet was dried, removing the leftover ethanol by evaporation. RNA was dissolved in a small volume (30 μl) of RNAse free water and was quantified and the purity evaluated on the basis of Abs_{260}/Abs_{280} value. The isolated RNA was subsequently analyzed by electrophoresis analysis on 1.2 % agarose gel, using MOPS as running buffer to check the presence of the two typical ribosomal RNA subunits, 18S and 28S. Before loading onto the gel, samples were heated for 10 min at 55 °C to disassemble the secondary structures of RNA eventually formed.

b) RT-PCR

RT-PCR was achieved as two-step reaction. In the first step a cDNA template from RNA mixture was amplified. A denaturation cycle for 10 min at 65 °C and immediately an annealing cycle at 4 °C was applied to a mixture containing 1 µg of RNA, 60 µM pDN6 random hexamer primer and PCR grade water, reaching a final volume of 11.4 µL. Then, a mix containing Transcriptor High Fidelity Reverse Tran-scriptase Reaction Buffer, 1× conc. (8 mM $MgCl_2$), 20 U Protector RNase Inhibitor, Deoxynucleotide Mix, 1 mM each, 5 mM DTT and 22U Transcriptor High Fidelity Reverse Transcriptase, up to a final volume of 20 µL, was prepared.The enzymatic reaction was performed for 1 h at 42 °C for the elongation cycle, followed by the inactivation of the enzyme for 15 min at 70 °C. The second step was the reaction with DNA polymerase to amplify the heavy and light chains of the F_{ab} fragment of the mAbs using a mix of degenerated primers reported in Tables 2 and 3. The PCR reaction was prepared as following: FastStart Buffer 1x (2 mM $MgCl_2$), 0.2 mM PCR Nucleotide Mix, 2U FastStart Taq DNA Polymerase, 7.5 µM both forward and reverse primers, 1 µL of template cDNA and water, PCR grade, up to a final volume of 50 µL. The PCR cycles and parameters were set up as reported in Table 1. The final PCR products were evaluated by electrophoresis analysis, loading the samples onto a 1 % agarose gel and using TBE 0.5x (45 mM Tris-borate, 1 mM EDTA) as running buffer, to assess the correct size of the amplified regions in term of pairs of bases. The nucleotide sequences were analysed using Finch TV software, aligned using BLAST program and amino acid sequences were derived using the program “Translate” from ExPASy proteomic server.

Table 1. PCR cycle parameters

PCR phase	Temp	Time period	N. of cycles
Initial denaturation	94°C	2 minutes	1 cycle
Denaturation	94°C	15 seconds	10 cycles
Annealing	55°C	30 seconds	1 cycle
Elongation	68°C	30 seconds	35 cycles
Final elongation	72°C	7 minutes	1 cycle
Cooling	4°C		

Table 2. Degenerated primers library of Heavy chain of Fab

	Forward primers	**%**
1	BamH1 5’-cggggatcc CAG GTY CAR CTG CAG CAG YCT GG- 3’	33
2	5’-cggggatcc GAG GTY CAG CTG CAR CAR TCT GG- 3’	28
3	5’-cggggatcc CAG GTG CAG CTG AAG GAG TCA GG- 3’	8
4	5’-cggggatcc GAR GTG AAG CTG GTG GAR TCT GG- 3’	21
5	5’-cggggatcc GAG ATC CAG CTG CAG CAG TCT GG- 3’	6
6	5’-cggggatcc CAG ATC CAG TTG GTG CAG TCT GG3’-3’	4
	Reverse primers	
1	5’-CGA GGA GAC KGT GAS HGW GGT- 3’	
2	5’-CGA AGA GAC AGT RAC CAG AGT- 3’	

Table 3. Degenerated primers library of Light chain of Fab

	Forward primers	**%**
1	5’-SAM ATT GTK CTS ACH CAR TC- 3’	30
2	5’-GAY ATC CAG ATG ACH CAR WC- 3’	18
3	5’-GAT GTT GTG ATG ACC CAR AC- 3’	12
4	5’-GAY ATT GTG ATG CAN CAG KC- 3’	25
5	5’-GAT GTT TTG ATG ACC CAG TC- 3’	6
6	5’-GAC ATC AAG ATG ACC CAG TC- 3’	5
7	5’-GAC ATT GTG ATG TCA CAG TC- 3’	4
	Reverse primers	
1	HindIII 5’-cccaagctt CCG TTT KAT YTC CAR YTT KGT SCC- 3’	
2	5’-cccaagctt CCG TTT CAG YTC CAG CTT GGT CCC- 3’	

2.7 COMPUTATIONAL STUDY

Computational studies (Homology modelling and Docking Study) were performed in collaboration with the research group of Prof. Lucia Falcigno and Dr. Luisa Calvanese, from niversity of Naples " Federico II", Department of Pharmacy.

a) Homology modelling

Prior performing the docking study on the antigen-Fab complex, the model of Fab for each selected mAb (10D1 and 1B4) was built by homology modelling. The identification of the template showing the highest sequence identity for the light and heavy chains of each mAb and the subsequent sequence alignment were performed by using PIGS (Prediction of Immunoglobulin Structure) and PSI-BLAST (Position Specific Iterative BLAST) servers (http://circe.med.uniroma1.it/pigs/; http://blast.ncbi.nlm.nih.gov).

A multiple sequence alignment of 10D1 and 1B4 Fab fragments, in combination with sequences depositated in the database of the software, was achieved; subsequently the CDRs on light and heavy chains variable fragments, were predicted by SSM program (Structure Similarity Match) on the basis of secondary structure homology to the antibodies reported in the database. Subsequently, a pair-wise sequence alignment was performed between 10D1 and 1B4 Fab fragments, allowing a specific comparative analysis. Thus, the molecular model of Fab fragment for each antibody was built by homology with known crystal structures from PBD of the previously identified templates.

Finally, a comparative study was performed on the overlay of the two Fab models to evidence and remark differences on the paratope region.

b) Docking

Docking studies were performed using the selected NMR structure of the synthetic human CFC[112-150] domain and the Fab model built by homology modelling. The complexes were generated with a blind method by ClusPro 2.0 software, a fully automated algorithm and discrimination method for the prediction of protein complexes.

Since the complex of interest contains an antibody fragment, the "Antibody mode" was selected, positioning the molecule with the largest size (Fab) as the fixed part, reported as receptor, and the antigen (hCFC) as the dynamic part, considered as ligand.

The docking algorithms evaluate billions of putative complexes, retaining a preset number with favorable surface complementarities. A filtering method is then applied to this set of structures, selecting those with good electrostatic and desolvation free energies for further clustering.

This fast algorithm has been developed for filtering docked conformations with good surface complementarity, and ranking them based on their clustering properties. The free energy filters select complexes with lowest desolvation and electrostatic energies. Clustering is then used to smooth the local minima and to select the ones with the broadest energy wells-a property associated with the free energy at the binding site **[143]**. The docked structures exhibiting the best scores (lowest energy and largest cluster size) were selected, energy- minimized by Haddock software (High Ambiguity Driven protein-protein Docking, http://haddock.science.uu.nl/) and the binding energy was calculated by submission of the model to the Dcomplex web server (http://sparks.informatics.iupui.edu/song/complex.html).

Each selected complex was subsequently analyzed by PyMOL software (https://www.pymol.org), a based molecular visualization system and a more detailed analysis was perform by COCOMAPS (bioCOmplexes COntact MAPS, https://www.molnac.unisa.it/BioTools/cocomaps/) server, to calculate the specific contact regions at the antigen-Fab binding interface, by making use of intermolecular contact maps. COCOMAPS output includes three different contact maps, as well as tables reporting detailed information about the interacting residues, the residues at the interfaces (defined on the basis of the buried surface upon complex formation), and the inter-molecular H-bonds **[144]**.

2.8 mAb STRUCTURAL CHARACTERIZATION BY PROTEOLYTIC CLEAVAGE

Immunoglobulins digestion by papain is an universal methodology to generate antibody fragments, more suitable than the intact IgG molecule, by a proteolytic approach. In addition to papain, pepsin and ficin are even routinely used to cleave IgGs.

Papain is a cysteine protease, consisting of a single polypeptide chain with three disulfide bridges and a sulfhydryl group that requires the presence of L-Cysteine, as reducing agent, to exert its catalytic activity. The concentration of L- Cysteine is critical to papain activity to produce Fab or $F(ab')_2$ fragments. Papain cleaves at level of bonds involving basic amino acids (Arg and Lys are preferred) and involving Phe, in which the residue following the Phe is preferred **[145]**.

Pepsin, unlike other peptidases, is able to hydrolyze only peptide bonds, not amide or ester linkages. The specific cleavage sites include peptide bonds involving residues with an aromatic acid on either side of the bond, especially if the other residue is also aromatic or a dicarboxylic amino acid. Pepsin cleavage occurs at the hinge region, below the interchain disulfide bridges, splitting the IgG molecule into a bivalent $F(ab')_2$ and a fragmentated Fc **[146]**.

Ficin is a thiol protease characterized by an active site containing only one reactive Cysteine. This enzyme cleaves proteins at the carboxyl side of many aminoacids, including basic (Lys and Arg) and aromatic (Tyr) residues and it is routinely used to generate $F(ab')_2$ fragments from mouse IgG1 antibodies resistant to the treatment with pepsin **[147]**.

Thus, papain is commonly used to cleave the IgG molecule into two Fab units, that still retain the antigen binding ability, and an intact Fc portion. An alternative strategy to generate the monovalent fragment is the single step reduction of the $F(ab')_2$ to the so-called F(ab') with 2-MEA (2-Mercaptoethanolamine) or Cysteamine, a reducing agent selective to the disulfide bridges of the hinge region.

For structural characterization of IgG, the choice of the protease is strictly dependent on specific isotype. Mouse antibodies are reported to exhibit a subclass-dependent susceptibility (IgG2b>IgG3>IgG2a>$IgG1_)$ to proteases **[102]**. In detail, IgG1, IgG2a and IgG3 are known to be susceptible to pepsin cleavage, allowing the production of F(ab')$_2$ fragment, even successfully obtained by ficin action on IgG1 **[147]**. By contrast, F(ab')$_2$ can not be obtained by treatment of IgG2b neither with papain nor with pepsin **[148]**.

a) Digestion of 1B4 mAb by papain

Since the selected 1B4 mAb belongs to the IgG2b subclass, papain was used to split the antibody into two Fabs and one Fc fragments. A preliminary small-scale digestion was conducted to set up the optimal conditions, after a time-course procedure, monitoring the proteolytic process after 2h, 4h and 6h. The reaction was achieved at neutral pH in PBS buffer, pH 7.4. Firstly, papain was pre-activated by 5 mM L-Cysteine for 10 min at room temperature, subsequently 2 mM EDTA (heavy-metal chelator required to enhance the enzyme activation, performed by the Cysteine) and mAb were added and the final mixture was incubated for 4h at 37 °C in a water bath. The optimal enzyme:substrate ratio was fixed at 1:100 (w/w). The reaction was stopped by addition of 25 mM Iodoacetamide, leaving the mixture for 20 min at rt in the dark to ensure complete alkylation of free Cysteines.

b) O-deglycosylation of 1B4 mAb

To optimize the proteolytic cleavage of 1B4 mAb to generate a functional Fab fragment, the removal of the peculiar O-glycosylations localized on the Thr221 of the C$_H$2 domain of the IgG2b antibodies, was required. Despite the N-deglycosylation of IgG1 molecules, achievable in a single step reaction with PNGase F, there is not a comparable enzyme able to perform O-deglycosylation in a single passage. Indeed, the removal of O-linked oligosaccarides requires two different enzymes, the sialidase to cleave the oligosaccaryde chains and the O-glycodisase to completely remove the hydrolized chains.

Sialidase is usually required to remove the N-acylneuraminic acids (sialic acids), that commonly represent the terminal region of the O-linked glycan chains, linked to the hydroxyl side-chain of Ser or Thr residues. This enzyme shows a broad spectrum activity, exerting the release of $\alpha(2\rightarrow3)$, $\alpha(2\rightarrow6)$, $\alpha(2\rightarrow8)$ and $\alpha(2\rightarrow9)$ linked syalic acids from complex glycans, allowing its use when a non-specific removal of sialic linkages is required. By contrast, O-glycosidase is able to cleave only the most common core structure consisting of the disaccharide Gal-β-(1→3)-GalNAc α-linked to the hydroxyl group of Ser or Thr residues **[149]**.

Indeed, a first preliminary small-scale deglycosylation process was performed to set up the optimal conditions. Before initiating the digestion with papain, the 1B4 mAb was firstly incubated with 0.05 U/mL sialidase in 50 mM Sodium Phosphate buffer, pH 6.0, for 24h at 37 °C in a water bath. Secondly, the antibody was buffer-exchanged into 50 mM Sodium Phosphate pH 5.0, so as to be incubated with 0.12 U/mL O-glycosydase for additional 24h at 37 °C. The deglycosylation was monitored by SDS-PAGE analysis on a 12% polyacrylamide gel under non reducing and reducing conditions. Once confirmed that the heavy chains of the antibody were deglycosylated, the subsequent proteolytic cleavage was performed with papain following the procedure reported above.

2.9 CIRCULAR DICHROISM SPECTROSCOPY

Structural analyses were achieved on each generated fragment, to evaluate wether the final product still retained its correct secondary structure and folding. CD analyses were conducted using a Jasco spectropolarimeter, J-710 model, equipped with a Peltier system to control temperature. Samples were prepared in 10 mM Sodium Phosphate, pH 7.5 at a concentration of 0.2 mg/mL and filtered through a 0.22 µm filter; 110-QS quartz cuvettes of 1.0 mm light path length were used. Spectra were collected within the wavelength range of 250-190 nm in far-UV region at scan rate of 20 nm/min, with a data pitch of 0.2 nm, a band-width of 1 nm and a response time of 4 seconds.

On every sample, five independent spectra were recorded, averaged and smoothed using the Spectra Manager software, version 1.53 (Easton, MD, USA). Buffer scans were recorded under the same conditions and subtracted.

2.10 EXPRESSION STRATEGY OF RECOMBINANT CHIMERIC 1B4 *r*Fab

The periplasmic expression strategy was chosen to produce the recombinant chimeric Fab from 1B4 mAb in *Esherichia coli* host strain. Compared to the cytoplasmic expression, this approach is more suitable, especially when the target protein contains fundamental disulfide bonds. This strategy takes many advantages: the oxidizing enviroment of periplasm favours the correct formation of disulfide bonds and their isomerization is catalyzed by periplasmic enzymes such as oxido-reductases and disulfide isomerase; the low presence of proteins in the diluted periplasmic environment prevents aggregation of the target protein, usually observed within the cytoplasm; the final recombinant product contains its authentical N-terminal region, since the signal sequence is cleaved by specific signal peptidases after periplasmic translocation, avoiding the presence of an unwanted initial Met residue, not belonging to the expressed target protein. The latter is a very important advantage because the extra-Met has been reported to reduce the biological activity and stability of the final protein or even, when it is present on therapeutic proteins, may be responsible of immunogenic response **[150]**. Finally, the recovery of the target protein from the periplasm can be achieved by a simple osmotic shock or cell wall permeabilization, without disrupting the cytoplasmic membrane, so as to avoid release of contaminants from the cytoplasm. Although these advantages, the expression strategy involving the periplasmic translocation still presents disadvantages, including a very limited expression yield due to the loss of the target protein that can be found also in the culture medium. An additional inconvenient may be the uncompleted translocation of the target protein from the cytoplasm, expecially protein with high molecular weight can be physically trapped in the cytoplasmic membrane. Thus, with regard to the Fab fragment (50 kDa), this size is not a limiting factor for the periplasmic translocation. A further important parameter is the balance between the translation and secretion processes, since a high translation rate can overload the capacity of the transport machinery, allowing the accumulation of extra-expressed protein in inclusion bodies. Indeed, to avoid this side effect, the choice of a not very strong promoter and a suitable secretion mechanism is recommended **[151]**. The secretion mechanisms used by Gram negative bacteria, including *E. coli*, are classified as type I, type II and type III. The type I machinery, commonly used for the secretion of high-molecular-weight toxins and exoenzymes transports proteins in a single step across the inner and outer cell membranes without a periplasmic intermediate passage **[152]**. The components of this secretion system are two inner membrane proteins (HlyB and HlyD) that belong to the ATP binding cassette (ABC) family of transporters, and an endogenous outer membrane protein, TolC **[153]**. This translocation can also be influenced by components of other secretion pathways, including SecB **[154]**.

a) *Ad hoc* design and engineering of pET-26(+) vector for periplasmic expression

The periplasmic expression strategy exploited to express the chimeric 1B4 *r*Fab is characterized by two steps: 1) the initial synthesis of the single heavy and light chains in cytoplasm, where the reducing environment keeps them separated, and 2) the subsequent translocation into the periplasm space, promoted by the pelB leader sequence, where the oxidizing environment helps the two chains to assemble, allowing the correct formation of the five disulfide bridges (one interchain and four intrachain), critical for the folding of the Fab, so as to obtain a stable soluble protein.

Thus, the 1B4 *r*Fab was constructed as composed of a murine variable region belonging to the 1B4 anti-Cripto mAb and a human constant region belonging to the humanized Trastuzumab (Herceptin®), currently used in clinical treatment of HER2 positive breast carcinoma and metastatic breast carcinoma **[155]**.

The mouse sequences were determined by sequencing of the specific cDNA after RT-PCR, as described in Chapter II (Section 2.6 of Methods), while the human sequences of Trastuzumab were directly taken from DrugBank (DB00072). In addition, the innovative part of the chimeric 1B4 *r*Fab takes advantage from the insertion of the short linker sequence at the C-terminal of the C_H1 domain, suitable as recognition site for the M-TGase enzyme, so as to carry out a site-specific conjugation at the Glutamine residue, exemplified as Q in Fig. 2.1 of additional elements, including PEG, albumin, *r*Fab itself, cytotoxic agent, generating new *r*Fab formats, avoiding a traditional unselective chemical conjugation.

Table 4. Nucleotidic sequences of each element componing the gene encoding the recombinant chimeric Fab protein

Component	Nucleotidic sequence
pelB1/pelB2	ATGAAATAC CTG CTG CCG ACC GCT GCT GCT GGT CTG CTG CTC CTC GCT GCC CAG CCG GCG ATG GCC
VL $_{1B4}$	***
CL $_{Her}$	ACCGTTGCTGCGCCAAGTGTGTTCATTTTCCCTCCTTCCGATGAACAGCTGAAAAGTGGCACTGCAAGCGTTGTATGCCTGTTGAACAACTTCTATCCGCGTGAAGCCAAAGTTCAGTGGAAAGTCGATAATGCCTTACAAAGCGGCAATAGCCAGGAATCTGTGACAGAGCAGGATTCGAAGGATTCGACCTATTCCCTGTCAAGCACGCTGACTCTGTCCAAAGCGGACTATGAGAAACACAAAGTGTATGCGTGTGAAGTGACCCATCAAGGACTCAGTAGCCCAGTCACCAAGTCATTCAATCGTGGCGAATGC
RBS linker	CCACTAGAAATAATTTTGTTTAACTTTAAGAAGGAGATATACAA
VH $_{1B4}$	***
CH $_{Her}$	GCATCTACGAAAGGTCCGAGCGTATTTCCGTTAGCTCCGTCGTCAAAATCCACCTCAGGCGGTACTGCCGCACTTGGCTGTTTGGTGAAAGACTACTTTCCGGAACCTGTCACAGTTTCCTGGAATAGTGGGGCGCTGACTAGCGGCGTGCATACGTTTCCAGCGGTTCTGCAGAGCTCTGGACTGTATTCCCTCTCAAGTGTCGTCACCGTTCCCTCCTCCAGCTTAGGGACCCAGACGTATATCTGCAACGTTAATCACAAACCGTCGAATACCAAAGTGGACAAGCGCGTAGAACCCAAAAGCTGC
M-TGase linker	GGGAGTGGTGCCCTGCAACCAACACAGGGTGCGATGCCGGCG

*** Sequences cannot be reported.

The nucleotidic sequence of this designed gene, adapted to the bacterial expression, using the codon usage optimized for *E. coli*, encodes the following elements:

pelB1-VL$_{1B4}$-CL$_{Her}$-RBS-pelB2-VH$_{1B4}$-CH$_{Her}$-Tgase linker peptide

1. pelB1 is the leader sequence of the light chain
2. VL$_{1B4}$ is the variable region of the light chain from 1B4 mAb
3. CL$_{Her}$ is the constant region of the light chain from Trastuzumab
4. RBS (Ribosomal binding site) is the linker containing the nucleotidic sequence recognized and bound by the ribosome to start protein translation; this linker is required in this position to rebind and keep the mRNA linked to the ribosome to initiate the heavy chain translation when the completed light chain is released
5. pelB2 is the leader sequence of the heavy chain
6. VH$_{1B4}$ is the variable region of the heavy chain from 1B4 mAb
7. CH$_{Her}$ is the constant region of the heavy chain from Trastuzumab
8. M-TGase linker is the additional sequence, in which Glutamine residue is crucial for the enzyme recognition and site-specific transglutamination

The synthetic gene of 1539 bp, purchased from MWG Eurofins, was cloned in the pET-26b(+)vector, possessing Kanamycin resistance, to generate a new dicistronic plasmid, named PL564.

For cloning, the synthetic cDNA and pET-26b(+) vector were opportunely hydrolysed in the presence of *BlpI* and *KpnI* restriction enzymes. The digested fragment and vector were extracted from 0.8% agarose gel using QIAquick Gel Extraction Kit. Ligation reaction was set up 4 °C o.n. and the product was electroporated into TOP10F' *E. coli* cells. Some positive clones were isolated using QIAprepSpin Miniprep kit and the correct cloning was confirmed by nucleotide sequencing. The nucleotidic sequences were analyzed using Finch TV program.

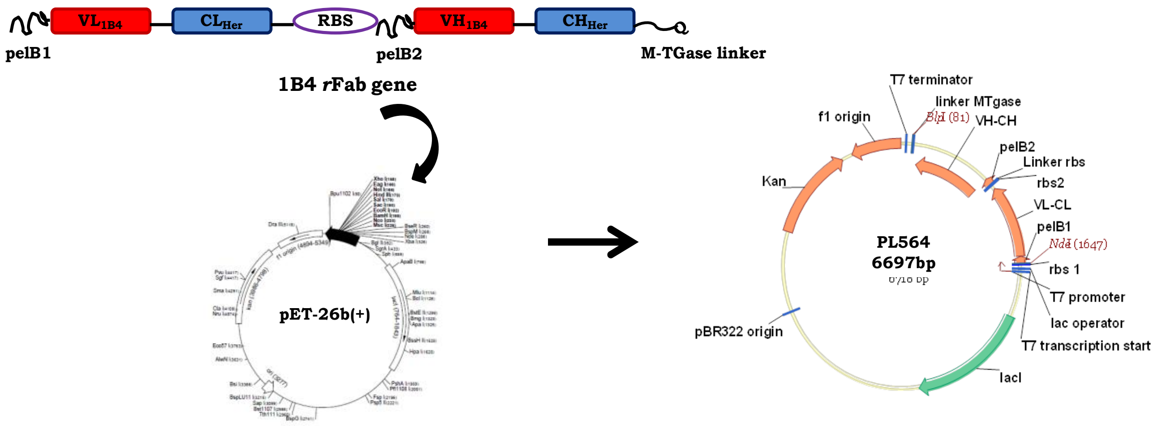

Figure 2.1: Schematic representation of the expression vector construction: the synthetic gene encoding the 1B4 *r*Fab fragment was inserted into the commercial pET-26b(+) vector, creating the new plasmid PL564, to be employed to transform *E.coli* BL21(DE3) host strain.

b) Expression of 1B4 *r*Fab

E. coli BL21(DE3) cells were chemically transformed with 200 ng of PL564 plasmid and cultured in 1 L of LS_{10} medium (1% soya peptone, 0.5% yeast extract, 1% NaCl) supplemented with 0.1 % glucose and using Kanamycin (30 µg/ml) as antibiotic, with an orbital shaking of 250 rpm at 37 °C until the OD reached 0.5-0.6 at 600 nm. Thus, the colonies were transferred into a new medium, FM1 0.5x (2% yeast extract, 1% soya peptone, 0.3% K_2HPO_4, 0.06% KH_2PO_4, 0.8% glycerol) supplemented with 4 mM $MgSO_4$. Tryptone and yeast extract provide the nitrogen and basic nutrients, including growth factors needed for cell growth; NaCl is necessary to provide a suitable osmotic equilibrium, helping to maintain an isotonic environment and glucose is added as the main carbon and energy source, needed for the bacterial growth cycle, as well as the glycerol.

Moreover, inorganic salts ($MgSO_4$, NaCl, $CaCl_2$, KCL, $NaHCO_3$, potassium phosphate) are essential components to allow bacteria to growth and keep their cellular functions and simultaneously to avoid drop of pH due to catabolic products, preventing bacterial death. Magnesium sulfate supplies the magnesium ions required for enzymatic reactions related to the replication of DNA.

Then, expression of the 1B4 *r*Fab protein was optimized by induction with 1 mM IPTG (isopropyl-β-D-thiogalacto-pyranoside), incubating bacterial cells at 30 °C o.n. under orbital shaking (250 rpm). Bacterial cultures were harvested by centrifugation at 8000 rpm for 20 min at 4 °C and finally stored at -80 °C.

c) Purification of 1B4 *r*Fab

The periplasmic extraction of 1B4 *r*Fab protein was achieved by re-suspending the pellet in lysis buffer containing 100 mM Tris-HCl and 10 mM EDTA, pH 7.,4 and protease inhibitors cocktail (Complete EDTA free tablet, Roche) The mixture was left in incubation o.n. at 30 °C, under shaking (250 rpm). The extract was clarified by centrifugation at 20000 rpm for 30 min at 4 °C to separate the periplasmic fraction from the other undesirable cell components and debris. The extract was initially salified in 4 M NaCl to be purified by HIC onto a column (26 mm x 30 cm) packed with Phenyl Sepharose 6 Fast Flow resin, using an AKTA Purifier system. The stationary phase was previously sanitized with 1 M NaOH and equilibrated with Binding buffer (50 mM Tris-HCl, pH 7.0, 3.5 M NaCl) and Elution buffer (50 mM Tris-HCl, pH 7, and 0.25 M NaCl). Prior applying onto the column, the periplasmic extract was filtered (0.22 μM steril filter) and the purification process was achieved at a flow rate of 10 mL/min monitoring the Abs at 280 nm. The unbound fraction was washed away until the absorbance reached the baseline, then the bound fraction, containing the 1B4 *r*Fab protein, was eluted. The proteins pool was subsequently purified by IEC using a strong cation exchanger resin SP Sepharose Fast Flow packed in a column (26mm x 28 cm), sanitized with 0.1 M NaOH prior to use. The stationary phase was equilibrated with 50 mM Tris-HCl, pH 7.0, and operating at a flow rate of 10 mL/min, following a linear gradient from 50 mM to 1 M NaCl. The 1B4 *r*Fab fragment was eluted in the fraction washed with equilibration buffer. The recovered fraction containing the 1B4 *r*Fab protein was subsequently basified with 0.1 M NaOH, pH 9.0, to perform the final purification step on the strong anion exchanger Q

Sepharose Fast Flow resin packed in a column (16 mm x 20 cm), previously sanitized with 0.1 M NaOH. Before applying the sample, the resin was equilibrated with 20 mM Tris-HCl, pH 9.0. The elution of the 1B4 *r*Fab was performed at a flow rate of 15 mL/min , with 50 mM Tris-HCl, pH 8.0, and all the fractions were finally collected.

A further purification step was achieved by SEC on a Superdex 200 column (10 mm x 30 cm) to assess the presence of aggregates. Gel filtration analysis was carried out using as running buffer 25 mM Tris, pH 7.5, and 50 mM NaCl, operating at flow rate of 0.5 mL/min and monitoring the Abs at 280 nm.

2.11 SDS-PAGE AND WESTERN BLOT ANALYSES

The purified 1B4 *r*Fab protein was analyzed by SDS-PAGE on a 15% polyacrylamide gel under reducing and non-reducing conditions, using Laemmli 1x (25 mM Tris base, 0.2 M Glycine, 0.1% SDS, pH 8.3) as running buffer. To reduce the samples, 10% (v/v) β-Mercaptoethanol was added to the solution and the final mix was boiled for a few minutes at 100 °C. Separated proteins were stained with Coomassie Brilliant Blue. For immunoblotting, 1 μg of 1B4 *r*Fab protein was loaded onto a 15% SDS-PAGE gel and then transferred onto a PVDF membrane, using the Transfer Buffer (10 mM TrisBase, 0.1 M Glycine, 0.1 % SDS and 10 % Methanol), by a semi-dry procedure, using the Trans-blot system SD Semi-dry Transfer cell system (Biorad). A constant voltage of 18 eV was applied for 20 min at r.t.

The membrane was blocked with TBS-T buffer (20 mM Tris-HCl, pH 7.5, 500 mM NaCl, 0.05% Tween 20) containing 5% NFDM and incubated for 1 h at r.t. The membrane was then washed three times with TBS-T and incubated with the solution of HRP-conjugated Anti-human IgG (Fab specific) diluted 1:1000 in TBS-T containing 2.5% NFDM.

After extensive washing, blotted 1B4 *r*Fab was detected both by using ECL substrate kit (Supersignal Pierce) to acquire the membrane on ChemiDoc instrument (Bio-rad) by QuantityOne software and finally a colorimetric detection was performed with OPTI-4CN substrate kit (Biorad).

2.12 1B4 *r*Fab-hCFC COMPLEX ANALYSIS BY SE-HPLC

A simple methodology was used to preliminarily evaluate the formation of the antigen-Fab complex in solution by SE-HPLC, on a Zorbax GF-250 column (4.6 x 250 mm), comparing the elution time of the 1B4 *r*Fab alone and complexed with the synthetic hCFC[112-150] polypeptide, used as antigen. The molar ratio 1B4 *r*Fab:hCFC was 1:4, dissolved in 25 mM Tris-HCl, pH 7.5, and 50 mM NaCl. The analysis was carried out using 0.1 M K_2HPO_4, pH 7.4, with the addition of 3% Isopropanol, setting up a constant flow rate of 0.35 mL/min.

2.13 CHEMICAL SYNTHESIS, PURIFICATION AND IDENTIFICATION OF THE BIFUNCTIONAL LINKER PEPTIDE

A short linker peptide was designed to covalently keep together two 1B4 *r*Fab arms, allowing the formation of an artificial recombinant 1B4 *r*Fab$_2$.
Thus, the linker peptide was chemically synthesized by a typical step-wise solid phase Fmoc procedure, purified by RP-HPLC and finally the correct molecular mass of the product was determined by LC-ESI-TOF-MS analysis. The methodology used to perform chemical synthesis, purification and identification of the peptide are reported in Chapter II (Sections 2.1.a and 2.1.c respectively.).

2.14 1B4 *r*Fab-*r*Fab CONJUGATION REACTION CATALYZED BY M-TGase ENZYME

To generate the dimeric Fab, reported as 1B4 *r*Fab$_2$, an enzymatic strategy, alternative to the traditional chemical conjugation to the sulfhydryl goup of free Cysteine residues, was explored using M-TGase, supplied by Bio-ker. This enzyme selectively catalyzes acyltransfer reactions between the γ-carboxamide group of Glutamine (chemically inert under physiological conditions) and the primary ε-amino group of Lysine, leading to the formation of catabolically stable isopeptide bonds, by a transamination reaction. The Glutamine residue is required be located in a flexible region of the protein and flanked by specific amino acids **[156]**. This approach is very smart since guarantees site-specific and stoichiometric functionalization of labelled molecules, avoiding the limitations related to the chemical approach, including site-aspecificity, variable stoichiometry and a final heterogenous population of conjugated products.

To reach this aim, the 1B4 *r*Fab was produced with the additional sequence containing Gln residue to be exploited as labeling site. The transamination catalyzed by M-TGase is reported in Figure 2.2, where also possible side reactions are illustrated.

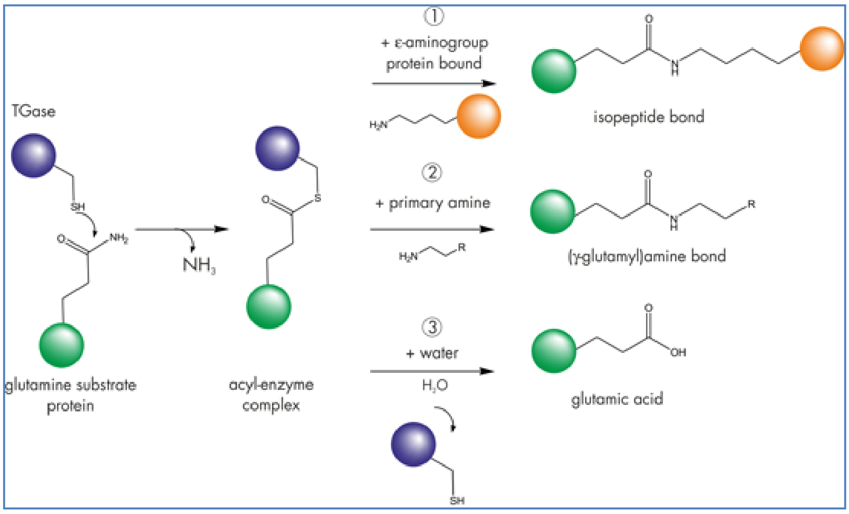

Figure 2.2: Schematic illustration of the three possible reactions catalyzed by M-TGase enzyme **[157]**.

With regard to the reaction performed in this study, the Gln substrate protein is represented by the additional sequence on the C_H1 domain of the 1B4 *r*Fab, otherwise the ε-aminogroup is provided by Lys residue of the bifunctional linker. A critical parameter to limit the promiscuity of M-TGase is the availability of amino groups, thus to avoid the unwanted deamination reaction with the consequent generation of Glutamic acid, a rich excess of amino groups is required.

A preliminary series of pilot reactions were conducted exploring different conditions of all the parameters involved in the conjugation process (1B4 *r*Fab:linker molar ratio, enzyme concentration, ion strength of the buffer, temperature and incubation time period) to set up the final optimal conditions.

2.15 PURIFICATION OF 1B4 *r*Fab NEW FORMATS

a) Purification of 1B4 *r*Fab$_2$ and 1B4 *r*Fab-Doxo by IEC

After the specific incubation time period, he reaction mixtures were purified by ion-exchange chromatography using a cation exchanger resin (MacroCap SP), previously equilibrated with 20 mM NaAc, pH 4.5. Throughout the purification process a linear gradient of NaCl, starting from 0 mM and reaching 350 mM in 15 column volumes, was applied, at a constant flow rate of 2 mL/min.

b) 1B4 *r*Fab$_2$ analysis by SE-HPLC

In detail, a second step of purification was performed only on 1B4 *r*Fab$_2$ by a SE-HPLC, using a Zorbax GF-250 column (4.6 x 250 mm) and 63 mM K_2HPO_4, pH 7.3, plus 3% Isopropanol, was used as elution buffer to separate the dimeric 1B4 *r*Fab$_2$ from the unfunctionalized monomeric 1B4 *r*Fab as well as to evaluate the products in terms of molecular weight and purity grade.

2.16 GENERATION OF ADC

An universal strategy currently used to enhance the therapeutic potential of monoclonal antibodies and their fragments is their conjugation with a cytotoxic drug generating a so-called ADC (antibody drug conjugates) product.

In this study we investigated the feasibility of conjugating a cytotoxic agent to the 1B4 *r*Fab and for this purpose we designed a strategy for the attachment of Doxorubicin through a mixed approach of chemical and enzymatic reactions. Doxorubicin is an anthracycline antibiotic that binds to nucleic acids by specific intercalation of the planar anthracycline nucleus with the DNA double helix. It is widely used to produce regression in disseminated neoplastic conditions, including acute lymphoblastic leukemia, acute myeloblastic leukemia, neuroblastoma, breast carcinoma, ovarian carcinoma, gastric carcinoma, Hodgkin’s disease and malignant lymphoma **[158]**. However, as for many cytotoxic compounds it is unable to discriminate between healthy and cancer cells, thus resulting a highly toxic compound when is used at concentrations above a given threshold and especially in on healthy tissues. ADC have the advantage of overcoming these issues by exploiting the antibody selectivity for the homing and eventual release of the cytotoxic payload on diseased tissues overexpressing specific antigens. In our case, the final ADC product (1B4 *r*Fab-Doxo), exhibits the selectivity of 1B4 *r*Fab toward tumor target cells overexpressing human CR-1 protein on their surface and the high cell killing effect held by Doxorubicin. This should therefore potentially improve the anti-tumor activity by concentrating the compound on the cancer site and at the same time reduce the side effects of the cytotoxic drug.

a) ADC-conjugation strategy design

The 1B4 *r*Fab-Doxo, like typical ADC products, was designed as composed by three main elements: the antibody portion, the linker and the payload. The linker was in this case a peptide with the ability to selectively join together the antibody fragment and Doxorubicin conjugated with a heterobifunctional linker. We used the commercial spacer 4-Maleimidobutyric acid *N*-hydroxysuccinimide ester (Sigma-Aldrich) containing two reactive groups, localized at opposite sides, corresponding to the amine-reactive N-hydroxysuccinimide (NHS ester) and the sulfhydryl-reactive maleimide group.

The NHS ester group reacts with primary amines at basic pH conditions (between 7 and 9) leading to the formation of stable amide bonds; on the other side the reactivity of maleimide group to the sulfhydryl groups at pH 6.5-7.5, allows the formation of stable thioeter bonds. This cross-linker was also chosen by virtue of its favorable properties, including high stability at physiological pH, its function as non-cleavable linker and cell membrane permeability.

As shown, we also designed a short peptide derivative Ac-cys-Lys-ala-NH_2 containing a D-Cysteine, required to form the thioeter bond with the reactive maleimide group of the commercial linker, and a Lysine residue required to allow the M-TGase-catalyzed enzymatic conjugation of Doxorubicin to the 1B4 *r*Fab. D-Alanine was used as a spacer. The amino acids were used in D configuration to prevent linker degradation by cellular proteases during the permanence in the bloodstream. The ADC-conjugation strategy is outlined in Fig. 2.3. Such approach should lead to the specific attachment of one copy of Doxorubicin to a specific site of the antibody.

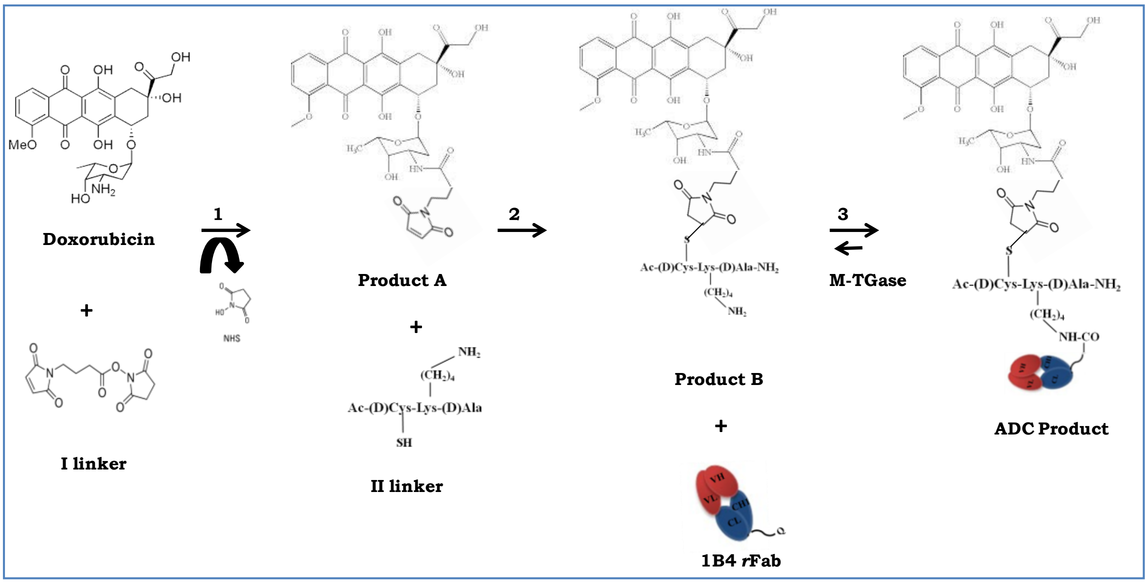

Figure 2.3: Schematic representation of the three step strategy designed to create the 1B4 *r*Fab-Doxo derivative (ADC product).

The first step (1) is represented by the formation of the amide bond between the free primary amine of Doxorubicin and the NHS ester of the I linker, via reaction with NHS and formation of the Product A. In the second step (2) the short peptide is linked to the Doxorubicin-I linker (Product A) exploiting the maleimide group that, reacting with the free sulfhydryl group on the Cys residue through an electrophilic addition reaction, allows the formation of a stable and non reducible tioether bond and the formation of the intermediate compound, named Product B.

While the first two steps are chemical reactions, the last one is the site-specific conjugation catalyzed by the M-TGase enzyme. The transamination reaction occurs between the free primary amine of the Lys residue belonging to the II linker and the Gln residue localized on the C-terminal sequence of 1B4 *r*Fab.

As depicted in Fig. 2.4, the 1B4 *r*Fab-Doxo product (A) could potentially bind to the cell surface receptor (Cripto-1), forming the ADC-receptor complex, that is subsequently internalized into the cytoplasm via a lysosome-mediated endocytosis process. In the strongly acid environment of lysosomal vesicles, the linker is cleaved and the antibody is degraded by the proteases, so as to allow the release of the cytotoxic drug, leading to cell death.

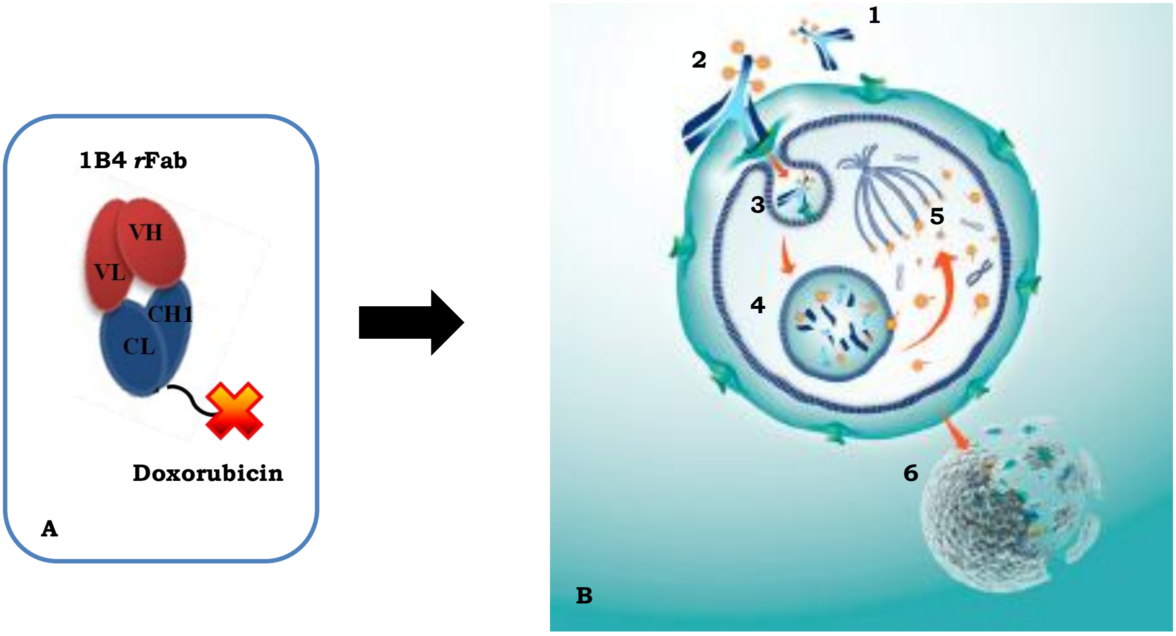

1. **ADC in bloodstream**
2. **ADC-receptor binding**
3. **ADC-receptor complex internalization**
4. **Antibody portion removal in lysosome**
5. **Cytotoxic agent release**
6. **Cell death (Apoptosis)**

Figure 2.4: Steps of typical ADC mechanism (**B**) **[141].** In this study the ADC product is represented by the 1B4 *r*Fab fragment conjugated to the cytotoxic agent Doxorubicin (**A**).

b) Preparation of Doxorubicin-I linker-II linker compound

Doxorubicin hydrochloride (4.5 mg; 7.8 μmol) was dissolved in DMF and the cross-linking agent (reported as I linker, Ac-CKA-NH$_2$ *ad hoc* linker peptide) was added (3.1 mg, 12 μmol) and the pH was adjusted to around 8 by addition of 2M DIEA. Subsequently, for three times the same amount of I linker was added to the solution, opportunely adjusting the pH with DIEA. The mixture was left under shaking o.n. at rt, assessing the reaction progression by HPLC and ESI-MS. The mixture was finally diluted in H$_2$0 + 0.1%TFA, and purified by RP-HPLC applying a gradient of CH$_3$CN starting from 5% up to 70% in 15 min, at a constant flow rate of 12 mL/min and monitoring the Abs at 280 nm, as reported in section 2.1.c. The correct product (Product B) was checked by mass spectrometry.

c) Conjugation of 1B4 *r*Fab with Doxorubicin

The second step of the ADC preparation was the conjugation of the 1B4 *r*Fab fragment to the Product B (Doxorubicin-I linker-II linker) via M-TGase reaction. The enzymatic reaction was performed adding Product B, dissolved in DMSO, to the 1B4 *r*Fab at 2:1 w/w ratio (Product B : *r*Fab) in presence of M-TGAse (0.25 U/mL) in 1 M KH_2PO_4, pH 8.2, buffer, o.n. at rt.

After the incubation time period, the complete reaction mixture was purified by cation exchange chromatography as described previously in section 2.15.a and subsequently each isolated peak was analyzed by SDS-PAGE on a 12% polyacrylamide gel and by LC-ESI-TOF-MS (see section 2.1.c) to assess the integrity and purity of the final products.

2.17 PRELIMINARY *IN VITRO* ASSAYS OF 1B4 mAb ON HUMAN CANCER CELLS OVER-EXPRESSING CR-1 PROTEIN

a) Cell culture

All human cell lines were purchased from ATCC (American Type Culture Collection) except the C16 cell line, provided by the Aalborg University Hospital of Aalborg (Denmark). These cells were derived from patients exhibiting clinical features of glioblastoma.

All the human cancer cell lines used in this study were cultured in T175 flasks, using complete DMEM-F12 medium (Dulbecco’s modified Eagle’s medium-F12) supplemented with 10% FCS, and 1% penicillin/streptomycin. Cultures were kept in incubator at 37 °C, with a humidified atmosphere containing 5% CO_2. Medium was changed routinely twice per week and when cells reached 80-90% confluence, they were split 1:5 or 1:10 into a new flask containing fresh medium.

b) Quantitative RT-PCR

Quantitative real-time PCR was carried out on GEO human colon cancer cells to measure the mRNA levels corresponding to human CR-1. Total RNA extraction was performed as previously described (section 2.6.a); the following qRT-PCR reactions were conducted using SYBR Green PCR master mix on an iCycler instrument (Bio-Rad). hGAPDH was used as internal control. The primers (Sigma-Aldrich) used are reported in Table 5.

Table 5. Primers used for qRT-PCR

	Forward	Reverse
hGAPDH	5’-GAAGGTGAAGGTCGGAGTC-3’	5’-GAAGATGGTGATGGGATTTC-3’
hCR-1	5’-CACGATGTGCGCAAAGAGA-3’	5’-TGACCGTGCCAGCATTTACA-3’

c) Western blot analyses

After washing twice in PBS pH 7.4, cells were trypsinized in the incubator 5 min at 37 °C. Then, a triple volume of fresh medium was added and cells were harvested by centrifugation at 300 rpm for 5 min at 20 °C. Pellets were washed, and after aspiration of supernatants were lysed using RIPA buffer (0.1% SDS, 50 mM Tris-HCl pH 7.4, 1% Igepal, 0.25% sodium deoxycholate, 1 mM EDTA, 150 mM NaCl), adding 1x Mini Protease Inhibitor Cocktail including phosphatase inhibitors prior to use; the mixture was left for 30 min at 4 °C. The total cellular lysate was quantified by Bradford assay and 30-50 μg were loaded onto a 12% polyacrylamide gel, under reducing conditions (with 10% β-Mercaptoethanol), after short heating at 100 °C in a boiling water bath.

To detect the 1B4 effect on Cripto-1 activity in H9 corresponding to hESC (human embryonic stem cells), BT549 and Hs578T (human breast cancer cells) and NTERA/2D (human teratocarcinoma cells), both the commercial antibody (600401997 Rockland) and the 1B4 mAb were used at 1 μg/mL. Membranes were probed with an anti-SRC (MBS 85070433 MyBiosurce), anti-Nodal (EP2058Y Epitomics), anti P-Smad (MBS835580 MyBiosource), anti-Phospho MAPK (MBS837439 MyBiosource) and anti-β Actin antibody (C4:SC-47778 Santa-Cruz) in accordance to the manufacturer’s protocol.

The Western blot and the detection were carried out using the method previously described in section 2.11.

d) Immunofluorescence

Immunostaining on GBM cell lines was performed on non-permeabilized cells, previously fixed in 4% PFA on 24-well plate, seeded at a density of 50000 cells/well. Cells were washed twice with PBS pH 7.4 (0.5 mL/well) and incubated with 0.3 mL/well of 1% BSA in PBS pH 7.4 (blocking buffer) for 30 min at r.t. Then, 0.2 mL/well of the primary antibody solution was added at 5 μg/mL in blocking buffer o.n at 4 °C. As positive control, the commercial anti-Cripto-1 antibody (MAB2772 R&D Systems) was used. After three washes (5 min each wash) with 0.5 mL/min of washing buffer (composed by the blocking buffer diluted 1:50 in PBS pH 7.4), the AlexaFluor555 conjugated secondary antibody (Ab150114 LifeTechnologies) diluted 1:200 in incubation buffer, was added and incubated for 30 min at r.t. Then, after washing the nuclear staining was performed using Hoechst 33342 (Invitrogen), 0.2 mL/well, diluted 1:1000 in H_20, leaving the plate in incubation for 15 min at r.t.

e) Proliferation assays

GBM cell lines

C16 and U87 cell lines were seeded in T75 flasks at a density of 2000 cells/cm^2 and left in incubation 24h. Then, the medium was changed and the fresh medium containing 1B4 mAb at a concentration of 0.2 μM was added; as negative control medium without mAb was also added. Cells were fixed in 4% PFA and cell growth rate at the starting point and after 96 hours was evaluated using Cell Trace CFSE Cell Proliferation Kit (Invitrogen). CFSE is a cell-tracing reagent that passively diffuses into cells. It is colorless and non-fluorescent until the acetate groups are cleaved by intracellular esterases to yield highly fluorescent carboxyfluorescein succinimidyl ester. The succinimidyl ester group reacts with intracellular amines, forming fluorescent conjugates that are well retained and can be fixed with aldehyde fixatives. Excess unconjugated reagent and by-products passively diffuse to the extracellular medium, where they can be washed away.

GEO cells

Proliferation assay on GEO colorectal cancer cell line, was achieved monitoring the growth rate at the starting point, after 48h, 72h and 96h adding 1B4 mAb the first day and freshly every 24h at two different concentrations (0.1 μM and 0.2 μM), using untreated cells as negative reference. Hoechst nuclear staining was employed as cell tracing, to monitor the cellular replication rate. The blue fluorescent Hoechst dye is a cell permeable nucleic acid stain, that binds to the DNA selectively at the AT regions. Moreover, this dye is highly sensitive to DNA conformation and chromatin state in cells, and it is even able to detect nuclear damage. The Hoechst dye and the CFSE above mentioned, are useful vital stains for the flow cytometric recognition of DNA damage and other viability measurements by monitoring the emission spectral shifts of the dyes.

The proliferation degree both in GBM and GEO cell lines was monitored by FACS analysis, on a Beckman Coulter instrument, and the data were analyzed using Kaluza Analysis software.

f) Trypan blue exclusion test

Viability assay was performed on C16 and U87 cell lines, cultured following the procedure above described. To count viable and unviable cells 0.4% Trypan Blue (Sigma-Aldrich) was used according to the manufacturer's instructions. The counting was performed in a 4x4 square counting chamber, using a 10x magnification. Trypan Blue is the one of the most routinely stains used to perform dye exclusion procedures for viable cell counting. This method is based on the principle that live (viable) cells do not take up certain dyes, whereas dead (unviable) cells do. Moreover, staining facilitates the visualization of cell morphology.

g) Migration assay (wound healing assay)

A scratch assay was performed to evaluate wether the 1B4 mAb exerted any effect on the migration of GBM cell lines. Cells were seeded on a 24-well plate (700 μL/well) with a cell density of 8000 cells/cm^2. The following day, the medium was replaced with fresh medium containing 1B4 mAb at three different concentrations (0-1 μM, 0.2 μM and 0.4 μM), otherwise a negative control lane was filled with simple medium without adding the antibody and the remaining empty wells were filled with PBS to avoid the evaporation process. A scratch was performed using a 200 μL tip, kept 90° angled. Thus, the migration rate was monitored for 24h, using a Zeiss Axio Observer Z1 microscope equipped with an incubator to keep the temperature at 37 °C. The images were taken every 30 minutes for 24h and finally were processed by Wimasis server (https://mywim.wimasis.com).

CHAPTER III

RESULTS

III.1 GENERATION AND BIOCHEMICAL CHARACTERIZATION OF SPECIFIC ANTI-CFC MONOCLONAL ANTIBODIES

1.1 CHEMICAL SYNTHESIS, PURIFICATION, CHARACTERIZATION AND REFOLDING OF HUMAN CFC DOMAIN AND MUTANTS

hCFC [112-150] domain, reported in Fig. 3.1, and its three related variants in which H120 or W123 or both residues were replaced with A, is reported in Table 1. Polypeptides were synthesized as acetylated and amidated products by solid phase synthesis (Fig. 3.1).

Figure 3.1: Amino acid sequence of hCFC[112-150]. The disulfide bridges scheme is reported (C1-C4, C2-C6, C3-C5).

Table 1. hCFC[112-150] domain variants synthesized as reduced products

hCFC [112-150]	Amino acid Sequence	MW amu
Wild-type	Ac-KENCGSVP**H**DT**W**LPKKCSLCKCWHGQLRCFPQAFLPGCD-NH_2	4475.235
H120A	Ac-KENCGSVP**A**DTWLPKKCSLCKCWHGQLRCFPQAFLPGCD-NH_2	4360.101
W123A	Ac-KENCGSVPHDT**A**LPKKCSLCKCWHGQLRCFPQAFLPGCD-NH_2	4409.173
H120W123AA	Ac-KENCGSVP**A**DT**A**LPKKCSLCKCWHGQLRCFPQAFLPGCD-NH_2	4294.039

Crude products were purified under reducing conditions by RP- HPLC, as described in section II.2.1.a of Methods. The refolding process was monitored by analytical RP-HPLC as described in section II.2.1.b of Methods.

Fig. 3.2 reports a panel of representative RP-HPLC profiles recorded during the refolding process of the wild-type hCFC[112-150]. As shown, at t_0 (Fig. 3.2 A) the peak corresponding to the reduced purified hCFC[112-150] polypeptide eluted at 7.5 min. After 1h (t_1), the oxidized form already started to appear (Fig. 3.2 B) with a peak at 6.9 min. After 3h (t_3) the RP-HPLC profile shows only one peak at 6.9 min, corresponding to the fully oxidized synthetic hCFC[112-150] (Fig. 3.2 D). This shift of 0.6 minutes between t_0 and t_3 species confirmed that the spontaneous refolding process was complete, since the reduced species were not present anymore. In addition, this result revealed that the hCFC [112-150] domain possessed the proper sequence since only polypeptides with a correct sequence can spontaneously refold, otherwise truncated polypeptides show side reactions due to polymerization or low solubility issues. The refolded products were re-purified to obtain the final homogenous material, as described in section II.2.1.c of Methods. Finally, for each polypeptide the purity and the formation of the disulphide bridges were estimated by LC-ESI-TOF-MS. All the products showed high purity grade (by over 90%), and, as expected, a molecular weight decreased of 6 amu compared to the unfolded precursor, due to the formation of the three disulfide bridges (see Table 2). The ESI-TOF mass spectra of the refolded and reduced hCFC[112-150] are reported in Fig. 3.3.

Table 2. MW and purity grade of final products

hCFC [112-150]	Theor MW amu	Exp MW amu	Purity %
Wild-type	4469.235	4469.04	> 95
H120A	4354.101	4352.99	> 90
W123A	4403.173	4403.02	> 90
H120W123AA	4288.039	4286.97	> 90

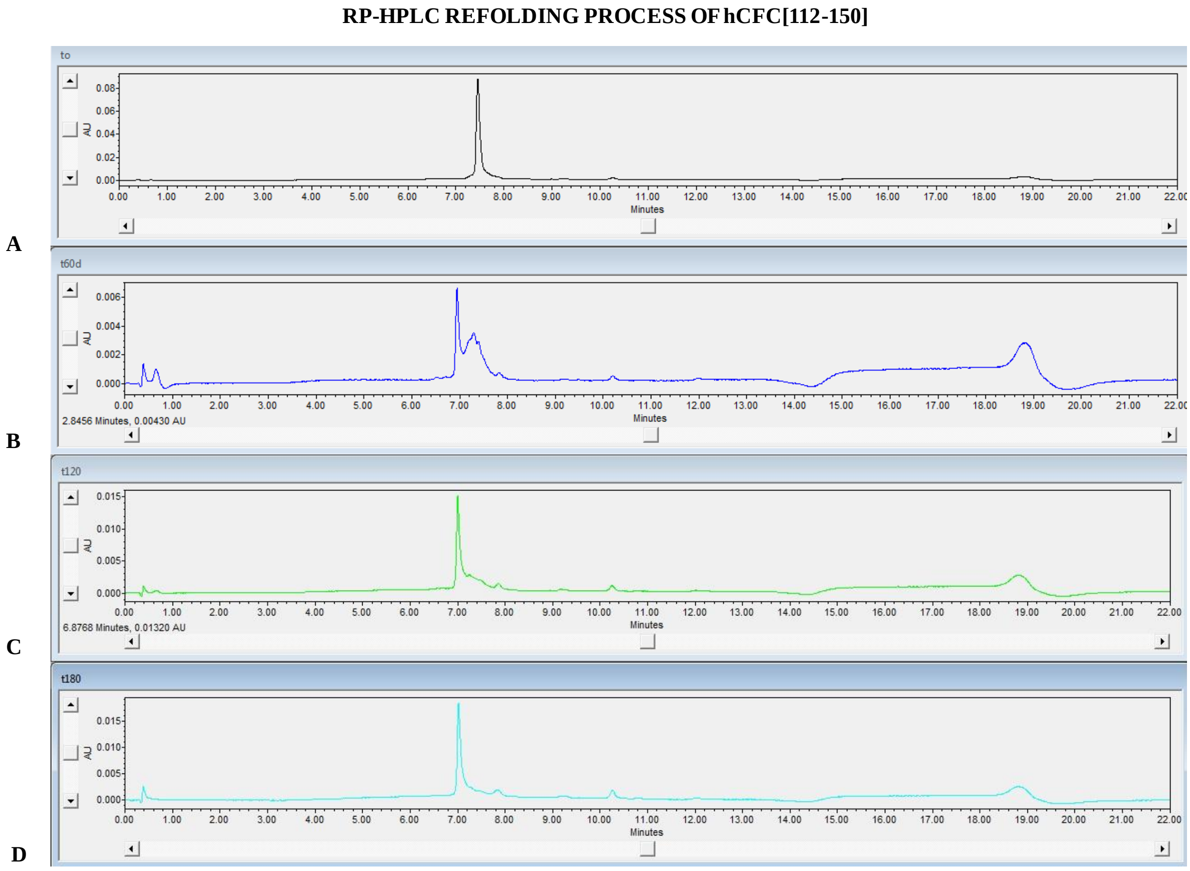

Figure 3.2: Overlay of the hCFC[112-150] refolding process monitored by RP-HPLC analysis: at time 0 (t0, A); after 1 h, (t_1, B); after 2h, (t_2, C), and after 3h, (t_3, D).

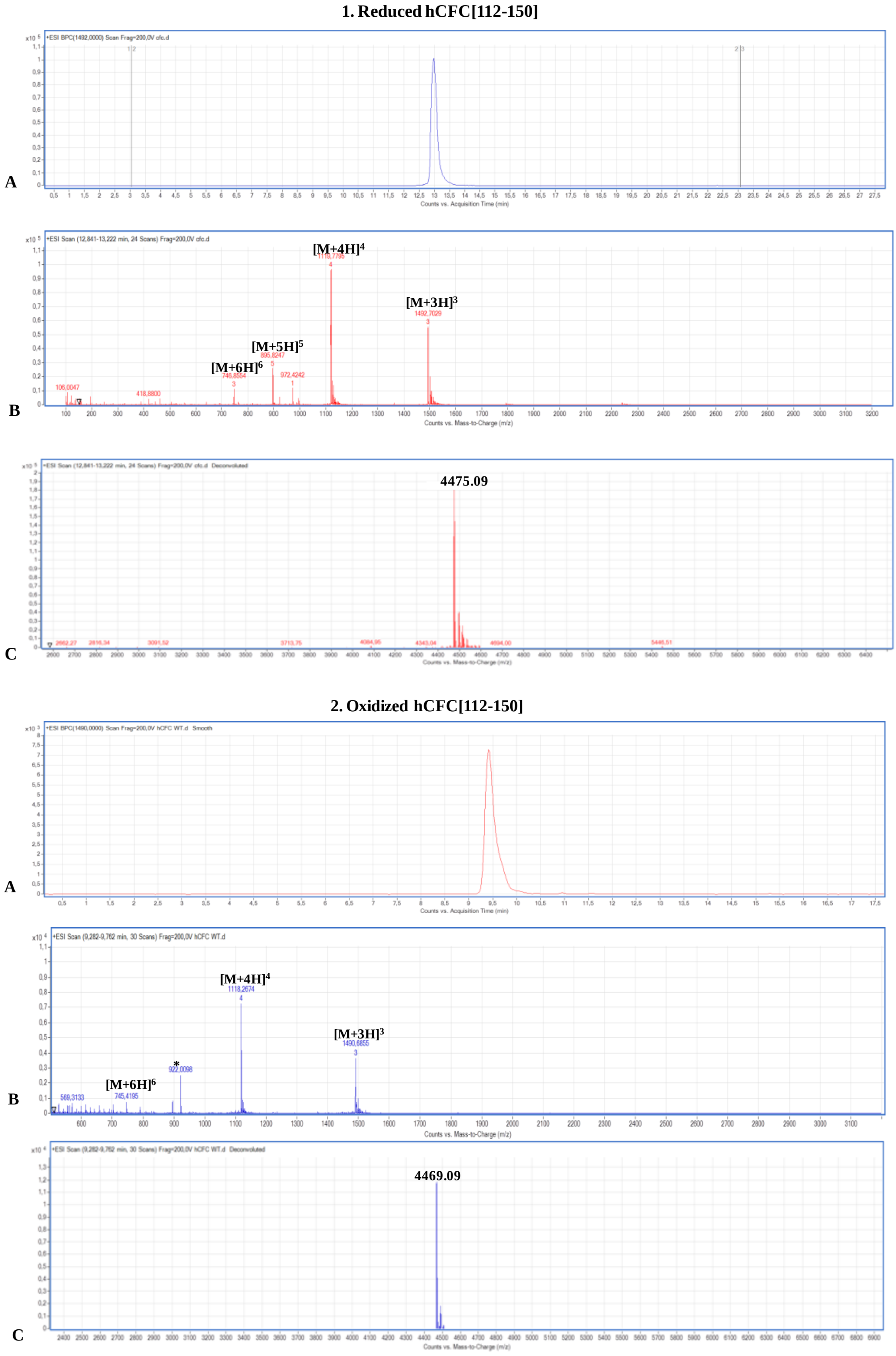

Figure 3.3: LC-ESI-TOF-MS analyses of reduced (1) and oxidized hCFC[112-150] (2). In each panel RP-HPLC base peak chromatogram (A), m/z mass spectrum (B) and deconvoluted spectrum (C) are reported.

1.2 ELISA SCREENING OF HYBRIDOMA SUPERNATANTS ON hCFC[112-150] AND hCFC[112-150]W123A

A preliminary hybridoma supernatant screening ELISA assay was set up using synthetic wild-type hCFC[112-150] domain obtaining only 7 positive clones, indicated as 10D1, 7A4, 3F6, 4H2, 6D4, 1B4 and 1D10. Furthermore, with the aim to identify antibodies recognizing residues strictly involved in the interaction with ALK4, a second round of screening was performed. An ELISA assay was thus carried out using both the synthetic wild-type hCFC[112-150] and hCFC[112-150]W123A variant, where Triptophan123 (W123), known to be - together with Histidine120 (H120) - a hot spot residue for the ALK4 interaction, was mutated to Alanine (A).

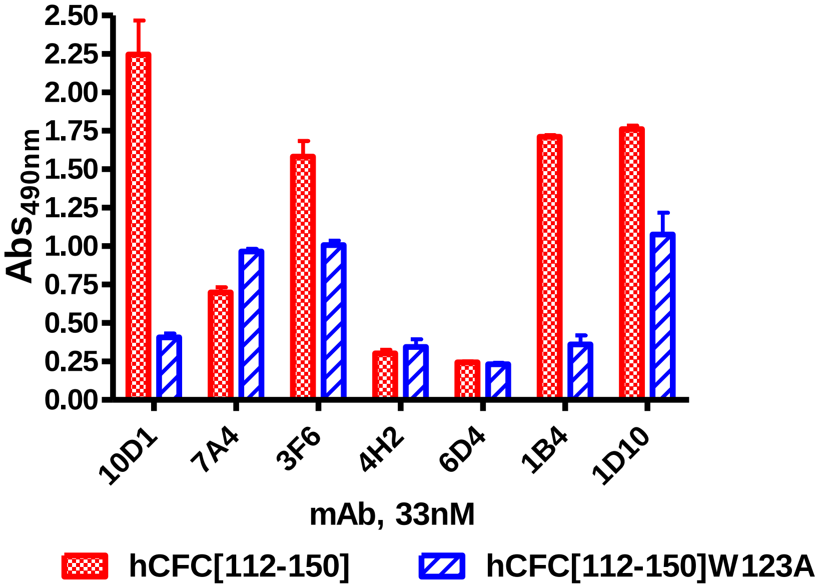

Figure 3.4: Preliminary ELISA screening of the hybridoma supernatants on the synthetic wild-type hCFC[112-150] domain and the singly mutated hCFC[112-150]W123A variant.

The absorbance values for 5 clones (10D1, 7A4, 3F6, 1B4 and 1D10) were found to have a higher signal compared to others (4H2 and 6D4), indicating a better antigen recognition. In addition, only two clones, 10D1 and 1B4, among the 5 positive ones, did recognize the wild-type hCFC[112-150] better than the singly mutated variant, suggesting that they specifically bind the CFC region containing W123.

1.3 PURIFICATION OF ANTI-CFC MONOCLONAL ANTIBODIES

Five selected clones were purified by affinity chromatography on protein G column, as described in Methods (section II.2.4). The typical affinity chromatography profile of a purification from hybridoma supernatant is reported in Fig. 3.5. IgGs elution (Peak B) was performed after several injections of supernatant (in this case 5), washing away the unbound fraction (Peaks A) with the binding buffer (PBS, pH 7.4).

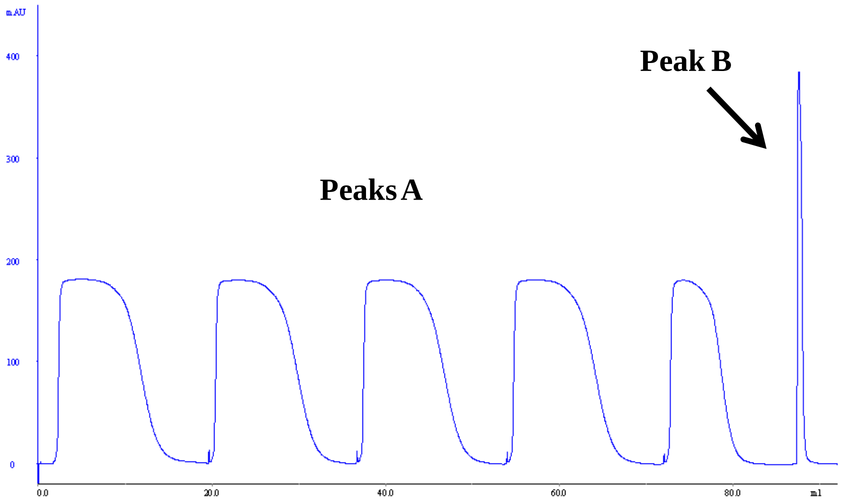

Figure 3.5: Representative chromatographic profile of an affinity protein G purification of hybridoma supernatant.

Next, the presence of antibody aggregates was evaluated by SEC using a Superdex200 column. All mAbs showed a similar elution profile, with a retention volume of 11-12.5 mL, corresponding to a 150 kDa molecular weight. Immediately after affinity purification all antibodies were essentially monomeric with only a very small fraction of aggregates detected. In Fig. 3.6 a representative size exclusion chromatogram of one mAb (A) and an SDS-PAGE analysis (B) of the final purified mAbs are reported. Also SDS-PAGE analyses under non reducing conditions showed that mAbs did not undergo aggregation; the different mobility on the gel is correlated to their different glycosylation status.

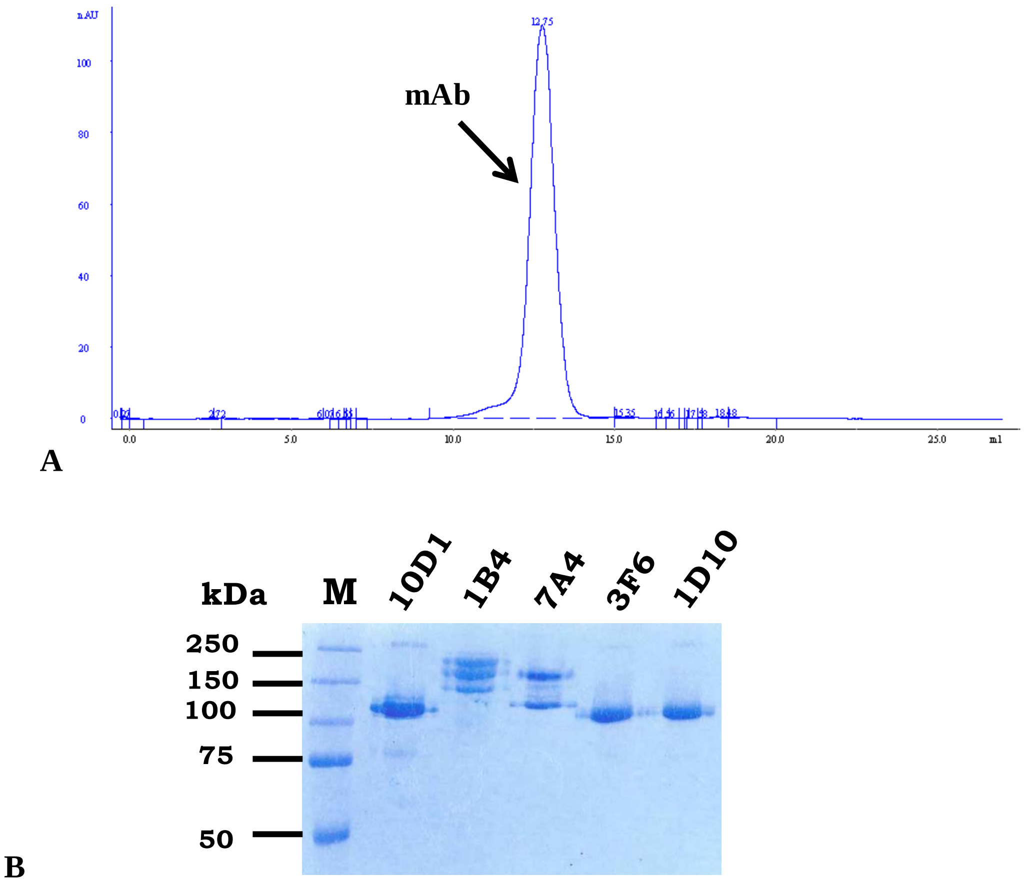

Figure 3.6: **A.** SE-chromatografic profile of a mAb. **B.** SDS-PAGE analysis on a 10% polyacrylamide gel of each purified mAb.

The different features of the mAbs, evidenced by SDS-PAGE analysis, were confirmed by the isotypization (reported in Table 3) revealing that while 1B4 is an IgG2b, the remaining four mAbs (10D1, 7A4, 3F6 and 1D10) belong to the more common IgG1 sub-class.

Table 3. mAb isotypes

mAb	Isotype
10D1	IgG$_1$
7A4	IgG$_1$
3F6	IgG$_1$
1B4	IgG$_{2b}$
1D10	IgG$_1$

The murine IgG1 are known to contain N-linked oligosaccharides, almost entirely fucosylated, at Asn297 of the C$_H$2 domain of both heavy chains **[159]**. On the other hand IgG2b mAbs are known to possess O-linked oligosaccharides at Thr221 in the hinge region **[160]**. In conclusion, the SDS-PAGE analysis of 1B4 mAb was in accordance to the data reported by Kim *et al.* **[161]**, since only mouse IgG2b antibodies exist as three phenotypes (detected as three bands on the gel), that differ each other in the sialylation status of the heavy chain, so their typical mobility is the consequence of the different acidity of the heavy chain.

1.4 SPR DOSE-RESPONSE BINDING ASSAYS OF mAbs ON *rh*CR-1

The ability of selected monoclonal antibodies to recognize the full-length *rh*CR-1 protein was evaluated by SPR assays. For each antibody a dose-dependent assay at increasing concentrations (reported in Table 4), was performed using a *rh*CR-1 functionalized sensor chip, prepared as described in Methods (section II.2.5). A low immobilization density (600 RU) of protein was preferred to limit mass transfer, rebinding effects, and cross-linking of the bivalent analyte (mAb) that can bind to two molecules of ligand, avoiding an accurate evaluation of the kinetic parameters.

Table 4. Analyte concentrations tested on *rh*CR-1

10D1	**1B4**	**7A4**	**1D10**
0.12 nM	0.5 nM	0.12 nM	50 nM
0.25 nM	1 nM	0.25 nM	100 nM
0.5 nM	2.5 nM	0.5 nM	200 nM
1 nM	5 nM	1 nM	300 nM
1.5 nM	10 nM	1.5 nM	

The separated kinetic rate constants and the final affinity constant were extrapolated using the Langmuir 1:1 binding model, and they are reported as k_a (association rate constant) and k_d (dissociation rate constant), while the K_D (apparent binding affinity constant) is the result of the k_d/k_a ratio. By comparing the kinetic fitting curves and residual plots related to each mAb, by virtue of the K_D towards the target protein, 10D1 displayed the highest affinity (K_D = 0.07 nM) as result of fast association rate and very slow dissociation rate. As shown in the overlay of the sensorgrams, reported in Fig. 3.7, the dissociation was practically undetectable. 1B4 mAb (Fig. 3.8) acted almost like the 10D1 mAb, exhibiting a good association (k_a=1.4x10^5 $M^{-1}s^{-1}$) combined to a very slow dissociation (k_d= 3.7x10^{-5} s^{-1}) rate, providing a K_D value (0.24 nM) higher than the 10D1.

Moreover, the interaction of 7A4 mAb to *rh*CR-1 (Fig. 3.9) revealed a K_D value of 2.6 nM. This loss of affinity was due to a faster dissociation rate (k_d =1.7 x10^{-3} s^{-1}) rather than to the association rate (k_a= 4x10^6 $M^{-1}s^{-1}$) compared to the 10D1 and 1B4 antibodies. 1D10 mAb (Fig. 3.10) was still able to bind *rh*CR-1 but the interaction was very weak, revealing a 57 nM K_D, about 1/1000 lower than the K_D displayed by the 10D1. Finally, the 3F6 mAb did not recognize *rh*CR-1 (reported as NB in Table 9) even at very high concentration (1 µM). These data suggest that the epitope of 3F6 antibody probably contains residues at the interface with the EGF-like domain thus not accessible in the full-length protein.

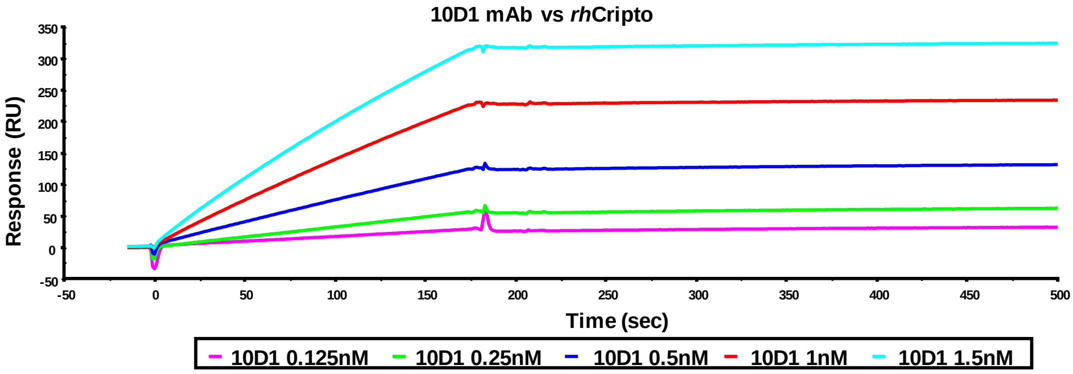

Table 5. Kinetic rate and apparent affinity constants of 10D1 mAb binding to *rh*CR-1

10D1	k_a (1/Ms)	k_d(1/s)	K_D (M)	SE (RI)
0.5 nM	1.31*10^6	1.74*10^{-4}	1.33*10^{-10}	0.0239
1 nM	1.68*10^6	7.99*10^{-5}	4.75*10^{-11}	0.0784
1.5 nM	1.75*10^6	6.65*10^{-5}	3.80*10^{-11}	0.175
average	1.58*10^6	1.07*10^{-4}	7.28*10^{-11}	0.0924

Figure 3.7: Sensorgrams overlay and kinetic parameters table of 10D1 mAb binding to *rh*CR-1.

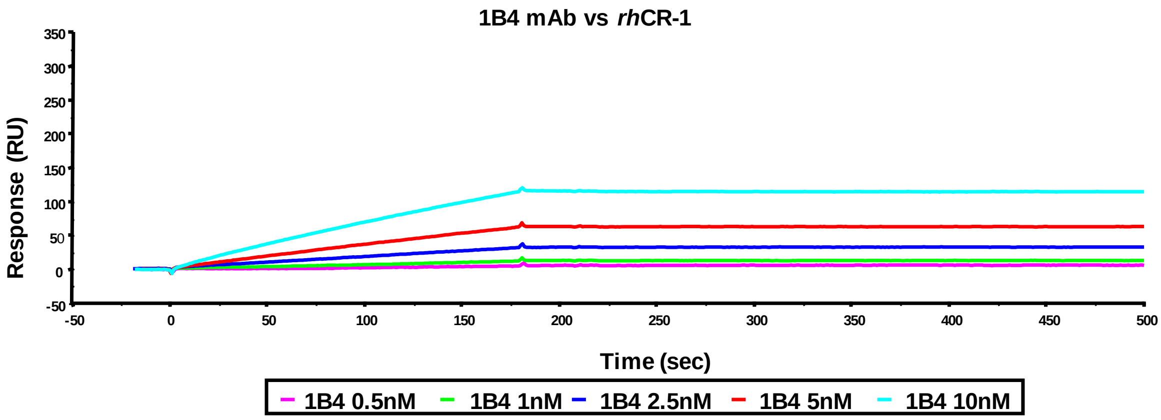

Table 6. Kinetic rate and apparent affinity constants of 1B4 mAb binding to *rh*CR-1

1B4	k_a (1/Ms)	k_d(1/s)	K_D (M)	SE (RI)
0.5 nM	$1.34*10^{5}$	$2.12*10^{-5}$	$1.58*10^{-10}$	0.0286
1 nM	$6.89*10^{4}$	$1.25*10^{-5}$	$1.81*10^{-10}$	0.028
2.5 nM	$7.19*10^{4}$	$1.82*10^{-5}$	$2.53*10^{-10}$	0.024
5 nM	$2.19*10^{5}$	$4.94*10^{-5}$	$2.25*10^{-10}$	0.0298
10 nM	$2.13*10^{5}$	$8.23*10^{-5}$	$3.86*10^{-10}$	0.0575
average	$1.41*10^{5}$	$3.67*10^{-5}$	$2.41*10^{-10}$	0.0336

Figure 3.8: Sensorgrams overlay and kinetic parameters table of 1B4 mAb binding to *rh*CR-1.

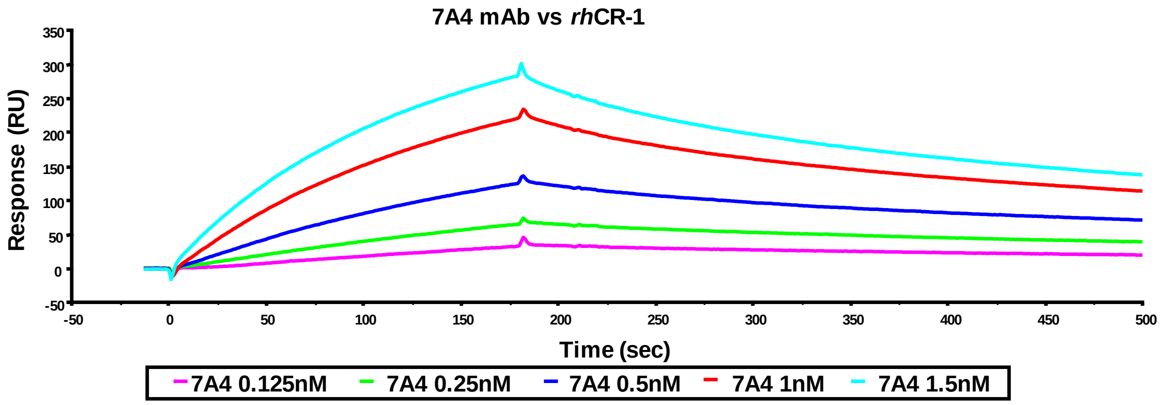

Table 7. Kinetic rate and apparent affinity constants of 7A4 mAb binding to *rh*CR-1

7A4	k_a (1/Ms)	k_d(1/s)	K_D (M)	SE(RI)
0.125 nM	$1.46*10^{5}$	$1.71*10^{-3}$	$1.17*10^{-8}$	0.0437
0.25nM	$4.10*10^{6}$	$1.74*10^{-3}$	$4.24*10^{-10}$	0.0641
0.5nM	$6.01*10^{6}$	$1.80*10^{-3}$	$3.00*10^{-10}$	0.101
1nM	$5.23*10^{6}$	$1.72*10^{-3}$	$3.29*10^{-10}$	0.152
1.5nM	$4.46*10^{6}$	$1.77*10^{-3}$	$3.97*10^{-10}$	0.143
average	$3.99*10^{6}$	$1.75*10^{-3}$	$2.63*10^{-9}$	0.101

Figure 3.9: Sensorgrams overlay and kinetic parameters table of 7A4 mAb binding to *rh*CR-1.

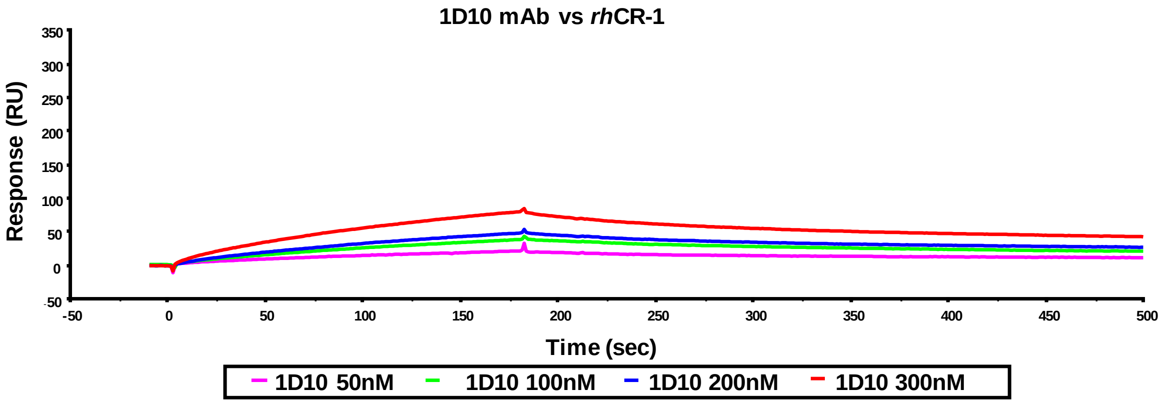

Table 8. Kinetic rate and apparent affinity constants of 1D10 mAb binding to *rh*CR-1

1D10	k_a (1/Ms)	k_d(1/s)	K_D (M)	SE (RI)
50nM	$6.52*10^{4}$	$1.05*10^{-3}$	$1.61*10^{-8}$	0.0522
100nM	$3.29*10^{4}$	$1.36*10^{-3}$	$4.14*10^{-8}$	0.0341
200nM	$1.92*10^{4}$	$1.72*10^{-3}$	$8{,}95*10^{-8}$	0.0829
300nM	$2.16*10^{4}$	$1.76*10^{-3}$	$8.13*10^{-8}$	0.130
average	$3.47*10^{4}$	$1.47*10^{-3}$	$5.71*10^{-8}$	0.0748

Figure 3.10: Sensorgrams overlay and kinetic parameters table of 1D10 mAb binding to *rh*CR-1.

In summary, by comparing all mAbs (see Table 9), we found that the 10D1 and 1B4 mAbs displayed sub-nanomolar affinity (K_Ds = 0.07 nM and 0.24 nM) towards *rh*CR-1, therefore represent promising molecules to be used to target human Cripto-1. The antibodies also denoted high specificity, recognizing residues on the surface of the CFC domain involved in the binding to ALK4 receptor.

Table 9. KD values of mAbs vs *rh*CR-1

mAb	KD (nM)
10D1	0.07
1B4	0.24
7A4	2.6
3F6	NB
1D10	57.0

1.5 10D1 AND 1B4 SPECIFICITY TEST ON *rh*CR-/*rm*Cr-1

ELISA assays were carried out to test the specificity of selected antibodies to human Cripto-1 versus the murine variant. The two full-length proteins (h-Cripto-1, Uniprot code:P13385; m-Cripto-1. Uniprot code: P51865) share an overall sequence identity of 63.38 %, however the identity within the CFC domains is about 85% (Fig. 3.11).

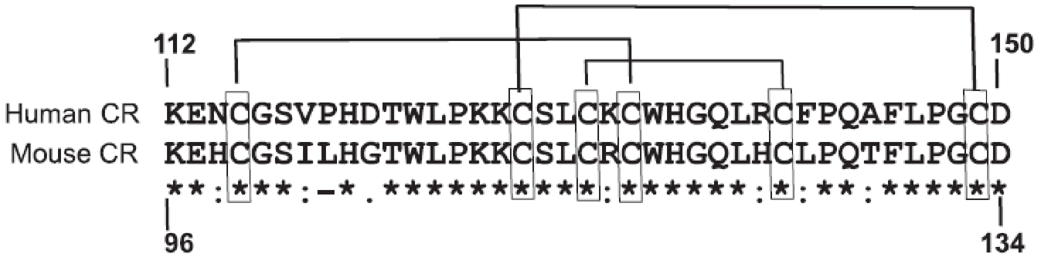

Figure 3.11: Amino acid sequence alignment of CFC domains belonging to human and murine form of Cripto-1. A remarkable hallmark is the conserved “hot spots” H120 and W123 in human CR-1 corresponding to H104 and W107 in mouse Cr-1.

As shown in Fig. 3.12, Elisa assays, performed as described in Methods (II.2.3.d section) coating both human and mouse recombinant Cripto-1, revealed that both mAbs recognize the human protein in a highly specific and dose-dependent fashion, being almost unable to bind the mouse variant. According to the SPR results, 10D1 mAb confirmed its higher affinity to human Cripto-1 compared to 1B4 mAb, exhibiting an increased absorbance even at very low amounts (12 ng).

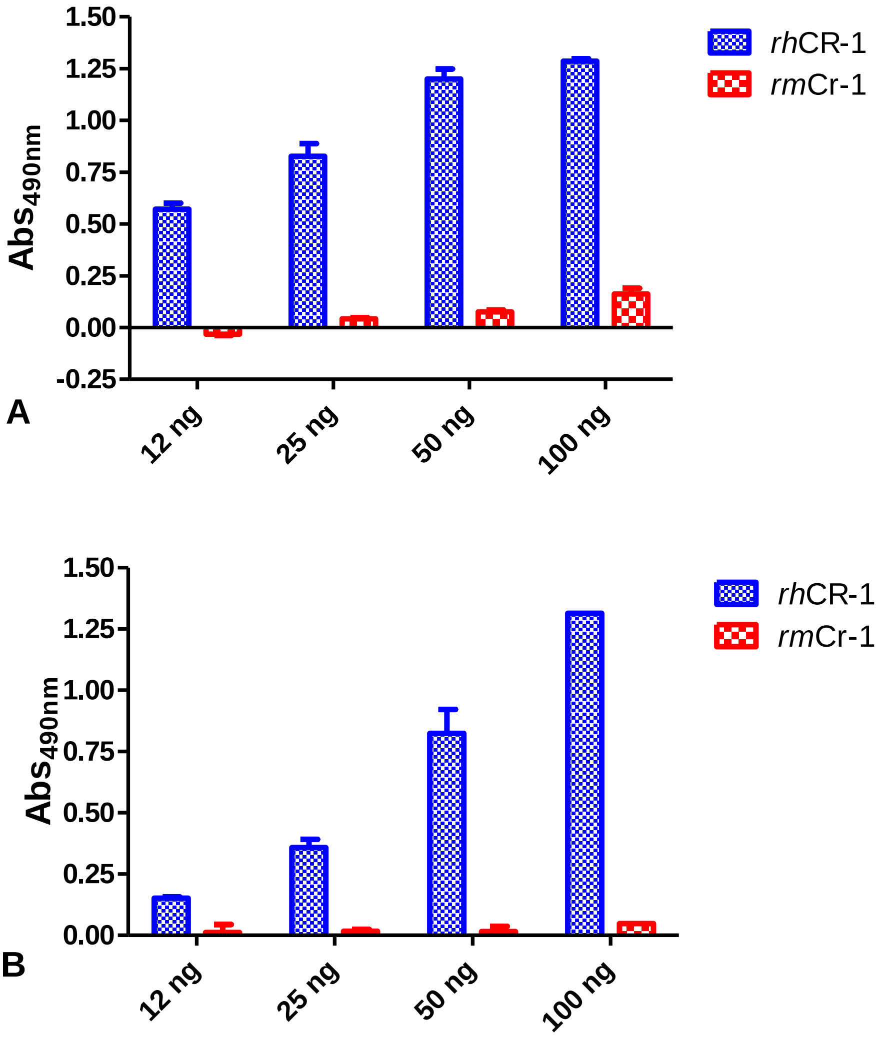

Figure 3.12: Bar graphs of the ELISA assays, carried out using recombinant Cripto proteins (human and mouse) at a range of increasing concentrations (12ng-25ng-50ng-100ng) detected by 10D1 (A) and 1B4 (B) mAbs, used at a concentration of 6.7 nM.

1.6 PRELIMINARY BINDING ASSAYS OF *rh*CR-1 TO *rh*ALK4

ELISA and SPR binding assays were performed to determine the affinity constant underlying the interaction between CR-1 and its fisiological partner, ALK4 receptor.

These preliminary data were next used to set up the optimal conditions to carry out competition assays with the 1B4 mAb. Using an ELISA assay, a dose-response binding of *rh*CR-1 to *rh*ALK4 was confirmed; such binding was characterized by an affinity constant of about 0.4 nM.

The interaction of *rh*ALK4 to *rh*CR-1, monitored by SPR, instead, revealed a K_D of about 4.6 nM, supported by association and dissociation rates of 1.56×10^{5} $M^{-1}s^{-1}$ and of 7.21×10^{-4} s^{-1}, respectively.

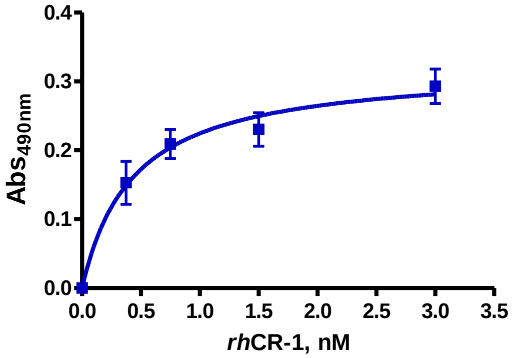

Figure 3.13: Dose-response ELISA assay showing the binding of *rh*CR-1 to *rh*ALK4 receptor.

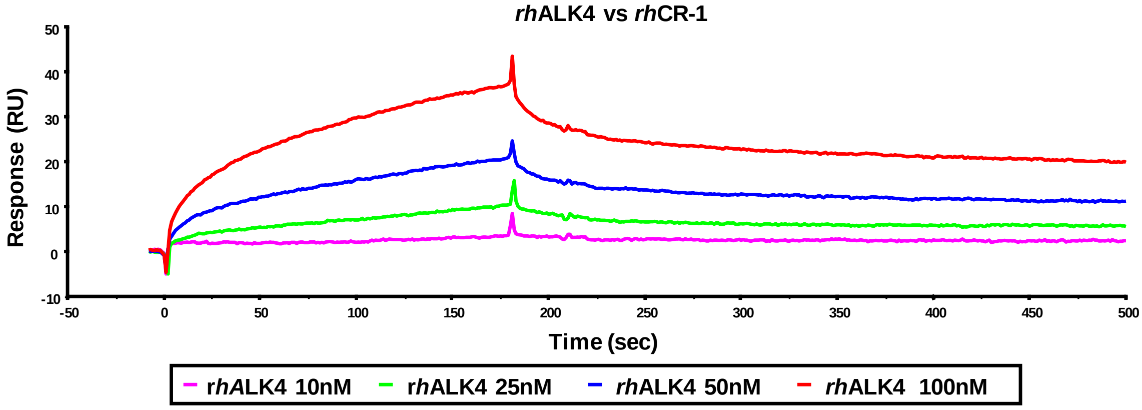

Table 10. Kinetic rate and apparent affinity constants of *rh*ALK4 binding to *rh*CR-1

rhALK4	k_a(1/Ms)	k_d(1/s)	K_D (M)	SE(RI)
25 nM	$1.41*10^5$	$6.40*10^{-4}$	$4.53*10^{-9}$	0.0658
50 nM	$1.58*10^5$	$5.66*10^{-4}$	$3.57*10^{-9}$	0.110
100 nM	$1.68*10^5$	$9.57*10^{-4}$	$5.70*10^{-9}$	0.131
average	$1.56*10^5$	$7.21*10^{-4}$	$4.60*10^{-9}$	0.153

Figure 3.14: Sensorgrams overlay and kinetic parameters table of *rh*ALK4 binding to *rh*CR-1.

1.7 DETECTION OF *rh*CR-1 BY 1B4 mAb IN ELISA CAPTURE ASSAY

The capture system, optimized using the commercial anti-Cripto polyclonal antibody in coating and the selected 1B4 mAb as primary detecting antibody, revealed that the lowest amount of *rh*CR-1 detectable by 1B4 was about 700 pg, as shown in the graph in Fig. 3.15. Here, the ng of protein are reported as a function of the absorbance measured at 450 nm.

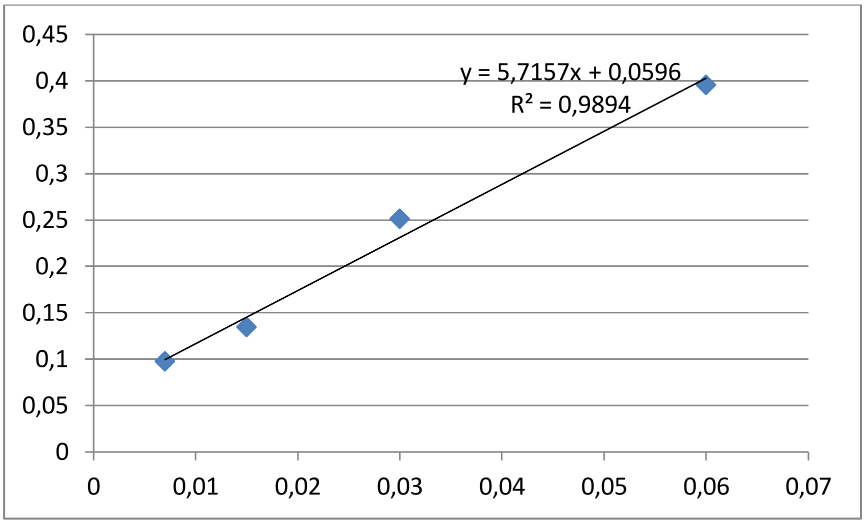

Figure 3.15: Calibration curve resulting by the detection of serially diluted *rh*CR-1 solutions. On the graph, the ng of *rh*CR-1 are reported as a function of the Abs$_{450nm}$, detected by 1B4 mAb, using the capture system.

1.8 COMPARATIVE EPITOPE STUDY BETWEEN 10D1 AND 1B4 mAbs

a) Insights into the antigen-Fab xomplex by computational studies

The search for the best template for the Fab fragment of each selected antibody gave different results. For the 10D1, the best template was a Fab fragment reported with the 3grw PDB file name in the RCSB database (www.rcsb.org). Thus, a 92.73% sequence homology was observed for the variable region of the light chain (V_L), while a 63.78% homology for the variable region of the heavy chain (V_H). By contrast, a perfect match (100% of homology) was found between the sequences of the whole constant region.

On the other hand, for the 1B4 mAb, two templates (1cbv and 1d5i), exhibiting the highest sequence homology for the variable region were found. More exactly, the 1cbv had a 95.65% identity on the V_L domain, while the 1d5i showed a higher homology (75.83%) compared with the V_H domain. Furthermore, 1cbv was shown to possess a higher sequence homology (100%) to the C_L region than 1d5i (72.25%). For the C_H region, the opposite situation was observed, since 1d5i was demonstrated to have a 100% identity homology, instead of 48.86% shown by 1cbv.

Once identified the best template for each mAb, the sequence alignment of 10D1 and 1B4 Fab fragments was performed, providing a 75.7% identity sequence. Simoultaneously CDRs were predicted on the basis of the secondary structure, as determined by homology sequence and homology to crystal structures of IgGs reported in the pdb database.

The six CDRs, three belonging to the light chain (L1, L2 and L3) and three to the heavy chain (H1, H2 and H3), were predicted as reported in Table 11 and in Fig. 3.16.

Table 11. Identified CDRs of 10D1 and 1B4 mAbs

CDR	10D1	1B4
H1	S24-Y31	A25-Y32
H2	Y51-N56	S52-Y56
H3	M99-Q115	F98-Q108
L1	S26-A32	S26-Y37
L2	Y49-T56	K55-S61
L3	Q90-P95	Q95-P100

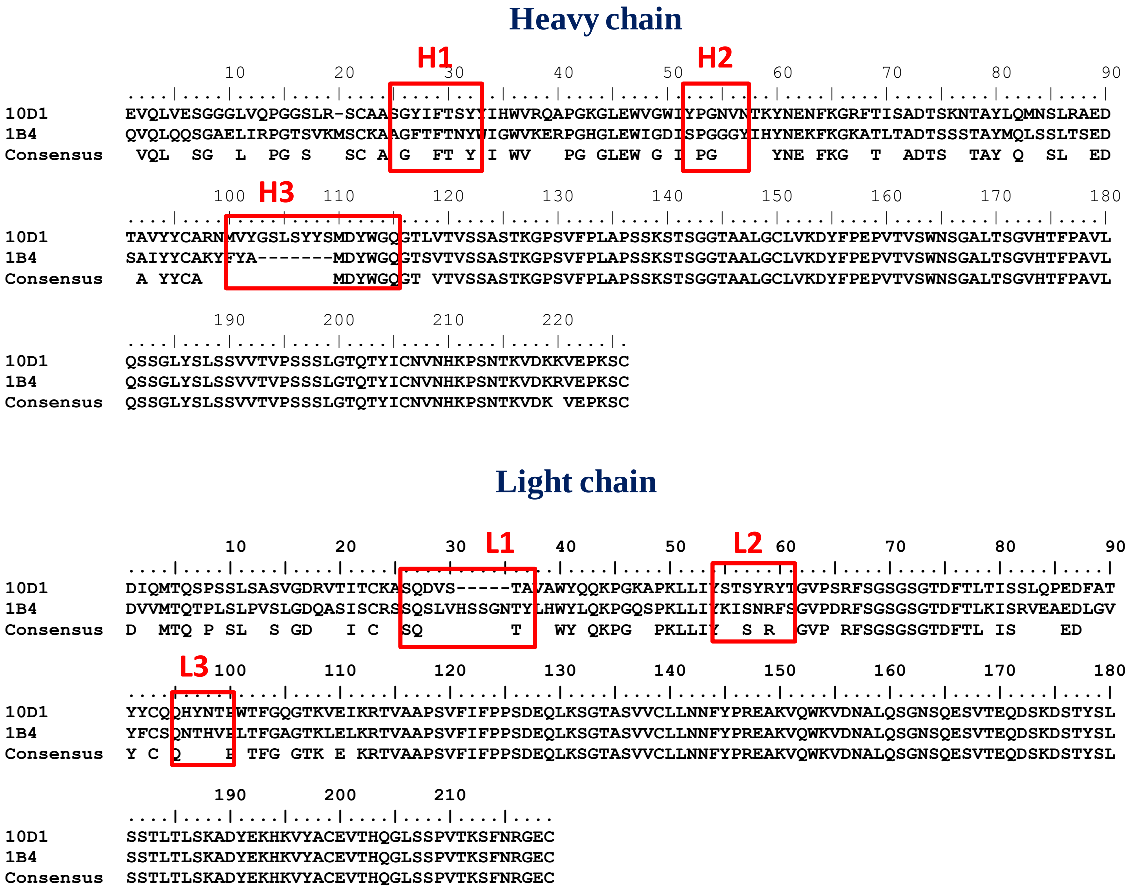

```
                   10        20        30        40        50        60        70        80        90
           ....|....|....|....|....|....|....|....|....|....|....|....|....|....|....|....|....|....|
10D1       EVQLVESGGGLVQPGGSLR-SCAASGYIFTSYYIHWVRQAPGKGLEWVGWIYPGNVNTKYNENFKGRFTISADTSKNTAYLQMNSLRAED
1B4        QVQLQQSGAELIRPGTSVKMSCKAAGFTFTNYWIGWVKERPGHGLEWIGDISPGGGYIHYNEKFKGKATLTADTSSSTAYMQLSSLTSED
Consensus   VQL  SG  L  PG S   SC A G  FT Y I WV   PG GLEW G I PG     YNE FKG  T  ADTS  TAY Q  SL  ED

                  100       110       120       130       140       150       160       170       180
           ....|....|....|....|....|....|....|....|....|....|....|....|....|....|....|....|....|....|
10D1       TAVYYCARNMVYGSLSYYSMDYWGQGTLVTVSSASTKGPSVFPLAPSSKSTSGGTAALGCLVKDYFPEPVTVSWNSGALTSGVHTFPAVL
1B4        SAIYYCAKYFYA-------MDYWGQGTSVTVSSASTKGPSVFPLAPSSKSTSGGTAALGCLVKDYFPEPVTVSWNSGALTSGVHTFPAVL
Consensus   A YYCA            MDYWGQGT VTVSSASTKGPSVFPLAPSSKSTSGGTAALGCLVKDYFPEPVTVSWNSGALTSGVHTFPAVL

                  190       200       210       220
           ....|....|....|....|....|....|....|....|....|.
10D1       QSSGLYSLSSVVTVPSSSLGTQTYICNVNHKPSNTKVDKKVEPKSC
1B4        QSSGLYSLSSVVTVPSSSLGTQTYICNVNHKPSNTKVDKRVEPKSC
Consensus  QSSGLYSLSSVVTVPSSSLGTQTYICNVNHKPSNTKVDK VEPKSC
```

```
                   10        20        30        40        50        60        70        80        90
           ....|....|....|....|....|....|....|....|....|....|....|....|....|....|....|....|....|....|
10D1       DIQMTQSPSSLSASVGDRVTITCKASQDVS-----TAVAWYQQKPGKAPKLLIYSTSYRYTGVPSRFSGSGSGTDFTLTISSLQPEDFAT
1B4        DVVMTQTPLSLPVSLGDQASISCRSSQSLVHSSGNTYLHWYLQKPGQSPKLLIYKISNRFSGVPDRFSGSGSGTDFTLKISRVEAEDLGV
Consensus  D  MTQ P SL  S GD   I C  SQ        T   WY QKPG  PKLLIY  S R  GVP RFSGSGSGTDFTL IS    ED

                  100       110       120       130       140       150       160       170       180
           ....|....|....|....|....|....|....|....|....|....|....|....|....|....|....|....|....|....|
10D1       YYCQQHYNTPWTFGQGTKVEIKRTVAAPSVFIFPPSDEQLKSGTASVVCLLNNFYPREAKVQWKVDNALQSGNSQESVTEQDSKDSTYSL
1B4        YFCSQNTHVPLTFGAGTKLELKRTVAAPSVFIFPPSDEQLKSGTASVVCLLNNFYPREAKVQWKVDNALQSGNSQESVTEQDSKDSTYSL
Consensus  Y C Q    P TFG GTK E KRTVAAPSVFIFPPSDEQLKSGTASVVCLLNNFYPREAKVQWKVDNALQSGNSQESVTEQDSKDSTYSL

                  190       200       210
           ....|....|....|....|....|....|....|....
10D1       SSTLTLSKADYEKHKVYACEVTHQGLSSPVTKSFNRGEC
1B4        SSTLTLSKADYEKHKVYACEVTHQGLSSPVTKSFNRGEC
Consensus  SSTLTLSKADYEKHKVYACEVTHQGLSSPVTKSFNRGEC
```

figure 3.16: Sequence alignment of separated heavy and light chains of 10D1 and 1B4 mAbs. The specific CDRs are reported in the red boxes.

The model of the Fab fragments, obtained with a RMSD (root mean squared deviation) of 1.11 Å for the backbone atoms, showed the canonical secondary structure proper of Ig-like domain, made up of a β-sheet motif, in which the β-loops correspond to the CDRs.

Comparing the models built for each mAb, we found that the 10D1 mAb (reported in red in Fig. 3.17) has a longer H3 loop (17 residues) and a shorter L1 loop (7 residues) compared to those of 1B4 mAb (reported in blue), whose H3 loop has 6 residues, while the L1 loop contains 12 residues.

Such differences could explain the different affinity exhibited by the two mAbs toward hCFC as well as *rh*CR-1 protein.

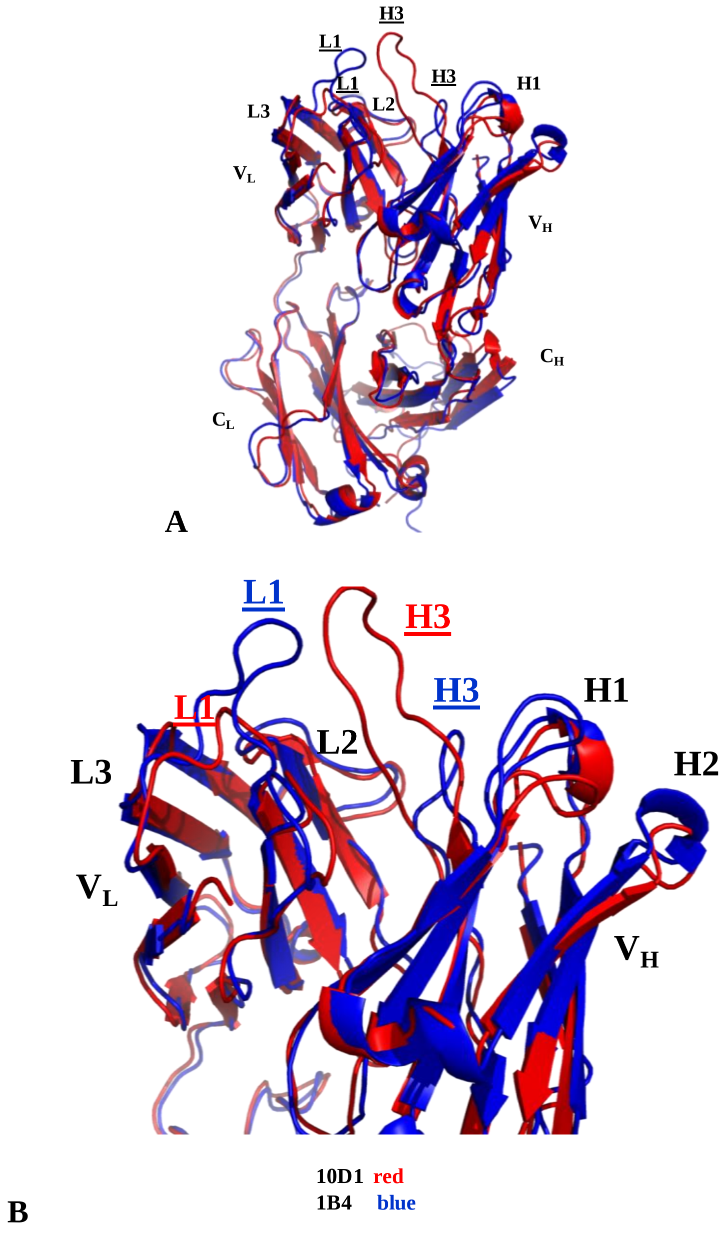

Figure 3.17: A. Fab models of 10D1 (red) and 1B4 (blue) mAbs built by homology modelling. Fabs are made up of four domains: variable (V_L) and constant (C_L) domains of the light chain, and the variable (V_H) and the first constant (C_H) domain of the heavy chain. **B.** Zoom of the variable fragment (Fv), containing only the variable regions of the light and heavy chains (V_L and V_H respectively), The six loops corresponding to the CDRs (three on the light chain and three on the heavy chain) are reported. Loops H3 and L1 differing in length are underlined.

Docking studies performed on the complex formed by the Fabs and the hCFC antigen gave similar results for both 10D1 and 1B4 mAbs.

Considering the energy-minimized antigen-Fab complex, both 10D1 and 1B4 mAbs appeared to interact with the hCFC domain in a similar manner, denoting a comparable binding energy (Ebind = -11.35 kcal/mol and -10.47 kcal/mol for 10D1 and 1B4 respectively).

Moreover, following a more detailed visual inspection of the binding interface, on the basis of the contact residues map of each complex, we identified a hydrophobic-polar groove at the contact interface, in which favourable hydrophobic interactions were detected in combination with H-bonds. Such surface formed a pocket in which H120 and W123 of hCFC can easily insert. In Tables 12 and 13 the COCOMAPS analysis results are reported. For each identified favourable residue, the position on the loop is reported, specifying if the binding contribution is given to H120 or W123.

Table 12. 10D1-hCFC contact residues

Residue position	H120	W123
H3	M99 (H-bond)	V100
H3	V100	Y101
H3	Y101	G102
H3	G102	S103
L2	Y49	
L2	Y55	
L2	T56 (H-bond)	

Table 13. 1B4-hCFC contact residues

Residue position	H120	W123
H3	Y101 (H-bond)	F100
H3	A102	Y101
H3	M103	
L2	Y54	
L2	F60	

As revealed by the contact maps, the major contibution to the binding is provided by residues belonging to the H3 loop, which are able to interact with both H and W residues of the epitope, extablishing favourable hydrophobic interactions. Moreover, a few aromatic residues (Y and F), embedded in the L2 loop, give a contribution only to H120.

Considering the 10D1-hCFC contact region, the residues exposed by the H3 loop to both H120 and W123 are represented by V100, Y101 and G102. Instead, L2 loop exposes two Y (49 and 55) exclusively to H120. On the other hand, at the binding interface of the 1B4-hCFC complex, the aromatic rings of F100 and Y101, belonging to the H3 loop, can be involved in aromatic and/or π-stacking interactions. This kind of interactions can potentially be established also by Y49, Y54 and F60 exposed on the L2 loop, which is bent on the opposite side of the H3 loop.

Indeed, the comparison between the contact regions of the two mAbs revealed that the 10D1 exposes to the antigen more residues than the 1B4, as expected since the H3 loop belonging to the 10D1 mAb is longer than that one of 1B4; despite this difference, both mAbs show at the binding interface residues with a comparable polarity. Moreover, two residues are conserved (M and Y). A remarkable hallmark is the amino acid composition of the L2 loop. As can be seen, a perfect match is observable between the aromatic residues residing within the two peptide segments, since Y49 and Y55 of 10D1 find as corresponding residues the Y54 and F60 of 1B4 (See Fig. 3.18 and 3.19).

Analysing the entire antibody-antigen complex, a further difference is detectable between the two mAbs: 10D1 exposes to hCFC a wider contact region than 1B4, which indeed forms a more compact complex compared to the one obtained with 10D1, suggesting a high fit capability towards the antigen. Remarkably, 1B4 forms a pocket perfectly surrounded by the H3-L2 loop motif, in which the epitope can protrude, leading to the formation of a typical key-lock model.

Interestingly, the favourable hydrophobic interactions shown by both 10D1 and 1B4 are similar to those found at the binding interface of the complex hCFC-ALK4 **[23]**, where Y55 and F56 of the receptor were shown to be responsible of aromatic interactions with H120 and W123 of hCFC (See Fig. 3.18 and 3.19).

These models thus provide a picture of how 10D1 and 1B4 bind the CFC domain of Cripto-1 and presumably can neutralize the ALK4 binding and activation.

hCFC-10D1 COMPLEX

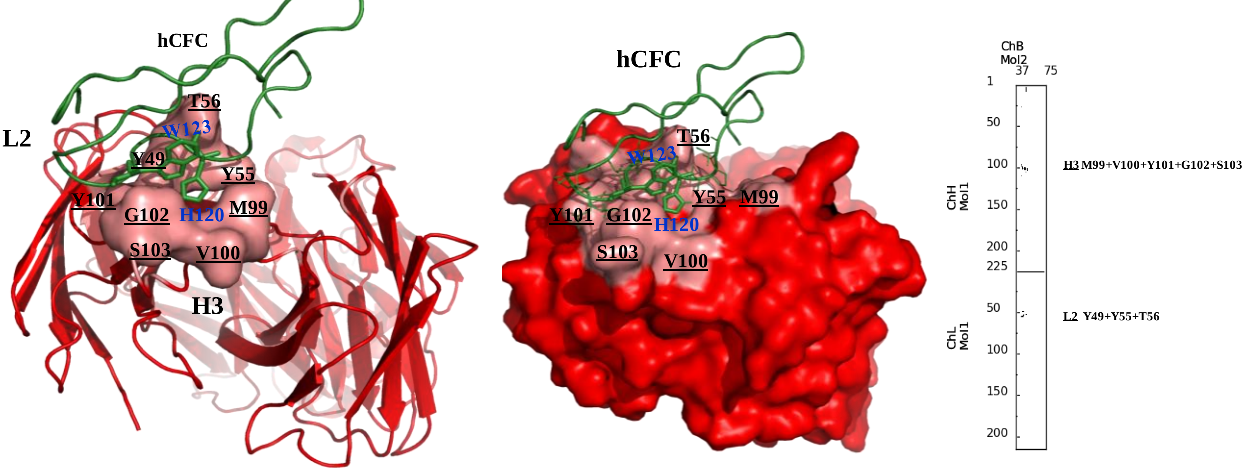

Ebind=-11,35 kcal/mol

Figure 3.18: Representation of the interaction at the binding interface of 10D1 Fab fragment (stick model on the left and Connolly surface area on the right) and hCFC (stick model). On the contact region the crucial residues for the antibody-antigen recognition are underlined. In addition, the contact map is reported on the right side of the figure.

hCFC-1B4 COMPLEX

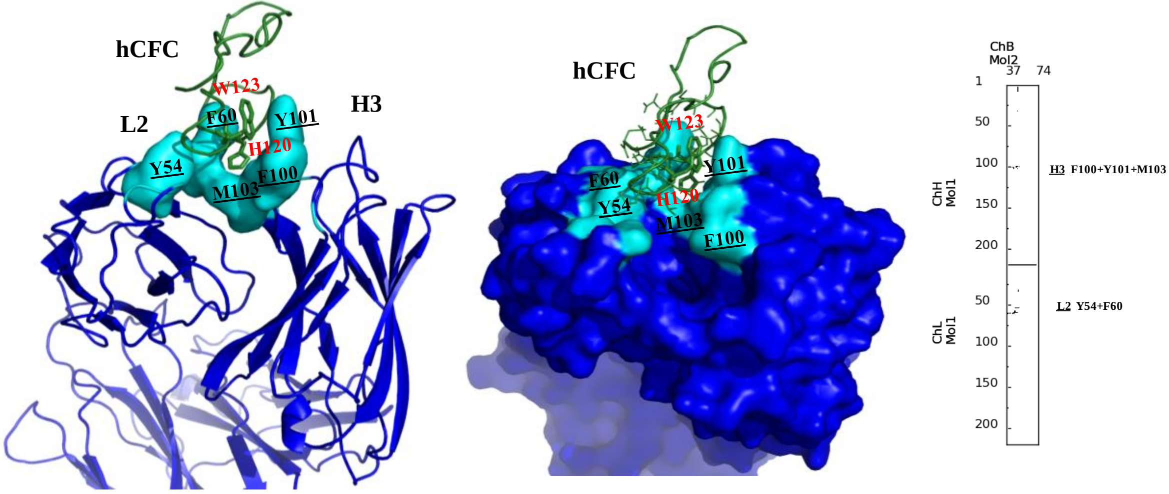

Ebind=-10,47 kcal/mol

Figure 3.19: Representation of the interaction at the binding interface of 1B4 Fab fragment (stick model on the left and Connolly surface area on the right) and hCFC (stick model). On the contact region the crucial residues for the antibody-antigen recognition are underlined. In addition, the contact map is reported on the right side of the figure.

This computational study provided valuable informations about the binding surface of the antibody-antigen complex, thus can be the basis to design recombinant fragments and improving them by site-directed mutagenesis studies and to generate new variants of these fragments to eventually select the best molecule in terms of affinity and specifity to the antigen.

b) Epitope mapping assays

An epitope mapping study was performed to delineate those residues on hCFC responsible of antibody recognition. The study was performed by the combination of ELISA and SPR assays, using the wild-type hCFC[112-150] and three chemically generated variants: hCFC[112-150]H120A, hCFC[112-150]W123A and hCFC[112-150]H120AW123A.

ELISA assays

Dose-dependent ELISA binding assays between 10D1 and 1B4 mAbs and synthetic wild-type hCFC[112-150] and mutated domains were carried out as described in the Methods (section 2.3.d).

As shown in Fig. 3.20 A, 10D1 was still able to recognize the hCFC[112-150]H120A mutant, whereas no binding was detected to hCFC[112-150]W123A and hCFC[112-150]H120AW123A.

1B4, instead, bound only the wild type hCFC[112-150], as shown in Figure 3.20 B.

To better evaluate the loss of binding we used the binding signal obtained with the mAbs at 4 nM, assuming as 100% the one obtained with the wild-type hCFC.

As shown in Fig. 3.21, 10D1 showed around 60% loss of binding toward H120A variant and around 75% toward W123A mutant. Under these conditions the doubly mutated H120AW123A showed a residual binding of only about 15% .

Under the same conditions, mutations occurred at the same residues on hCFC led to about 80% loss of binding with 1B4. Data are thus suggestive of the relevant role played by both H120 and W123 residues in the binding to the antibodies.

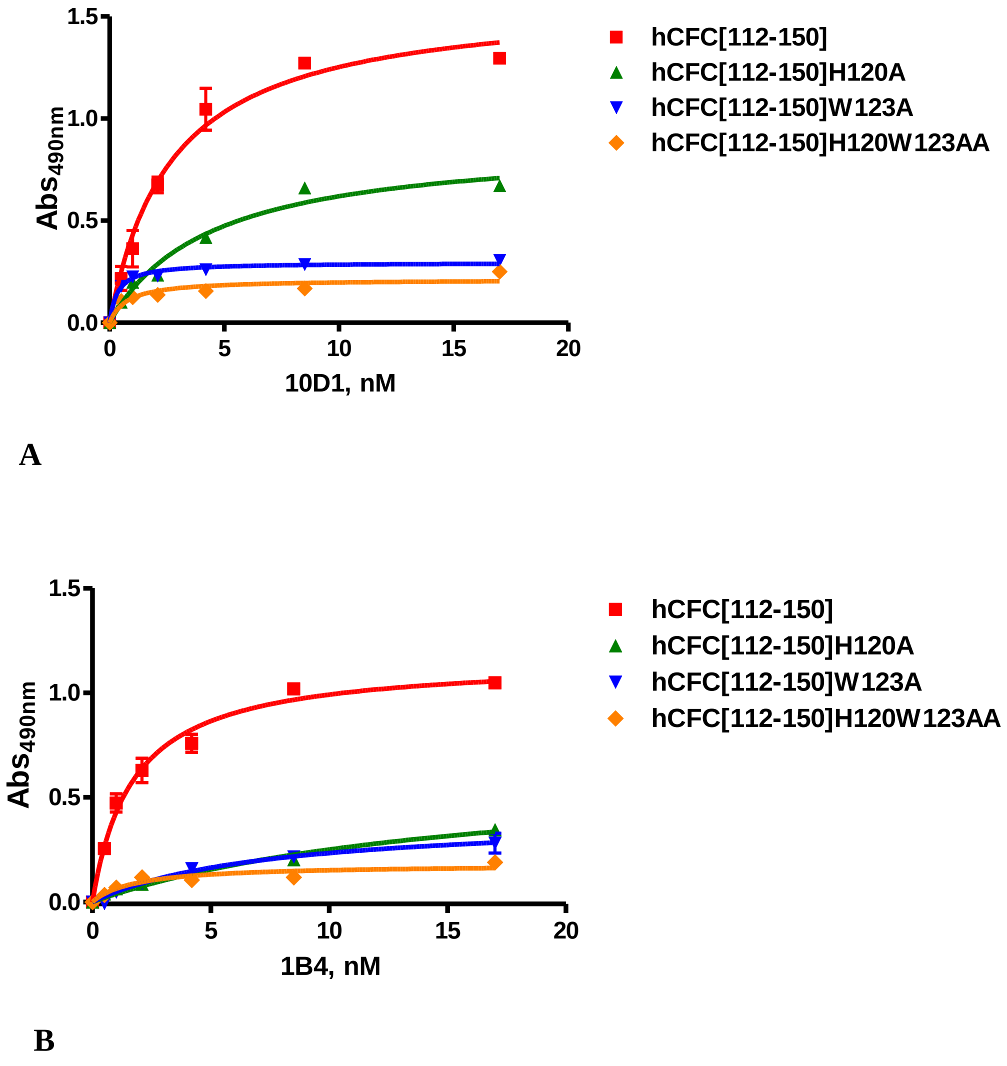

Figure 3.20: ELISA epitope mapping. Dose-response curves are reported for 10D1 (A) and 1B4 (B) mAbs.

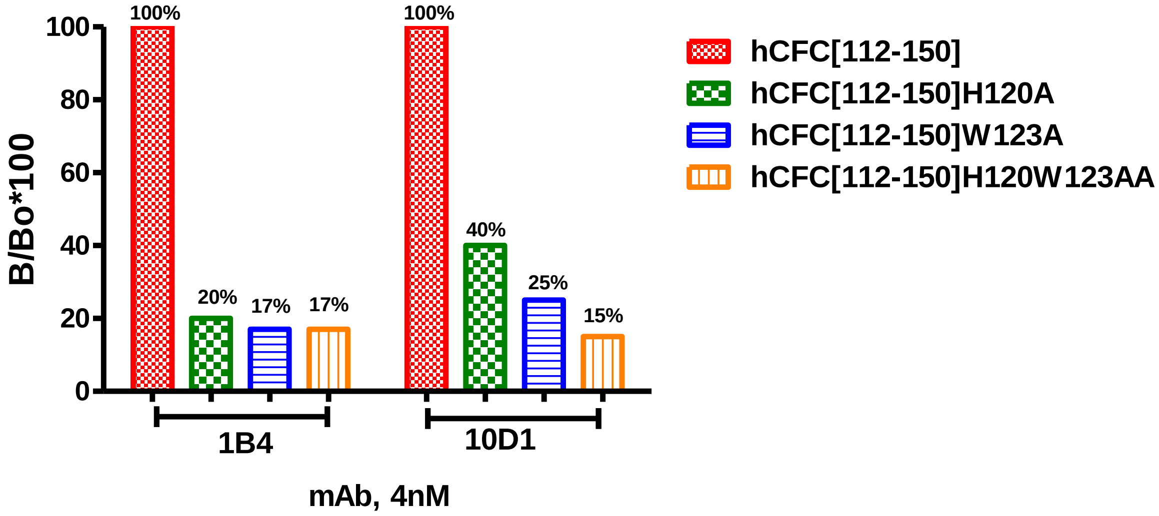

Figure 3.21: ELISA epitope mapping. Normalization bars graph in which the binding of each mAb (4 nM) to hCFC variants is expressed as percentage of binding.

SPR assays

ELISA epitope mapping results were supported by SPR analyses, by which a more detailed insight is provided about the antigen-antibody interaction, defined in terms of association and dissociation rate constants. The preliminary dose-response binding of the full-length *rh*CR-1 to the immobilized mAbs revealed K_D values corresponding to ~3.5 nM and ~70 nM on 10D1 and 1B4 mAbs respectively. The interaction of both 10D1 and 1B4 mAbs with the specific antigen, the synthetic wild-type hCFC[112-150], was underlined by K_D values of 2 nM and 30 nM, respectively, denoting their high specificity. By comparing the binding curves of 10D1 to wild-type and H120A hCFC domains, this mAb displayed toward the mutant less favorable kinetics parameters revealing that this interaction was less strong, since the antigen-antibody complex underwent a very fast dissociation with a final K_D = 14 nM, which is ten-fold lower than that one of wild-type hCFC (K_D = 1.8 nM). Moreover, the interaction with the W123A mutant (K_D = 200 nM) exhibited a dramatic loss of affinity through the dissociation rate, that was faster than the wild-type domain, thus suggesting that these mutations negatively influence the strength of antigen-antibody complex. Finally, the interaction with the doubly mutated H120W123AA domain showed a very fast dissociation and we could not determine any dissociation parameter. These data confirmed that both residues H120 and W123 are strongly involved in the binding with the antibody (see also Fig. 3.22 through 3.26).

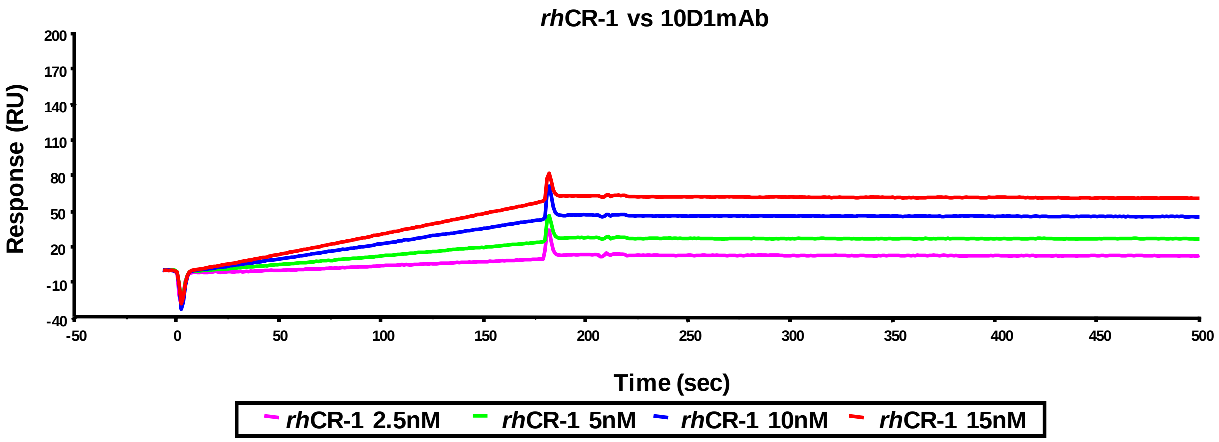

Table 14. Kinetic rate and apparent affinity constants of *rh*CR-1 binding to 10D1 mAb

***rh*CR-1**	**k_a (1/Ms)**	**k_d (1/s)**	**K_D (M)**	**SE (RI)**
2.5 nM	$1.10*10^{5}$	$1.46*10^{-4}$	$1.33*10^{-9}$	0.033
5 nM	$9.70*10^{3}$	$2.43*10^{-5}$	$2.50*10^{-9}$	0.0226
10 nM	$5.98*10^{3}$	$3.72*10^{-5}$	$6.22*10^{-9}$	0.0362
15 nM	$2.06*10^{4}$	$8.39*10^{-5}$	$4.08*10^{-9}$	0.0378
average	$3.66*10^{4}$	$7.29*10^{-5}$	$3.53*10^{-9}$	0.0324

Figure 3.22: Sensorgrams overlay and kinetic parameters table of *rh*CR-1 binding to 10D1 mAb.

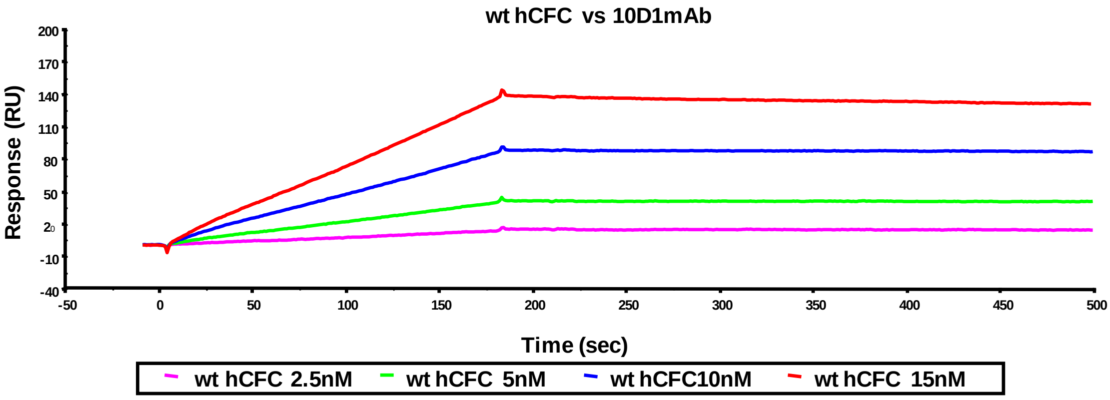

Table 15. Kinetic rate and apparent affinity constants of wild-type hCFC binding to 10D1 mAb

wt hCFC	**k_a (1/Ms)**	**k_d (1/s)**	**K_D (M)**	**SE (RI)**
2.5 nM	$3.51*10^{4}$	$1.44*10^{-4}$	$4.10*10^{-9}$	0.0393
5 nM	$2.16*10^{4}$	$4.63*10^{-6}$	$2.14*10^{-10}$	0.0364
10 nM	$1.12*10^{4}$	$2.06*10^{-5}$	$1.85*10^{-9}$	0.0428
15 nM	$1.34*10^{5}$	$1.54*10^{-4}$	$1.15*10^{-9}$	0.103
average	$5.05*10^{4}$	$8.08*10^{-5}$	$1.83*10^{-9}$	0.0553

Figure 3.23: Sensorgrams overlay kinetic parameters table of wild-type hCFC[112-150] domain binding to 10D1 mAb.

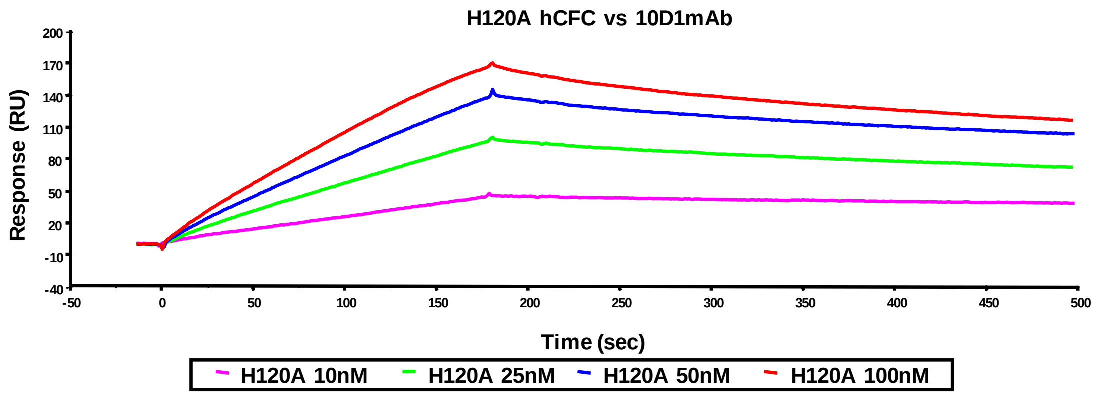

Table 16. Kinetic rate and apparent affinity constants of H120A hCFC binding to 10D1 mAb

H120A	k_a (1/Ms)	k_d (1/s)	K_D (M)	SE (RI)
10 nM	$1.57*10^{4}$	$5.14*10^{-4}$	$3.28*10^{-8}$	0.0404
25 nM	$6.12*10^{4}$	$9.94*10^{-4}$	$1.63*10^{-8}$	0.120
50 nM	$2.60*10^{5}$	$9.15*10^{-4}$	$3.52*10^{-9}$	0.0686
100 nM	$3.47*10^{5}$	$1.15*10^{-3}$	$3.32*10^{-9}$	0.109
average	$1.71*10^{5}$	$8.93*10^{-4}$	$1.40*10^{-8}$	0.0845

Figure 3.24: Sensorgrams overlay and kinetic parameters table of the singly mutated hCFC[112-150] H120A domain binding to 10D1 mAb.

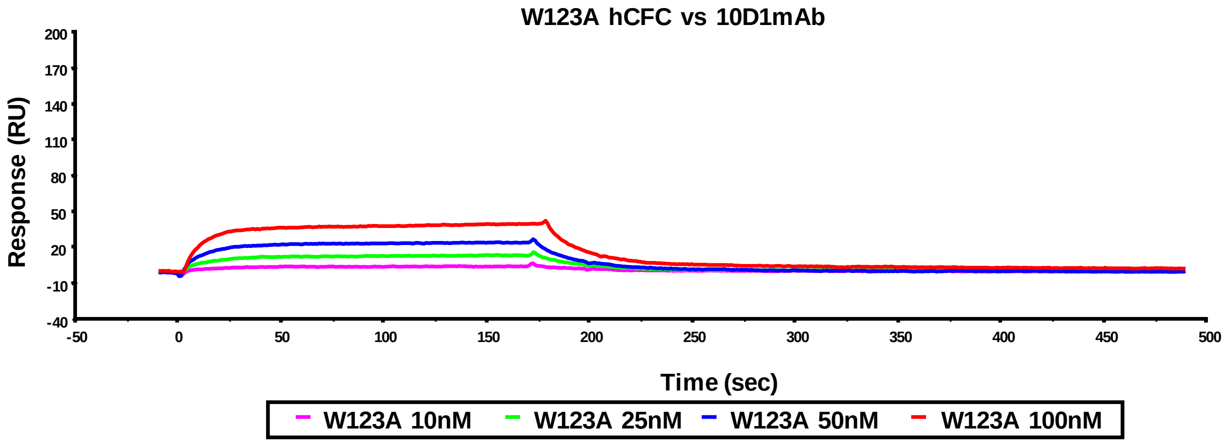

Table 17. Kinetic rate and apparent affinity constants of W123A hCFC binding to 10D1 mAb

W123A	k_a (1/Ms)	k_d (1/s)	K_D (M)	SE (RI)
10 nM	$2.29*10^{6}$	0.034	$1.48*10^{-8}$	0.0878
25 nM	$3.63*10^{5}$	0.043	$1.18*10^{-7}$	0.124
50 nM	$1.71*10^{5}$	0.0583	$3.42*10^{-7}$	0.145
100 nM	$1.66*10^{5}$	0.0644	$3.88*10^{-7}$	0.369
average	$7.48*10^{5}$	$4.99*10^{-2}$	$2.16*10^{-7}$	0.181

Figure 3.25: Sensorgrams overlay and kinetic parameters table of the singly mutated hCFC[112-150] W123A domain binding to 10D1 mAb.

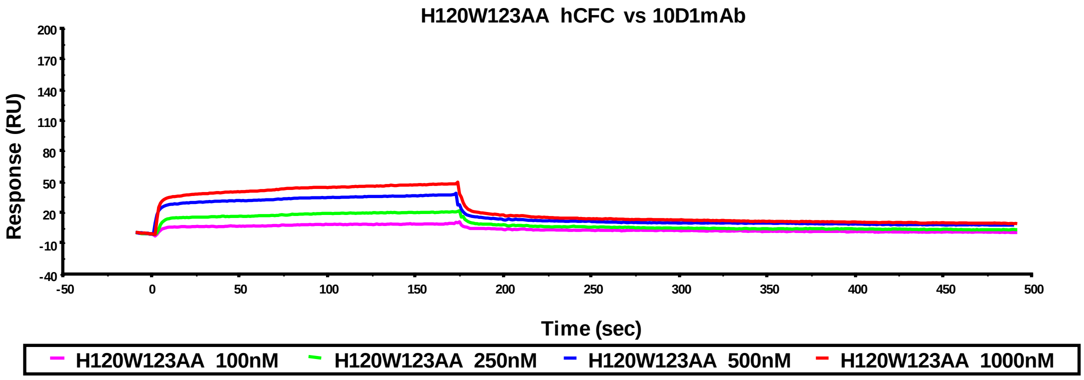

NO FITTING

Figure 3.26: Sensorgrams overlay of the doubly mutated hCFC[112-150] H120W123AA domain binding to 10D1 mAb. No fitting means that the kinetic parameters did not converge to any value.

The comparison of kinetic parameters between the interaction of 1B4 mAb and synthetic wild-type hCFC[112-150] to the H120A mutant, denoted a decreased affinity towards the mutated form of the domain, due to a reduced association constant, the dissociation constants were comparable, instead. Thus, the K_D value extrapolated from the wild-type hCFC-1B4 mAb was ~30 nM, while the K_D corresponding to the binding to the H120A mutant was 355 nM. The binding to the W123A variant exhibited kinetic constants comparable to the wild-type hCFC, but the resulting K_D value (127 nM) was ten fold lower (30 nM), since less polypeptide was captured by the antibody.

Finally, the H120W123AA mutant showed an affinity constant (K_D=157 nM) ten fold lower compared to the wild type. Kinetics parameters showed unfavorable association and dissociation constants revealing the importance of both mutated residues for the recognition and for the stabilization of the complex (see also Fig. 3.27 through 3.31). All the extrapolated K_D values are summarized in Table 23.

.

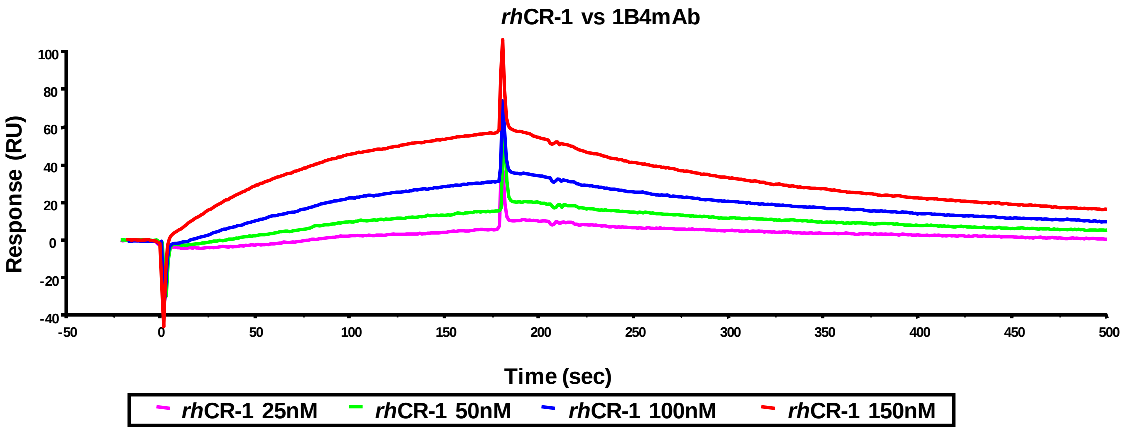

Table 18. Kinetic rate and apparent affinity constants of *rh*CR-1 binding to 1B4 mAb

*rh*CR-1	k_a (1/Ms)	k_d (1/s)	K_D (M)	SE (RI)
25 nM	$1.08*10^5$	$4.20*10^{-3}$	$3.91*10^{-8}$	0.0410
50 nM	$3.93*10^4$	$3.68*10^{-3}$	$9.36*10^{-8}$	0.0327
100nM	$6.14*10^4$	$3.52*10^{-3}$	$5.73*10^{-8}$	0.0538
150nM	$3.66*10^4$	$3.46*10^{-3}$	$9.44*10^{-8}$	0.0851
average	$5.84*10^4$	$3.51*10^{-3}$	$6.84*10^{-8}$	0.0531

Figure 3.27: Sensorgrams overlay and kinetic parameters table of *rh*CR-1 binding to 1B4 mAb.

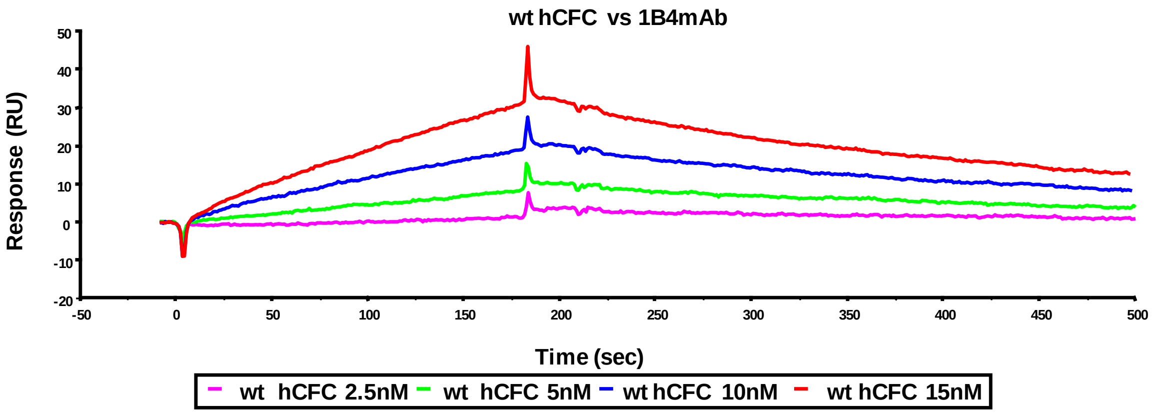

Table 19. Kinetic rate and apparent affinity constants of wild-type hCFC binding to 1B4 mAb

wt hCFC	k_a (1/Ms)	k_d (1/s)	K_D (M)	SE (RI)
2.5 nM	$4.77*10^4$	$3.09*10^{-3}$	$6.47*10^{-8}$	0.0374
5 nM	$1.29*10^5$	$2.58*10^{-3}$	$2.00*10^{-8}$	0.0515
10 nM	$1.01*10^5$	$2.81*10^{-3}$	$2.78*10^{-8}$	0.0554
15 nM	$2.23*10^5$	$3.08*10^{-3}$	$1.38*10^{-8}$	0.0622
average	$1.25*10^5$	$2.89*10^{-3}$	$3.16*10^{-8}$	0.0516

Figure 3.28: Sensorgrams overlay and kinetic parameters table of wild-type hCFC[112-150] domain binding to 1B4 mAb.

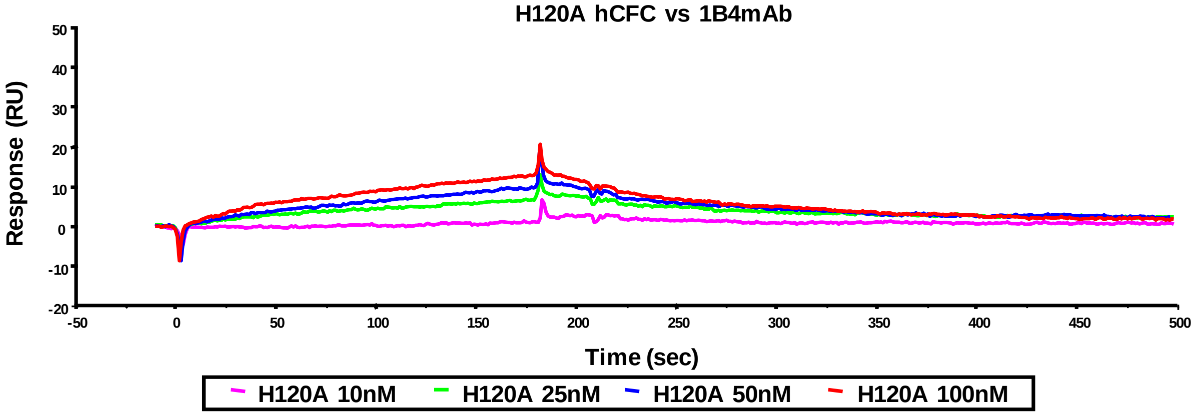

Table 20. Kinetic rate and apparent affinity constants of H120A hCFC binding to 1B4 mAb				
H120A	**k_a (1/Ms)**	**k_d (1/s)**	**K_D (M)**	**SE (RI)**
2.5 nM	$1.26*10^5$	$3.34*10^{-3}$	$2.65*10^{-8}$	0.0439
5 nM	$1.63*10^5$	$4.37*10^{-3}$	$2.68*10^{-8}$	0.036
10 nM	$1.32*10^4$	$5.33*10^{-3}$	$4.05*10^{-7}$	0.031
15 nM	$6.74*10^3$	$6.47*10^{-3}$	$9.61*10^{-7}$	0.0413
average	$7.72*10^4$	$4.88*10^{-3}$	$3.55*10^{-7}$	0.038

Figure 3.29: Sensorgrams overlay and kinetic parameters table of the singly mutated hCFC[112-150]H120A domain binding to 1B4 mAb.

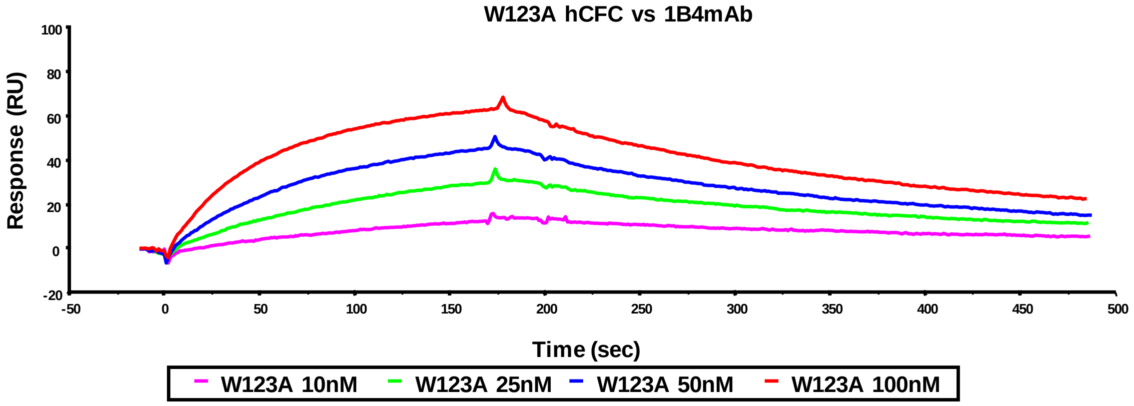

Table 21. Kinetic rate and apparent affinity constants of W123A hCFC binding to 1B4 mAb				
W123A	**k_a (1/Ms)**	**k_d (1/s)**	**K_D (M)**	**SE (RI)**
10nM	$7.55*10^3$	$3.31*10^{-3}$	$4.38*10^{-7}$	0.032
25nM	$1.35*10^5$	$3.79*10^{-3}$	$2.82*10^{-8}$	0.0499
50nM	$1.78*10^5$	$3.78*10^{-3}$	$2.12*10^{-8}$	0.0597
100nM	$1.60*10^5$	$3.53*10^{-3}$	$2.20*10^{-8}$	0.112
average	$1.20*10^5$	$3.60*10^{-3}$	$1.27*10^{-7}$	0.0634

Figure 3.30: Sensorgrams overlay and kinetic parameters table of the singly mutated hCFC[112-150]W123A domain binding to 1B4 mAb.

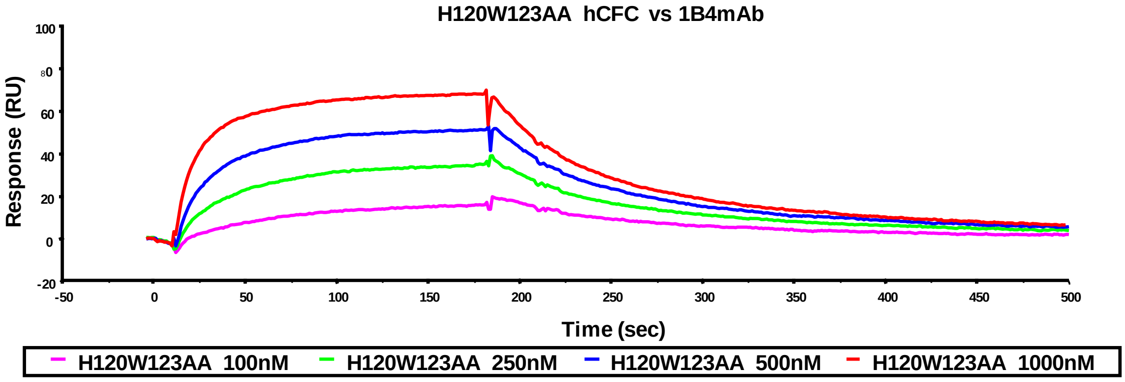

Table 22. Kinetic rate and apparent affinity constants of H120W123AA hCFC binding to 1B4 mAb

H120W123 AA	k_a (1/Ms)	k_d (1/s)	K_D (M)	SE (RI)
100 nM	$9.36*10^4$	$9.90*10^{-3}$	$1.06*10^{-7}$	0.0531
250 nM	$6.70*10^4$	$8.43*10^{-3}$	$1.26*10^{-7}$	0.134
500 nM	$4.90*10^4$	$8.13*10^{-3}$	$1.66*10^{-7}$	0.404
1000 nM	$3.91*10^4$	$8.95*10^{-3}$	$2.29*10^{-7}$	0.754
average	$6.22*10^4$	$8.85*10^{-3}$	$1.57*10^{-7}$	0.336

Figure 3.31: Sensorgrams overlay and kinetic parameters table of the doubly mutated hCFC[112-150]H120W123AA domain binding to 1B4 mAb.

Table 23. K_D values summary of the epitope mapping assays

	10D1 **nM**	**1B4** **nM**
***rh*CR-1**	3.53	68.4
wt hCFC	1.83	31.6
hCFC H120A	14	355
hCFCW123A	216	127
hCFCH120W123AA	no fitting	157

In conclusion, the SPR results are in accordance to the ELISA results, suggesting that both mAbs are specific towards the region of the hCFC domain containing the two residues, H120 and W123, known to be “hot spots” for the interaction CR-1/ALK4. Thus, these mAbs are promising candidates as neutralizing antibodies, to block the interaction between the protein and its receptor. By the thermodynamic and kinetic binding analysis it appears that 1B4 binds more efficiently to both W123 and H120, whereas 10D1 interacts only with W123.

1B4 was selected for further studies and to generate the recombinant Fab fragment to be subsequently developed as potential therapeutic tool targeting CR-1 with high specificity.

III.2 GENERATION AND BIOCHEMICAL CHARACTERIZATION OF 1B4 FUNCTIONAL Fab FRAGMENTS AND NEW FORMATS

2.1 PROTEOLYTIC CLEAVAGE OF 1B4 mAb

a) Papain digestion of 1B4 antibody

Initially, a proteolytic cleavage with papain was carried out to obtain a functional Fab fragment of the 1B4 mAb. After 4h of incubation, the highly heterogenous proteolytic pool was purified in a two-step process: a protein G affinity chromatography followed by SEC, as reported previously in Chapter II (section 2.4 of Methods).

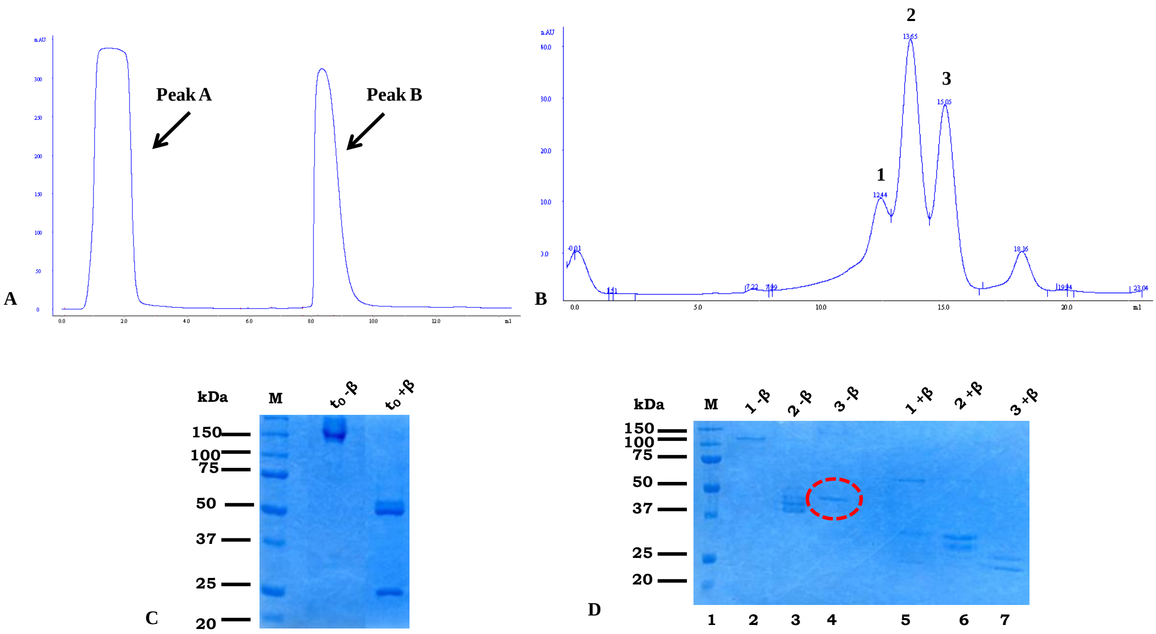

Figure 3.32: Chromatographic profiles of 1B4 papain digest purification. **A)** Protein G affinity chromatography. **B)** SE-chromatography. SDS-PAGE analyses on a 12% polyacrylamide gel under non reducing and reducing conditions of the whole 1B4 antibody at the starting point t_0 (**C**) and of the separated peaks eluted after SEC analysis (**D**).

The SEC profile of the products obtained by protein G purification, showed three different peaks, corresponding to three different species, as detectable on the SDS-PAGE 12% gel, under non reducing and reducing conditions (Fig. 3.32 D). Peak 1, eluted at a 12.44 mL retention volume, corresponded to a fragment of about 100 kDa (lane 2). This fragment is the so-called Fab/c, a typical product generated by the cleavage of IgG2b sub-class (the 1B4 isotype), instead of the $F(ab')_2$. The Fab/c is made up of a single Fab unit linked to the Fc portion by one intact heavy chain, thus under reducing conditions the three observed bands (50 kDa, 30 kDa and 25 kDa) are the intact heavy chain, half an Fc portion and the light chain respectively (lane 5). This asymmetric cleavage is typical of the IgG2b isotype **[175]** because they posses two heavy chains asymmetrically O-glycosylated in the hinge region. In fact, the whole antibody, analyzed by SDS-PAGE (Fig. 3.32 C) under reducing conditions (t_0 +β), exhibited two bands at around 50 kDa with a different mobility, corresponding to the two heavy chains, probably because the slower minor band is more acidic than the other one. Moreover, peak 2, with a retention volume of 13.65 ml, corresponded to the Fc portion (Fig. 3.32 D, lane 3), that normally appears at a molecular weight of 30 kDa but in this case showed more than one band, due to the different glycosylation status of the C_H2 domain of the heavy chain. Finally, peak 3, eluted at 15.05 ml corresponded to the Fab fragment, with a molecular weight of around 45-50 kDa. Indeed, under non reducing conditions (lane 4) this fragment showed a homogenous band at around 45 kDa, while under reducing conditions (lane 7) the two separated bands were distinguished as the heavy chain (the upper one) and the light chain (the lower one). Moreover, since 1B4 is an IgG2b, the sub-class most sensitive to the proteases attack, the antibody was totally splitted and no uncleaved product was observed.

b) Comparative conformational analysis between 1B4 mAb and its proteolytic Fab

A conformational analysis by circular dichroism in the region of far-UV was carried out to compare the parental 1B4 mAb with its Fab fragment to evaluate if the final proteolytic product retained its correct secondary structure after the catalytic action of papain. As shown in Fig. 3.33 A, the CD spectrum of the 1B4 mAb had a negative extreme position at 217 nm, with a broad amplitude and a positive extreme position at 202 nm, perfectly in accordance to a canonical β-sheet secondary structure, typical of the IgG molecules. Compared to the intact antibody, the spectrum of the Fab fragment (Fig. 3.33 B) showed the same position for the negative extreme at 217 nm and a minimal shift in the position of the positive extreme to 200 nm. A remarkable difference was the negative portion in the spectrum of the Fab, characterized by an additional weak absorbance at 235 nm, not belonging to a canonical IgG2b. Thus, an overall β-sheet secondary structure could be defined even for the Fab fragment, but presumably the proteolytic reaction damaged some residues that normally exert a structural function.

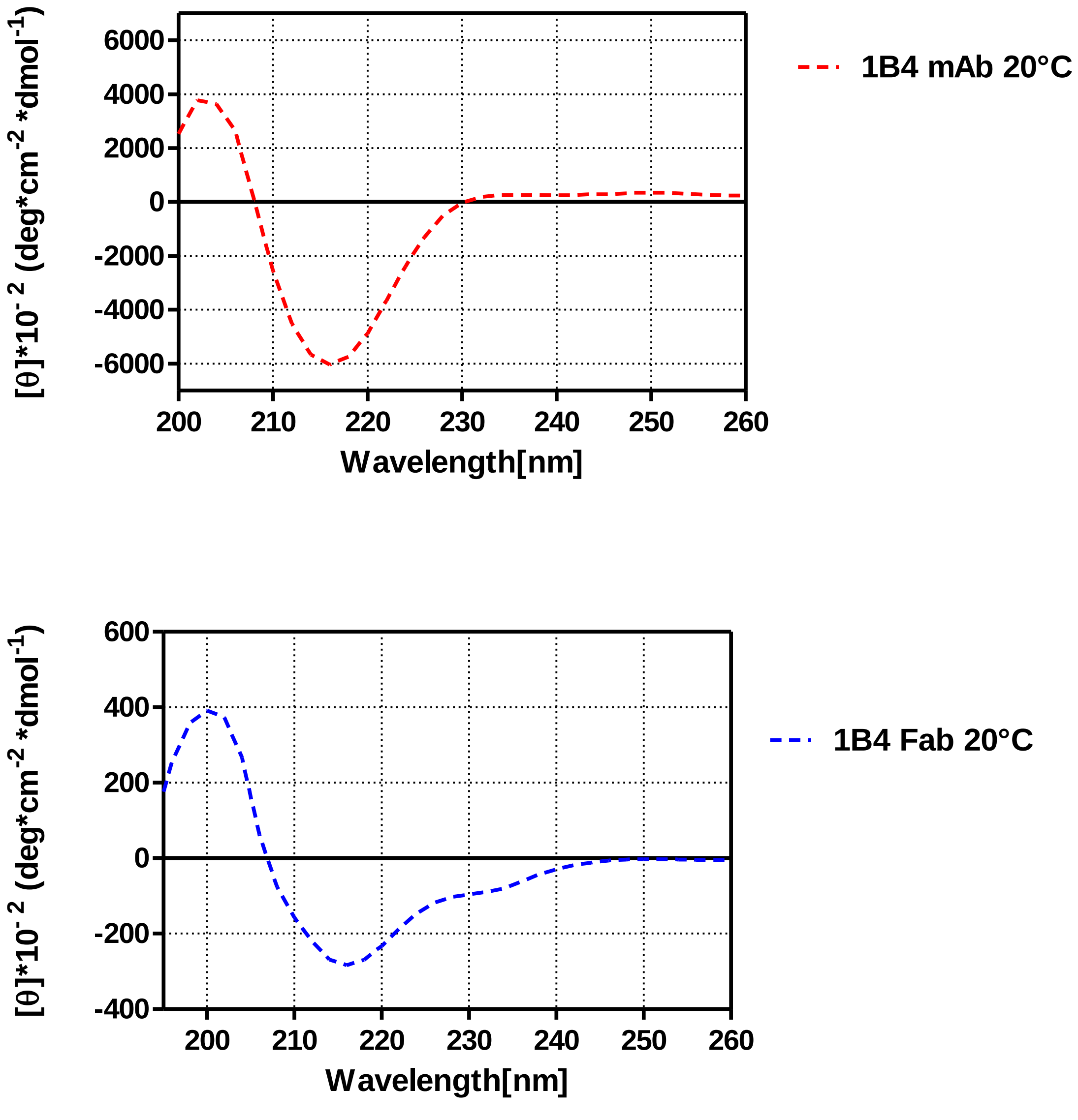

Figure 3.33: CD spectra of the full-size 1B4 mAb (**A**) and the Fab fragment generated by papain digestion (**B**).

Given the poorly productive proteolytic reaction (very low yield of 15%) carried out on the whole IgG molecule, related to the generation of by-products, predominantly the Fab/c fragment and other unimportant fragments, the digestion process required an optimization performing a preventive O-deglycosylation of the mAb, to allows the hinge region to become more easily accessible to the papain attack. Thus, the 1B4 mAb was submitted to a two-step deglycosylation (firstly with Sialidase and secondly with O-glycosidase) and the resulting products were analyzed by SDS-PAGE analysis onto a 12% polycrylamide gel (Fig. 3.34 A), under both non reducing and reducing conditions, comparing the untreated antibody molecule with the molecule after a total incubation time period of 48h.

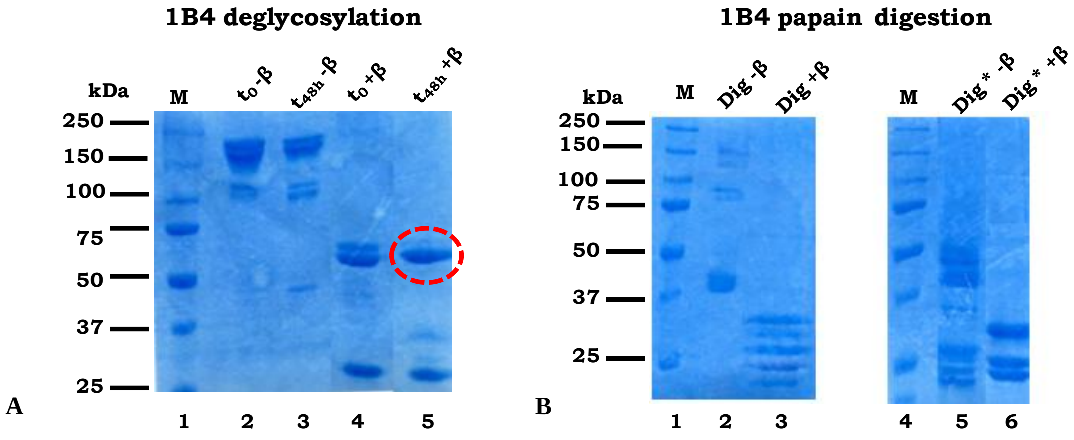

Figure 3.34: SDS-PAGE analyses of 1B4 deglycosylation reaction (**A**) and of deglycosylated 1B4 digestion (Dig*) compared to the normal 1B4(Dig) (**B**).

As can be seen in Fig. 3.34 A, the final product of the deglycosylation process, under non reducing conditions (lane 3) showed a phenotype still comparable to the wild-type antibody (lane 2), but remarkable differences were observed on the heavy chains under reducing conditions, as they indeed migrated as a single homogenous band at around 50 kDa (lane 5 in the red circle), instead of the two separated haevy chains (lane 4) with different mobility. The different O-deglycosylation status influenced, as expected, the 1B4 mAb cleavage by papain, because comparing the papain digest of the wild-type form (Dig) with the deglycosilated form (Dig*), differential fragments were detectable (Fig. 3.34 B, gel on the left). The papain digest of the normal antibody under non reducing conditions (lane 2) exhibited a consistent band at 45 kDa, corresponding to the Fab fragment, while still contained uncleaved antibody (150 kDa) and in addition the canonical Fab/c fragment (110 kDa), thus under reducing conditions (lane 3) many heterogenous bands were detected between 37 kDa and 20 kDa, corresponding to the reduced Fab and Fc with asymmetic oligosaccharide chains. By contrast, the deglycosilated 1B4 antibody digest under non reducing conditions (lane 5) lacked the bands with high molecular weight (uncleaved IgG and Fab/c fragment), confirming that the hinge region was sensitive to the papain catalytic action, allowing the production of Fab (around 45 kDa) and less important fragments, typically migrating at 17-24 kDa. Moreover, the deglycoslylation effect on the heavy chains was notable even under reducing conditions (lane 6), thus, in addition to the two separated chains belonging to the Fab (~25 kDa), a single band (30 kDa) corresponding to the homogenous Fc portion, lacking the oligosaccharide chains, was detected. However, this approach to obtain antibody Fabs has been abandoned since, given the costs (enzymes) and the time-consuming procedure, it appears not suitable for a scaling process to generate large amounts of material.

c) SPR affinity binding assay of Fab to *rh*CR-1

The Fab fragment obtained by this proteolytic procedure was tested by SPR to assess if it bound to the target protein, *rh*CR-1. A dose-dependent binding assay was performed testing the analyte at concentrations ranging between 50 nM and 750 nM, and comparing the fragment with the full-size antibody.

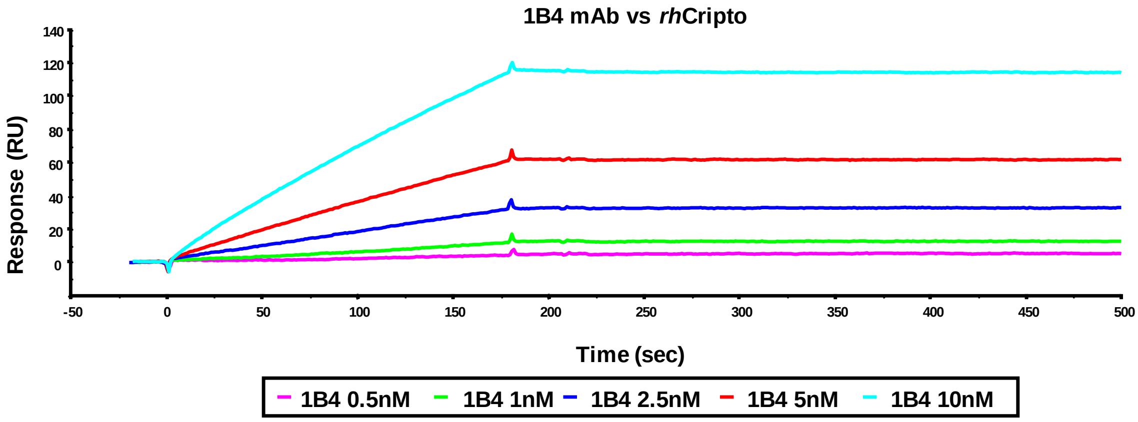

Table 24. Kinetic rate and apparent affinity constants of 1B4 mAb binding to *rh*CR-1

1B4	k_a (1/Ms)	k_d(1/s)	K_D (M)	SE (RI)
0.5 nM	$1.34*10^{5}$	$2.12*10^{-5}$	$1.58*10^{-10}$	0.0286
1 nM	$6.89*10^{4}$	$1.25*10^{-5}$	$1.81*10^{-10}$	0.028
2.5 nM	$7.19*10^{4}$	$1.82*10^{-5}$	$2.53*10^{-10}$	0.024
5 nM	$2.19*10^{5}$	$4.94*10^{-5}$	$2.25*10^{-10}$	0.0298
10 nM	$2.13*10^{5}$	$8.23*10^{-5}$	$3.86*10^{-10}$	0.0575
average	$1.41*10^{5}$	$3.67*10^{-5}$	$2.41*10^{-10}$	0.0336

Figure 3.35: Sensorgrams overlay and kinetic parameters table of the 1B4 mAb binding to *rh*CR-1.

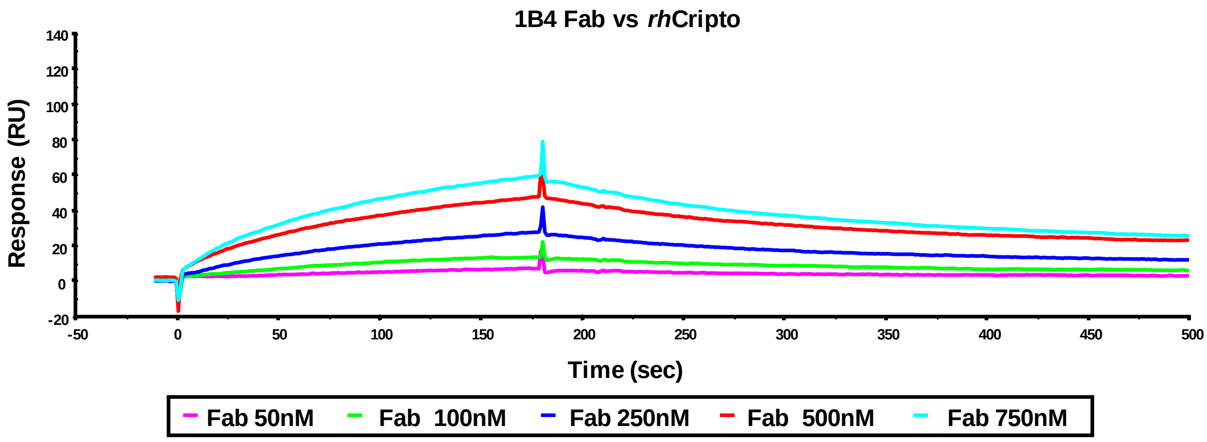

Table 25. Kinetic rate and apparent affinity constants of 1B4 proteolytic Fab binding to *rh*CR-1

1B4 Fab	k_a (1/Ms)	k_d (1/s)	K_D (M)	SE(RI)
50nM	$6.37*10^3$	$2.55*10^{-3}$	$4.00*10^{-7}$	0.0238
100nM	$4.97*10^4$	$2.12*10^{-3}$	$4.27*10^{-8}$	0.0408
250nM	$2.32*10^4$	$3.32*10^{-3}$	$1.43*10^{-7}$	0.0409
500nM	$1.65*10^4$	$2.61*10^{-3}$	$1.58*10^{-7}$	0.0896
1000nM	$1.13*10^4$	$2.57*10^{-3}$	$2.28*10^{-7}$	0.168
average	$2.14*10^4$	$2.63*10^{-3}$	$1.94*10^{-7}$	0.0726

Figure 3.36: Sensorgrams overlay and kinetic parameters table of the 1B4 proteolytic Fab binding to *rh*CR-1.

Comparing the binding curves and the kinetic parameters of the whole antibody with the Fab fragment, we observed a dramatic loss of affinity, deriving from a reduced association rate ($k_a = 2*10^4\ M^{-1}s^{-1}$) and an increased dissociation rate ($k_d = 2.6*10^{-3}\ s^{-1}$). The resulting K_D was 200 nM, a thousand fold lower compared to that one of the whole mAb (0.24 nM). This affinity decrease is not explainable as a simple consequence of the Fab monovalency, but it is probably due to a loss of structural stability of the fragment, as suggested by the circular dichroism analysis. We hypothesized that an unspecific cleavage was operated within the CDRs by papain and such modification induced the drastic affinity drop.

In conclusion, the first attempt to generate a functional Fab fragment using a proteolytic approach unfortunately led to a product characterized by a loss of binding affinity to the antigen.

Given the disadvantages of the antibody proteolytic fragmentation, such as heterogeneity of the product fragments, the time-consuming reaction condition optimization as well as for the deglycosylation and low yield, a more suitable and productive method has been explored. Therefore the production of a Fab fragment as recombinant protein has been set up using the bacterial expression in *Escherichia Coli*, an affordable system in terms of cost and time required to obtain high yield.

2.2 GENERATION OF THE RECOMBINANT CHIMERIC 1B4 Fab (1B4 *r*Fab)

a) Expression and purification of 1B4 *r*Fab as recombinant protein

The PL564 plasmid, generated by cloning the synthetic gene (1539 bp) encoding the target 1B4 *r*Fab protein (Fig. 3.37) into the pET-26b(+) vector, was used to perform the periplasmic expression strategy. Thus, the plasmid was successfully transformed in *E. coli* BL21(DE3) host strain and the expression was optimized at 30 °C, using 1 mM IPTG.

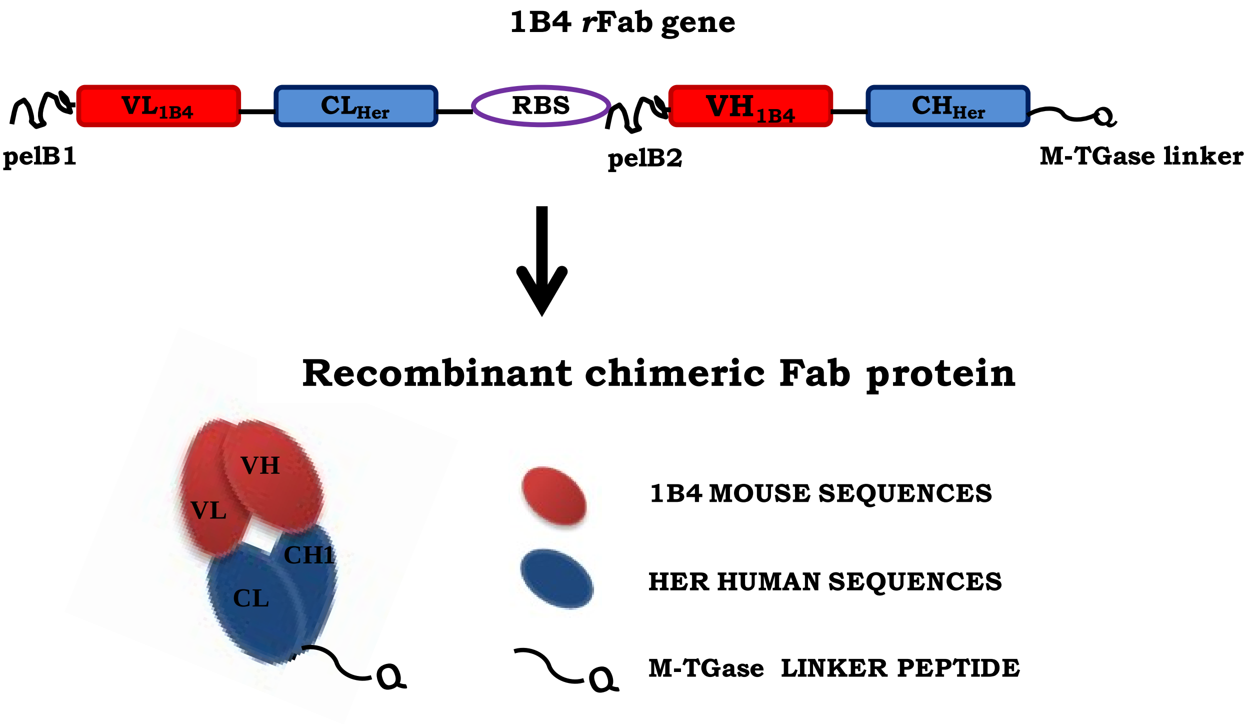

Figure 3.37: Scheme of the synthetic gene constructed to encode the corresponding recombinant chimeric 1B4 Fab protein.

After periplasmic extraction (described in section 2.10.c of Methods), with the aim of removing all the other contaminant proteins occurring in the periplasmic space of the bacterial cells, a stepwise purification process including HIC cromatography and two ion-exchange chromatography steps (reported in Fig. 3.38

A and B) was conducted. A further purification by SEC (Fig. 3.38 C) was performed to evaluate the presence of any aggregates and to ensure homogeneity and high purity of the 1B4 *r*Fab. As shown in the SEC profile, the main peak eluted with a retention volume of 16.0 mL in accordance to a molecular weight of around 50 kDa, preceded by a minor peak at retention volume of 12.0 mL and corresponding to the aggregated 1B4 *r*Fab. At the end of the purification process, the final product exhibited a high purity, estimated by over 95%, as detected by RP- HPLC analysis (Fig. 3.38 D). The homogeneity and purity are two important pre-requisites to set up crystallographic study of complex 1B4 *r*Fab- synthetic hCFC domain as well as for *in vitro* and *in vivo* test.

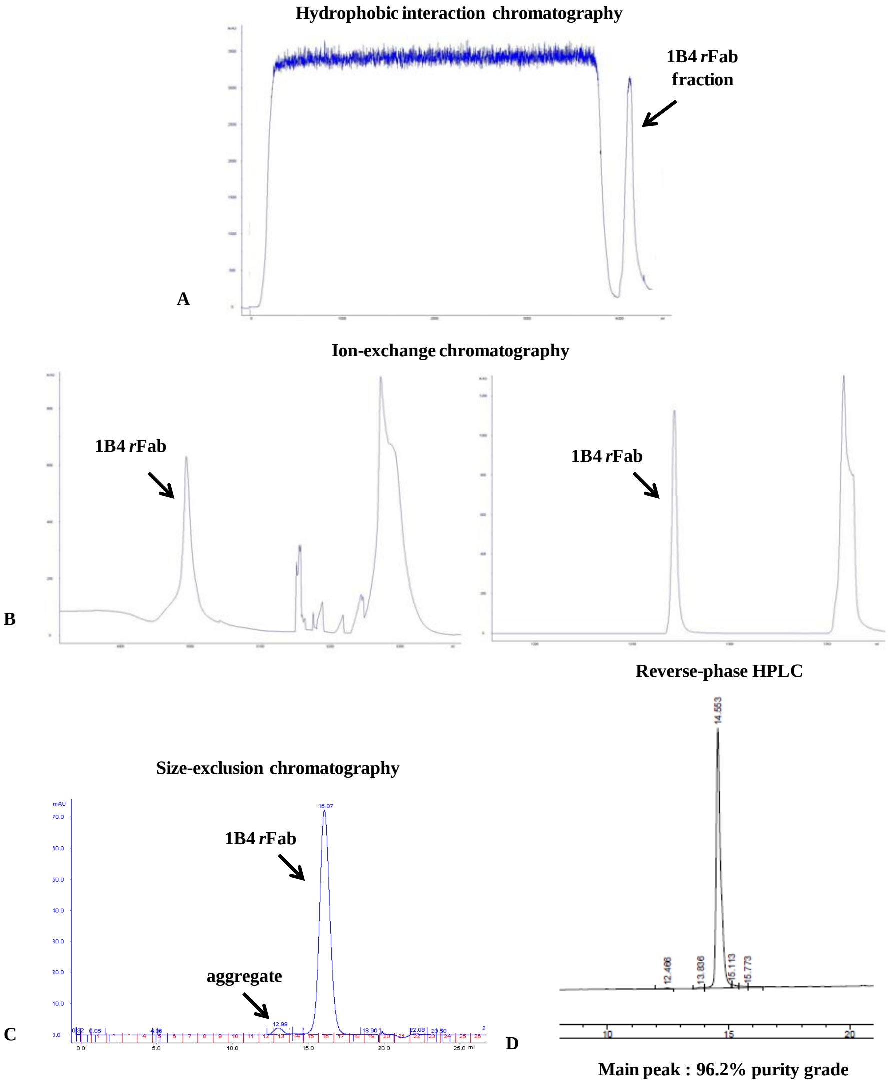

Figure 3.38: Multi-step purification of the 1B4 *r*Fab protein, starting from HIC chromatogram of the whole periplasmic lysate (**A**); Anion and cation exchange chromatography profile respectively (**B**); the SEC profile (**C**) and the final RP-HPLC profile (**D**).

b) Identification of 1B4 *r*Fab

SDS-PAGE and Immunoblotting analyses

The protein corresponding to the predominant peak of SEC was analyzed on a 15% SDS-PAGE gel to perform a first rough estimation of the 1B4 *r*Fab molecular weight . As expected, under non reducing conditions, the 1B4 *r*Fab protein exhibited a homogenous band at around 45-50 kDa, while under reducing conditions (by addition of 10% β-Mercaptoethanol), two separated bands characterized by a different mobility were clearly detectable; the slower was the heavy chain, containing also the M-TGase linker at the C-terminus; the faster was the light chain (See Fig. 3.39 A). The identity of the 1B4 *r*Fab was assessed also by western blot analysis, using an anti-human Fab antibody (Fig. 3.39 B).

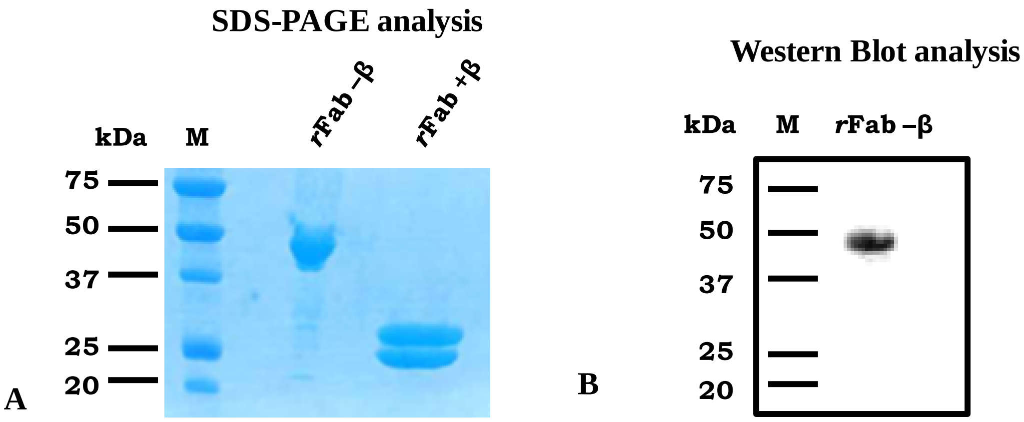

Figure 3.39: SDS-PAGE 12% gel analysis of the SEC product under non-reducing and reducing conditions (**A**).Western blot analysis using the anti-human Fab antibody (**B**).

LC-ESI- TOF-MS Analysis

The identity and integrity of 1B4 *r*Fab was then confirmed by LC-ESI-TOF-MS analysis. For this analysis the fragment was mildly reduced with 50 mM DTT at 37 °C to ensure the reduction of the interchain disulfide bond, a procedure that splitted the 1B4 *r*Fab into the light and heavy chains while maintaining intact the four internal disulfide bridges. The RP-HPLC profile of the LC-ESI-TOF-MS analysis (Fig. 3.40) showed the two distinct chains eluting at different retention times on the basis of their different hydrophobicity: The light chain (abbreviated as LC) preceded the heavy chain (HC) through the elution.

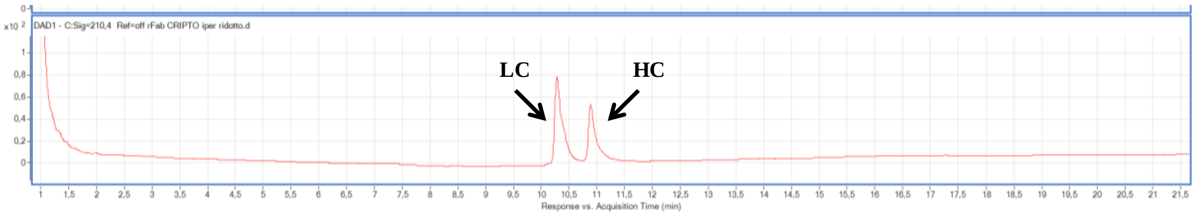

Reduced 1B4 *r*Fab

Figure 3.40: RP-HPLC profile of the LC-ESI-TOF analysis on the reduced 1B4 rFab in which the first peak is represented by the light chain while the second peak corresponds to the heavy chain instead.

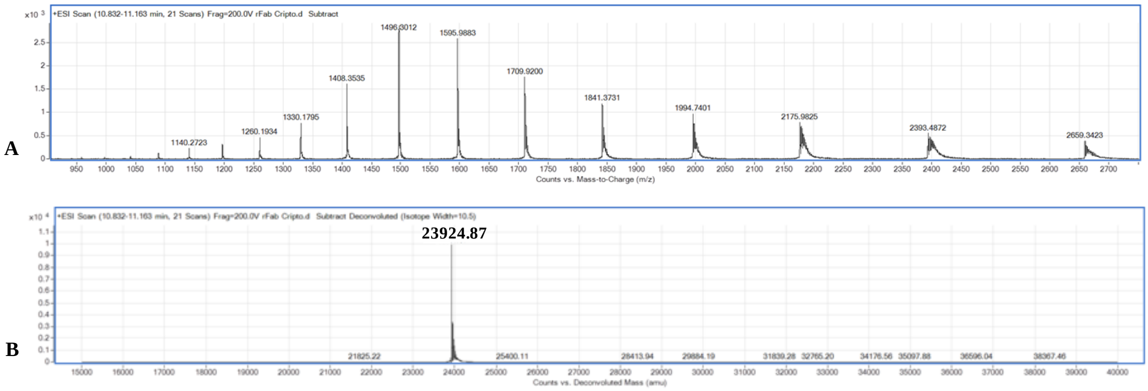

Light chain (LC)

Figure 3.41: Panel of the LC-ESI-TOF-MS analysis of the single light chain belonging to the 1B4 *r*Fab: m/z multicharged spectrum (**A**) and spectrum deconvolution (**B**).

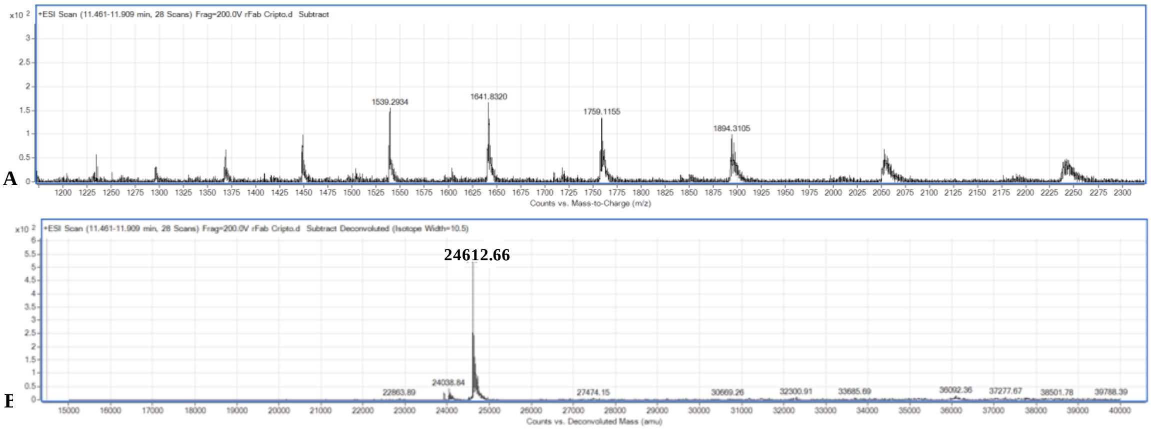

Heavy chain (HC)

Figure 3.42: Panel of the LC-ESI-TOF-MS analysis of the single heavy chain belonging to the 1B4 *r*Fab: m/z multicharged spectrum (**A**) and spectru deconvolution (**B**).

The mass spectra revealed the correct molecular weight of each chain (reported in Table 26), corresponding, as expected, to the chain with the intact two intradomain disulfide bridges. Moreover, the molecular weight of the heavy chain was in agreement with the presence of the sulfhydryl group on the free Cysteine of the C_H1 domain in addition to the two intact intradomain disulfide bonds.

Table 26. Molecular mass of each single chain of 1B4 *r*Fab

	Theor MW amu	Exp MW amu
Light chain	23924.8	23924.8
Heavy chain	24612.6	24612.6

c) Comparative conformational and stability study between 1B4 *r*Fab and Her *r*Fab by circular dichroism.

To evaluate the correct folding of the generated 1B4 *r*Fab and its stability, a circular dichroism comparative study was carried out using as reference the recombinant Fab from Trastuzumab, whose C_L and C_H1 domains are contained in the 1B4 *r*Fab. The CD spectra in far-UV region of both recombinant Fab proteins revealed a quite similar secondary structure profile. In detail, the Trastuzumab recombinant Fab, hereafter named Her *r*Fab, exhibited a canonical β-sheet secondary structure, proper of the IgG domain with a negative band at 218 nm and a positive band at 204 nm. The CD analysis of the 1B4 *r*Fab fragment confirmed the occurrence of β-sheet motifs, denoting only a small difference seen as a negative band at 216 nm and a positive band at 200 nm, probably due to the combination of two different isotypes, IgG1 (Trastuzumab) and IgG2b (1B4 mAb), instead of the homogenous Her *r*Fab.

Then, the thermal denaturation of each fragment, conducted starting from 20 °C up to the final temperature of 95 °C, revealed a melting temperature (Tm) of 86°C and 71°C for Her *r*Fab and 1B4 *r*Fab, respectively. These data suggest that 1B4 *r*Fab (Fig. 3.43 A) is less stable compared to the Her *r*Fab (see Fig. 3.43 B). Although the anti-Cripto Fab is less stable than the Her *r*Fab, this parameter can not be considered negative, since the Tm proper of a Fab belonging to an IgG2b normally corresponds to 60 °C, thus the chimeric fragment shows a gain of stability compared to a canonical Fab of the same IgG isotype **[162]**.

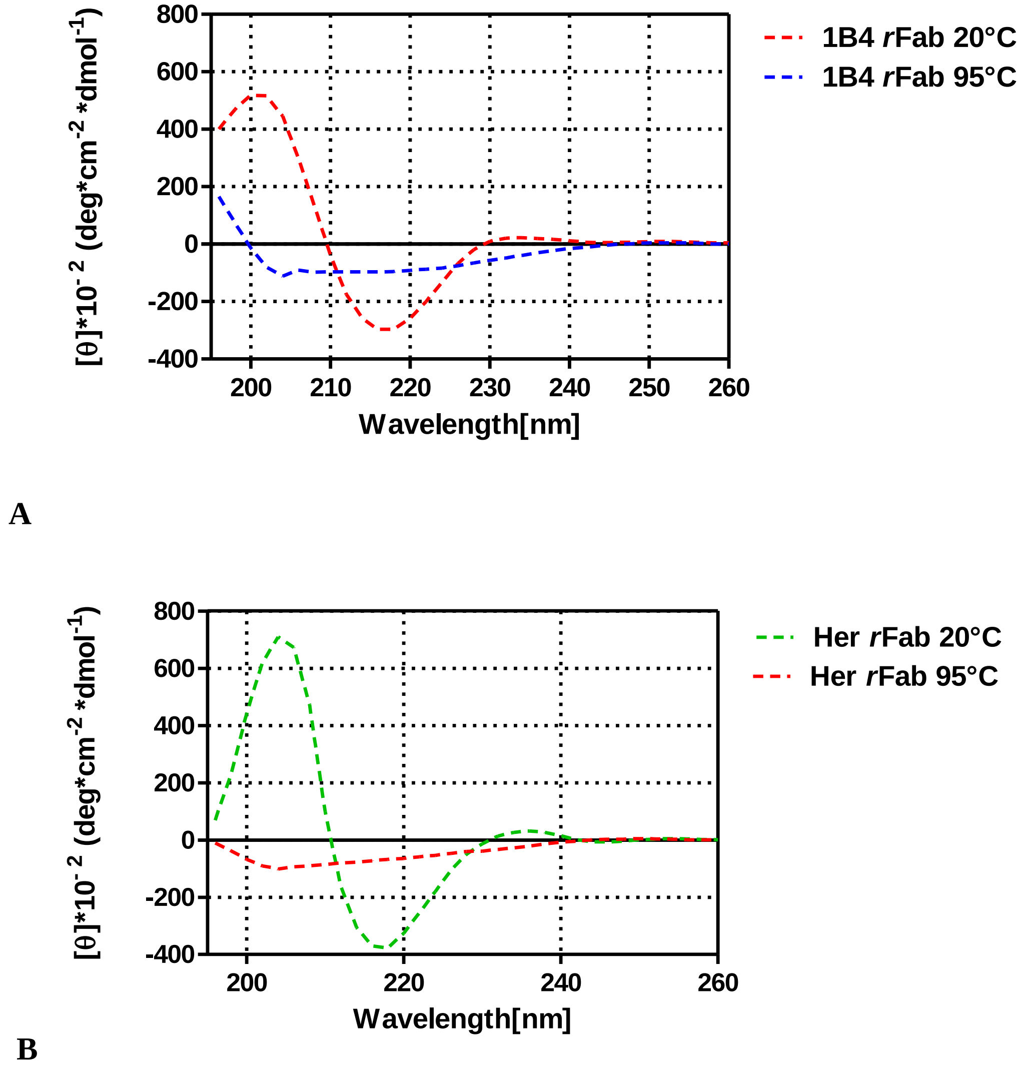

Figure 3.43: Far-UV spectra of recombinnant chimeric Fab from 1B4 mAb (1B4 *r*Fab). Red color indicates the native conformation, while the blue color indicates the denaturated form after heating at 95 °C (**A**). Far-UV CD spectra overlay of the recombinant Fab from Trastuzumab (Her *r*Fab). Green color indicates the native conformation, the red color indicates the denaturated form after heating at 95 °C (**B**).

d) Affinity Binding assays of 1B4 *r*Fab to the synthetic hCFC[112-150] domain

ELISA and SPR binding assays were carried out on the newly generated 1B4 *r*Fab to evaluate the influence of human constant domain on Fab ability to retain the high affinity toward its specific antigen, hCFC domain, and even toward the full-length *rh*CR-1 protein, compared to the whole antibody.

ELISA assays

As previously described, dose -response ELISA binding assays were performed coating synthetic wild-type hCFC[112-150] domain at a fixed concentration of 110 nM and testing the 1B4 *r*Fab at increasing concentrations from 0.6 nM up to 40 nM, compared to the parental 1B4 mAb, as described in section 2.3.d of Methods . A K_D of about 12 nM was extrapolated by data fitting using a non linear regression analysis of data points (Fig. 3.44). This value was lower compared to that one of the whole 1B4 antibody determined using the same approach (K_D = 1.7 nM).

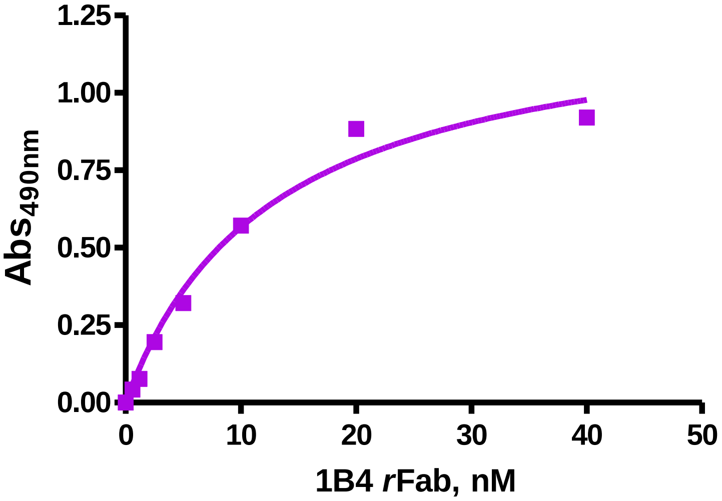

Figure 3.44: Dose-response ELISA binding assay of 1B4 *r*Fab to the synthetic wild-type hCFC[112-150] polypeptyde.

A further ELISA assay (Fig. 3.45) was performed to verify the specificity of the 1B4 *r*Fab to the *rh*CR-1 versus the *rm*Cr-1, following the procedure reported in Chapter II section 2.3.e. Compared to the intact 1B4 mAb, the 1B4 *r*Fab recognized *rh*CR-1 with a dose-dependent trend, although it required a higher concentrantion (100 nM) than the full-size antibody (6.7 nM). However, even the recombinant fragment specifically recognized *rh*CR-1 instead of the mouse variant, starting from the amount corresponding to 25 ng of protein.

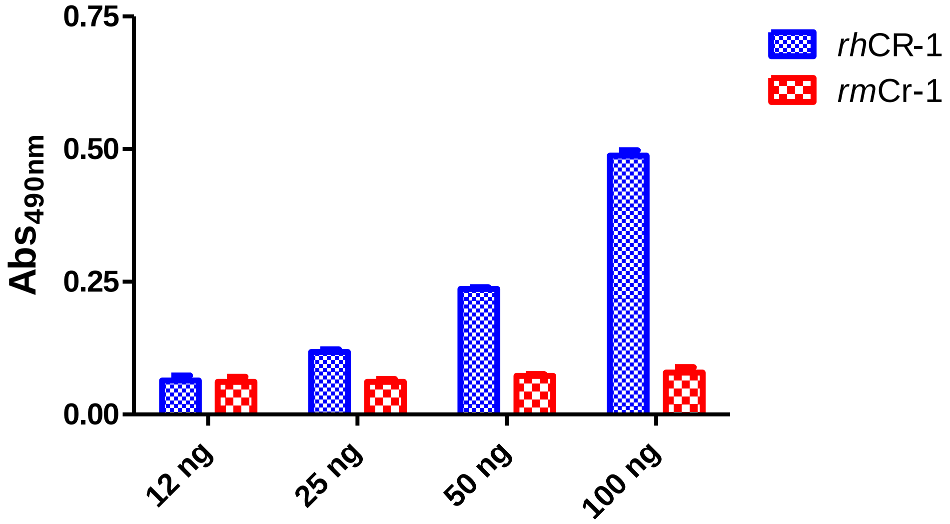

Figure 3.45: Bars graph of the ELISA specificity binding assay of 1B4 *r*Fab to *rh*CR-1 versus *rm*Cr-1.

SPR assays

After validation of antigen recognition by the 1B4 *r*Fab by ELISA, to define precisely the interaction with the target protein in terms of association and dissociation constant rates, a SPR binding assay between 1B4 *r*Fab and *rh*CR-1 was carried out. Thus, the analyte was injected onto the immobilized *rh*CR-1, using a range of concentrations between 1 nM and 10 nM.

The kinetic parameters (k_a and k_d), extrapolated fitting the binding curves, revealed a loss of affinity toward the target protein, displaying an apparent affinity (K_D = 6 nM) about ten fold lower than the whole antibody 1B4 (K_D = 0.24 nM). Interestingly, the 1B4 *r*Fab exhibited a k_a more favorable than the whole antibody, probably due to smaller size and the orientation of CDRs perfectly exposed and accessible to the antigen in the absence of the remaining IgG molecule. In spite of the quicker association rate, the 1B4 *r*Fab showed a much higher dissociation rate, about one hundred fold higher than that one displayed by the parental antibody. This suggested a faster interaction with the target protein, but it was not strong enough to stabilize the antigen-Fab complex.

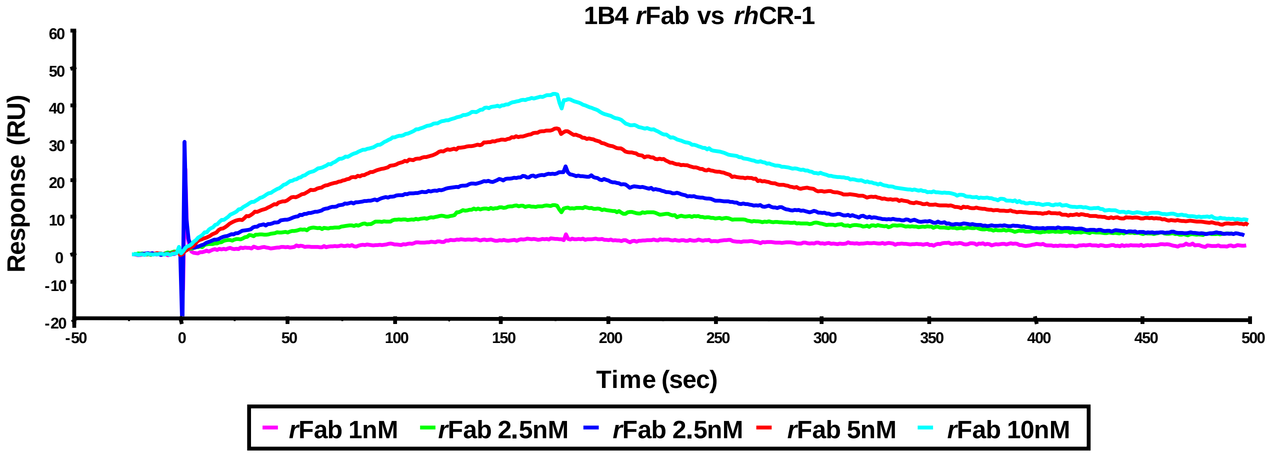

Table 27. Kinetic rate and apparent affinity constants of 1B4 *r*Fab binding to *rh*CR-1

1B4 *r*Fab	k_a (1/Ms)	k_d (1/s)	K_D (M)	SE (RI)
1nM	$7.73*10^5$	$3.21*10^{-3}$	$4.16*10^{-9}$	0.0628
2.5nM	$2.41*10^6$	$2.87*10^{-3}$	$1.19*10^{-9}$	0.0665
5nM	$1.85*10^6$	$5.44*10^{-3}$	$2.93*10^{-9}$	0.0597
7.5nM	$1.28*10^5$	$4.57*10^{-4}$	$3.56*10^{-9}$	0.042
10nM	$2.58*10^5$	$5.07*10^{-3}$	$1.97*10^{-9}$	0.038
average	$1.08*10^6$	$3.41*10^{-3}$	$6.31*10^{-9}$	0.05675

Figure 3.46: Sensorgrams overlay and kinetic parameters table 1B4 *r*Fab binding to *rh*CR-1.

In summary, the SPR analysis confirmed the ELISA results, revealing that the monovalency of the 1B4 *r*Fab unit negatively influences the binding affinity toward both the hCFC antigen and the full length *rh*CR-1. On the basis of these data, we hypothesised that the antibody bivalency plays a crucial role in the antigen-antibody interaction.

Indeed, a strategy to improve the binding affinity of the monovalent 1B4 *r*Fab was the artificial restoring of the bivalency of a full antibody, without the Fc portion, possibly generating a recombinant homodimer composed of two 1B4 *r*Fab units, joined together by a simple short linker peptide.

e) Preliminary analysis of the antigen-1B4 *r*Fab complex

To investigate the effective antigen-antibody interaction, a crystallographic study could be required on the antigen-Fab complex, to precisely localize the binding site. For this purpose, a preliminary experiment was conducted to confirm the formation of the antigen-Fab complex prior to carry out possible crystallographic study. A simple SE-HPLC comparative analysis was performed between the single 1B4 *r*Fab and after incubation with the synthetic hCFC[112-150]. The chromatographic profile of the 1B4 *r*Fab showed a single peak at a retention time of 7.488 min (Fig. 3.47 A), corresponding to a protein with a molecular weight of about 50 kDa. In contrast, the elution profile of the 1B4 *r*Fab-hCFC mixture (Fig. 3.47 B) exhibited a predominant peak at a retention time of 7.564 min, corresponding to the 1B4 *r*Fab-antigen complex and a second less intense peak at around 11 min, corresponding to the hCFC peptide excess, non associated to the 1B4 *r*Fab.

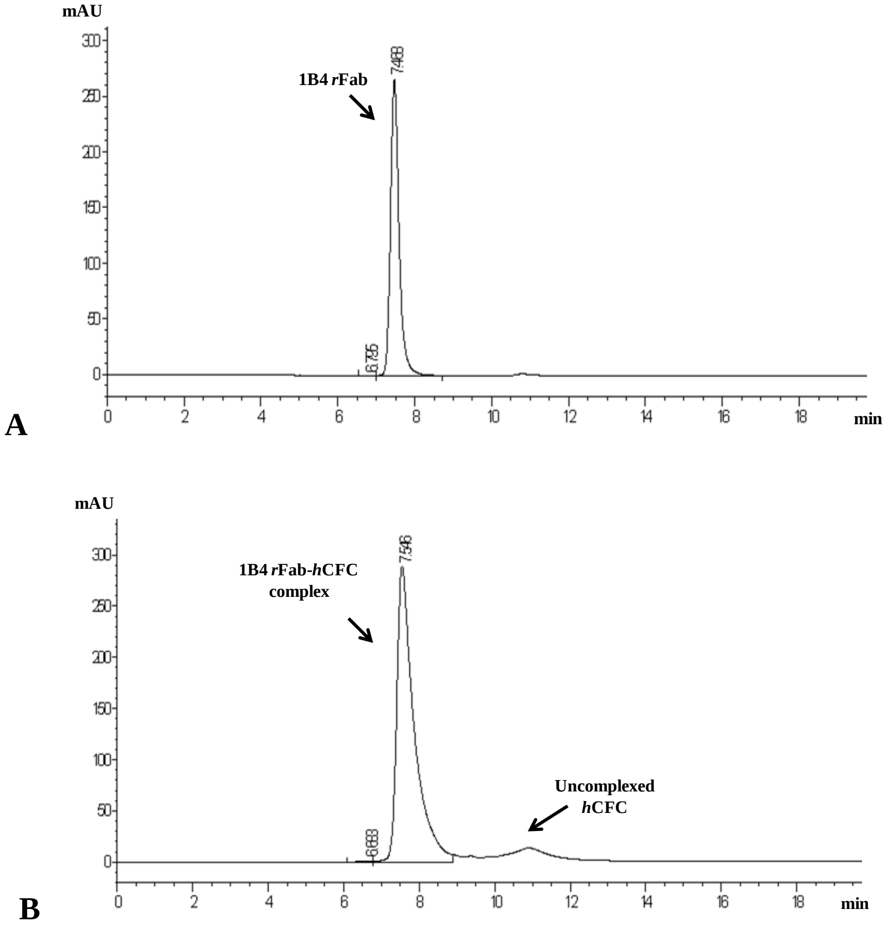

Figure 3.47: SE-HPLC profiles of the sinlge 1B4 *r*Fab (A) and the 1B4 *r*Fab-hCFC mixture (B).

The difference in retention time and the shape of the resulting new peak clearly showed that the complex was formed and eluted at a longer retention time, as expected. The occurrence of the two molecules within the same fractions under the peak was confirmed by SDS-PAGE analysis (not shown).

2.3 GENERATION OF ARTIFICIAL 1B4 *r*Fab$_2$

a) Chemical synthesis, purification and identification of the bifunctional linker peptide

The bifunctional linker peptide, designed to join together two 1B4 *r*Fab units to create the dimeric derivative, called 1B4 *r*Fab$_2$, was synthesized as acetylated and amidated product, purified by RP-HPLC and the correct molecular mass was determined by LC-ESI-TOF-MS analysis. The linker, possessing a very simple amino acid sequence, Ac-KAYA-GA-KAYA-CONH$_2$, had a molecular mass corresponding to 1053.6 amu (See Fig. 3.48).

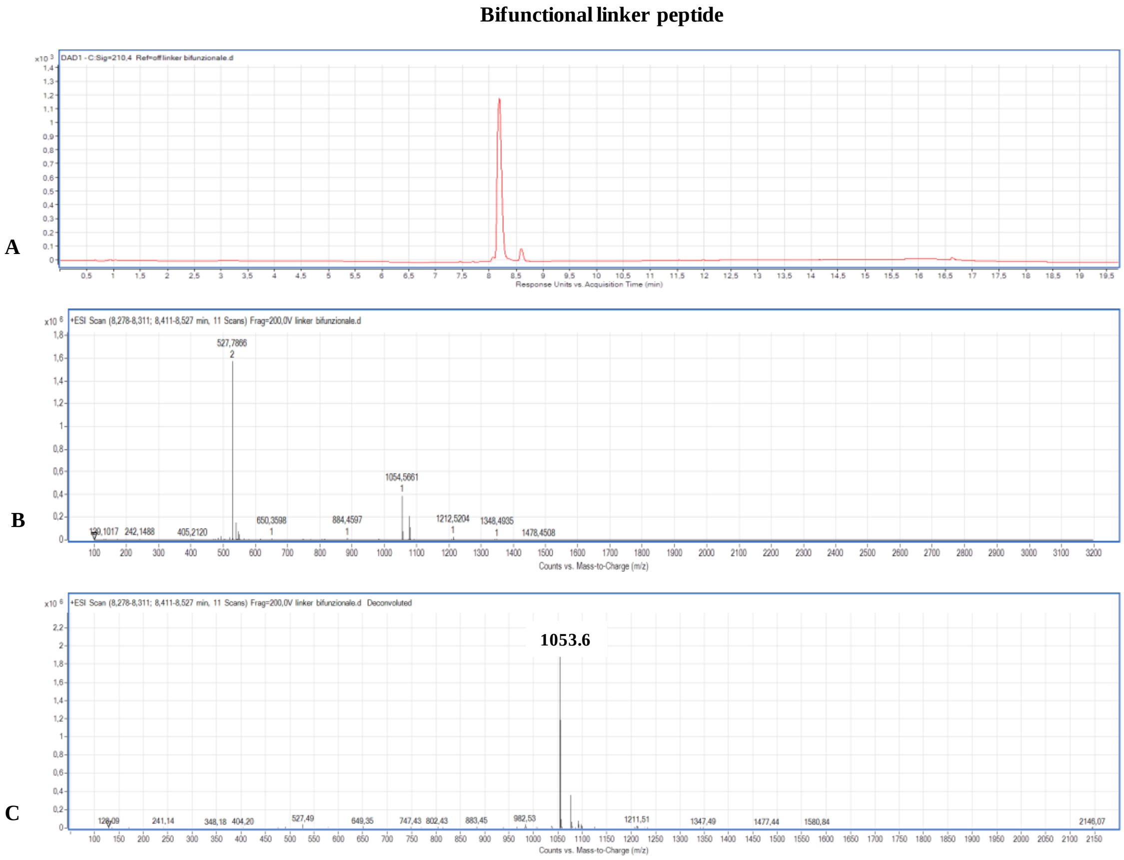

Figure 3.48: LC-ESI-TOF-MS analysis of the short linker pepride. In this panel RP-HPLC profile (A), m/z spectrum (B) and deconvoluted peak (C) are reported.

The two KAYA motives permit the formation of the isopeptide bonds, catalyzed by the M-TGase enzyme simultaneously with two 1B4 *r*Fab monomers. The KAYA motif was identified in a previous study as optimally recognized and processed by the M-TGase **[163]**. Gly (G) and Ala (A) residues were inserted between the two KAYA sequences as a spacer.

b)1B4 *r*Fab-*r*Fab conjugation reaction and purification

To create the artificial 1B4 *r*Fab$_2$ the transamidation reaction was performed as illustrated in Fig. 3.49. The M-TGase enzyme catalyzes the formation of the isopeptide bond between the ε-aminogroup belonging to the K residue of the linker peptide and the γ-carboxamide group of the Q residue belonging to the additional sequence at the C-terminus of the 1B4 *r*Fab C$_H$1 domain. Since the linker peptide is bifunctional, it allows the simultaneous conjugation of two 1B4 *r*Fab units.

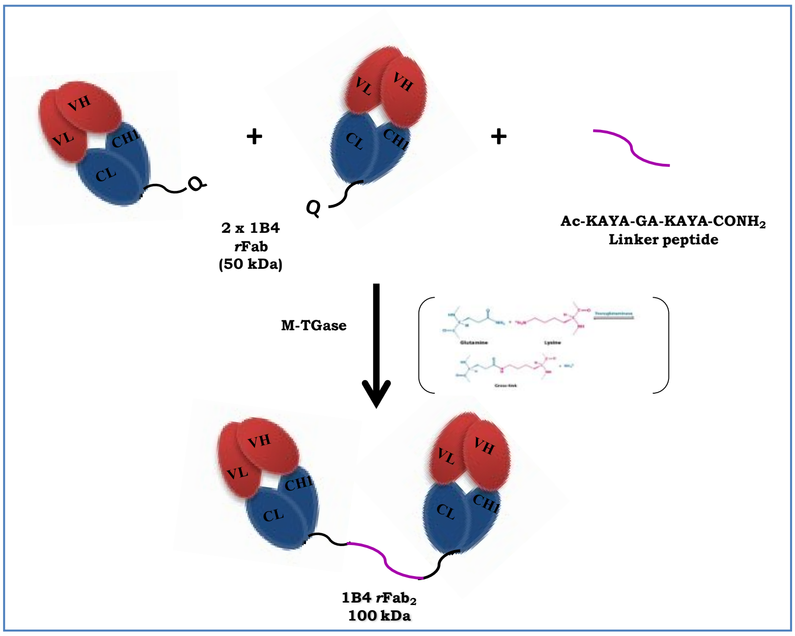

Figure 3.49: Schematic representation of the conjugation reaction, catalyzed by M-TGase enzyme, to create the artificial 1B4 *r*Fab$_2$ product.

After the conjugation reaction, carried out in 6h, the dimeric product was isolated from the reaction mixture, removing the unfunctionalized monomeric 1B4 *r*Fab by a cation exchange chromatography step as described in section 2.15 of Methods. The 1B4 *r*Fab$_2$ eluted in correspondance of a conducibility of 21.8 mS/cm. Finally, a further SE-HPLC analysis was performed on the reaction mixture (Fig. 3.50 A) and on the final product (Fig. 3.50 B) to determine its purity grade as well as its molecular weight.

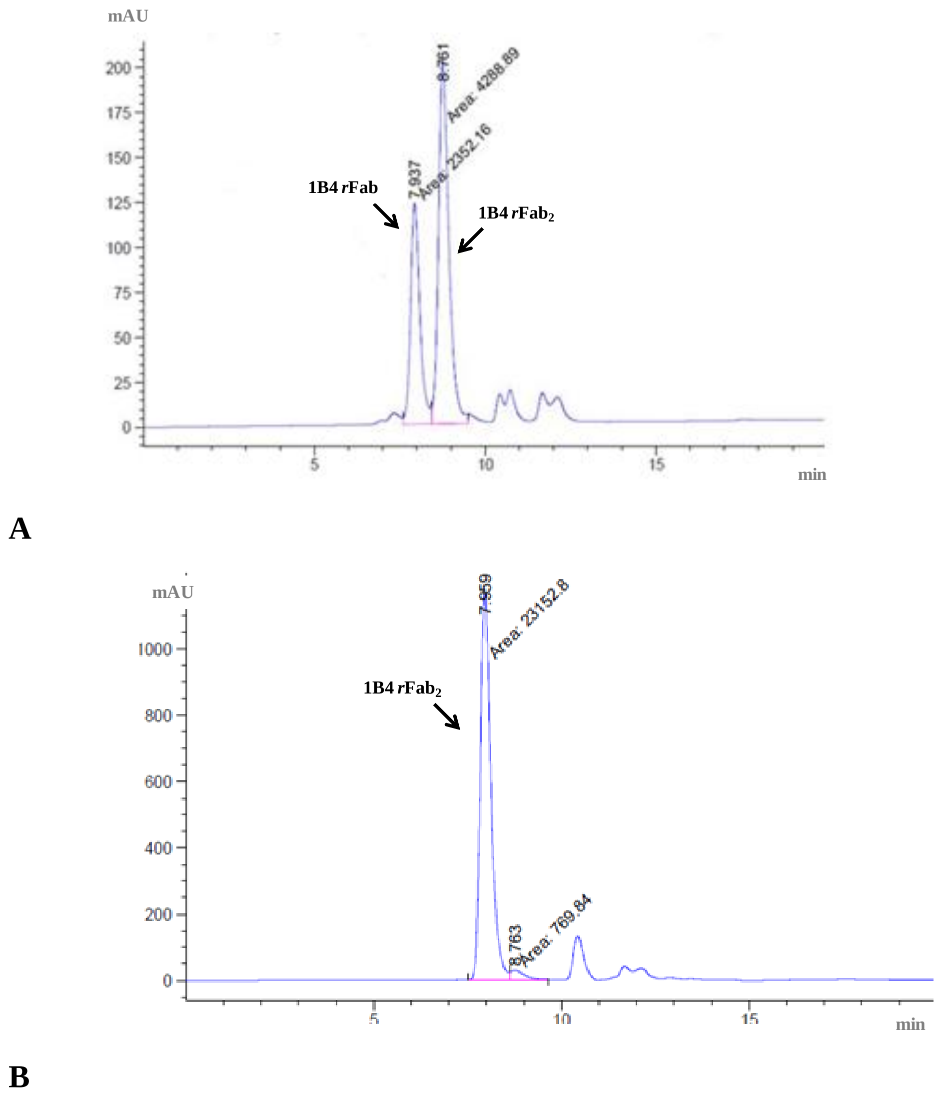

Figure 3.50: SE-HPLC profiles of the reaction mixture after 6h incubation time period (**A**) and of the isolated peak corresponding to the final rFab$_2$ product (**B**).

The first SE-HPLC chromatogram (Fig. 3.50 A) showed the presence of two different species eluting with a retention time shift of about 1 min, the first peak (7.937 min) corresponded to a protein possessing a molecular weight of about 100 kDa, in agreement to the dimeric derivative of the 1B4 *r*Fab. The second peak (8.761 min) corresponded to the monomeric 1B4 *r*Fab, with a MW of about 50 kDa. The comparison of the peak areas suggested a reaction yield of about 50%. The presence of the monomeric 1B4 *r*Fab after 6h incubation was due to the concomitant deamidation of the Gln side chain and generation of a M-TGase-inactive glutamic acid.

The second SE-HPLC profile (Fig. 3.50 B) revealed that the final functionalized product exhibited a purity grade by over 95%.

c)1B4 *r*Fab$_2$ Identification

A preliminary analysis by SDS-PAGE was carried out to evaluate the correct formation of the desired product. For this purpose the 1B4 *r*Fab at the beginning of the reaction (t_0) was compared with the final dimeric product, after 6h reaction (t_{6h}) by western blot analysis, carried out using the specific anti-human Fab antibody. As shown in Fig. 3.51 (A and B), the monomeric 1B4 *r*Fab migrated as a single compact band at 50 kDa, by contrast the dimeric product, although had a molecular weight of 100 kDa, apparently migrated like a protein of 150 kDa. This behavior was expected for the presence of the bifunctional linker that providing a high flexibility confers to the molecule a less compact globular structure, thus with an apparent higher molecular weight.

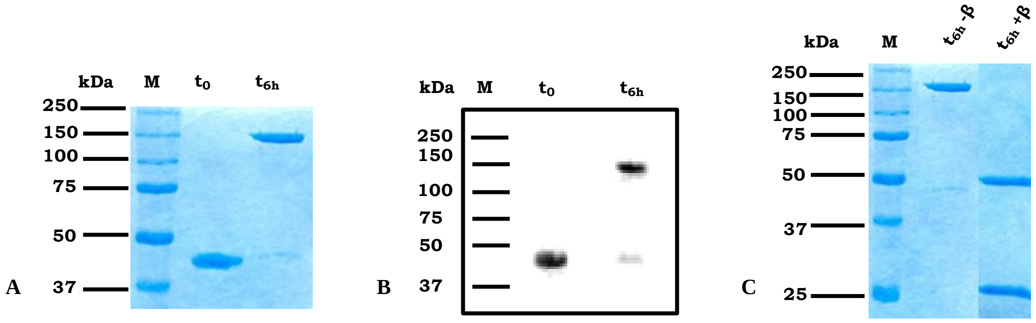

Figure 3.51: SDS-PAGE (**A**) and western blot (**B**) analyses on both 1B4 *r*Fab (t_0) and bivalent *r*Fab$_2$ (t_{6h}) when the reaction is finished. SDS-PAGE analysis of the final dimeric product under non-reducing and reducing conditions (**C**).

The structural differences between the artificial 1B4 *r*Fab$_2$ and a canonical F(ab')$_2$ can be appreciate even by SDS-PAGE under reducing conditions, revealing the presence of two bands with a different MW (Fig. 3.51 C). This is in agreement with the artificial nature of this product, because the band at 50 kDa corresponded to the heavy chains covalently linked by the bifunctional linker, resistant to the reducing agent, while the band at 25 kDa corresponded to the light chains, separated from the heavy chains after the reduction of the interchain disulfide bond. Unlikely, a proteolytic F(ab')$_{2,}$ when reduced, normally exhibits two bands at around 25 kDa, corresponding to the completely separated heavy (slower) and light (faster) chains.

d) Affinity binding assays of 1B4 *r*Fab$_2$ to hCFC domain and *rh*CR-1 protein

ELISA assays

The 1B4 *r*Fab$_2$ was subsequently characterized by ELISA and SPR binding assays to assess the generation of a functional protein, able to recognize and bind the single antigen, the specific CFC domain as well as the whole *rh*CR-1 protein, evaluating if the artificial bivalent fragment possessed a binding affinity comparable to the full-size antibody. Thus, a dose-response ELISA binding assay (Fig. 3.52) was performed using the synthetic hCFC[112-150] polypeptide in coating (110 nM) and the analyte at increasing concentrations (in the range comprised between 0.7 nM and 25 nM).

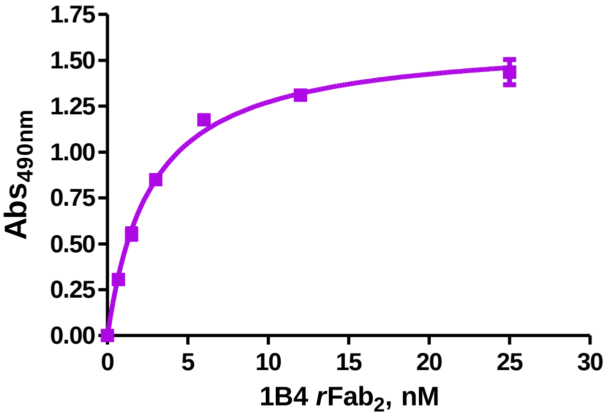

Figure 3.52: Dose-response ELISA binding assay of 1B4 *r*Fab$_2$ to the synthetic wild-type hCFC[112-150] polypeptyde.

Comparing the *r*Fab$_2$ derivative with the parental 1B4 antibody, they remarkably exhibited the same trend, suggesting that the respective affinity constants were comparable: for the antibody was 1.7 nM, for the dimeric protein was 2.7 nM, indicating the importance of the bivalency for the interaction with the antigen (to be compared with the K_D of the monomeric 1B4 *r*Fab of 12 nM).

Furthermore, a preliminary ELISA binding assay was carried out to test the ability of the 1B4 *r*Fab$_2$ to bind the full-length *rh*CR-1 protein and simultaneously to confirm the high specificity toward the human form versus the murine form. We achieved the experiment under the same conditions used in the assay with the 1B4 whole antibody (the full procedure is reported in Chapter II section 2.3.d). As expected, like the parental antibody, even the bivalent fragment was selective to the human form of CR-1 protein, showing a binding characterized by a dose-dependent trend (Fig. 3.53).

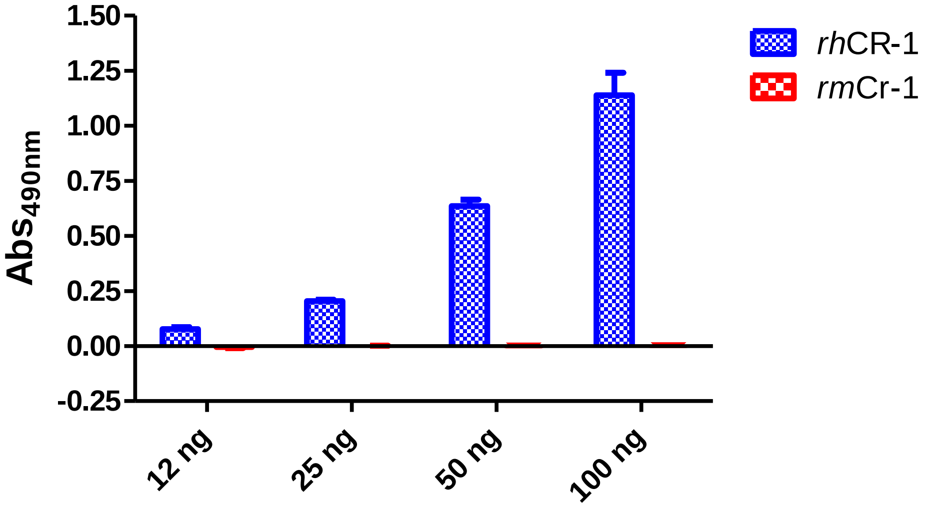

Figure 3.53: Bar graphs of ELISA assay, carried out using recombinant Cripto protein (human and murine) at a range of increasing concentrations (12 ng-25 ng-50 ng-100 ng) detected by 1B4 *r*Fab$_2$, used at a concentration of 10 nM.

SPR assays

We next analyzed the binding to *rh*CR-1 by SPR technique using a chip with immobilized *rh*CR-1. Solutions of the 1B4 *r*Fab$_2$ at increasing concentrations were passed on the ligand observing dose-response signals (Fig. 3.54). The kinetic parameters, exprapolated from the binding/dissociation curves, revealed a surprisingly emprovement of the binding affinity of the 1B4 *r*Fab$_2$ compared to the single 1B4 *r*Fab unit, confirming that bivalency played a crucial role in the recognition of the target protein and of the specific CFC domain, as seen by ELISA. The K$_D$ estimated for the artificial 1B4 *r*Fab$_2$ was about 0.26 nM, very similar to that determined for the full length antibody (0.24 nM), while for the monomeric fragment the K$_D$ value was 6.5 nM.

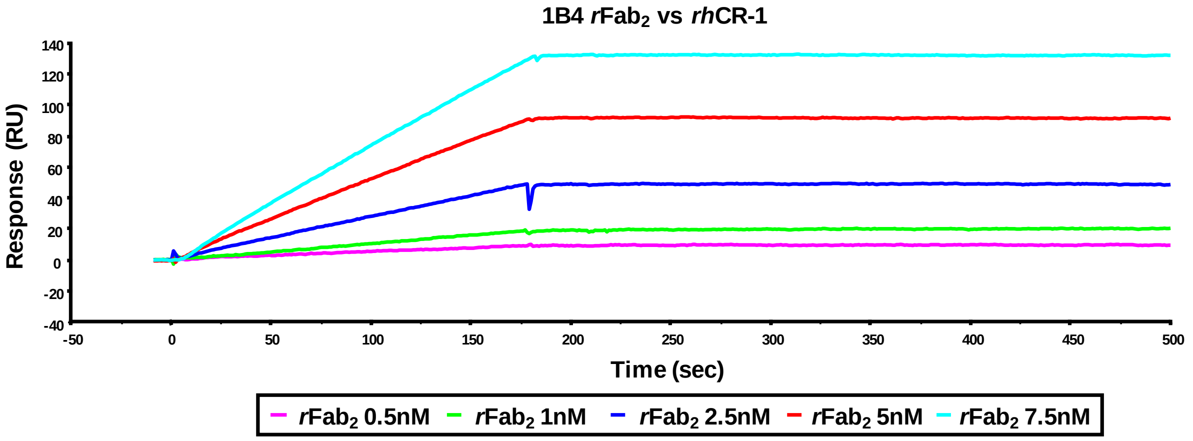

Table 28. Kinetic rate and apparent affinity constants of 1B4 *r*Fab$_2$ binding to *rh*CR-1

1B4 *r*Fab$_2$	**k_a (1/Ms)**	**k_d (1/s)**	**K_D (M)**	**SE (RI)**
0.5 nM	$1.00*10^{5}$	$2.95*10^{-5}$	$2.94*10^{-10}$	0.0408
1 nM	$1.48*10^{5}$	$8.65*10^{-5}$	$5.86*10^{-10}$	0.0322
2.5 nM	$1.12*10^{5}$	$2.81*10^{-5}$	$2.51*10^{-10}$	0.037
5 nM	$1.78*10^{5}$	$1.83*10^{-5}$	$1.03*10^{-10}$	0.0499
7.5 nM	$1.52*10^{5}$	$1.64*10^{-5}$	$1.08*10^{-10}$	0.0479
average	$1.38*10^{5}$	$3.58*10^{-5}$	$2.68*10^{-10}$	0.04156

Figure 3.54: Sensorgrams overlay and kinetic parameters table of 1B4 *r*Fab$_2$ binding to *rh*CR-1.

In conclusion, the new 1B4 *r*Fab$_2$ format displayed a functional behavior comparable to the whole parental antibody, showing a remarkably enhanced binding affinity compared to the monomeric 1B4 *r*Fab fragment.

Thus, artificially restoring the bivalency, the new fragment exhibits a powerful gain of affinity, matching the one of the whole antibody.

2.4 GENERATION OF 1B4 *r*Fab-DOXORUBICIN ADC

The identity of the two linkers (I linker and II linker) used for conjugation were confirmed by mass spectrometry. All conjugation steps were monitored by RP-HPLC analyses. In Fig. 3.55, an overlay of chromatographic profiles of the reaction between Doxorubicin and I linker after 1 and 3 days, is reported. As shown, after 24h (green) two main sharp peaks with different elution times were observed, where the first corresponded to the free Doxorubicin (retention time: 11.4 min) and the second to the Doxorubicin functionalized with the I linker (retention time: 12.7 min).

After 3 days, the RP-HPLC profile (black) changed, showing the disappearance of the unreacted Doxorubicin at retention time of 11.4 min, and the increase of the peak at 12.7 min due to the Doxorubicin- I linker product.

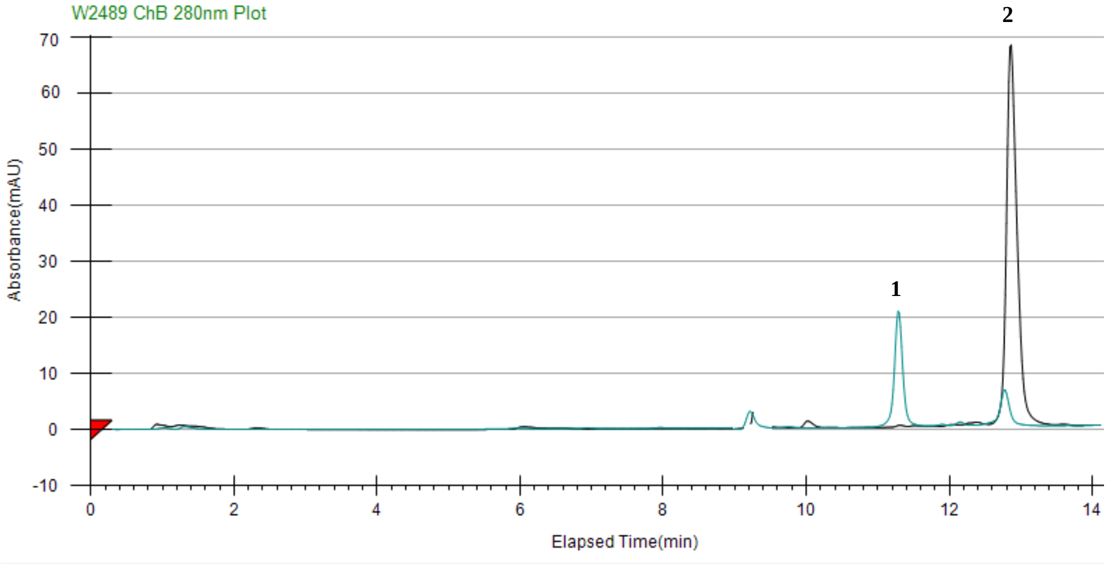

Figure 3.55: Overlay plot of the RP-HPLC profiles corresponding to the reaction mixture containing Doxorubicin and I linker, after 1 day (green) and after 3 days (black).

The second step was the conjugation between the intermediate product Doxorubicin-I linker indicated as Product A (see scheme reported in the Fig. 2.4 in Methods) and the II linker to obtain the Product B (Doxorubicin-I linker-II linker). The RP-HPLC chromatogram (Fig. 3.56) clearly showed the presence of two main peaks: the predominant peak (peak 1), at 11.2 min, corresponding to Product B (Doxorubicin-I linker-II linker) and the second peak (peak 2), at a retention time of 12.7 min, corresponding to the excess of the starting Doxorubicin-I linker product. The final product, obtained with a yield of 64%, was finally analyzed by ESI-MS to assess the correct molecular mass, found to be 1070 amu (not shown).

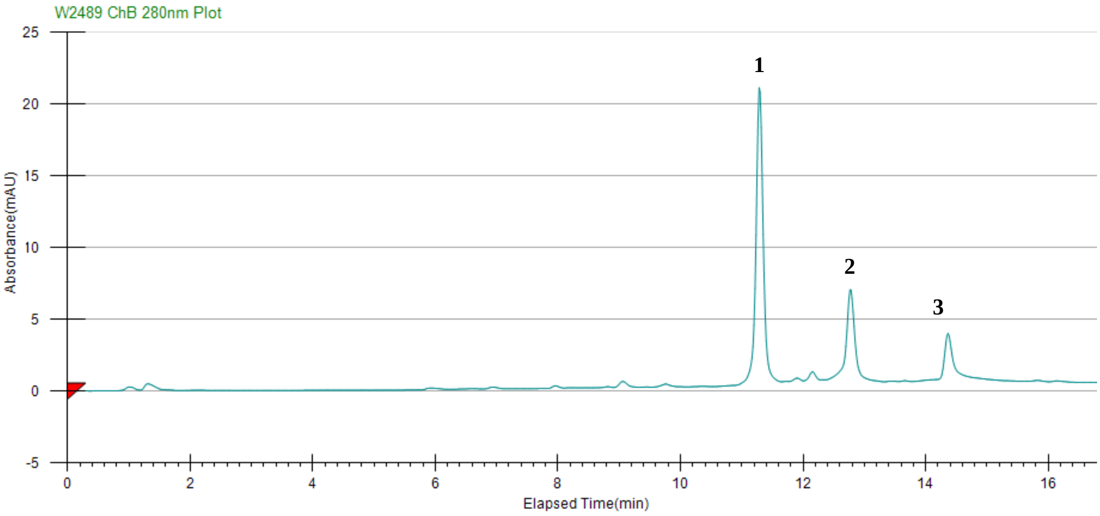

Figure 3.56: RP-HPLC profile of the conjugation reaction of the intermediate product (Doxorubicin-I linker) with the Ac-CKA-NH_2 linker (II linker).

Next, Product B was isolated by preparative RP-HPLC and used to perform the enzymatic reaction with the 1B4 *r*Fab via M-TGase under the reported conditions (section 2.16.b of Methods). The reaction mixture, composed of the Doxorubicin previously functionalized with the two linkers, the 1B4 *r*Fab and the M-TGase, was monitored by RP-HPLC analysis. To isolate the desired ADC product, the reaction mixture was purified by cation-exchange chromatography (section 2.15 of Methods). As shown in the chromatographic profile (Fig. 3.57), the excess of Doxorubicin did not interact with the matrix and eluted in the equilibration phase; two peaks of comparable intensity (reported as A and B), probably corresponding to different species of 1B4 *r*Fab-Doxo, eluted during the linear gradient from 0 mM to 350 mM NaCl.

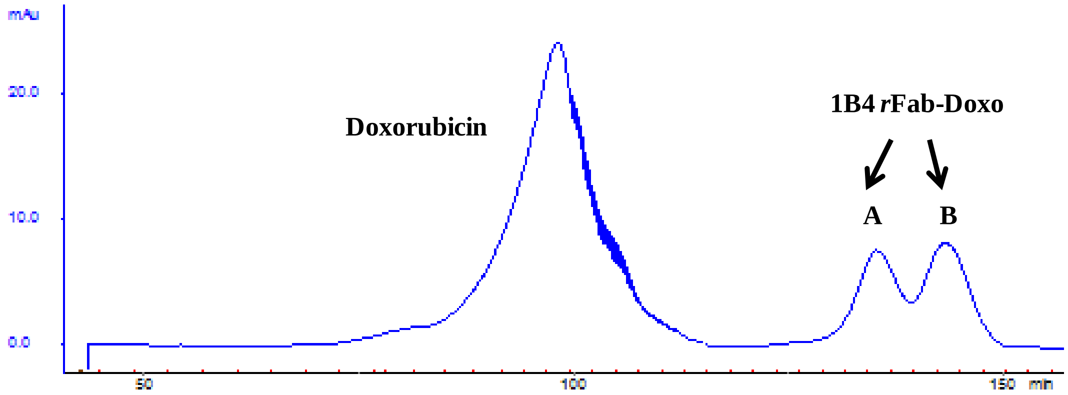

Figure 3.57: IEC profile of the reaction mixture containing the three components: Doxorubicin-I linker-II linker, 1B4 *r*Fab and M-TGase enzyme.

The two isolated peaks, A and B, were analyzed by SDS-PAGE onto a 12% polyacrylamide gel under non reducing and reducing conditions, to have a comparison with the wild-type 1B4 *r*Fab (t_0) (see Fig. 3.58). As expected, all three species migrated as a single band at 45 kDa under non-reducing and reducing conditions and showed an apparent integrity and homogeneity.

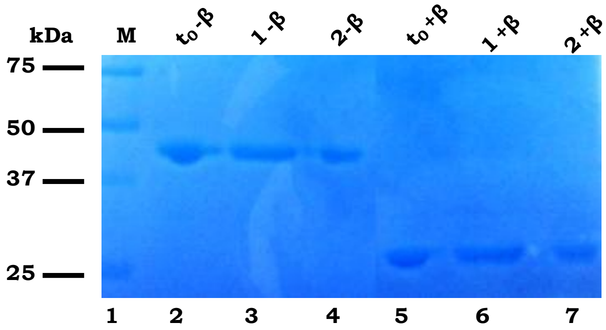

Figure 3.58: SDS-PAGE analysis of each eluted peak (A and B) compared to the unconjugated 1B4 *r*Fab (t_0).

Next, an LC-ESI-TOF-MS analysis was performed on each single peak isolated by IEC to identify the corresponding products. The mass spectrometry analysis was carried out after mildy reduction with 20 mM DTT to separate the two chains, while retaining the intra-disulfide bridges.

Both samples exhibited the same UV profile where the first peak and the second one corresponded to the light chain (LC) and heavy chain (HC), respectively (Fig. 3.59 A).

The light chain mass spectrum deconvolution of each sample confirmed the same experimental MW, in perfect agreement with the theoretical one (MWtheor/ MWexp 23924.5/ 23924.5 amu).

These data confirmed the integrity of the light chain as well as the specificity of the conjugation reaction on the heavy chain.

By contrast, the chromatographic peak corresponding to the heavy chain was not homogeneous, thus suggesting the presence of different species for both the ion-exchange separated products (peak A and peak B).

The deconvolution of the mass spectrum of the heavy chain derived from peak A (Fig. 3.59 C) revealed the occurrence of at least four products: the correct ADC product 1B4 (*r*Fab-Doxorubicin-I linker-II linker) with a molecular mass of 25664.1 (peak 4); the unconjugated 1B4 *r*Fab, with a molecular mass of 24611.9 amu (peak 3) and two remaining peaks (peak1 and peak2) corresponding to two degradation products of the C-terminal linker.

In detail, the peak 1 (23617.4 amu) had the linker cleaved at the A residue next to the K, while peak 2 (24056.5 amu) corresponded to the species in which the linker was cleaved at the T residue.

The high amount of unfunctionalized species was presumably due to the reversibility of the enzymatic reaction rather than to uncomplete conjugation of the fragment.

Likewise, the mass spectrum of peak B (Fig. 3.59 D) displayed the presence of four species. In this case, the products exhibited a molecular weight corresponding to dehydrated products (all MW had a Δmass of -18 Da). The exact position where this side-reaction occurred needs further investigation.

In Table 29, all products identified as heavy chain conjugation products are reported (* indicates the dehydrated products).

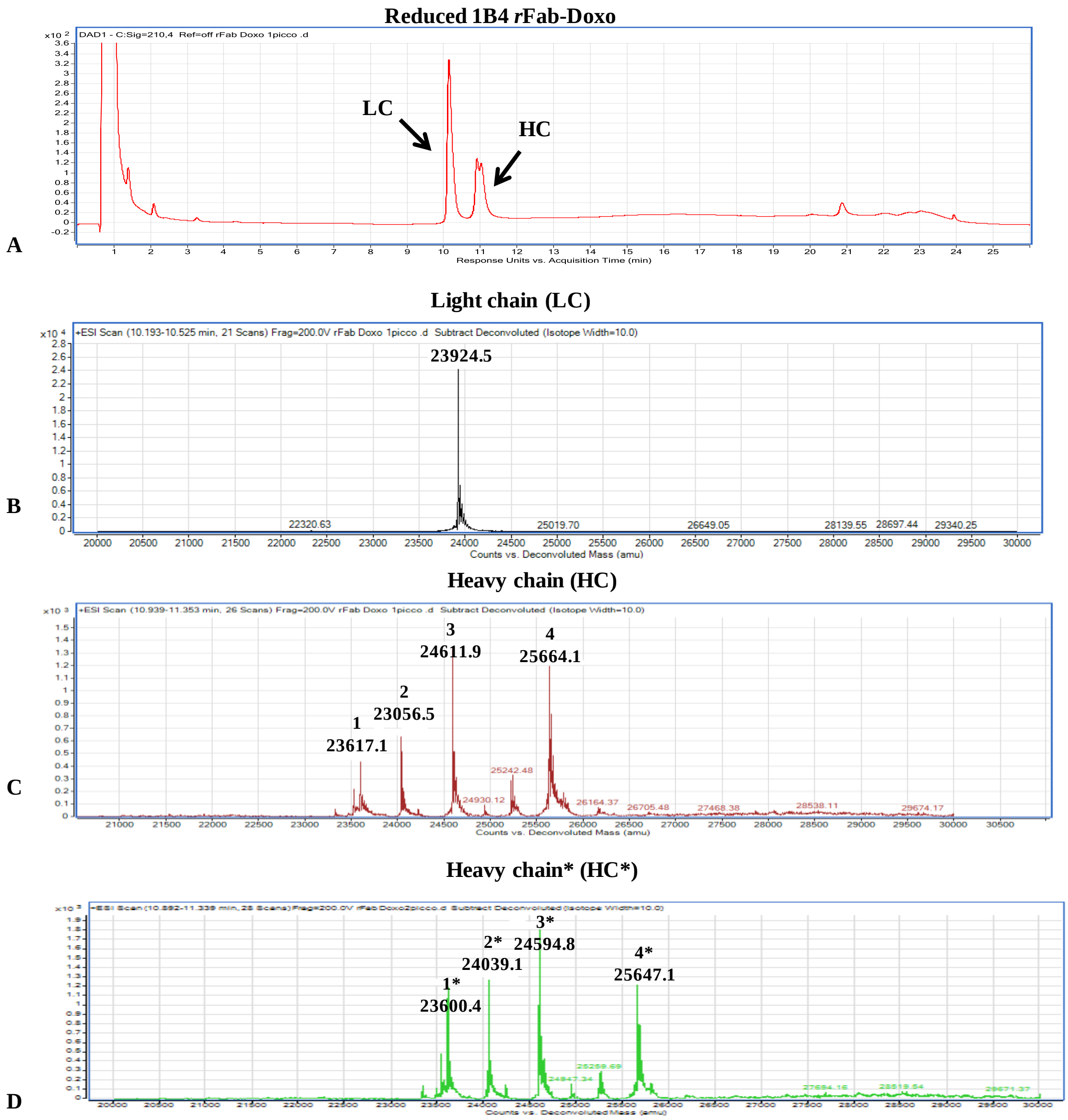
Reduced 1B4 *r*Fab-Doxo

Light chain (LC)

Heavy chain (HC)

Heavy chain* (HC*)

Figure 3.59: LC-ESI-TOF-MS analyses of the reduced 1B4 *r*Fab-Doxo. UV profile at 280 nm (**A**). Mass spectrum deconvolution of the light chain (**B**). Mass spectrum deconvolution of the heavy chain from the Peak A (**C**) and from the Peak B (**D**), isolated by IEC.

Table 29. MW of Heavy chain conjugation products

Product	Theor MW (amu)	Exp MW (amu) Peak	Exp MW (amu) Peak*
HeavyChain-GSGA	23617.4	**1** 23617.1	**1*** 23600.4
HeavyChain-GSGAKQPT	24057.0	**2** 24056.5	**2*** 24039.0
HeavyChain-GSGAKQPTQGAMPA	24612.6	**3** 24611.9	**3*** 24594.8
HeavyChain-GSGAKQPTQGAMPA-Doxorubicin	25664.6	**4** 25664.1	**4*** 25674.1

In conclusion, the 1B4 *r*Fab-Doxo was generated. The conjugation reaction was not very efficient, as the final product was obtained mixed with other side reaction impurities. Most side products were correlated to the simultaneous formation of undesired degraded fragments as well as to the reversibility of the enzymatic reaction. An optimization process is required to improve the production of this ADC.

III.3 PRELIMINARY *IN VITRO* ASSAYS OF 1B4 mAb ON HUMAN CANCER CELLS OVER-EXPRESSING CR-1 PROTEIN

3.1 Detection of human CR-1 in GBM cell lines

Since the expression of human CR-1 has been recently demonstrated by Pilgaard et al. [45] also in IV grade glioblastoma multiforme tumor cells (GBM), a study to test 1B4 mAb was conducted at the laboratory of the Prof. Meg Duroux, Dept. of Biomedicine of Aalborg University.

We used two GBM cell lines, the commercial U87 and the C16, provided by the Aalborg University Hospital, in which expression levels of CR-1 were found.

A preliminary detection of CR-1 by western blot analysis was performed using both the 1B4 antibody and the commercial polyclonal anti-cripto antibody directed against the 41-55 region of N-terminal part of CR-1 (not shown). Then the detection of human CR-1 was assessed by Immunofluorescence, as described in section 2.17.d of Methods. As shown in Fig. 3.60, the 1B4 mAb staining was comparable to the signal obtained with the commercial antibody. The staining of CR-1 without permeabilization of cells, confirmed the ability of 1B4 mAb to recognize the form of the target protein anchored to the cell membrane.

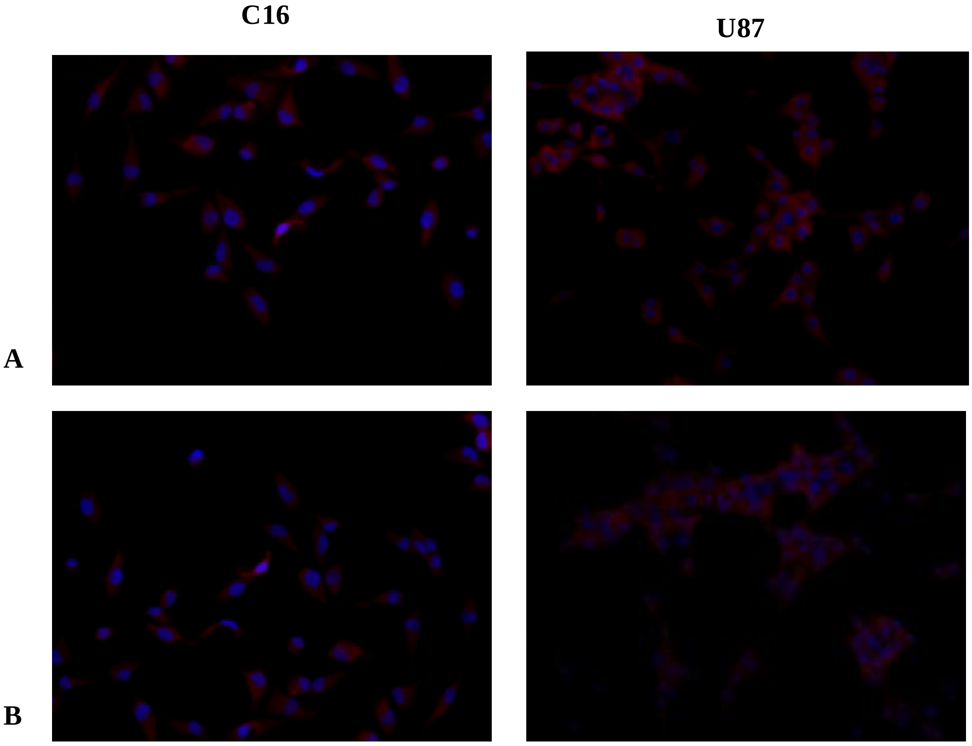

Figure 3.60: Immunostaining obtained by merge of Hoechst nuclear dye (blue) and AlexaFluor555 signal (red). In this image the comparison of commercial antibody (left) and 1B4 mAb (right) fluorescence signal is reported.

3.2 Functional assays on GBM cell lines

To investigate the intracellular pathways on which the 1B4 mAb exerts a possible inhibition effect to block both anchored and soluble CR-1 protein and to further evaluate its possible use as a therapeutic tool, some functional assays were carried out.

a) Proliferation assay

The proliferation assay was conducted measuring the emission of the CFSE by FACS analysis. Cells were treated using the 1B4 mAb at 0.2 µM (30 µg/mL). The outcome was negative and as shown in the Fig. 3.61, after 4 days the fluorescence emitted by the untreated cells (D4 Ctrl) was overlaying to the fluorescence emitted by the treated population (D4 mAB), showing the same shift as the population at the starting point (D0 Ctrl). This shift indicates the cell proliferation, since the signal decreases compared to the starting population, denoting that the cellular division has happened. In fact from the comparison of the emitted signal value (X-Med) for both cell lines the untreated and treated cells show a comparable value. In C16 population it was 0.3 for the treated cells, while it was 0.4 for the negative control. The same behavior was observed for the U87, in which the negative control and the treated population exhibited exactly the same X-Med value of 0.5. These data suggest that the 1B4 antibody was not able to inhibit the cell proliferation of both cell lines.

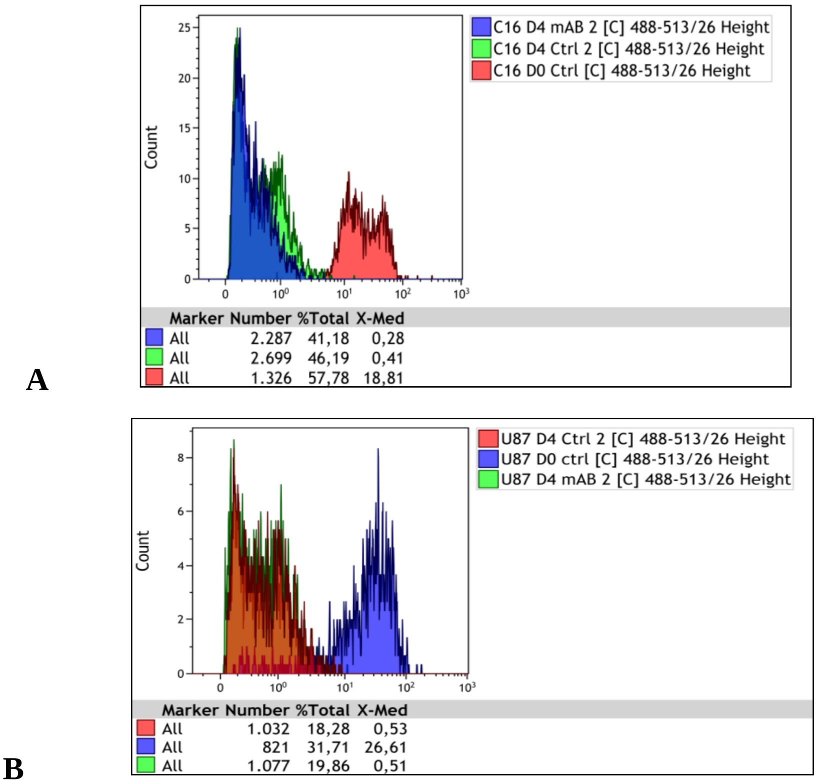

Marker	Number	%Total	X-Med
🟦 All	2.287	41,18	0,28
🟩 All	2.699	46,19	0,41
🟥 All	1.326	57,78	18,81

Marker	Number	%Total	X-Med
🟥 All	1.032	18,28	0,53
🟦 All	821	31,71	26,61
🟩 All	1.077	19,86	0,51

Figure 3.61: FACS analysis plots of the proliferation assays conducted on C16 (**A**) and U87 (**B**) cell lines, using CFSE as cell tracing.

b) Cell viability assay by trypan blue exclusion test

Since the FACS analysis of the proliferation assay does not provide any information about cell death induction by the 1B4, a viability assay was performed to evaluate the capability of the mAb to promote cell death instead of blocking cell proliferation. The effect of the antibody was evaluated determining the percentage of unviable and viable cells after treatment with 0.2 and 0.4 µM of 1B4 mAb after 2 days and 4 days; untreated cells were used as negative control (CTL).

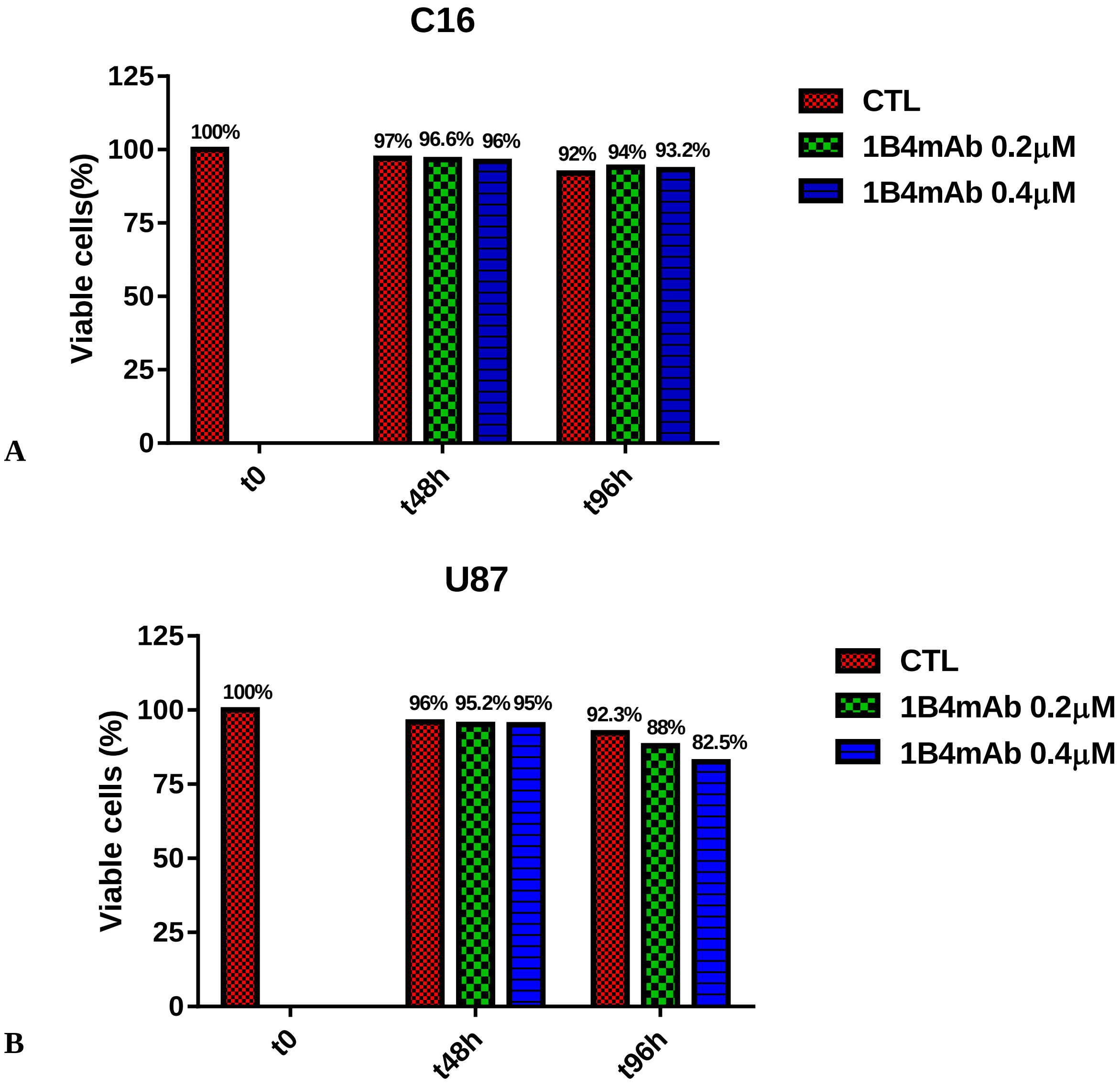

Figure 3.62: Viability assays performed using trypan blue exclusion test on C16 (A) and U87 (B) cell lines at the indicated exposure times.

As shown in Fig. 3.62 A, C16 cells underwent only a slightly detectable decrease of viability by comparison to negative control. Also treatment of U87 (Fig. 3.62 B) cells with 0.2 µM 1B4 led to a slight decrease of viability (12%), which was essentially unchanged (17.5%) when the concentration of mAb was doubled. Probably, a much higher concentration of mAb is required to observe cell death effects.

c) Migration assay

A migration assay was carried out by the scratch methodology - that mimics the wound healing process - so as to determine the ability of the 1B4 mAb to reduce or totally block cell migration. The migration assay on C16 revealed that the antibody had not any inhibition activity. Instead, the migration degree of treated cells seemed to progressively increase at 0.2 µM and 0.4 µM concentrations of antibody (See Fig. 3.63 A). Indeed, the scratch area (expressed as % of all the covered area) resulted to be less wide than the area of the negative control (CTRL) as calculated by the Wimasis server.

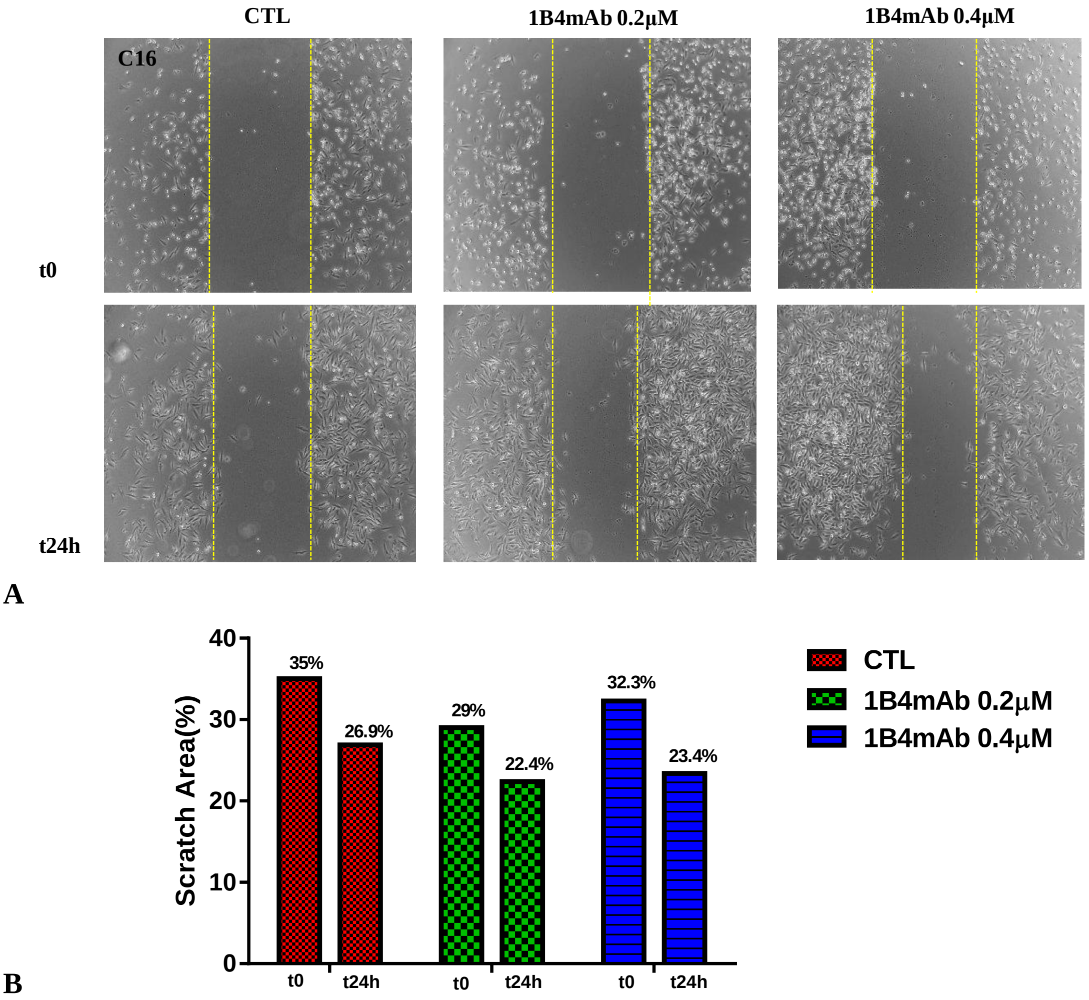

Figure 3.63: Migration assay on C16. The wound healing-mimicking effect was monitored for 24h (**A**). Plot of the values of scratch area, reported as % of the total covered area (**B**).

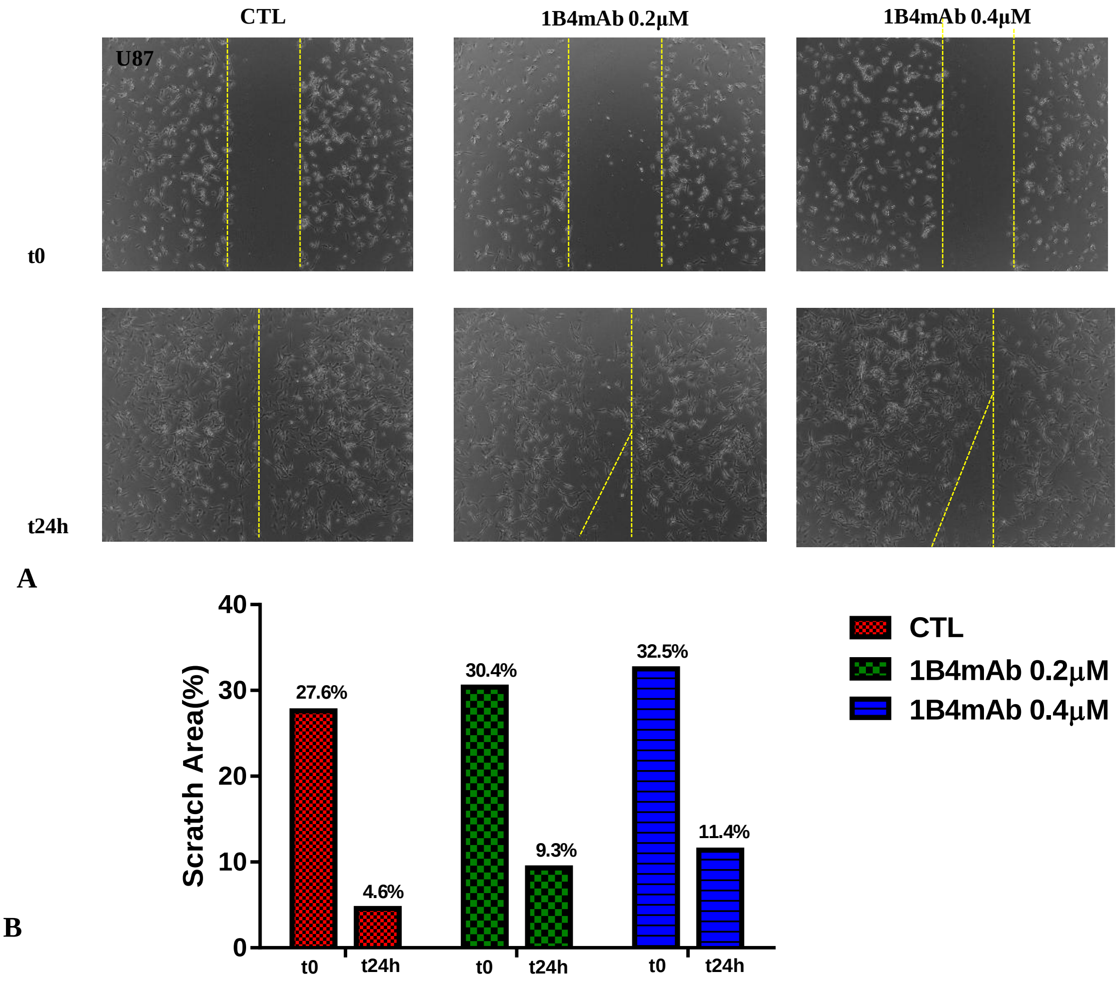

Figure 3.64: Migration assay on U87. The wound healing was monitored for 24h (**A**) Plot of the values of scratch area, reported as % of the total covered area (**B**).

At variance with the C16, the migration assay performed on U87 provided different results. Indeed, as shown in Fig. 3.64 A, a slight decrease of migration degree was observed after 24h after treatment at both the two concentrations (9.3 % of scratch area versus 4.6% of the control at 0.2 µM and 11.4% versus 4.6% of the control for the 0.4 µM treatment). The 1B4 antibody had therefore a slightly inhibitory effect on the migration of these cells and the effect appeared to be also dependent on the antibody concentration. Likely, a higher concentration of antibody was required to induce a more sustained inhibition of cell migration and further investigations are underway.

In conclusion, the 1B4 mAb tested on GBM cell lines (C16 and U87), exhibited the ability to detect the target CR-1 protein, but it was not able to exert functional effects on proliferation and death. A slight decrease of cell motility was instead detecdted on U87 cells, but this requires further investigations at higher antibody concentrations. The different behavior on the two cell lines can be attributed to a difference in expression of CR-1 at higher levels in C16 than in U87, as already determined **[45].**

3.3 1B4 mAb activity on colorectal cancer cells

We evaluate the activity of 1B4 also on GEO colorectal cancer line. Before starting the antibody treatment, we verified the expression levels of human CR-1, using the P19 mouse teratocarcinoma cell line as negative control. As shown in Fig. 3.65, the GEO cell lines expressed high levels of the Cripto-1 mRNA compared to the control, so on these cells, we started the treatment with the 1B4 mAb and monitored the effect after 24h and 96h.

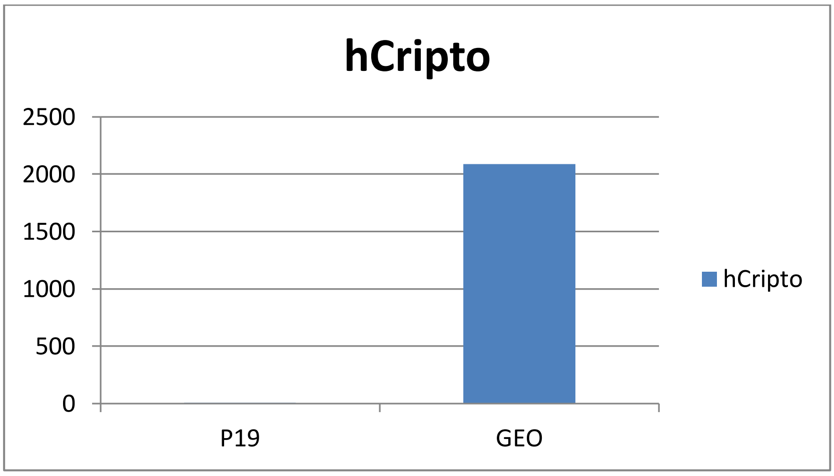

Figure 3.65: qRT-PCR data related to the expression levels of human CR-1 mRNA in GEO cells.

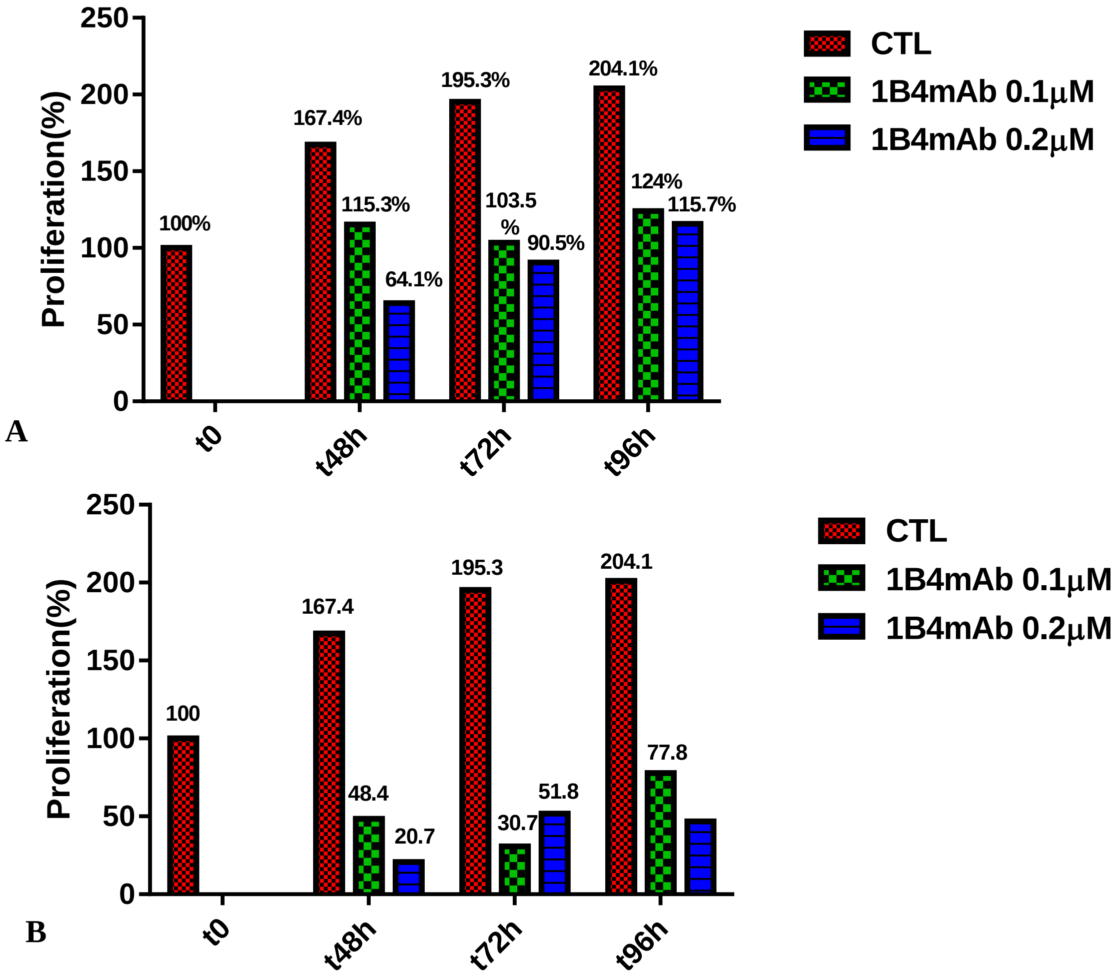

Figure 3.66: Proliferation assay as performed on GEO cells treated with 1B4 and monitored after 24h, 72h and 96h. Data are shown for the single dose addition (0.1 μM and 0.2 μM) (A) and after daily fresh addition of the antibody at the same concentrations (B).

A first assay was carried out by adding 1B4 mAb only at the first day and comparing the proliferation rate of untreated cells (CTL) with that one of the treated cells. As shown in Fig. 3.66 A, an anti-proliferative effect was already detected after 48h and was also dose-dependent (32% inhibition at 0.1 μM and 62% inhibition at 0.2 μM). Instead, at the second (48h) and at the fourth day (96h) the antibody lost its activity, likely due to degradation in the cell medium, so the cells started to re-grow. Interestingly, when the antibody was added freshly every 24h, the anti-proliferative activity was remarkably enhanced. Indeed, only about 20% and 11% of the cells were still viable at 24h after treatment with 0.1 μM and 0.2 μM antibody, respectively. The effect was persistent also after 48h and 96h, although some cell re-growth was observed also under these conditions.

3.4 Effect of 1B4 mAb on melanoma cancer cells

Since the expression of CR-1 has been also reported in melanoma cancer cells by Strizzi et al. [57], the 1B4 mAb was also tested on human melanoma cell lines. This study was performed by the research group at the Ann & Robert H. Lurie Children's hospital of Chicago led by Prof. Mary Hendrix.

The 1B4 mAb was firstly tested by western blot analysis on a panel of melanoma cell lines to determine its ability to recognize human CR-1 in this cancer cells (Fig. 3.67).

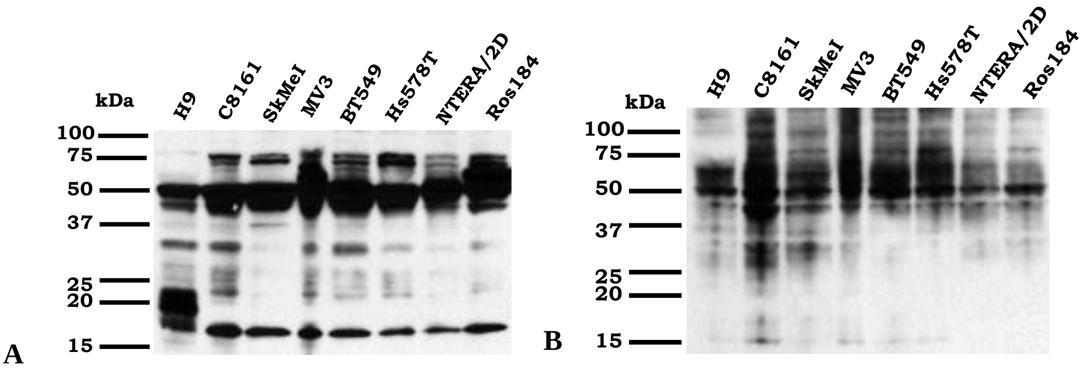

Figure 3.67: Western blot analyses on melanoma cell lines (C8161, SkMeI, MV3, Ros184) comparing the commercial antibody (**A**) with the 1B4 mAb (**B**). The remaining cell lines were used as positive control.

As shown, by comparing the bands detected by the commercial anti-Cripto antibody (Fig. 3.67 A) with those stained by the 1B4 mAb (B), it was evident that the commercial antibody readily recognized the core protein (~18 kDa), whereas the 1B4 antibody was more efficient in detecting the heavier CR-1 isoforms corresponding to the differential glycosylation status of the protein (44 kDa, 50kDa).

The C8161 cell line (malignant melanoma) was chosen to perform a functional assay to evaluate if the 1B4 mAb was able to block the phosphorylation of Smad2/3 Nodal-dependent and eventually of MAPK and c-Src, triggered by a Nodal-independent mechanism (Fig. 3.68).

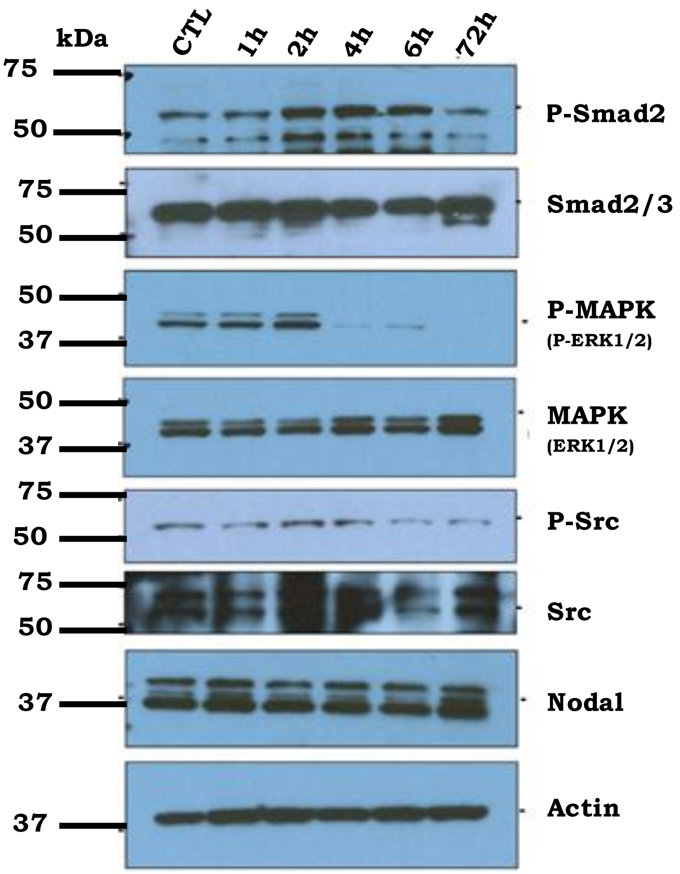

Figure 3.68: Western blot analysis on C8161 treated with 1B4, to detect the phosphorylated forms of CR-1 cellular partners.

As shown in Fig. 3.68, the 1B4 mAb exerted a weak negative effect on Smad2/3 phosphorylation, only after 72h. At intermediate time intervals, the antibody actually increased the Smad2/3 activation, whereas after 72h a sustained reduction was observed. Instead, the antibody strongly and persistently (up to 72h) blocked the phosphorylation of ERK1/2 yet after 4h. This suggested a strong inhibitory effect on the Nodal-independent signaling pathways mediated by raf/ras and shc and this hypothesis was further confirmed by the inhibition of activation of Src at 6h until 72h.

These findings indicate that in C8161 cell line, in which CR-1 is co-expressed with Nodal, the 1B4 mAb can intensively block the phosphorylation of MAPK and Src induced by CR-1 via a Nodal- independent mechanism, which is mediated by the interaction of the CR-1 CFC with GRP78 and/or with Glypican-1.

CHAPTER IV

DISCUSSION

Human Cripto-1 (CR-1) is the founding member of the EGF-CFC superfamily that exhibits different functions depending on the organism in which its members are expressed. CR-1 is a key regulator of embryogenesis, promoting the differentiation of embryonic stem cells, and it is involved in organogenesis, with a predominant function in the neuronal and cardiac development. As many other developmental growth factors, CR-1 also promotes tumorigenesis, by regulating cell proliferation, migration, epithelial-mesenchimal transition, survival and angiogenesis. It is therefore described as an oncogenic growth factor. CR-1 is composed by two functional Cysteine Rich Domains, EGF-like and CFC, both independently involved in various interactions with several partners which mediate its pro-oncogenic activity. Each domain consists of about 40 amino acids and contains three disulfide bridges that render them highly compact structures. While the EGF-like domain is involved in the interaction with members of the TGF-β family (Nodal, GDF1, GDF3), ALK7 and Glypican-1 **[26,28,29,34,47]**, the CFC domain is reported to interact with the ALK4 receptor and GRP78 hsp70, which both, through different signaling pathways, activate major anti-apoptotic mechanisms **[28,31]**.

CR-1 is highly expressed in a wide range of human solid tumors (breast, colon, brain, lung, melanoma) whereas it is poorly expressed or completely absent in adult normal tissues **[36]**. CR-1 is therefore a well-established therapeutic target for those type of tumours where the protein is overexpressed. In addition, since high levels of soluble CR-1 are detectable in plasma of patients affected by breast, colon and glioblastoma tumors, CR-1 may be considered as a novel serologic marker for early diagnosis of tumors over-expressing this protein.

CR-1 can promote tumorigenesis acting as a non competitive antagonist of Activin B or as a co-receptor of Nodal. In both cases the binding of CR-1 to ALK4 receptor, via the CFC domain, is fundamental to trigger the Smads cascade that ultimately lead to the expression of tumor-related factors. On the basis of these premises we have designed a strategy based on the use of monoclonal antibodies to block the several activities exerted by CR-1 through its CFC domain. The CFC domain of CR-1 is readily accessible by chemical synthesis as demonstrated by several papers reporting its assembling, refolding and disulfide pattern **[19,164]** and its 3D structure **[165]**. The 39-residues long polypeptide has a natural propensity to refold forming the correct pattern of disulfide bridges, a property that suggests it is an independent structural module of the protein, other than a functional motif. However, the domain by itself has poor recognition properties toward the ALK4 receptor **[26]** (the binding to GRP78 has not been tested yet) and could be used therefore as a soluble inhibitor only at high concentrations. Attempts are underway to use a soluble variant of ALK4 to inhibit CR-1, generated as a dimeric FC-fused protein (PCT n° 7820620, filed Sep 14, 2004). One very versatile option for inhibiting the CFC-mediated CR-1 activity is to generate monoclonal antibodies specifically targeting such region and capable of masking the ALK4 and the GRP78 binding site. mAbs have the advantage of very high specificity, generally high affinity and the perspective of producing them in large amounts from engineered cells or hybridomas. Previously, mAbs against the CR-1 CFC domain have been reported **[25]**, however, such antibodies have never been developed to the stage of a therapeutic, nor characterized in terms of binding affinity, epitope delineation and sequence. This last point is of huge importance in the perspective of antibody humanization strategies and for the generation of new antibody formats, including recombinant Fab, Fab_2, scFv or other similar fragments which have simplified structures, higher tissue penetration features, versatility in terms of affinity enhancement, reduction of immunogenicity, increase of stability, structure modifications to increase half-life and other properties.

Using the synthetic, fully refolded human CFC domain of CR-1 – [112-150] residues - we immunized mice and generated mAbs against this key structural motif using the hybridoma technique. mAbs binding the original antigen, have been further selected to choose those able to: i) bind the full length protein and ii) bind it in proximity of the H120 and W123 residues of CFC strongly involved in the binding to ALK4. Several mAbs binding the domain have thus been further tested to select those enable to recognize the H120/W123 mutated molecule, so that they are endowed with the ability to bind the side chains of these selected residues and therefore with the potential of inhibiting the interaction with both ALK4 and GRP78. The antibodies have been prepared in sufficient amounts to perform a number of biochemical studies, including binding to the synthetic human CFC, binding to human and mouse recombinant CR-1, inhibition of the binding to ALK4. Remarkably, the two mAbs isolated by this approach, 10D1 and 1B4, exhibit both the ability to selectively recognize the human variant over the mouse (See Fig. 3.11 for a sequence comparison) and to also be selective toward the fully refolded human CFC domain. The K_Ds of the interaction between 10D1 and 1B4 with CR-1 were 70 pM and 240 pM, respectively. These observations suggest two important features of the selected antibodies: i) they bind conformational epitopes, though a partial recognition of the unfolded protein still occurs with a lower affinity, as suggested by poor recognition of rhCR-1 in western blot experiments (data not shown); ii) both antibodies likely also bind the residue D121 which is only present in the human variant (in the mouse sequence there is a glycine) and localized between H120 and W123.

Full sequencing of the 1B4 and 10D1 antibodies CDRs allowed the generation of molecular models of their 3D structures and, using docking softwares, also 3D models of the antibody-CFC complexes have been generated and deeply studied. The mutual interacting surfaces from both the CFC and the antibodies CDR have been clearly identified and finely mapped, so to gain insights for further affinity maturation or humanization studies. We next sought to investigate the biological properties of these antibodies. Most studies were performed with the 1B4 on different cancer cell lines overexpressing CR-1 to test the cell killing and migration blocking activity. While no pro-apoptotic activity was shown in GBM cell lines (U87 and C16), only a modest anti-migration activity was observed only on the U87 line. At variance, a strong cell killing activity was observed on the GEO cancer cell line expressing high levels of the CR-1 mRNA compared to the control. Under these conditions, the antibody at 100 nM and 200 nM, killed between 80% and 90% of cells after 24h.

Preliminary attempts to obtain the Fab fragment from 1B4 mAb by proteolytic approach failed, since only partially active fragment was generated, displaying a 100-fold binding affinity reduction compared to the intact IgG. Therefore, this approach was soon abandoned in favor of the recombinant preparation of a partially humanized (chimeric), C-terminally modified recombinant Fab. The recombinant Fab of 1B4 (1B4 *r*Fab) was generated using the humanized scaffold of the well-known Trastuzumab antibody in the perspective of using it in *in vivo* experiments. On the C-terminus of the heavy chain, a M-TGase recognition sequence was introduced with the aim of conjugating, in a very specific manner, molecular synthons on the side chain of a Glutamine residue. The recombinant Fab was thus expressed in an *E.Coli* host strain with a signal peptide that –

favouring the polypeptide translocation into the periplasmic space – allowed the contextual refolding of the Fab. This approach was successful, as it allowed the rapid preparation of several mg of the desired Fab. The antibody fragment was fully characterized in terms of structure and binding affinity toward the single hCFC antigen and the full-length *rh*CR-1 protein. Indeed, by SPR we measured a K_D of only 6 nM, largely reduced compared to the 240 pM K_D exhibited by the full-size antibody.

To improve the affinity, an innovative artificial dimeric format of the Fab (1B4 *r*Fab_2) was designed and obtained. The dimer was achieved by using a pseudo-symmetrical homobifunctional linker able to join together two Fab molecules under the conditions of enzymatic conjugation with M-TGase. The approach was successful, since we could achieve a dimeric artificial Fab with a MW of about 100 kDa held together by isoamide bonds between the Lysine side chains of the linker and the Glutamine side chain of the M-TGase consensus sequence. Remarkably, this bivalent fragment exhibited a K_D of 270 pM, which is similar to that one displayed by the full-size antibody.

Using the 1B4 *r*Fab as scaffold we next explored the possibility to also generate ADCs (Antibody Drug conjugates) exploiting the occurrence of the M-TGase conjugation site. ADCs are new, smart molecules where the high specificity of antibody portion is complemented by the high cytotoxic activity of the linked payload. Antibody specificity for antigens selectively expressed on the surface of cancer cells is exploited to deliver high activity, otherwise toxic compounds to such cells, thus allowing reduction of their cytotoxic potential in normal tissues and increasing it at the site of the tumour. Also this approach was successful, since the designed strategy was applied to prepare an ADC with the 1B4 *r*Fab and Doxorubicin. The strategy was based on both chemical and enzymatic steps, whereby Doxorubicin was first chemically conjugated to a linker bearing an amino-group (the ε-amino group of a Lysine). In a second step, such amino group was site-specifically conjugated to the C-terminal of the *r*Fab heavy chain in order to have one single Doxorubicin molecule linked to the antibody fragment. The analytical characterization of the 1B4 *r*Fab-Doxo conjugate demonstrated that the expected reactions had occurred and that the expected compound was isolated. Biological assays are underway to assess the activity of this new molecule.

In conclusion, we have generated mAbs having very high affinity to the CFC domain of human CR-1 and we have deeply characterized them at biochemical level to determine their affinity toward the target. In addition to a biochemical approach, by computational studies on Fab-antigen complex, we have investigated how they interact with the antigen at molecular level. Finally, starting with the 1B4 mAb, we have explored which are the perspective for the utilization of this antibody as a biotherapeutic (*in vivo* blocking of CR-1 activity) or as a diagnostic agent for the detection of the protein in biological fluids of patients overexpressing the protein. Preliminary data on selected Cripto-expressing cancer cells suggest that the 1B4 mab has a potential as single-treatment biotherapeutic. Also a major application for the generation of ADCs is expected, given the high selectivity of the antibody and possibility to produce recombinant Fab format bearing a site-specific conjugation site.

REFERENCES

1.
Salomon DS, Bianco C, Ebert AD, Khan NI, De Santis *et al*. 2000 The EGF-CFC family: novel epidermal growth factor-related proteins in development and cancer. *Endocr Relat Cancer*;7(4):199-226.

2. Ciccodicola A, Dono R, Obici S, Simeone A, Zollo M, Persico MG. 1989 Molecular characterization of a gene of the 'EGF family' expressed in undifferentiated human NTERA2 teratocarcinoma cells. *EMBO J*.;8(7):1987-91.

3. Bianco C, Salomon DS. 2010 Targeting the embryonic gene Cripto-1 in cancer and beyond.*Expert Opin Ther*.; 20(12):1739-49.

4. de Castro NP, Rangel MC, Nagaoka T, Salomon DS, Bianco C. 2010 Cripto-1: an embryonic gene that promotes tumorigenesis.*Future Oncol*.;6(7):1127-42.

5. Dono R, Scalera L, Pacifico F, Acampora D, Persico MG & Simeone A 1993 The murine cripto gene: expression during mesoderm induction and early heart morphogenesis. *Development* 118 1157–1168.

6. Zhang J, Talbot WS & Schier AF 1998 Positional cloning identifies zebrafish one-eyed pinhead as a permissive EGF-related ligand required during gastrulation. *Cell* 92 241– 251.

7. Gritsman K, Zhang J, Cheng S & Heckscher E 1999 The EGF-CFC protein one-eyed pinhead is essential for nodal signaling. *Cell* 97 121–132.

8. Brandt R, Normanno N, Gullick WJ, Lin J-H *et al*. 1994 Identification and biological characterization of an epidermal growth factor-related protein:Cripto-1. *J Biol Chem*;269 17320–17328.

9. Kenney NJ, Smith GH, Maroulakou IG, Green JH, Muller WJ, Callahan R, Salomon DS & Dickson RB 1996 Detection of amphiregulin and Cripto-1 in mammary tumors from transgenic mice. *Molecular Carcinogenesis* 15 44–56.

10. Seno M, DeSantis M, Kannan S, Bianco C, Tada H, Kim N, Kosaka M, Gullick WJ, Yamada H & Salomon DS 1998 Purification and characterization of a recombinant human cripto-1 protein. *Growth Factors* 15 215–229.

11. Niemeyer CC, Persico MG & Adamson ED 1998 Cripto: roles in mammary cell growth, survival,differentiation and transformation. *Cell Death and Differentiation* 5 440–449.

12. Niemeyer CC, Spencer-Dene B, Wu JX & Adamson ED 1999 Preneoplastic mammary tumor markers: Cripto and Amphiregulin are overexpressed in hyperplastic stages of tumor progression in transgenic mice. I*nternational Journal of Cancer* 81 588–591.

13. Minchiotti G, Parisi S, Liguori G, Signore M, Lania G, Adamson ED, Lago CT & Persico MG 2000 Membrane-anchorage of Cripto protein by glycosylphosphatidylinositol and its distribution during early mouse development. *Mechanisms of Development* 90 133–142.

14. Shen MM, Wang H & Leder P 1997 A differential display strategy identifies *Cryptic*, a novel EGF-related gene expressed in the axial and lateral mesoderm during mouse gastrulation. *Development* 124 429–442.

15. Kinoshita N, Minshull J & Kirschner MW 1995 The identification of two novel ligands of the FGF receptor by a yeast screening method and their activity in *Xenopus* development. *Cell* 83 621–630.

16. Dono R, Montuori N, Ruocchi M, De Ponti-Zilli L, Ciccodicola A & persico MG. Isolation and characterization of the CRIPTO autosomal gene and its X-linked related sequence. Am J Hum Genet. 1991; 118, 1157-1168.

17. Schiffer SG, Foley S, Kaffashan A, Hronowski X, Zichittella AE, Yeo CY, Miatkowski K, Adkins HB, Damon B, Whitman M, Salomon D, Sanicola M, Williams KP 2001 Fucosylation of Cripto is required for its ability to facilitate nodal signaling. *J Biol Chem*.;276(41):37769-78.

18. Foley S.F., Herman W. T. van Vlijmen, Raymond E. Boynton, Heather B. Adkins, Anne E. Cheung, Juswinder Singh, Michele Sanicola, Carmen N. Young and Dingyi Wen 2003 The CRIPTO/FRL-1/CRYPTIC (CFC) domain of human Cripto : Functional and structural insights through disulfide structure analysis, Eur. J. Biochem. 270, 3610–3618.

19. Calvanese L, Saporito A, Oliva R, D' Auria G, Pedone C, Paolillo L, Ruvo M, Marasco D, Falcigno L. 2008 Structural insights into the interaction between the Cripto CFC domain and the ALK4 receptor.J Pept Sci.;15(3):175-83.

20. Calvanese L, Marasco D, Doti N, Saporito A, D'Auria G, Paolillo L, Ruvo M, Falcigno L. 2010 Structural investigations on the Nodal-Cripto binding: a theoretical and experimental approach. Biopolymers. 93(11):1011-21.

21. Adkins HB, Bianco C, Schiffer SG, Rayhorn P, Zafari M, Cheung AE, et al. 2003 Antibody blockade of the Cripto CFC domain suppresses tumor cell growth in vivo. J Clin Invest. ; 112:575–587.

22. Bianco C, Strizzi L, Rehman A, Normanno N, Wechselberger C, Sun Y, Khan N, Hirota M, Adkins H, Williams K, Margolis RU, Sanicola M, Salomon DS 2003 A Nodal- and ALK4-independent signaling pathway activated by Cripto-1 through Glypican-1 and c-Src. Cancer Res.;63(6):1192-7.

23. Gray PC, Harrison CA, Vale W. 2003 Cripto forms a complex with activin and type II activin receptors and can block activin signaling. Proc Natl Acad Sci U S A ;100(9):5193-5198.

24. Yeo C, Whitman M. 2001 Nodal signals to Smads through Cripto-dependent and Cripto-independent mechanisms. Mol Cell.;7(5):949-57.

25. Bianco C, Adkins HB, Wechselberger C, Seno M, Normanno N, De Luca A, Sun Y, Khan N, Kenney N, Ebert A, Williams KP, Sanicola M, Salomon DS 2002 Cripto-1 activates nodal- and ALK4-dependent and -independent signaling pathways in mammary epithelial Cells.Mol Cell Biol.;22(8):2586-97.

26. De la Cruz JM, Bamford RN, Burdine RD, Roessler A, Barkovich AJ, Donnai D,·Schier AF, Muenke M. 2002.A loss-of-function mutation in the CFC domain of TDGF1 is associated with human forebrain defects Hum Genet 110 :422–428.

27. Shani G, Fischer WH, Justice NJ, Kelber JA, Vale W, Gray PC 2008 GRP78 and Cripto form a complex at the cell surface and collaborate to inhibit transforming growth factor beta signaling and enhance cell growth. Mol Cell Biol.;28(2):666-77.

28. Bianco C, Mysliwiec M, Watanabe K, Mancino M, Nagaoka T, Gonzales M, Salomon DS 2008 Activation of a Nodal-independent signaling pathway by Cripto-1 mutants with impaired activation of a Nodal-dependent signaling pathway.FEBS Lett. ;582(29):3997-4002.

29. Watanabe K, Hamada S, Bianco C, Mancino M, Nagaoka T, Gonzales M, Bailly V, Strizzi L, Salomon DS 2007 Requirement of glycosylphosphatidylinositol anchor of Cripto-1 for trans activity as a Nodal co-receptor. J Biol Chem.;282(49):35772-86.

30. Yan YT, Liu JJ, Luo Y, Chaosu E, Haltiwanger RS ,Abate-Shen C,Shen MM 2002 Dual Roles of Cripto as a Ligand and Coreceptor in the Nodal Signaling Pathway MOLECULAR AND CELLULAR BIOLOGY; 22(13): 4439–4449.

31. Shi S , Ge C, Luo Y, Hou X, Haltiwanger RS, and Stanley P 2007 The Threonine That Carries Fucose, but Not Fucose, Is Required for Cripto to Facilitate Nodal Signaling J Biol Chem.;282(28):20133-41.

32. Hu XF, Xing PX 2005 Cripto as a target for cancer immunotherapy. Expert Opin Ther Targets; 9(2):383-94.

33. Bianco C, Strizzi L, Ebert A, Chang C, Rehman A, Normanno N 2005 Role of Human Cripto-1 in Tumor Angiogenesis , J Natl Cancer Inst.;97(2):132-41.

34. D'Aniello, C., Lonardo, E., Iaconis, S., Guardiola, O., Liguoro, A.M., Liguori, G.L., Autiero, M., Carmeliet, P. & Minchiotti, G. (2009). G protein-coupled receptor APJ and its ligand apelin act downstream of Cripto to specify embryonic stem cells toward the cardiac lineage through extracellular signal-regulated kinase/p70S6 kinase signaling pathway. *Circ Res*, 105(3):231-238.

35. Bianco, C., Rangel, M.C., Castro, N.P., Nagaoka, T., Rollman, K., Gonzales, M. & Salomon, D.S. (2010). Role of Cripto-1 in stem cell maintenance and malignant progression. *Am J Pathol*, 177(2):532-540).

36. Watanabe K, Meyera MJ, Strizzi L, Lee JM, Hendrix MJC, Vonderhaara BK, Salomon DS 2010, Cripto-1 Is a Cell Surface Marker for a Tumorigenic, Undifferentiated Subpopulation in Human Embryonal Carcinoma Cells; Stem Cells; 28(8): 1303–1314

37. A De Luca, L Lamura, L Strizzi, C Roma, A D'Antonio, N Margaryan, G Pirozzi1, M-Y Hsu, G Botti, E Mari, MJC Hendrix, DS Salomon and N Normanno 2011, Expression and functional role of CRIPTO-1 in cutaneous melanoma British Journal of Cancer ; 105, 1030 – 1038.

38. Strizzi L, Margaryan NV, Gilgur A, Hardy KM, Normanno N, Salomon DS, Hendrix MJC 2013, The significance of a Cripto-1-positive subpopulation of human melanoma cells exhibiting stem cell-like characteristics; Cell Cycle 12:9,1450–1456.

39. Park KS, Raffeld M, Moon YM, Xi L, Bianco C 2014, CRIPTO1 expression in EGFR-mutant NSCLC elicits intrinsic EGFR-inhibitor resistance, J Clin Invest.;124(7):3003-15.

40. Pilgaard L, Mortensen JH, Henriksen M et al. 2014 Cripto-1 expression in glioblastoma multiforme. Brain Pathol. ; 24(4):360-70.

41. Calvanese L, Sandomenico A, Caporale A, Focà A, Focà G, D'Auria G, Falcigno L, Ruvo M. 2015. Conformational features and binding affinities to Cripto, ALK7 and ALK4 of Nodal synthetic fragments. *J Pept Sci.*In press.

42. Reissmann, E., Jornvall, H., Blokzijl, A., Andersson, O., Chang, C., Minchiotti, G., Persico, M.G., Ibanez, C.F. and Brivanlou, A.H. (2001) The orphan receptor ALK7 and the Activin receptor ALK4 mediate signaling by Nodal proteins during vertebrate development. Genes Dev. 15, 2010–2022.

43. Gray PC, Shani G, Aung K, Kelber J, Vale W. (2006). Cripto binds transforming growth factor beta (TGF-beta) and inhibits TGF-beta signaling. Mol Cell Biol 26: 9268–9278.

44. Xing PX, Hu XF, Pietersz GA, Hosick HL, McKenzie IF. Cripto: a novel target for antibody-based cancer immunotherapy. Cancer Res. 2004; 64:4018–4023.

45. McKenzie, IFC.; Xing, PX.; Hu, XF. Antibodies against cancer. US 0119514. 2010.

46. Nagaoka T, Karasawa H, Castro N, Rangel MC, Salomon DC, Bianco C. 2012 An evolving web of signaling networks regulated by Cripto-1 *Growth Factors,* ; 30(1): 13–21.

47. Kelber, J.A., Panopoulos, A.D., Shani, G., Booker, E.C., Belmonte, J.C., Vale, W.W. & Gray, P.C. 2009. Blockade of Cripto binding to cell surface GRP78 inhibits oncogenic Cripto signaling via MAPK/PI3K and Smad2/3 pathways. Oncogene, 28(24) : 2324-2336.

48. Nagaoka T, Karasawa H, Turbyville T, Rangel MC, Castro NP, Gonzales M,et al.2013 Cripto-1 enhances the canonical Wnt/beta-catenin signaling path-way by binding to LRP5 and LRP6 co-receptors. Cell Signal;25:178–89.

49. Nusse R, Fuerer C, Ching W, Harnish K, Logan C, Zeng A, ten Berge D, Kalani Y. 2008. Wnt signaling and stem cell control. Cold Spring Harb Symp Quant Biol 73:59–66.

50. Bianco C, Kannan S, De Santis M, Seno M, Tang CK, Martinez-Lacaci I,et al. 1999 Cripto-1 indirectly stimulates the tyrosine phosphorylation of erb B-4through a novel receptor. J Biol Chem ;274:8624–9.

51. Hu XF, Li J, Yang E, Vandervalk S, Xing PX. Anti-Cripto Mab inhibit tumour growth and overcome MDR in a human leukaemia MDR cell line by inhibition of Akt and activation of JNK/ SAPK and bad death pathways. Br J Cancer. 2007; 96:918–927.

52. Bianco C & Salomon DS 2010. Targeting the embryonic gene Cripto-1 in cancer and beyond Expert Opin Ther Pat. 20(12): 1739–1749.

53. Sapra P, Hooper AT, O'Donnell CJ, Gerber HP. Investigational antibody drug conjugates for solid tumors.Expert Opin Investig Drugs. 2011;20(8):1131-49.

54. Poljak R. J., Amzel L. M.. Avey H. P., Chen B. L., Phizackerley R. P. and Saul F. 1973Three-dimensional structure of the Fab’ fragment of a human immunoglobulin at 2.8-A resolution. Proc. natn. Acad. Sri. U.S.A. 70, 3305-3310.

55. Poljak R. J., Amzel L. M., Chen B. L., Phizackerley R. P. and Saul F. (1974) The three-dimensional structure of the Fab’ fragment of a human myeloma immunoglobuhn at 2.0-A resolution. Proc. natn. Acad. Sci. U.S.A. 71, 3440-3444.

56. Schiffer M., Girling R. L., Ely K. R. and Edmundson A. B.1973 Structure of a).-type Bence-Jones protein at 3.5-A resolution. Biochemistry 12, 4620-4631.

57. Segal D. M., Padlan E. A., Cohen G. H., Rudikoff S.. Potter M. and Davies D. R. 1974 The three-dimensional structure of a phosphorylcholine-binding mouse immunoglobulin Faband the nature of the antigen binding site. Proc. natn. Acud. Sci. U.S.A. 71, 4298-4302.

58. Feige MJ, Hendershot ML and Buchner J 2009. How antibodies fold Trends in Biochemical Sciences 35(4).

59. Padlan EA. 1994 Anatomy of the antibody molecule Molecular Immunology; 31 (3) 169-217.

60. Pink JR, Milstein C. Inter heavy-light chain disulphide bridge in immune globulins. Nature 1967; 214:92-4.

61. Milstein C, Pink JR. Structure and evolution of immunoglobulins. Prog Biophys Mol Biol 1970; 21:209-63.

62. Frangione B, Milstein C, Pink JR. Structural studies of immunoglobulin G. Nature 1969; 221:145-8.

63. Frangione B, Milstein C, Franklin EC. Intrachain disulphide bridges in immunoglobulin G heavy chains. The Fc fragment. Biochem J 1968; 106:15-21.

64. De Preval C, Pink JR, Milstein C. Variability of interchain binding of immunoglobulins. Interchain bridges of mouse IgG2a and IgG2b. Nature 1970; 228:930-2

65. Salfeld JG. Isotype selection in antibody engineering. Nat Biotechnol 2007; 25:1369-72.

66. Carter PJ. Potent antibody therapeutics by design. Nat Rev Immunol 2006; 6:343-57.

67. Reichert JM, Rosensweig CJ, Faden LB, Dewitz MC. Monoclonal antibody successes in the clinic. Nat Biotechnol 2005; 23:1073-8.

68. Jefferis R, Lefranc M. Human immunoglobulin allotypes. MAbs 2009; 1:1-7.

69. Köhler G, Milstein C: Continuous cultures of fused cells secreting antibody of predefined specificity. Nature 1975; 256: 495–497.

70. Morrison SL, Johnson MJ, Herzenberg LA,Vernont T, 1984; Chimeric human antibody molecules: Mouse antigen-binding domains with human constant region domains; Proc. Nati. Acad. Sci. USA; 81:6851-6855.

71. de la Cruz EMC, Tellers M, Chan C, Salmon P, Robinson DK, Markusen J: Development of transfection and high-producerscreening protocols for the CHOK1SV cell system. Mol Biotechnol 2006; 34: 179–190.

72. Smith GP: Filamentous fusion phage: novel expression vectors that display cloned antigens on the virion surface. Science 1985; 228: 1315–1317

73. Lonberg N 2005. Human antibodies from transgenic animals *Nature Biotechnology* 23, 1117 – 1125.

74. Fujimori K, Covell DG, Fletcher JE, Weinstein JN (1990). A modeling analysis of monoclonal antibody percolation through tumors: a binding-site barrier. J Nucl Med 31: 1191–1198.

75. Roopenian DC, Akilesh S (2007). FcRn: the neonatal Fc receptor comes of age. Nat Rev Immunol 7: 715–725.

76. Chames P, Baty D (2000). Antibody engineering and its applications in tumor targeting and intracellular immunization. FEMS Microbiol Lett 189: 1–8.

77. Ternant D, Paintaud G (2005) Pharmacokinetics and concentrationeffect relationships of therapeutic monoclonal antibodies and fusion proteins. Expert Opin Biol Ther; 5: S37–S47.

78. Yamada T (2010) Therapeutic Monoclonal Antibodies Keio J Med 2011; 60 (2): 37–46.

79. Nimmerjahn F, Ravetch JV (2007). Antibodies, Fc receptors and cancer. Curr Opin Immunol 19: 239–245.

80. Siberil S, Dutertre CA, Boix C, Bonnin E, Menez R, Stura E et al. (2006).Molecular aspects of human FcgammaR interactions with IgG: functional and therapeutic consequences. Immunol Lett 106: 111–118.

81. Scott AM, Wolchok JD & Old LJ 2012. Antibody therapy of cancer *Nature Reviews Cancer* 12, 278-287.

82. Van Cutsem, E. et al. Cetuximab and chemotherapy as initial treatment for metastatic colorectal cancer.N. Engl. J. Med. 360, 1408–1417 (2009).

83. Hudis, C. A. Trastuzumab-mechanism of action and use in clinical practice. N. Engl. J. Med. 357, 39–51 (2007).

84. Weiner, G. J. Rituximab: mechanism of action. Semin. Hematol. 47, 115–123 (2010).

85. Hodi, F. S. et al. Improved survival with ipilimumab in patients with metastatic melanoma. N. Eng. J. Med. 363, 711–723 (2010).

86. Senter, P.D. (2009). Potent antibody drug conjugates for cancer therapy. Current Opinion in Chemical Biology, 13, 235–244.

87. Jones, P. T., P. H. Dear, J. Foote, M. S. Neuberger & G. Winter: Replacing the complementarity-determining regions in a human antibody with those from a mouse. *Nature*., 321, 522-5 (1986).

88. K.J. Hanf, Methods Mol. Biol. 899 (2005) 127–144.

89. Saldhana, J. W.: Molecular Engineering I:Humanization. In: Handbook of therapeutic antibodies. Dubel S. Wiley-VCH, Weinheim (2007).

90. E.A. Padlan, C. Abergel, J.P. Tipper, FASEB J. 9 (1995) 133–139.

91. Hanf KJM et al., Antibody humanization by redesign of complementarity-determining region residues proximate to the acceptor framework Methods 65 (2014) 68–76.

92. C. Chothia, A.M. Lesk, J. Mol. Biol. 196 (1987) 901–917.

93. SV. Kashmiri, M. Iwahashi, M. Tamura, E.A. Padlan, D.E. Milenic, J. Schlom, Crit. Rev. Oncol. Hematol. 38 (2001) 3–16.

94. Riechmann L., M. Clark, H. Waldmann & G. Winter: Reshaping human antibodies for therapy. *Nature*., 332, 323-7 (1988).

95. De Pascalis, R., M. Iwahashi, M. Tamura, E. A. Padlan, N. R. Gonzales, A. D. Santos, M. Giuliano, P. Schuck, J. Schlom & S. V. Kashmiri: Grafting of "abbreviated" complementarity-determining regions containing specificity-determining residues essential for ligand contact to engineer a less immunogenic humanized monoclonal antibody. *J. Immunol*., 169, 3076-84 (2002).

96. Roguska MA, Pedersen JT, Keddy CA, Henry AH et al., 1993. Humanization of murine monoclonal antibodies through variable domain resurfacing. Proc. Nati. Acad. Sci. 91: 969-973,

97. Dall'Acqua WF, Damschroder MM, Zhang J, Woods RM et al., 2005 Antibody humanization by framework shuffling Methods 36 (2005) 43–60.

98. Wu, A. M. & Senter, P. D. Arming antibodies: prospects and challenges for immunoconjugates. *Nature Biotech.* 23, 1137–1146 (2009).

99. Deckert, P. M. Current constructs and targets in clinical development for antibody-based cancer therapy. *Curr. Drug Targets* 10, 158–175 (2009).

100. de Bono, J. S. & Ashworth, A. Translating cancer research into targeted therapeutics.*Nature* 467, 543–549 (2010).

101. Weiner, L. M., Surana, R. & Wang, S. Monoclonal antibodies: versatile platforms for cancer immunotherapy. *Nature Rev. Immunol.* 10, 317–327 (2010).

102. Parham P. On the fragmentation of monoclonal IgG1, IgG2a, and IgG2b from BALB/c mice. J Immunol. 1983 ;131(6):2895-902.

103. Griffin L, Lawson A. Antibody fragments as tools in crystallography. *Clinical and Experimental Immunology*. 2011;165(3):285-291.

104. Ni Y, Chen R. Extracellular recombinant protein production from Escherichia coli. Biotechnol Lett (2009) 31:1661–70.

105. Schmidt FR. Recombinant expression systems in the pharmaceutical industry. Appl Microbio lBiotechnol (2004) 65:363–72.

106. Skerra A, Plückthun A. Assembl of af unctional immunoglobulin Fv fragment in Escherichia coli. Science (1988) 240:1038–41.

107. Better M, Chang CP, Robinson RR, Horwitz AH. Escherichia coli secretion of an active chimeric antibody fragment. Science (1988) 240:1041–3.

108. Inoue Y, Ohta T,Tada H, Iwasa S, Udaka S, Yamagata H. Efficient production of a functional mouse/human chimeric Fab' agains thuman urokinase-typep lasminogen activator by Bacillusbrevis. Appl Microbiol Biotechnol (1997) 48:487–92.

109. Wu SC,Ye R,Wu XC,Ng SC, Wong SL.Enhanced secretory production of a single-chain antibody fragment from Bacillussubtilis byco-production of molecular chaperones. J Bacteriol (1998) 180:2830–5.

110. David F, Westphal R, Bunk B ,Jahn D, Franco-Lara E. Optimization of antibody fragment production in Bacillus megaterium: the role of metal ions on protein secretion. J Biotechnol (2010) 150:115–24

111. Jeong KJ, Jang SH, Velmurugan N. Recombinant antibodies:engineering and production in yeast and bacterial hosts. Biotechnol J (2011) 6:16–27.

112. Daniell H, Streatfield SJ, Wycoff K. Medical molecular farming: production of antibodies, biopharmaceuticals and edible vaccines in plants. *TrendsPlant Sci* (2001) 6:219–26.

113. Frenzel A, Hust M and Schirrmann T 2013 Expression of recombinant antibodies Frontiers in immunology 217 (4):217.

114. Niklas J, Schräder E, Sandig V, Noll T, Heinzle E.Quantita tive characterization of metabolism and metabolic shift sduring growth of the new human cell line AGE1.HN using time resolved metabolic fluxanalysis. *Bioprocess Biosyst Eng* (2011) 34:533–45.

115. Gomord V, Chamberlain P, Jefferis R, Faye L. Biopharmaceutical production in plants: problems, solutions and opportunities. *Trends Biotechnol* (2005) 23:559–65.

116. Holliger P, Hudson PJ (2005). Engineered antibody fragments and the rise of single domains. Nat Biotechnol 23: 1126–1136.

117. Bird RE, Hardman KD, Jacobson JW, Johnson S, Kaufman BM, Lee SM et al. (1988). Single-chain antigen-binding proteins [published rratum appears in Science 1989 Apr 28; 244 (4903): 409]. Science 242: 423–426.

118. Robinson MK, Shaller C, Garmestani K, Plascjak PS, Hodge KM, Yuan QA et al. (2008). Effective treatment of established human breast tumor xenografts in immunodeficient mice with a single dose of the alpha-emitting radioisotope astatine-211 conjugated to anti- HER2/neu diabodies. Clin Cancer Res 14: 875–882.

119. Dooley H, Flajnik MF, Porter AJ (2003). Selection and characterization of naturally occurring single-domain (IgNAR) antibody fragments from immunized sharks by phage display. Mol Immunol 40: 25–33.

120. Fischer N, Leger O (2007). Bispecific antibodies: molecules that enable novel therapeutic strategies. Pathobiology 74: 3–14.

121. Lo AS, Zhu Q, Marasco WA (2008). Intracellular antibodies (intrabodies) and their therapeutic potential. In: Y. Chernajovsky, A. Nissim (Eds) Therapeutic Antibodies. Handbook of Experimental Pharmacology,181:343–373.

122. Boldicke T (2007). Blocking translocation of cell surface molecules from the ER to the cell surface by intracellular antibodies targeted to the ER. J Cell Mol Med 11: 54–70.

123. Stocks M (2006). Intracellular antibodies: a revolution waiting to happen? Curr Opin Mol Ther 8: 17–23.

124. Blick SK, Curran MP (2007). Certolizumab pegol: in Crohn's disease. BioDrugs 21: 195–201. discussion 202–3.

125. Muller D, Karle A, Meissburger B, Hofig I, Stork R, Kontermann RE (2007). Improved pharmacokinetics of recombinant bispecific antibody molecules by fusion to human serum albumin. J Biol Chem 282: 12650–12660.

126. Chames P, Van Regenmortel M, Weiss E and Baty D 2009 Therapeutic antibodies: successes, limitations and hopes for the future British Journal of Pharmacology (2009), 157, 220–233.

127. A.L. Nelson, E. Dhimolea, J.M. Reichert, Development trends for human monoclonal antibody therapeutics, Nat. Rev. Drug Discov. 9 (2010) 767–774.

128. Stephen C Alley, Nicole M Okeley and Peter D Senter 2010 Antibody–drug conjugates: targeted drug delivery for cancer Current Opinion in Chemical Biology 2010, 14:529–537

129. N.K. Damle, P. Frost, Antibody-targeted chemotherapy with immunoconjugates of calicheamicin, Curr. Opin. Pharmacol. 3 (2003) 386–390.

130. Wang L., Amphlett G., Blattler W.A., Lambert J.M., Zhang W. (2005) Structural characterization of the maytansinoid-monoclonal antibody immunoconjugate, huN901-DM1, by mass spectrometry. Protein Sci;14:2436–2446.

131. Sutherland MS, Sanderson RJ, Gordon KA, Andreyka J, Cerveny CG, Yu C, Lewis TS, Meyer DL, Zabinski RF, Doronina SO et al.: Lysosomal trafficking and cysteine protease metabolism confer target-specific cytotoxicity by peptide-linked anti- CD30-auristatin conjugates. J Biol Chem 2006, 281: 10540-10547.

132. Thorpe, P. E.,Wallace, P.M., Knowles, P. P., Relf,M.G., Brown, A. N. F.,Watson, et al. (1987). New coupling agents for the synthesis of immunotoxins containing a hindered disulfide bond with improved stability in vivo. Cancer Res 47:5924-5931.

133. Junutula J.R., Raab H., Clark S., Bhakta S., Leipold D.D., Weir S., Chen Y. et al. (2008) Site-specific conjugation of a cytotoxic drug to an antibody improves the therapeutic index. Nat Biotechnol;26:925–932.

134. A. Fontana, B. Spolaore, A. Mero, F. M. Veronese, Adv. Drug Delivery Rev. 2008, 60, 13 – 28.

135. Casi G., Neri D. (2012) Antibody-drug conjugates: basic concepts, examples and future perspectives. J Control Release;161:422–428.

136. Ducry L., Stump B. (2010) Antibody-drug conjugates: linking cytotoxic payloads to monoclonal antibodies. Bioconjug Chem;21:5–13.

137. C. Schliemann, D. Neri, Antibody-based targeting of the tumor vasculature, BBA: Rev. Cancer 1776 (2007) 175–192.

138. HP. Gerber, P.D. Senter, I.S. Grewal, Antibody drug-conjugates targeting the tumor vasculature. Current and future developments, MAbs 1 (2009) 247–253.

139. Chari R.V.J. (2008) Targeted cancer therapy: conferring specificity to cytotoxic drugs. Acc Chem Res;41:98–107.

140. Scott, a. M. et al. a phase I clinical trial with monoclonal antibody ch806 targeting transitional state and mutant epidermal growth factor receptors. Proc. Natl Acad. Sci. USA 104, 4071–4076 (2007).

141. Lambert JM and Chari RVJ 2014. Ado-trastuzumab Emtansine (T-DM1): An Antibody−Drug Conjugate (ADC) for HER2-Positive Breast Cancer J. Med. Chem., 57, 6949−6964.

142. Chen X, Ding G, Gao Q et al., 2013 A Human Anti-c-Met Fab Fragment Conjugated with Doxorubicin as Targeted Chemotherapy for Hepatocellular Carcinoma PLOS ONE | www.plosone.org (8):5.

143. Comeau SR, Gatchell DW, Vajda S and Camacho CJ 2004. ClusPro: a fully automated algorithm for protein–protein docking Nucleic Acids Research, (32): 96-99.

144. Vangone A, Spinelli R, Scarano V, Cavallo L, Oliva R. 2011. COCOMAPS: a web application to analyze and visualize contacts at the interface of biomolecular complexes. Bioinformatics. 27(20):2915-6.

145. Harlow E. and Lane D. 1988 Antibodies: A Laboratory Manual, Cold Spring Harbor Laboratory: 628-629.

146. Sweeney, P.J., and Walker, J.M. 1993. Enzymes of Molecular Biology, Burrell, M.M.: 290-291.

147. Mariani M, Camagna M, Tarditi L, Seccamani E 1991. A new enzymatic method to obtain high-yield F(ab)2 suitable for clinical use from mouse IgGl. Mol Immunol. 28(1-2):69-77.

148. Uchida, Y. et al.,(1979). J. Biochem., 86, 1573-85.

149. Ichihara-Tanaka, K., *et al.*, (1990) J. Biol. Chem., 265, 401.

150. Liao YD, Jeng JC, Wang CF, Wang SC, Chang ST. Removal of N-terminal methionine from recombinant proteinsby engineered E coli methionine aminopeptidase. Protein Sci 2004;13:1802–10.

151. Mergulhao F, Monteiro G. Secretion capacity limitations of the Sec pathway in Escherichia coli. J Microb. Biotechnol 2004;14:128– 33.

152. Binet R, Letoffe S, Ghigo JM, Delepelaire P, Wandersman C. Protein secretion by Gram-negative bacterial ABC exporters—a review. Gene 1997;192:7 – 11.

153. Fernandez LA, de Lorenzo V. Formation of disulphide bonds during secretion of proteins through the periplasmic-independent type I pathway. Mol Microbiol 2001;40:332– 46.

154. Sapriel G, Wandersman C, Delepelaire P. The N terminus of the HasA protein and the SecB chaperone cooperate in the efficient targeting and secretion of HasA via the ATP-binding cassette transporter. J Biol Chem 2002;277:6726– 32.

155. Piccart-Gebhart MJ, Procter M et al., Trastuzumab after Adjuvant Chemotherapy in HER2-Positive Breast Cancer.N Engl J Med 2005;353:1659-72.

156. A. Fontana, B. Spolaore, A. Mero, F. M. Veronese, Adv. Drug Delivery Rev. 2008, 60, 13 – 28.

157. http://zedira.com/Assays-and-substrates.

158. http://www.drugbank.ca/drugs/db00997.

159. Nose M, Wigzell H. 1983 Biological significance of carbohydrate chains on monoclonal antibodies. Proc Natl Acad Sci U S A.;80(21):6632-6.

160. Kohler G, HengaAner, H, and Schulman, MJ. 1978Eur: J. Immunol. 8, 82-88.

161. Kim HH, Yamaguchi Y, Masu K et al., 1994. 0-Glycosylation in Hinge Region of Mouse Immunoglobulin G2b JBC 269 (16):12345-12350.

162. Vermeer AWP, Norde W and van Amerongen A 2000. Biophysical Journal 79:2150-2154.

163. Caporale A, Selis F, Sandomenico A, Jotti GS, Tonon G and Ruvo M. (2014) The LQSP tetrapeptide is a new highly efficient substrate of microbial transglutaminase for the site-specific derivatization of peptides and proteins.Biotechnol. J. 2015, 10, 154–16.

164. Marasco D, Saporito A, Ponticelli S, Chambery A, De Falco S, Pedone C, Minchiotti G, Ruvo M. Chemical synthesis of mouse cripto CFC variants. Proteins. 2006 15;64(3):779-88.

165. Calvanese L, Saporito A, Marasco D, D'Auria G, Minchiotti G, Pedone C, Paolillo L, Falcigno L, Ruvo M. 2006 J Med Chem.;49(24):7054-62.

ABBREVIATIONS

Abs: Absorbance
ABTS: 2,2-Azino-bis(3-ethylbenzothiazoline-6-sulfonic acid)
amu: Atomic mass unit
APS: Ammonium persulfate
bp: base pair
BSA: Bovine serum albumin
CD: Circular dichroism
cDNcA: complementary DNA
CDR: Complemetarity determining region
CM5: Carboxy-methylated dextran sensor chip
DIEA: N,N-Diisopropylethylamine
DMEM-F12: Dulbecco’s modified eagle medium-F12
DMF: Dimethylformamide
DMSO:Dimetilsulphoxide
DTT: Dithiothreitol
ECL: Enhanced Chemiluminescence
EDC: 1-Ethyl-3-(3-dimethylaminopropyl)carbodiimide
EDTA: Ethylenediaminetetraacetic acid
ELISA: Enzyme linked immunosorbent assay
Fab: Fragment antigen-binding
FACS: Fluorescence-activated cell sorting
Fc: Fragment Cystallizable
Fmoc: Fluorenylmethyloxycarbonyl chloride
FPLC: Fast Protein Liquid Chromatography
GAM-HRP: Goat anti mouse-Horseradish peroxidase
GAR-HRP: Goat anti rabbit-Horseradish peroxidise
h: hours
HATU: 1-[Bis(dimethylamino)methylene]-1H-1,2,3-triazolo[4,5-b]pyridinium 3-oxid hexafluorophosphate
hCFC: Human Cripto_Frl-1_Cryptic *domain*
HEPES: 4-(2-hydroxyethyl)-1-piperazineethanesulfonic acid
HIC: Hydrophobic Interaction Chromatography
HPLC: High performance liquid chromatography
IgG: Immunoglobulin G
kDa: kiloDalton
kbp: kilobase pair
KLH: Keyhole Hemocyanin Limpet
LC-ESI-TOF-MS: Liquid Chromatography-Electron Spray Ionization-Time of flight-Mass Spectrometry
mAb: Monoclonal antibody
MBHA: resin 4-Methylbenzhydrylamine Hydrochloride Salt Resin
min: minutes
MOPS: 3-Morpholinopropanesulfonic acid
M-TGase: Microbial Transglutaminase
MW: Molecular Weight
NaAc: Sodium Acetate
NFDM: Not Fat Dry Milk
NHS: N-hydroxysuccinimide ester
OD: Optical Density
o.n.: overnight
OPD: o-Phenylenediamine dihydrochloride
OPTI-4-CN: 4-Chloro-1-naphthol
PBS: Phosphate-Buffered Saline
PBS-T: Phosphate-Buffered Saline-Tween20
PDA: Photodiode Array
PEG: Polyetilen gycole

PVDF: Polyvinylidene fluoride
psi: pound per square inch
*rh*ALK4: recombinant human ALK4
*rh*CR-1: Recombinant human Cripto-1
*rm*Cr-1: Recombinant mouse Cripto-1
RP-HPLC: Reverse phase-high performance liquid chromatography
rpm: Revolutions per minute
r.t.: room temperature
RT-PCR: Reverse transcriptase-Polymerase chain reaction
RU: Resonance Unit
SDS: Sodium Dodecyl Sulphate
SDS-PAGE: Sodium Dodecyl Sulphate - PolyAcrylamide Gel Electrophoresis
SEC: Size-exclusion chromatography
SE-HPLC: Size exclusion- high performance liquid chromatography
SPR: Surface Plasmon Resonance
TBE: Tris-Borate-EDTA buffer
TBS-T: Tris-Buffered Saline-Tween20
TEMED: Tetramethylethylenediamine
TFA: Trifluoroacetic Acid
TIS: Triisopropylsilane
U/ml: Unit/ml
UV: ultraviolet
- β: without β-Mercaptoethanol
+β: with β-Mercaptoetanol

APPENDIX

Throughout my PhD programme I also gave contribution to the following publications:

1. Conformational features and binding affinities to Cripto, ALK7 and ALK4 of Nodal synthetic fragments. Calvanese L, Sandomenico A, Caporale A, Focà A, Focà G, D'Auria G, Falcigno L, Ruvo M. *J Pept Sci*. 2015 (4):283-93. doi: 10.1002/psc.2733.

2. Design, Synthesis and Structural analysis of cyclopeptides against VEGF-Receptor
Caporale, G. Focà, N. Doti, A. Sandomenico and M. Ruvo. *Proceedings of the 23rd American Peptide,* Michal Lebl (Editor), American Peptide Society 2013.

3. A comparative structural and bioanalytical study of IVIG clinical lots.
A. Sandomenico, V.Severino, A. Chambery, A. Focà, G. Focà, C. Farina, M. Ruvo. *Molecular Biotechnology,* 54(3):983-95. doi: 10.1007/s12033-013-9655-7.

Research Article

Journal of PeptideScience

Received: 9 October 2014 Revised: 3 December 2014 Accepted: 3 December 2014

(wileyonlinelibrary.com) DOI 10.1002/psc.2733

Conformational features and binding affinities to Cripto, ALK7 and ALK4 of Nodal synthetic fragments

Luisa Calvanese,[a] Annamaria Sandomenico,[a,b] Andrea Caporale,[a] Annalia Focà,[c,d] Giuseppina Focà,[c,d] Gabriella D'Auria,[a,b,c] Lucia Falcigno[a,b,c]* and Menotti Ruvo[a,b]*

Nodal, a member of the TGF-β superfamily, is a potent embryonic morphogen also implicated in tumor progression. As for other TGF-βs, it triggers the signaling functions through the interaction with the extracellular domains of type I and type II serine/threonine kinase receptors and with the co-receptor Cripto. Recently, we reported the molecular models of Nodal in complex with its type I receptors (ALK4 and ALK7) as well as with Cripto, as obtained by homology modeling and docking simulations. From such models, potential binding epitopes have been identified. To validate such hypotheses, a series of mutated Nodal fragments have been synthesized. These peptide analogs encompass residues 44–67 of the Nodal protein, corresponding to the pre-helix loop and the H3 helix, and reproduce the wild-type sequence or bear some modifications to evaluate the hot-spot role of modified residues in the receptor binding.

Here, we show the structural characterization in solution by CD and NMR of the Nodal peptides and the measurement of binding affinity toward Cripto by surface plasmon resonance. Data collected by both conformational analyses and binding measurements suggest a role for Y58 of Nodal in the recognition with Cripto and confirm that previously reported for E49 and E50.

Surface plasmon resonance binding assays with recombinant proteins show that Nodal interacts *in vitro* also with ALK7 and ALK4 and preliminary data, generated using the Nodal synthetic fragments, suggest that Y58 of Nodal may also be involved in the recognition with these protein partners. Copyright © 2014 European Peptide Society and John Wiley & Sons, Ltd.

Additional supporting information may be found in the online version of this article at the publisher's web site.

Keywords: SPR, Nodal; peptides; NMR; TGF-beta

Introduction

Nodal belongs to the transforming growth factor-β (TGF-β) superfamily and plays essential roles in regulating embryonic development [1] and cell fate determination [2,3]. As with other growth factors, its late re-expression in adult tissues contributes to tumor development and progression. Nodal overexpression is indeed implicated in tumorigenesis, metastasis and cancer vascularization and has been associated to various cancers [4], including ovarian [5], pancreatic [6,7], endometrial [8], breast [9–11], prostate [12,13], testicular [14], brain [15,16], colon [17], melanoma [18,19] and hepatocellular carcinoma [20]. Because the TGF-β roles in tumorigenesis frequently reflect their function in embryonic development, in the current literature, their signaling pathways are observed with a special regard as possible therapeutic targets [10,16,21–24]. The overexpression of Nodal in numerous cancers, as well as its low abundance in normal tissues, makes Nodal a potential biomarker or antitumor target. In order to achieve this goal, many efforts have been made to fully understand how Nodal works in both normal and neoplastic conditions [4].

As for other TGF-βs, Nodal triggers the signaling functions through the interaction with the extracellular domains (ECD) of type I and type II serine/threonine kinase receptors. In particular, Nodal can signal via ActRIIB type II receptor and ALK7 or ALK4 type I receptors [25,26]. Effective signaling through ALK4 requires the

---

* *Correspondence to: Lucia Falcigno, Dipartimento di Farmacia, Università degli Studi di Napoli 'Federico II', via Mezzocannone 16, 80134, Napoli, Italy. E-mail: lucia.falcigno@unina.it*

Menotti Ruvo, Istituto di Biostrutture e Bioimmagini del CNR, via Mezzocannone, 16, 80134, Napoli, Italy. E-mail: menotti.ruvo@unina.it

a *CIRPeB, University of Naples Federico II, via Mezzocannone, 16, 80134 Napoli, Italy*

b *Istituto di Biostrutture e Bioimmagini del CNR, via Mezzocannone, 16, 80134 Napoli, Italy*

c *Dipartimento di Farmacia, University of Naples Federico II, via Mezzocannone, 16, 80134 Napoli, Italy*

d *Bioker Multimedica, via P. Castellino, Napoli, 111 Italy*

Abbreviations: *ActRIIB, activin type II receptor B; ACN, Acetonitrile; ALK, activin receptor-like kinase; CD, Circular Dichroism; ECD, extracellular domain; EDC, 1-Ethyl-3-(3-dimethylaminopropyl)carbodiimide; DMF, Dimethylformamide; DCM, Dichloromethane; DIEA, Di-isopropylethylamine; HATU, 1-[Bis(dimethylamino)methylene]-1H-1,2,3-triazolo[4,5-b]pyridinium 3-oxid hexafluorophosphate; HOBt, N-hydroxybenzotriazole; HPLC, High Performance Liquid Chromatography; LC-MS, Liquid Chromatography Mass Spectrometry; MeOH, Methanol; HOSu, N-Hydroxysuccinimide; rh, recombinant human; SPR, Surface Plasmon Resonance; TFA, Trifluoroacetic acid; TFE, Trifluoroethanol; TFE-d_3, 2,2,2-deuterated trifluoroethanol; TGF-β, transforming growth factor-β; TIS, Tri-isopropylsilane.*

additional interaction of Nodal with the co-receptor Cripto [27]. Cripto is a membrane protein bound to the extracellular surface via glycosylphosphatidylinositol linkages [28]. It belongs to the Epidermal Growth Factor - Cripto_FRL-1_Cryptic (EGF-CFC) family and contains two cysteine-rich domains: the EGF-like domain, highly homologous to epidermal growth factor domains, and the prototypical CFC domain. Both domains are compact structural modules held together by three disulfide bridges and likely further stabilized by reciprocal interactions. Cripto is required for the formation of the multimeric complex involving Nodal and the ALK4/ActRIIB receptors. Indeed, Cripto binds ALK4 by means of its CFC domain while it interacts with Nodal via the EGF-like domain [27] (Figure 1). It is worth remembering that Nodal is absent in most normal adult tissues, but, like its cognate co-receptor Cripto, is expressed in many different tumors where they potently promote cell proliferation and growth through the phosphorylation of Smads [4]. These findings make the Nodal–Cripto signaling pathway a very attractive target for tumor therapy [24]. Indeed, many efforts are currently made to develop specific Nodal inhibitors, mostly antibodies, which can interfere with one of the several interactions established by Nodal with Cripto or with ALK7 and efficiently interrupt the downstream Smad signaling [4]. Several groups have proposed anti-Nodal antibodies that potentially target its interaction with Cripto and block tumor growth in models of metastatic melanoma cells [29]. However, developing effective and selective inhibitors remains a very challenging task in absence of a more comprehensive view of the network of interactions established by these proteins and, more importantly, in absence of a detailed understanding of the structural features underlying mutual recognition. For these purposes, we have investigated the structural aspects underpinning the Nodal–Cripto binding and have reported the first molecular models of Nodal in complex with its receptors [30,31].

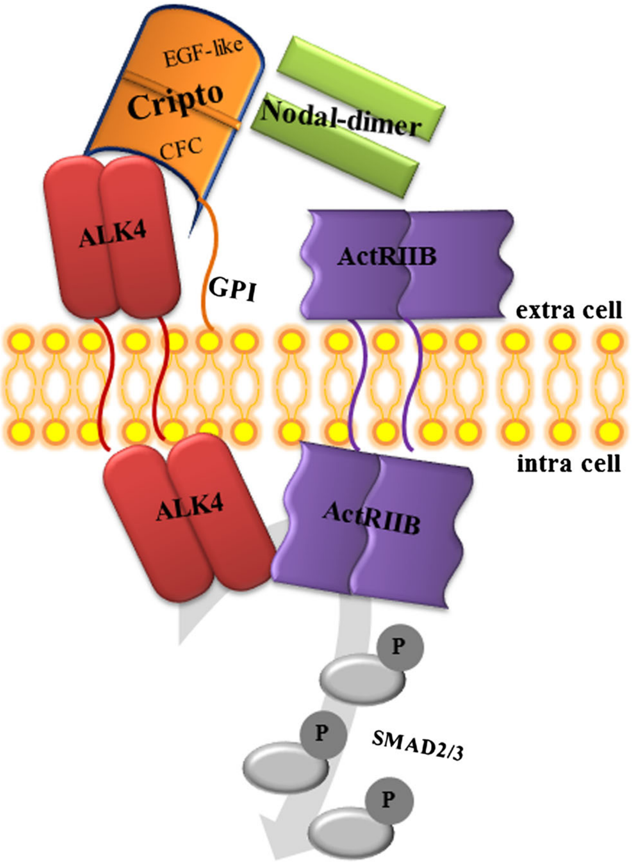

Figure 1. Schematic representation of ALK4/Cripto/Nodal/ActRIIB complex.

Nodal is a homodimer consisting of two subunits, each with three disulfide bonds, linked by an additional inter-chain covalent disulfide bond, highly conserved in the TGF-β superfamily [32] . The homology model of Nodal, we previously reported [30], shows the canonical, symmetric and elongated TGF-β topology (Figure 2). Each Nodal monomer is characterized by two pairs of antiparallel β-strands stretching out from the cysteine core-like fingers and by an α-helix (H3 helix). The typical curvature of these fingers creates concave and convex surfaces, namely wrist and knuckle regions, which enable the interaction of Nodal with type I and type II receptor binding epitopes, respectively. In particular, to the wrist region participate, the inner concave surface of the fingers of one monomer and the α-helix (H3 helix) and the pre-helix loop of the other monomer [33–35].

The molecular models of Nodal in complex with the ECDs of its type I receptors (ALK4 and ALK7), as well as with Cripto, were obtained by homology modeling and docking simulations. Also, potential binding epitopes were identified [30,31]. These comprise residues belonging to the Nodal wrist region. To validate such hypothesis, a series of new Nodal fragments has been now designed and synthesized. This series includes peptides from the pre-helix loop and the H3 helix of Nodal (residues 44–67) (Figure 2), and bears some mutations that will help to evaluate the role of selected hot spots in receptors binding, as discussed in the Results section.

Peptides have been synthesized, and their conformational features have been analyzed in solution by CD and NMR. To evaluate their binding affinity toward ALK4 and ALK7 receptors, as well as toward Cripto co-receptor, surface plasmon resonance (SPR) assays have been carried out. Also, a comparative binding analysis of Nodal to the ECD of recombinant human *rh*Cripto, *rh*ALK4 and *rh*ALK7 has been performed to assess that the reagents used are fully active in terms of recognition and that interacting surfaces are properly exposed.

The set of data, resulting from conformational analyses and binding measurements, provide useful information that confirms the reliability of the theoretical models. On these grounds, the design of new molecules, acting as antagonists in the Nodal-receptors complex formation, can be improved with the outlook to their therapeutic and diagnostic applications.

Materials and Methods

Reagents

Reagents for peptide synthesis were from Novabiochem (Laufelfingen, Switzerland), Inbios (Napoli, Italy) and GL Biochem (Shanghai, China). Solvents for peptide synthesis and purification, including ACN, DMF, DCM and MeOH were from Romil (Dublin, Ireland). Recombinant proteins were purchased from R&D system (MN, USA).

Peptides Synthesis and Purification

Peptides were prepared by stepwise solid-phase synthesis as C-terminally amidated molecules following standard Fmoc chemistry protocols. To increase the polypeptide's stability, the N-terminal and C-terminal ends were acetylated and amidated, respectively. A Rink-amide resin (substitution 0.53 mmol/g) and amino acid derivatives with standard protections were used in the synthesis [36]. The syntheses were performed under

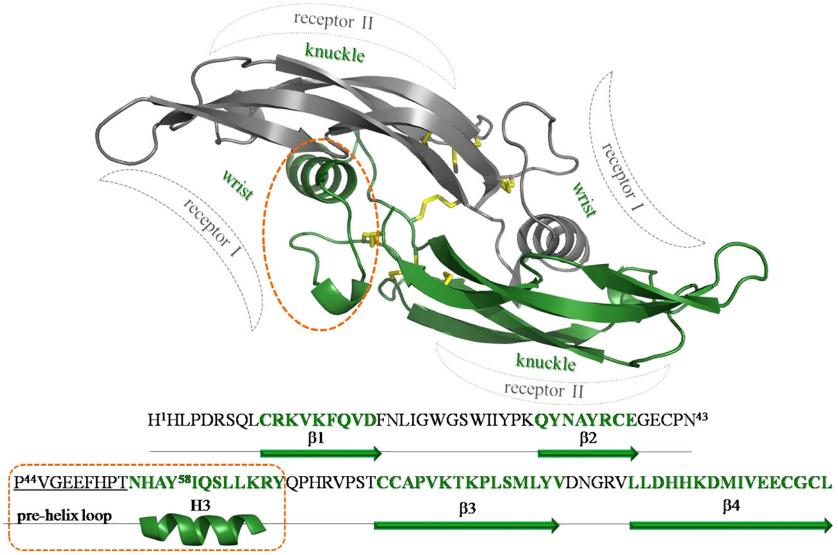

Figure 2. Ribbon representation of Nodal dimer model, with the two monomers colored in green and gray, respectively. The disulfide bridges are shown as yellow sticks. The Nodal wrist and knuckle regions, responsible for the binding to the type I and II receptors, are schematically indicated. At the bottom, both the primary and secondary structures of the Nodal monomer are reported. The Nodal fragment selected in this study is circled in orange.

canonical conditions of peptide synthesis (HATU/DIEA preactivation, fivefold excess of Fmoc-protected amino acids). Coupling and deprotection times were kept at 30 and 20 min, respectively. Finally, N-terminal acetylation was performed on the resin using acetic anhydride at 0.5 M in DMF with 5% DIEA, 20 min at room temperature. The cleavage of peptides from the solid support was performed by treatment with a TFA/TIS/water (90 : 5 : 5, v/v/v) mixture for 3 h at room temperature, affording the crude peptides after precipitation in cold diethylether. The precipitates were dissolved in water and were lyophilized. Products were purified to homogeneity by RP-HPLC using an ONYX monolithic C18 column (100 × 10 mm ID) applying a linear gradient of 0.05% TFA in ACN from 5% to 70% over 10 min (flow rate 20 mL/min). The purity and integrity of all peptides were estimated by LC-MS analyses using an LCQ mass spectrometer (ThermoFisher, Milano, Italy) coupled to a Surveyor system HPLC or an HCT Ultra ESI Ion Trap mass spectrometer (Bruker), coupled to a Waters Alliance HPLC system (Milford, MA, USA). LC-MS analyses were performed under conditions standardized for the detection of peptides in the positive mode. Typical gradients applied to elute the peptides were as follows: flow 0.2 mL/min; gradients from 5% solvent B (ACN, 0.05% TFA) to 70% solvent B in 10 min. Solvent A was H_2O, 0.08% TFA. Biobasic C18 50 × 2 mm ID columns (ThermoFisher, Milano, Italy) were used to separate peptides during LC-MS analyses.

Peptides were all prepared in amounts sufficient for the CD and NMR analyses and for the binding assays. Purities were $>95\%$ as determined by LC-MS analysis (Table 1).

Circular Dichroism Analysis

All CD analyses were performed using a JASCO J-710 spectropolarimeter (Halifax, Canada), equipped with a Peltier system for changing the temperature in a controlled way and quartz cuvettes 110-QS with 1.0 mm path length. Experiments were performed in 10 mM phosphate, pH 8.0 at a concentration of 0.5×10^{-5} M. In addition, spectra in the same buffer with added 20% of TFE were collected to increase the α-helix structure.

Spectra were collected within the wavelength range 250–190 nm at a scan rate of 50 nm/min, with a data pitch of 0.2 nm, a bandwidth of 1 nm and a response time of 4 s.

On every sample, five independent spectra were recorded, averaged and smoothed using the Spectra Manager software, version 1.53 (Easton, MD, USA). Buffer scans were recorded under the same conditions and subtracted.

NMR Analysis

NMR characterization of Nodal fragments was performed in a water/deuterated trifluoethanol TFE-d_3/H_2O 20 : 80 (v/v) mixture at 298 K. Samples were prepared by dissolving weighted amounts of each peptide in water (spectroscopic purity) and adding TFE-d_3 (Sigma-Aldrich Chemicals, St. Louis, MO, USA, 99.9% D) up to a final ratio of 80/20 v/v. Final concentrations were about 3 mM.

One-dimensional and two-dimensional NMR spectra were acquired on a Varian Inova spectrometer (Agilent Technologies, Palo Alto, California, USA), operating at a proton frequency of 500 MHz,

Table 1. Sequences of Nodal fragments investigated in this study

Peptide name	Sequence	Molecular Weight theor.	Molecular Weight exp.
Nodal[44-67]	Ac-PNPVGEEFHPTNHAYIQSLLKRYQ–NH_2	2880.2	2880.0
Nodal[44-67]EE-AA	Ac-PNPVGAAFHPTNHAYIQSLLKRYQ–NH_2	2764.1	2764.2
Nodal[44-67]PV-AA	Ac-PNAAGEEFHPTNHAYIQSLLKRYQ–NH_2	2826.1	2826.6
Nodal[44-67]Y-A	Ac-PNPVGEEFHPTNHAAIQSLLKRYQ–NH_2	2788.1	2788.2

located at the 'Centro Interdipartimentale di Metodologie Chimico-Fisiche (CIMCF)' of the University Federico II of Naples. Two-dimensional (2D) experiments, such as total correlation spectroscopy (TOCSY) [37], nuclear Overhauser effect spectroscopy (NOESY) [37], and double quantum-filtered correlated spectroscopy (DQFCOSY) were recorded by the phase-sensitive States-Haberkorn method [38]. The data file generally consisted of 512 and 2048 (4096 for DQFCOSY) data points in the ω1 and ω2 dimensions, respectively. TOCSY experiments were acquired with a 70 ms mixing time, while NOESY experiments were acquired with 300 ms mixing time. The water resonance was suppressed by using gradients [37]. Chemical shifts were referred to internal sodium 3-(trimethylsilyl) propionate 2,2,3,3-d_4.

Spectra were analyzed by using the CARA program [39,40]. Proton sequential assignments of the amino acid spin systems are reported as Supporting Information (Tables S1–S3). NOE intensities, evaluated by integration of cross-peaks in the 300 ms NOESY spectra, were converted into inter-proton distances by use of the CALIBA program [41]. Geminal protons were chosen as reference with a distance of 2.2 Å.

Computational Methods

Structure calculations for Nodal[44-67], Nodal[44-67]EE-AA and Nodal[44-67]Y-A started from 100 randomized conformers and used the standard CYANA-simulated annealing schedule [42] with 20 000 torsion angle dynamics steps per conformer. Three-dimensional structures were obtained by using inter-proton distances evaluated from NOEs as upper limits without the use of stereospecific assignments. All the conformers showed a fair agreement with experimental constraints showing no violations. The 40 conformers with the lowest final CYANA target function (TF) [43] values (TF average value = 0.42 ± 0.12 Å^2, 4.02E-02 ± 3.03E-02 Å^2, and 4.41E-02 ± 4.40E-02 Å^2 for Nodal[44-67], Nodal [44-67]EE-AA and Nodal[44-67]Y-A, respectively; mean global backbone RMSD = 3.51 ± 0.97 Å, 3.15 ± 0.65 Å, and 3.44 ± 0.69 Å for Nodal[44-67], Nodal[44-67]EE-AA and Nodal[44-67]Y-A) were subjected to restrained energy minimization by use of the SANDER module of the AMBER 6.0 package [44].

The 40 minimized structures were subjected to the program CHIMERA [45] that divided them, based on structural similarity (RMSD < 0.5), into 7 clusters for Nodal[44-67], 7 clusters for Nodal [44-67]EE-AA and 6 clusters for Nodal[44-67]Y-A. The structures present in the first cluster (13 for Nodal[44-67], 17 for Nodal [44-67]EE-AA and 12 for Nodal[44-67]Y-A) were chosen as representative of the conformational space accessible to the peptide. The molecular graphics program MOLMOL [46] was employed to perform the structural statistics analysis. Statistical data are reported as Supporting Information (Tables S4 and S5).

SPR Analyses

All analyses were performed on a Biacore 3000 instrument from GE Healthcare (Little Chalfont, UK) using certified HEPES Buffered Saline (HBS) buffer (20 mM Hepes, 0.15 M NaCl, pH 7.2, P20 at 0.005%), at 25 °C.

Human ALK4 (*rh*ALK4-ECD) and ALK7 (*rh*ALK7-ECD) and Cripto (*rh*Cripto) recombinant proteins were purchased from R&D system. Proteins immobilization was carried out on the flow cells of CM5 sensor chips at 5.0 μg/mL following the canonical EDC/HOSu (amine coupling) method, operating at 5 μL/min. In detail, human ALK7-ECD bearing as fusion protein Fc fragment human and Cripto recombinant proteins were efficiently immobilized in NaAc pH = 4.5. For human ALK4-ECD bearing as fusion Fc fragment and the Fc fragment alone derived from an unrelated IgG1 of the same isotype, the immobilization procedure was performed in sodium acetate (NaAc) pH = 4.0. An underivatized and Fc-derivatized (IgG1) surface were prepared and used as control blank. Analyses were carried out at a flow rate of 20 μL/min, injecting a constant volume of 60 μL of peptides solutions at concentrations ranging between 0.1 and 1.0 mM. Regenerations were performed by injecting 20 μL of a solution of 10 mM glycine, pH 2.7. The proteins were immobilized at a similar level (around 3000 RU), using the wizard procedure. All binding experiments were performed at 20 μL/min with a total contact time of 180 s (60 μL injected for every run) and the samples opportunely diluted in the HBS running buffer. For every single analysis, experimental sensorgrams were aligned, subtracted of blank signals and overlapped. The binding of synthetic peptides to ALK4, ALK7 and to Cripto was performed by injecting peptide solutions (60 μL injected for every run) at increasing concentrations, between 25 μM and 1 mM. All mathematical manipulations and fitting were performed using the BIA evaluation software, version 4.1 from GE Healthcare.

Results

Peptide Preparation

All peptides were obtained in yields ranging from about 20–30%. After purification, homogeneous products were isolated. Molecular weights were consistent with the expected values as assessed by LC-MS analyses (Table 1).

Binding of Nodal to the Immobilized Receptors

Before testing the binding of synthetic peptides to the different receptors, we first probed whether the interaction of full-length Nodal was productive under the chosen experimental conditions. To this end, we injected the recombinant protein at increasing concentrations over the three channels where the proteins were immobilized. As shown in Figure 3, Nodal binds in a dose-dependent manner to both Cripto and ALK7 and exhibiting K_Ds of 5.8 nM and 1.6 nM, respectively (Table 2). These values were indicative of very strong interactions and suggested that protein surfaces required for interaction were properly and well exposed. Surprisingly, Nodal was found to bind with high affinity (1.8 nM, Table 2) also the immobilized ALK4 (Figure 3B). That result was unexpected because, according to the accepted literature, Nodal/ALK4 binding occurs *in vivo* only in the presence of the co-receptor Cripto.

Computational Analysis

Through a computational analysis of the complex containing ALK4/Cripto/Nodal (Figure 4), and ALK7/Nodal (Figure 5), obtained by homology modeling and docking simulations [30], we identified Nodal residues potentially involved in the interaction with Cripto and ALK7.

In the ternary complex containing ALK4/Cripto/Nodal (Figure 4), the EGF-like domain of Cripto was predicted to form, with G87, T88, N79, T82 and G92 residues, a polar groove in which Nodal Y58 can pocket. Furthermore, favorable electrostatic interactions are observed between E49 and E50 lying on the pre-helix loop of Nodal and the Cripto R80 residue [30].

In the ALK7/Nodal complex (Figure 5), the binding is driven by hydrophobic interactions and hydrogen bonds. Of note, major

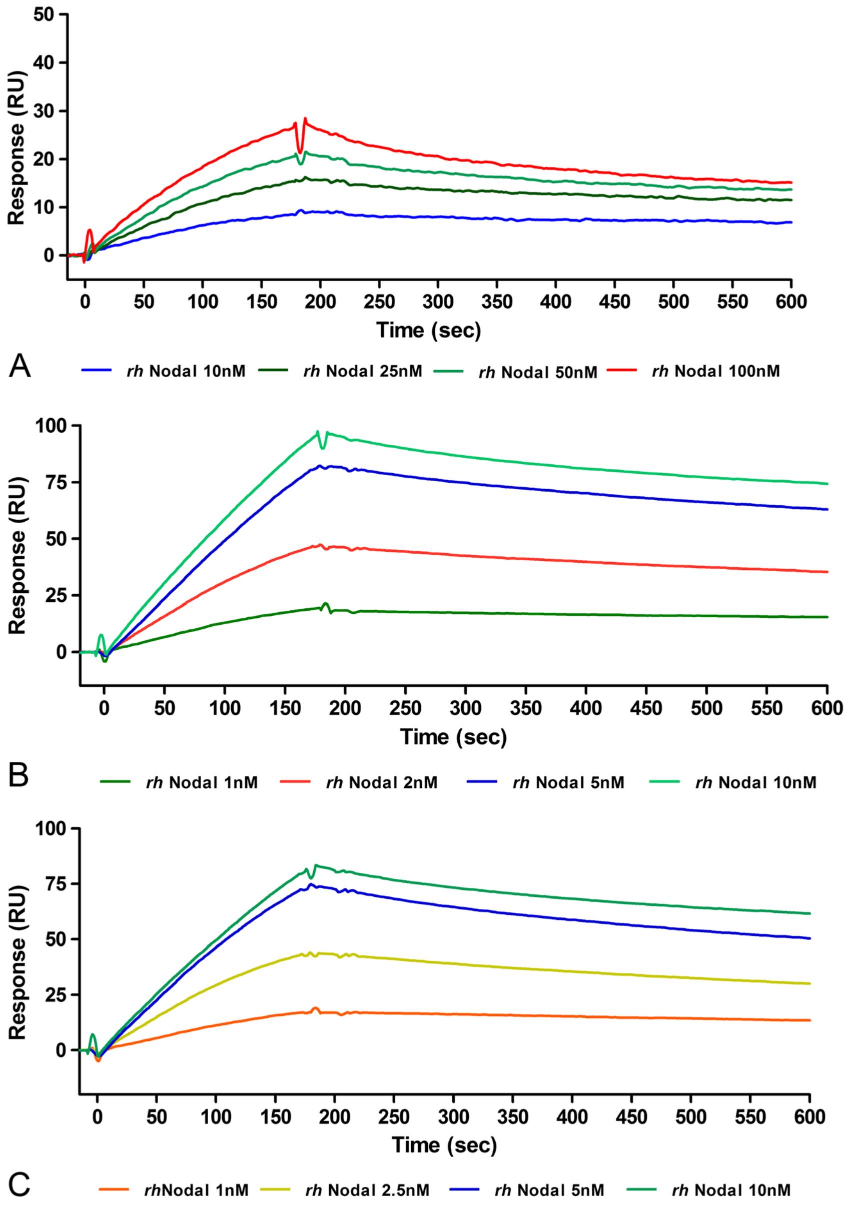

Figure 3. SPR dose–response binding sensorgrams between *rh*Nodal and (A) *rh*Cripto; (B) *rh*ALK4-ECD; and (C) *rh*ALK7-ECD, immobilized on CM5 sensor chips.

Table 2. K_Ds, K_as and K_ds for the interaction of soluble Nodal with the ECD of Cripto, ALK7 and ALK4

	K_D (M)	K_a (1/Ms)	K_d (1/s)
Cripto	$5.79 * 10^{-9}$	$3.20 * 10^{5}$	$6.11 * 10^{-4}$
ALK7	$1.58 * 10^{-9}$	$1.48 * 10^{6}$	$7.68 * 10^{-4}$
ALK4	$1.82 * 10^{-9}$	$1.49 * 10^{6}$	$5.80 * 10^{-4}$

binding interactions are driven by a single Nodal monomer and the residues involved belong to the α-helix H3 (Y58 and L62) and pre-helix loop of Nodal (P46 and V47) and to loop 23 of ALK7 (V51 and F52) [30].

In a previous study, we demonstrated that the entire 43–69 sequence of Nodal, encompassing the α-helix H3 and pre-helix loop region, is able to bind to Cripto, while peptides reproducing the helix H3 alone do not. Moreover, the substitution of the E49 and E50 pre-helix loop residues with alanine negatively affects the binding to Cripto, confirming their involvement in the interaction [30].

On this basis, we have now designed a set of Nodal-derived peptides comprising residues 44–67, still reproducing the helix H3 and pre-helix loop region of the protein but shorter than the first published ones [30] (Table 2). Indeed, the N-terminal cysteine (C43) and the C-terminal proline (P68) and histidine (H69) have been removed as not influencing the peptide structural and binding properties.

Single or double point Ala-mutated peptides have been synthesized, purified and characterized by mass spectrometry together with the unmodified molecule. A structural characterization by NMR and circular dichroism has been then carried out in the attempt of correlating binding and structural data. Binding to Cripto, ALK4 and ALK7 receptors has been analyzed for all the peptides by SPR assays.

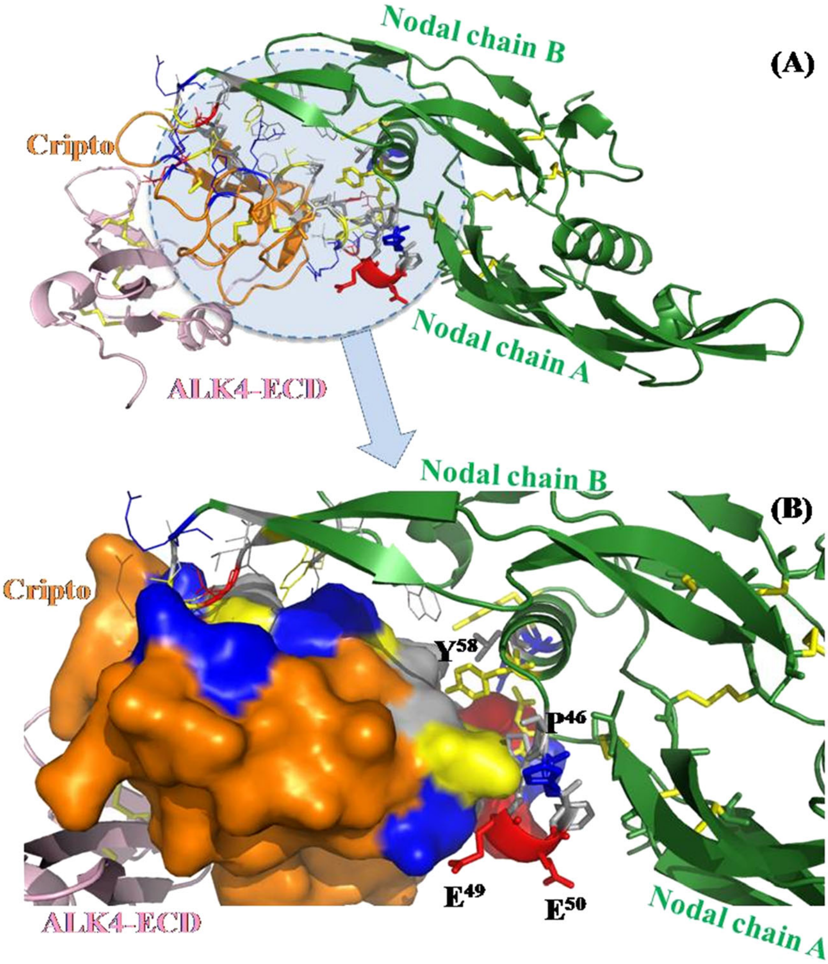

Figure 4. (A) Cartoon representation of the Nodal (green)/Cripto (orange)/ALK4-ECD (pink) complex model. (B) Cripto co-receptor is represented as Connolly surface (orange). Residues at the binding interface are colored by type.

Nodal[44-67] reproduces the 44–67 region of native human Nodal, while the first mutant, Nodal[44-67]EE-AA, bears Ala residues in place of E49 and E50; it was designed and prepared to confirm the role of the two acidic residues in the binding with Cripto [30] and a potential involvement in the interaction with ALK receptors. In the second mutant, Nodal[44-67]PV-AA, the P46 and V47 residues were replaced with alanines to verify the influence of the two hydrophobic residues of the pre-helix loop in the binding to Cripto and to ALKs. In the last mutant, Nodal[44-67]Y-A, the Y58 residue was substituted by alanine. Indeed, by analyzing the ALK7/Nodal [31] and ALK4/Cripto/Nodal molecular complexes, Y58 should be one of the residues mostly involved in the binding with the Nodal helix H3.

CD and NMR of Nodal Fragments

As shown, CD spectra (Figure 6) of peptides analyzed at 20° C in H_20 or buffer exhibited a negative band at 201 nm, typical of random coil structures. However, in presence of TFE, 20% all peptides adopted α-helical structures as suggested by the two negative bands at 207 nm and 223 nm and a positive band at 192 nm.

NMR characterization of Nodal fragments (Nodal[44-67], Nodal[44-67]EE-AA and Nodal[44-67]Y-A) was performed in a trifluoethanol/water TFE-d_3/H_2O 20 : 80 (v/v) mixture at 298 K.

Proton assignment was carried out with the procedure suggested by Wuthrich [47], and the chemical shifts are reported in Tables S1–S3 of the Supporting Information.

Negative deviations of the αCH proton chemical shift of each residue from random coil values [48] are observed for all the peptides from Y58 to R65 residues, indicating the presence of helical structures in this region (see Figure S1 of the Supporting Information). Positive deviations observed in the remaining parts suggest extended conformations.

These structural diagnoses were consistent with the NOE patterns. NOE long-range effects, such as (α_i, NH_{i+3}), (α_i, β_{i+3}) and (α_i, NH_{i+4}) contacts (Figure 7), confirmed the occurrence of helical conformations in the 59–65 segment of all the three examined peptides.

A set of 153 (87 intra-residual, 48 sequential and 18 long-range), 204 (115 intra-residual, 65 sequential and 24 long-range) and 181 (129 intra-residual, 32 sequential and 20 long-range) experimental NOE constraints for Nodal[44-67], Nodal[44-67]EE-AA and Nodal [44-67]Y-A, respectively, was used as upper limits of inter-proton distances for structure calculations by CYANA program [43].

For all the peptides, the 40 CYANA structures with the lowest values of target function were subjected to restrained energy minimization by use of the AMBER 6.0 package [44] and then clustered by CHIMERA program [45]. The structures contained in the first and most-populated cluster (13 structures for Nodal[44-67], 17 for

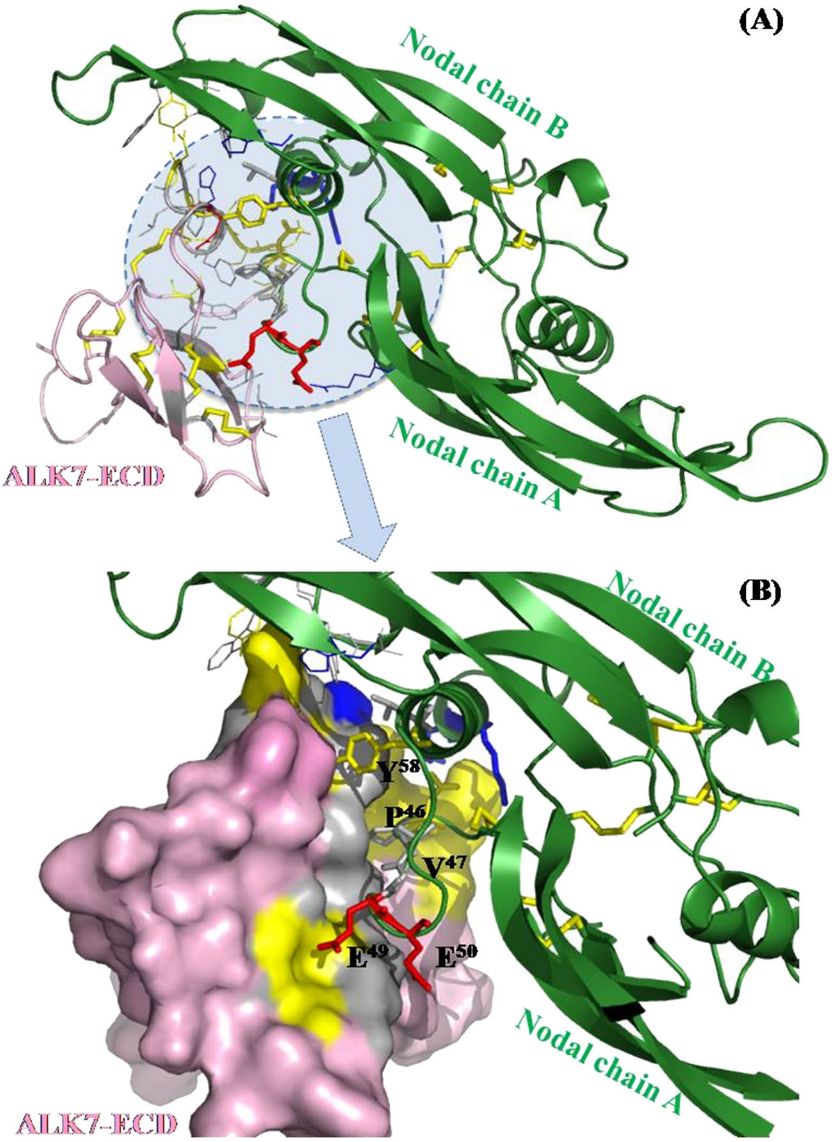

Figure 5. (A) Cartoon representation of the Nodal (green)/ALK7-ECD (pink) complex model. (B) ALK7 receptor is represented as Connolly surface (orange). Residues at the binding interface are colored by type.

Nodal[44-67]EE-AA and 12 for Nodal[44-67]Y-A) were chosen as representative of the conformational space accessible to the peptide. The statistics of the structural analysis are reported in Tables S4 and S5 of the Supporting Information.

For all the peptides, the representative clusters show structures characterized by an α-helix conformation in the 58–65 segment, where the backbone RMSD are 0.24 ± 0.12 Å, 0.26 ± 0.17 Å and 1.15 ± 0.41 Å for Nodal[44-67], Nodal[44-67]EE-AA, and Nodal[44-67]Y-A and a C-terminal flexible segment. It is worth noticing that the helical structure characterizing all three peptides reproduces the same secondary structure in the corresponding region of wild-type Nodal. In Figure 8, a superposition of the Nodal homology model (HM) [30] with the representative NMR structures of Nodal[44-67], Nodal[44-67]EE-AA and Nodal[44-67]Y-A, well represents this structural similarity. The backbone RMSD values, obtained by superimposing Nodal [44-67], Nodal[44-67]EE-AA and Nodal[44-67]Y-A NMR structures in the 58–65 segment of Nodal HM, are 0.41 Å, 0.60 Å and 0.30 Å, respectively.

The molecular model of Nodal[44-67]PV-AA was not computed, as it contains modifications that, occurring in the loop region, would not expectedly alter the helical conformation in the 58–65 tract, common to the other analogs. This hypothesis is corroborated by its CD spectrum that shows a profile similar to the others (Figure 6).

Surface Plasmon Resonance Analysis

We have studied the interaction between peptides reproducing the Nodal region 44–67 and the ECDs of ALK4, ALK7 and Cripto, evaluating the effect of specific substitutions of hot-spot residues within the pre-helix loop and helix H3 in protein recognition. SPR dose-dependent binding assays between each Nodal peptide and every single protein were carried out.

All sensorgrams obtained for the binding of Nodal peptides to immobilized Cripto, ALK4 and ALK7 recombinant proteins showed a similar kinetics profile with both fast association and dissociation rates resulting in typical ‘square-pulse’ sensorgrams (Figure 9 and

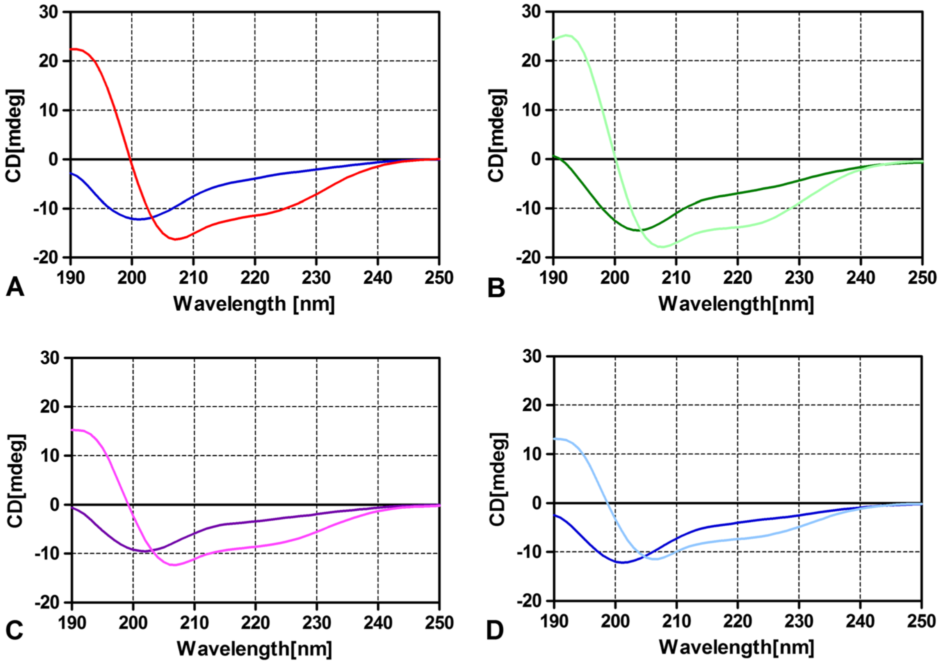

Figure 6. CD spectra of the Nodal fragments within the range 190–250 nm. (**A**) Nodal[44-67]: in water (blue line) and in water containing 20% TFE (v/v) (red line). (**B**) Nodal[44-67]EE-AA: in water (green line) and in water containing 20% TFE (v/v) (light green line). (**C**) Nodal[44-67]PV-AA: in water (violet line) and in water containing 20% TFE (v/v) (pink line). (**D**) Nodal[44-67]Y-A: in water (blue line) and in water containing 20% TFE (v/v) (cyan line).

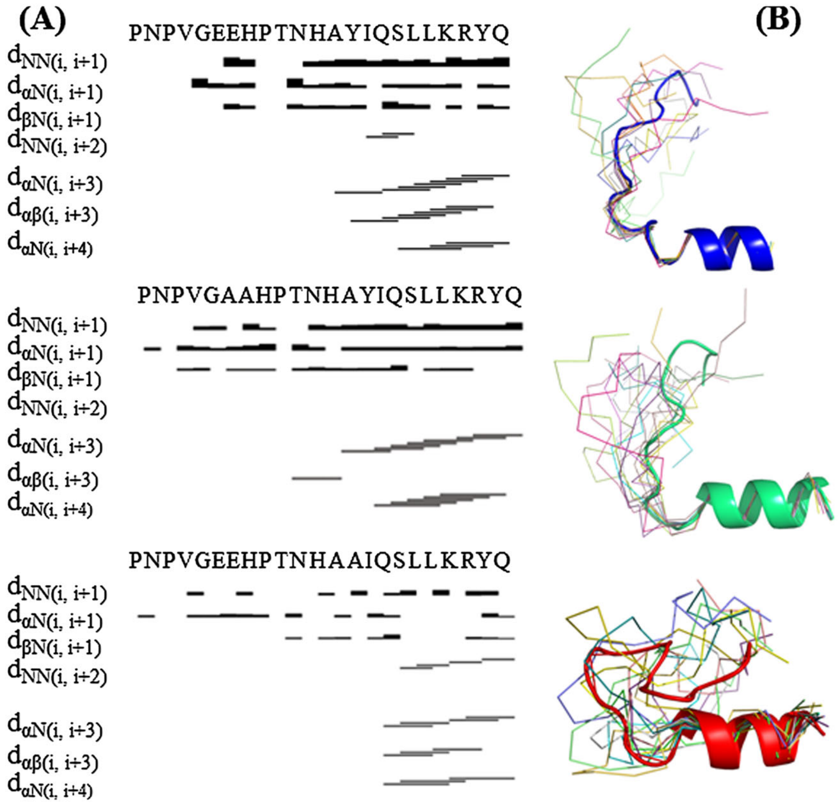

Figure 7. (**A**) NOE contacts graph for Nodal[44-67], Nodal[44-67]EE-AA and Nodal[44-67]Y-A. (**B**) Backbone superposition in the I59–Y66 segment of the structures constituting the first cluster. The representative structure of the cluster is shown with blue cartoon for Nodal[44-67], green cartoon for Nodal [44-67]EE-AA and red cartoon for Nodal[44-67]Y-A.

Figures S2 and S3 of the Supporting Information). Comparative binding data were extrapolated by curve fitting. Remarkably, although we could achieve good-fitting data for the binding of most peptides to Cripto (except for Nodal[44-67]Y-A), all calculations performed on binding and dissociation curves to ALK4 and ALK7 did not converge to significant values (data are summarized in Table 3).

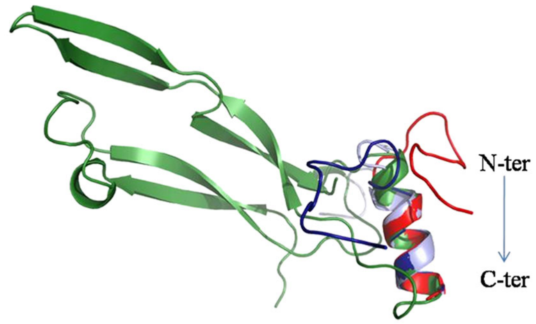

Figure 8. Structural overlap in the 58–65 segment of Nodal HM (green) [30] and the representative NMR structures of Nodal[44-67] (blue), Nodal[44-67] EE-AA (light blue) and Nodal[44-67]Y-A (red).

Table 3. Affinity constant values of Nodal[44-67] and related Ala-mutated peptides to immobilized *rh*Cripto

	K_D		
Peptide	Cripto	ALK4	ALK7
Nodal[44-67]	$1.39 * 10^{-6}$ M	nf	nf
Nodal[44-67]EE-AA	$13.3 * 10^{-6}$ M	nf	nf
Nodal[44-67]PV-AA	$3.42 * 10^{-6}$ M	nf	nf
Nodal[44-67]Y-A	nf	nf	nf

The K_D values were extrapolated by data fitting of dose-dependent binding curves using the BIA evaluation analysis package (version 4.1, Pharmacia Biosensor).

No fitting (nf) means that fitting of binding and association curves did not converge to any value.

According to this analysis and in agreement with previous findings [30], we concluded that replacing the two glutamic acids (E49 and E50) with alanines in Nodal[44-67] reduced the affinity by about ten times ($K_D = 13.3$ μM) compared with that obtained with the unmodified Nodal fragment ($K_D = 1.39$ μM). Conversely, the affinity constant ($K_D = 3.42$ μM) for Cripto of Nodal[44-67]PV-AA, in which P46 and V47 were substituted with alanines, resulted very close to that of the wild-type peptide, suggesting a relatively weak contribution of these residues to the binding with Cripto and to the stability of the overall complex. Nodal[44-67]Y-A very poorly associated with immobilized Cripto (Figure 9D), and, furthermore, attempts to fit the association and dissociation curves to derive the binding parameters were all unfruitful (Table 3). The results therefore suggest that the binding of Nodal to Cripto could be mediated by tyrosine on position 58 (Y58) and is further stabilized by the upstream glutamic acid pair (E49–E50). Following the same procedure, we found that none of the peptides tested displayed sufficient binding capacity for either ALK4 and ALK7. Kinetic data, reported in Table 4, show that the Nodal peptides exhibit very similar K_{off}s (Nodal [44-67]: $K_{off} = 2.86*10^{-3}\ s^{-1}$; Nodal[44-67]EE-AA: $K_{off} = 2.44*10^{-3}\ s^{-1}$; Nodal[44-67]PV-AA: $K_{off} = 2.40*10^{-3}\ s^{-1}$) and that the differences in affinity constants (K_D) for Cripto arise mainly from changes in the association rates (Nodal[44-67]: $2.51*10^{3}\ M^{-1}\ s^{-1}$; Nodal[44-67] PV-AA: $2.15*10^{3}\ M^{-1}\ s^{-1}$; Nodal[44-67]EE-AA: $3.23*10^{2}\ M^{-1}\ s^{-1}$). Such observations support the hypothesis that E49 and E50 positively affect the binding to Cripto by enhancing the association speed.

To try to further rationalize the data obtained and to gain a more comprehensive overview of the interaction between peptide fragments and target proteins, we also made a comparison of the RUmax values obtained for all molecules at a given concentration (0.1 mM). Data are reported in the Supporting Information as Figure S4 and reflect the values from sensorgrams reported in Figure 9 (A–D) and Figures S2 and S3. As shown, the most intense values are observed for the interaction between Nodal[44-67] with Cripto whereas the same molecule only very poorly binds the other receptors. Unexpectedly, peptides Nodal[44-67]EE-AA and Nodal[44-67] PV-AA were somehow captured by ALK4 and ALK7, although the

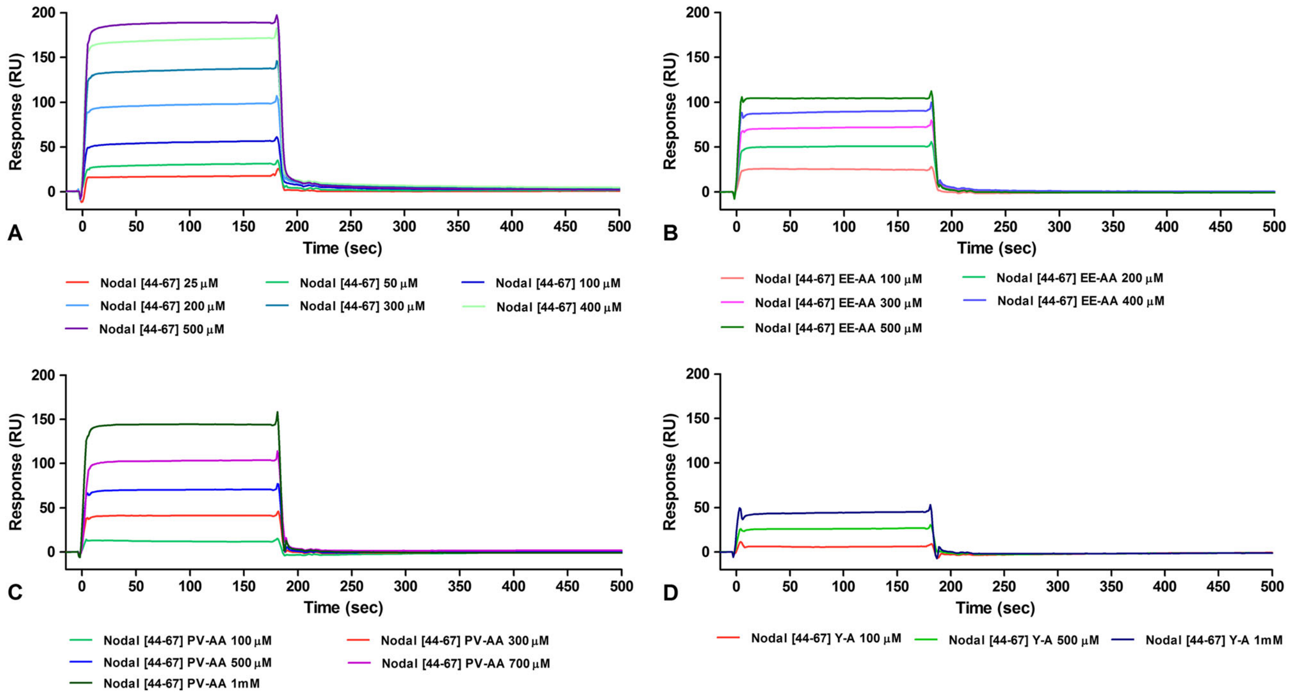

Figure 9. SPR sensorgrams obtained for the binding of Nodal peptides to immobilized *rh*Cripto. Dose–response curves were recorded at concentrations ranging between (**A**) 25–500 μM for Nodal[44-67]; (**B**) 100–500 μM for Nodal[44-67]EE-AA; (**C**) 100–1000 μM for Nodal[44-67]PV-AA; (**D**) 100–1000 μM for Nodal[44-67]Y-A.

Table 4. Kinetic constants extrapolated for the binding of Nodal [44-67] and related Ala-mutated peptides to immobilized *rh*Cripto

Peptide	K_{on} (M^{-1} s^{-1})	K_{off} (s^{-1})	K_D (M)
Nodal[44-67]	$2.51 * 10^{3}$	$2.86 * 10^{-3}$	$1.39 * 10^{-6}$
Nodal[44-67]EE-AA	$3.23 * 10^{2}$	$2.44 * 10^{-3}$	$13.3 * 10^{-6}$
Nodal[44-67]PV-AA	$2.15 * 10^{3}$	$2.40 * 10^{-3}$	$3.42 * 10^{-6}$
Nodal[44-67]Y-A	nf	nf	nf

The K_D values were obtained as the ratio between K_{off}s and K_{on}s.

Data were obtained using the BIA evaluation analysis package (version 4.1, Pharmacia Biosensor).

No fitting (nf) means that fitting of binding and association curves did not converge to any value.

kinetic parameters could not be determined (Tables 2 and 3). Thus, it seems that replacement of two glutamic acids (E49 and E50) or of proline 47 (P47) and valine 48 (V48) with alanine residues may favor the binding to the ALK receptors. These data could be explained by looking at the ALK7/Nodal complex binding epitope (Figure 5). Indeed, the model suggests that the Nodal E49–E50 residues are close to the ALK7 hydrophobic interface; therefore, when they are changed to alanine, the hydrophobic interactions could be enhanced. The same explanation could hold true also for ALK4, assuming that the theoretical ALK4/Nodal complex adopts the same topological structure as the ALK7/Nodal complex. Strikingly, the substitution of Y58 with alanine in Nodal[44-67]Y-A completely abolishes the binding to ALK4 and ALK7, indicating a possible role of such residue in the Nodal binding with these proteins.

Discussion

In this work, we have investigated some structural properties of the binding of Nodal with its type I receptors, ALK4 and ALK7, and with the co-receptor Cripto. An approach based on homology modeling, CD, NMR and SPR binding assays has been applied to design and study a set of synthetic peptides reproducing the pre-helix loop and the H3 α-helix region of Nodal. Nodal is reported to establish direct interactions with ALK7 and with Cripto, whereas the interaction with ALK4 was so far believed to be only mediated by Cripto. We find here for the first time that, at least *in vitro*, Nodal can directly and strongly interact with ALK4 too. However, whether this interaction occurs also *in vivo* or has a functional relevance remains to be established. We also evaluated for the first time the K_D for the Nodal/ALK7 interaction (1.58 nM). These strong interactions, together with that underlying the binding of Nodal with Cripto [30], also in the low nanomolar range, suggest that the members of the resulting molecular complex are very tightly associated, and their dissociation is a very difficult task. Using the synthetic peptides, we have further investigated the Nodal main residues involved in the binding with Cripto. Nodal binding residues have been identified using the previously published ALK4/Cripto/Nodal [30] and ALK7/Nodal [31] molecular models. On this basis, a series of Nodal fragments, which include residues 44–67 of the pre-helix loop and the H3 α-helix, have been synthesized with selected residue replacements to evaluate their putative role in receptor binding. The conformational NMR and CD analyses of Nodal peptides show their propensity to adopt α-helix structures, at least in the N-terminal tract reproducing the H3 α-helix of the parent protein. Remarkably, substitution of residues on positions 47–50 with alanines does not seem to affect the overall propensity of the peptide C-terminal tail to adopt the helical structure. Also, changing Y58 within the helix with an alanine poorly alters the structural features of the molecule.

The ability of Nodal fragments to bind to ALK4, ALK7 receptors and Cripto, evaluated by SPR assays, has shown a preferential recognition of the wild-type Nodal 44–67 fragment for Cripto. Indeed, changing the key residues E49, E50 and Y58 to alanines interferes with and strongly impairs the recognition with this protein. Our data are also suggestive of a minor role of P47 and V48. Remarkably, the mutated synthetic peptides Nodal[44-67]EE-AA and Nodal [44-67]PV-AA, likely because of an increase of the local hydrophobicity, are also attracted to some extent by the ALK4 and the ALK7 receptors, while the substitution of Y58 abolishes the binding. All together, these data suggest that the part of the molecular surface corresponding to this region of Nodal could be shared with the other two protein partners.

In conclusion, the results reported here confirm that the binding of Nodal to the receptor complex, comprising the type I receptors ALK7 and ALK4 via the co-receptor Cripto, is influenced by glutamic acid residues (E49 and E50) and by tyrosine 58 (Y58). Such residues appear crucial to modulate Nodal specificity for one or the other receptor, thus altering also its function.

Considering the outstanding implications of Nodal in cancer, elucidation of the structural features underlying its interaction with receptors and co-receptors is fundamental in the perspective of planning strategies aimed at targeting the Nodal/Cripto-ALK receptors–Smad axis for therapeutic purposes.

Although further structural studies are required to confirm *in vivo* our observations, the identification of such *hot-spot* residues is a primary step to develop new inhibitors, especially neutralizing antibodies and small high-affinity peptides reproducing the binding interfaces on both Nodal and ALK7. The finding that Nodal can bind directly ALK4, if confirmed by other studies, could suggest the existence of a new Cripto-independent axis, which could be, independently or in combination with, targeted for developing specific antagonists that disrupt the Nodal–receptor complex(es) and block the growth and proliferation of many cancer cells.

Acknowledgements

This work was supported by funds from FIRB MERIT no. RBNE08NKH7_003 and from the PON Ricerca e Competitività 2007–2013 (PON01_01602, PON01_02342) to MR. AS is fully supported by FIRB no. RBNE08NKH7_003.

References

1 Jornvall H, Reissmann E, Andersson O, Mehrkash M Ibanez CF. ALK7, a receptor for nodal, is dispensable for embryogenesis and left-right patterning in the mouse. *Mol. Cell. Biol.* 2004; **24**: 9383–9389.
2 James D, Levine AJ, Besser D Hemmati-Brivanlou A. TGFbeta/activin/nodal signaling is necessary for the maintenance of pluripotency in human embryonic stem cells. *Development* 2005; **132**: 1273–1282.
3 Pantic I. Cancer stem cell hypotheses: impact on modern molecular physiology and pharmacology research. *J. Biosci.* 2011; **36**: 957–961.
4 Quail DF, Siegers GM, Jewer M Postovit LM. Nodal signalling in embryogenesis and tumourigenesis. *Int. J. Biochem. Cell Biol.* 2013; **45**: 885–898.
5 Xu G, Zhong Y, Munir S, Yang BB, Tsang BK Peng C. Nodal induces apoptosis and inhibits proliferation in human epithelial ovarian cancer cells via activin receptor-like kinase 7. *J. Clin. Endocrinol. Metab.* 2004; **89**: 5523–5534.
6 Hermann PC, Huber SL, Herrler T, Aicher A, Ellwart JW, Guba M, Bruns CJ, Heeschen C. Distinct populations of cancer stem cells determine tumor

growth and metastatic activity in human pancreatic cancer. *Cell Stem Cell* 2007; **1**: 313–323.

7 Lonardo E, Hermann PC, Mueller MT, Huber S, Balic A, Miranda-Lorenzo I, Zagorac S, Alcala S, Rodriguez-Arabaolaza I, Ramirez JC, Torres-Ruiz R, Garcia E, Hidalgo M, Cebrian DA, Heuchel R, Lohr M, Berger F, Bartenstein P, Aicher A, Heeschen, C. Nodal/activin signaling drives self-renewal and tumorigenicity of pancreatic cancer stem cells and provides a target for combined drug therapy. *Cell Stem Cell* 2011; **9**: 433–446.

8 Papageorgiou I, Nicholls PK, Wang F, Lackmann M, Makanji Y, Salamonsen LA, Robertson DM, Harrison CA. Expression of nodal signalling components in cycling human endometrium and in endometrial cancer. *Reproductive Biol. Endocrinol.: RB&E* 2009; **7**: 122.

9 Quail DF, Walsh LA, Zhang G, Findlay SD, Moreno J, Fung L, Ablack A, Lewis JD, Done SJ, Hess DA, Postovit LM. Embryonic protein nodal promotes breast cancer vascularization. *Cancer Res.* 2012; **72**: 3851–3863.

10 Strizzi L, Hardy KM, Margaryan NV, Hillman DW, Seftor EA, Chen B, Geiger XJ, Thompson EA, Lingle WL, Andorfer CA, Perez EA, Hendrix MJ. Potential for the embryonic morphogen Nodal as a prognostic and predictive biomarker in breast cancer. *Breast Canc. Res.: BCR* 2012; **14**: R75.

11 Kirsammer G, Strizzi L, Margaryan NV, Gilgur A, Hyser M, Atkinson J, Kirschmann DA, Seftor EA, Hendrix MJ. Nodal signaling promotes a tumorigenic phenotype in human breast cancer. *Semin. Cancer Biol.* 2014.

12 Vo BT, Cody B, Cao Y Khan SA. Differential role of Sloan-Kettering Institute (Ski) protein in Nodal and transforming growth factor-beta (TGF-beta)-induced Smad signaling in prostate cancer cells. *Carcinogenesis* 2012; **33**: 2054–2064.

13 Lawrence MG, Margaryan NV, Loessner D, Collins A, Kerr KM, Turner M, Seftor EA, Stephens CR, Lai J, Postovit LM, Clements JA, Hendrix MJ. Reactivation of embryonic nodal signaling is associated with tumor progression and promotes the growth of prostate cancer cells. *Prostate* 2011; **71**: 1198–1209.

14 Spiller CM, Bowles J Koopman P. Nodal/Cripto signaling in fetal male germ cell development: implications for testicular germ cell tumors. *Int. J. Dev. Biol.* 2013; **57**: 211–219.

15 Lee CC, Jan HJ, Lai JH, Ma HI, Hueng DY, Lee YC, Cheng YY, Liu LW, Wei HW, Lee HM. Nodal promotes growth and invasion in human gliomas. *Oncogene* 2010; **29**: 3110–3123.

16 Tysnes BB, Satran HA, Mork SJ, Margaryan NV, Eide GE, Petersen K, Strizzi L, Hendrix MJ. Age-dependent association between protein expression of the embryonic stem cell marker Cripto-1 and survival of glioblastoma patients. *Translational oncology* 2013; **6**: 732–741.

17 Gong Y, Yu T, Chen B, He M Li Y. Removal of cardiopulmonary resuscitation artifacts with an enhanced adaptive filtering method: an experimental trial. *BioMed Res. Int.* 2014; **2014**: 140438.

18 Seftor EA, Seftor RE, Weldon DS, Kirsammer GT, Margaryan NV, Gilgur A, Hendrix MJ. Melanoma tumor cell heterogeneity: a molecular approach to study subpopulations expressing the embryonic morphogen nodal. *Semin. Oncol.* 2014; **41**: 259–266.

19 Topczewska JM, Postovit LM, Margaryan NV, Sam A, Hess AR, Wheaton WW, Nickoloff BJ, Topczewski J, Hendrix MJ. Embryonic and tumorigenic pathways converge via Nodal signaling: role in melanoma aggressiveness. *Nat. Med.* 2006; **12**: 925–932.

20 Chen J, Liu WB, Jia WD, Xu GL, Ma JL, Ren Y, Chen H, Sun SN, Huang M, Li JS. Embryonic morphogen nodal is associated with progression and poor prognosis of hepatocellular carcinoma. *PLoS One* 2014; **9**: e85840.

21 Ganapathy V, Ge R, Grazioli A, Xie W, Banach-Petrosky W, Kang Y, Lonning S, McPherson J, Yingling JM, Biswas S, Mundy GR, Reiss M. Targeting the transforming growth factor-beta pathway inhibits human basal-like breast cancer metastasis. *Mol. Cancer* 2010; **9**: 122.

22 Korpal M, Kang Y. Targeting the transforming growth factor-beta signalling pathway in metastatic cancer. *Eur. J. Cancer* 2010; **46**: 1232–1240.

23 Strizzi L, Hardy KM, Kirschmann DA, Ahrlund-Richter L Hendrix MJ. Nodal expression and detection in cancer: experience and challenges. *Cancer Res.* 2012; **72**: 1915–1920.

24 Wakefield LM, Hill CS. Beyond TGFbeta: roles of other TGFbeta superfamily members in cancer. *Nat. Rev. Cancer* 2013; **13**: 328–341.

25 Reissmann E, Jornvall H, Blokzijl A, Andersson O, Chang C, Minchiotti G, Persico MG, Ibanez CF, Brivanlou AH. The orphan receptor ALK7 and the activin receptor ALK4 mediate signaling by Nodal proteins during vertebrate development. *Genes Dev.* 2001; **15**: 2010–2022.

26 Schier AF, Shen MM. Nodal signalling in vertebrate development. *Nature* 2000; **403**: 385–389.

27 Yeo C, Whitman M. Nodal signals to Smads through Cripto-dependent and Cripto-independent mechanisms. *Mol. Cell* 2001; **7**: 949–957.

28 Minchiotti G, Manco G, Parisi S, Lago CT, Rosa F Persico MG. Structure-function analysis of the EGF-CFC family member Cripto identifies residues essential for nodal signalling. *Development* 2001; **128**: 4501–4510.

29 Khalkhali-Ellis Z, Kirschmann DA, Seftor EA, Gilgur A, Bodenstine TM, Hinck AP, Hendrix MJ. Divergence(s) in nodal signaling between aggressive melanoma and embryonic stem cells. *Int. J. Canc. J. Int. du Canc.* 2014.

30 Calvanese L, Marasco D, Doti N, Saporito A, D'Auria G, Paolillo L, Ruvo M, Falcigno L. Structural investigations on the Nodal-Cripto binding: a theoretical and experimental approach. *Biopolymers* 2010; **93**: 1011–1021.

31 Romano V, Raimondo D, Calvanese L, D'Auria G, Tramontano A Falcigno L. Toward a better understanding of the interaction between TGF-beta family members and their ALK receptors. *J. Mol. Model.* 2012; **18**: 3617–3625.

32 Lin SJ, Lerch TF, Cook RW, Jardetzky TS Woodruff TK. The structural basis of TGF-beta, bone morphogenetic protein, and activin ligand binding. *Reproduction* 2006; **132**: 179–190.

33 Greenwald J, Vega ME, Allendorph GP, Fischer WH, Vale W Choe S. A flexible activin explains the membrane-dependent cooperative assembly of TGF-beta family receptors. *Mol. Cell* 2004; **15**: 485–489.

34 Muenster U, Korupolu R, Rastogi R, Read J Fischer WH. Antagonism of activin by activin chimeras. *Vitam. Horm.* 2011; **85**: 105–128.

35 Thompson TB, Woodruff TK Jardetzky TS. Structures of an ActRIIB:activin A complex reveal a novel binding mode for TGF-beta ligand:receptor interactions. *Embo. J.* 2003; **22**: 1555–1566.

36 Fields GB, Noble RL. Solid phase peptide synthesis utilizing 9-fluorenylmethoxycarbonyl amino acids. *Int. J. Pept. Protein Res.* 1990; **35**: 161–214.

37 Bax A, Davis DG. MLEV-17-based two-dimensional homonuclear magnetization transfer spectroscopy. *J. Magn. Res.* 1985; **65**: 355–360.

38 States D, Haberhorn R Ruben D. A two-dimensional nuclear Overhauser experiment with pure absorption phase in four quadrants. *J. Magn. Res.* 1982; **48**: 286–292.

39 Delaglio F, Grzesiek S, Vuister GW, Zhu G, Pfeifer J Bax A. NMRPipe: a multidimensional spectral processing system based on UNIX pipes. *J. Biomol. NMR* 1995; **6**: 277–293.

40 Johnson BA. Using NMRView to visualize and analyze the NMR spectra of macromolecules. *Methods Mol. Biol.* 2004; **278**: 313–352.

41 Guntert P, Braun W Wuthrich K. Efficient computation of three-dimensional protein structures in solution from nuclear magnetic resonance data using the program DIANA and the supporting programs CALIBA, HABAS and GLOMSA. *J. Mol. Biol.* 1991; **217**: 517–530.

42 Guntert P, Mumenthaler C Wuthrich K. Torsion angle dynamics for NMR structure calculation with the new program DYANA. *J. Mol. Biol.* 1997; **273**: 283–298.

43 Guntert P. Automated NMR structure calculation with CYANA. *Methods Mol. Biol.* 2004; **278**: 353–378.

44 Pearlman DA, Case DA, Caldwell JW, Ross WS, Cheatham TE III, DeBolt S, Ferguson D, Seibel G, Kollman P. AMBER, a package of computer program for applying molecular mechanics, normal mode analysis, molecular dynamics and free energy calculations to simulate the structural and energetic properties of molecules. *Comp. Phys. Commun.* 1995; **91**: 1–41.

45 Pettersen EF, Goddard TD, Huang CC, Couch GS, Greenblatt DM, Meng EC, Ferrin TE. UCSF Chimera–a visualization system for exploratory research and analysis. *J. Comput. Chem.* 2004; **25**: 1605–1612.

46 Koradi R, Billeter M, Wuthrich K. MOLMOL: a program for display and analysis of macromolecular structures. *J. Mol. Graph.* 1996; **14**: 51–55, 29–32.

47 Wuthrich K. *NMR of Proteins and Nucleic Acids*, Wiley: New York, 1986.

48 Wishart DS, Sykes BD Richards FM. Relationship between nuclear magnetic resonance chemical shift and protein secondary structure. *J. Mol. Biol.* 1991; **222**: 311–333.

Supporting Information

Additional supporting information may be found in the online version of this article at the publisher's web site.

Proceedings of the 23rd American Peptide Symposium
Michal Lebl (Editor)
American Peptide Society, 2013

Design, Synthesis and Structural analysis of cyclopeptides against VEGF-Receptor

A. Caporale[1*], G. Focà[1,2*], N. Doti[1,2], A. Sandomenico[1,2] and M. Ruvo[1,2]
[1]CIRPeB, Via Mezzocannone, 16, 80134 Napoli, Italy
[2]CNR-IBB, Via Mezzocannone, 16, 80134 Napoli, Italy
**These authors contributed equally to this work*

Introduction

Angiogenesis is a physiological process mostly regulated by activation of VEGF receptors VEGF-R1 (Flt-1) and VEGF-R2 (KDR) by a set of structurally conserved ligands of the *Vascular Endothelial Growth Factor* (VEGF) family. Inappropriate receptor activation leads to pathological processes strictly correlated to tumour growth and their inhibition is a well-assessed strategy to stop or slow down cancer growth [**1**]. Both ligands and receptors have been targeted to block pathological angiogenesis, however a broad structural similarity amongst the different ligands and the two receptors makes difficult the design of new selective inhibitors. Several antiangiogenic compounds have been so far reported and developed at various stages [**2**]. A comparative analysis of known VEGFRs-binding peptides suggests that a minimum structural requirement for binding to VEGFR2 could be the motif XPR, where X is a hydrophobic residue crucial for receptor recognition. To identify new selective receptor inhibitors, we started from known VEGFR2-binding peptides [**3-5**] and designed and synthesized a small set of D-cyclopeptides containing this motif. A preliminary screening of their ability to bind to VEGFR1 and VEGFR2 by SPR was performed, showing that some of them bind both receptors with an affinity in the low micromolar range, whereas one is able to bind VEGFR1 in a selective manner.

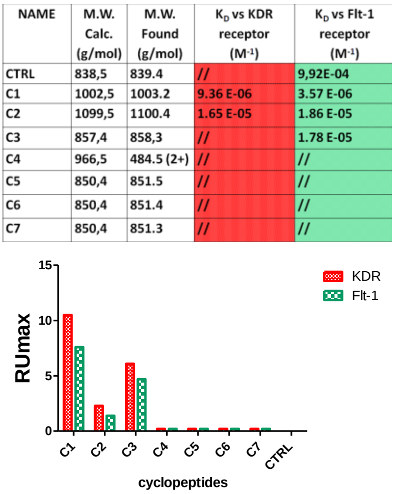

NAME	M.W. Calc. (g/mol)	M.W. Found (g/mol)	K_D vs KDR receptor (M^{-1})	K_D vs Flt-1 receptor (M^{-1})
CTRL	838,5	839.4	//	9,92E-04
C1	1002,5	1003.2	9.36 E-06	3.57 E-06
C2	1099,5	1100.4	1.65 E-05	1.86 E-05
C3	857,4	858,3	//	1.78 E-05
C4	966,5	484.5 (2+)	//	//
C5	850,4	851.5	//	//
C6	850,4	851.4	//	//
C7	850,4	851.3	//	//

Fig. 1. a) Names, MW and KDs for the two VEGFRs determined by dose-response binding assays. b) SPR screening: plot of RUmax achieved at the concentration of 20 µM for the

Results and Discussion

The library components were designed using as template two previously reported VEGFR binding peptides: the linear peptide ATWLPPR [**3**], denoted as "CTRL", and the cysteine-bridged CPQPRPLC peptide [**4; 5**]. Peptide C1 was the retro-inverso of the ATWLPPR lacking one Proline, to put the hydrophobic Leucine adjacent to the Arginine. Peptide C2 was the retro-inverso of ATWLPPR. The peptide C3 was designed to exchange the hydrophobic patch before the PPR motif with a charged residue. Peptides from C5 to C7 were designed as variants of peptide C3, by moving the "rp" motif along the sequence. Retro-inversion was introduced to increase proteolytic stability, maintaining the overall side chain topology, whereas cyclization was introduced to restrict the conformational freedom in solution.

The synthesis of the library was carried out on the solid phase, following the Sheppard's protocol using Fmoc protected Amino Acids and HATU as coupling reagent. The cyclization was carried out in slightly alkaline buffers (pH 8.0) on crude peptides. Purification was accomplished after reaction completion and acidification.

The interaction between VEGF mimetic cyclopeptides and VEGF-R1 and VEGF-R2 receptors was assessed by SPR assays using a BIACORE 3000 system. A CM5 sensor chip was covalently derivatized with recombinant KDR and Flt-1 proteins following an amino coupling strategy. The screening was performed simultaneously on both receptors, starting from a concentration of 20 nM until 20 μM. Data (Fig. 1b) showed that C1 and C2 bound to both VEGF-R1 and VEGF-R2 receptors while the C3 cyclopeptide seemed specific for Flt-1. To further investigate the binding in terms of affinity and specificity on both receptors, we carried out a dose-dependent assay for three positive cyclopeptides C1, C2 and C3. By fitting data using the BIAevaluation analysis package (version 4.1, Pharmacia Biosensor) we extrapolated the KD values (Fig. 1a). The C2 peptide bound with a similar KD to both receptors, while C1 recognized Flt-1 with a slightly increased affinity compared to KDR. In addition, we found a weak interaction of the linear and C3 peptides with Flt-1 receptor only.

In conclusion, we confirmed that the motif PR, preceded often by a hydrophobic residue, occurring in several VEGF receptor binding peptides , such as the sequence of PlGF-derived peptides [**4-6**], might be an important scaffold for binding to KDR and to Flt-1 [**3-5**]. We found that some of the library components bound both receptors (C1 and C2) with moderate affinity, whereas one of them, C3, selectively bound to Flt-1. Preliminary CD analyses (data not shown) suggest that the peptides adopt very different conformations in solutions and this, together with the different arrays of side chains can affect receptor recognition. NMR analyses are currently underway to investigate the contribution to binding deriving from side chains and/or backbone conformation.

Acknowledgments

We gratefully acknowledge the support from Regione Campania for PROGETTO "CAMPUS (Progetti di Ricerca industriale e sviluppo sperimentale") and MIUR for project FIRB-MERIT N° RBNE08NKH7 to M. Ruvo. We also thank Consiglio Nazionale delle Ricerche for project CCNC.

References

1. Folkman J, N Engl J Med, 1182-6 (1971)
2. National Cancer Institute, http://www.cancer.gov/cancertopics/factsheet/Therapy/angio genesis-inhibitors
3. Binétruy-Tounaire R et al., EMBO J, 1525-33 (2000)
4. Giordano RJ et al. PNAS, 5112-7 (2010)
5. Pasqualini et al. patent US2012/0028880 A1
6. Diana, D. et al., J Biol Chem, 41680-91 (2011)

Mol Biotechnol (2013) 54:983–995
DOI 10.1007/s12033-013-9655-7

RESEARCH

A Comparative Structural and Bioanalytical Study of IVIG Clinical Lots

Annamaria Sandomenico · Valeria Severino ·
Angela Chambery · Annalia Focà · Giuseppina Focà ·
Claudio Farina · Menotti Ruvo

Abstract Intravenous immunoglobulin are important biotherapeutics used in the replacement therapy for primary and secondary immunodeficiencies, chronic inflammatory disorders and several autoimmune haematologic disorders. Currently, a number of immunoglobulin intravenous (IVIG) products have been approved by the Food and Drug Administration (FDA) and are available commercially. It is known that small differences in the manufacturing processes as well as in the formulations may affect their clinical efficacy and tolerability. Therefore, given the complexity of the multi-step process required for the isolation of IVIG from human plasma, it is necessary to ensure a rigorous quality control of final products. We show here that a set of different bioanalytical techniques can be conveniently used to comparatively characterize, at a quantitative and qualitative level, different lots of IVIG preparations and to unveil randomly occurring impurities which can also affect the overall product stability. We have used circular dichroism, surface plasmon resonance and two-dimensional electrophoresis (2DE), and have demonstrated that this combination of bioanalytical approaches is very useful to improve the quality control of antibodies and to monitor the reliability of the IVIG manufacturing process.

Keywords IVIG · Circular dichroism · SPR · Biacore · Protein A · Thermal denaturation

Introduction

Intravenous immunoglobulin (IVIG) preparations have become the major plasma-derived product with increasingly important bio-therapeutic applications. Indeed, IVIG have been successfully employed for the treatment of several immunological and inflammatory diseases including replacement therapies for primary immunodeficiencies, such as X-linked agammaglobulinemia, hypogammaglobulinemia, some acute graft-versus-host diseases and chronic B cell lymphocytic leukaemia [1, 2]. In addition, IVIG preparations are also employed for the therapy of humoral immunodeficiencies related to several pathophysiological diseases. In this context, infusion of IVIG has been widely applied for the treatment and prevention of infectious and inflammatory diseases such as the coronary artery aneurysms in Kawasaki disease, the idiopathic thrombocytopenic purpura and the Guillain–Barrè syndrome. Moreover, minor neurologic and dermatologic pathologies are also treated off-label with IVIG.

Except for the replacement therapy, the IVIG mechanism of action is not yet fully understood. However, clinical evidences suggest their involvement in the modulation

---

Electronic supplementary material The online version of this article (doi:10.1007/s12033-013-9655-7) contains supplementary material, which is available to authorized users.

A. Sandomenico (✉) · V. Severino · A. Focà · G. Focà · M. Ruvo
Istituto di Biostrutture e Bioimmagini, Consiglio Nazionale delle Ricerche, via Mezzocannone, 16, 80134 Naples, Italy
e-mail: annamaria.sandomenico@gmail.com

A. Sandomenico · A. Focà · G. Focà · M. Ruvo (✉)
CIRPeB, via Mezzocannone, 16, 80134 Naples, Italy
e-mail: menotti.ruvo@unina.it

V. Severino · A. Chambery
Dipartimento di Scienze e Tecnologie Ambientali Biologiche e Farmaceutiche, via A. Vivaldi, 43, 81100 Caserta, Italy

C. Farina
Kedrion SpA, Loc. Ai Conti, 55051 Lucca, Castelvecchio Pascoli, Italy

of multiple networks related to the expression and function of Fc receptors, the activation of the complement and cytokine pathways and the regulation of cell growth. Some effects on the activation, differentiation and effector functions of dendritic, T and B cells have been also hypothesized [3, 4].

Intravenous immunoglobulin preparations contain a pool of polyclonal IgG antibodies extracted from the plasma derived from a high number of healthy blood donors. Although manufacturing processes have been significantly improved in the last two decades to increase purity and yield of IVIG molecules, almost all the purification strategies include an initial step based on the Cohn–Oncley ethanol fractionation. Additional procedures (e.g. ion exchange chromatography, ultrafiltration, enzymatic digestion, pH and ion strength variations and organic solvent–detergent partitioning) may be applied for removing proteins and other minor contaminants, for minimizing the formation of IgG aggregates and for inactivating and removing viral contaminants such as hepatitis B virus, hepatitis C virus and human immunodeficiency virus [5].

In this framework, critical issues in the pharmaceutical production of active products, such as antibodies, are mainly related to the reproducibility and safety of the industrial-scale manufacturing processes and to the cost optimization measures. Increasingly stringent legislation at national and international level ensures the quality and safety of drugs and the materials used in their production. Therefore, given the wide use of IVIG as bio-therapeutics in a broad range of applications, there is a growing demand of powerful and reliable methodologies for the control of the IVIG production process aimed to guarantee the consistency, the quality and safety of the final drug. Although different commercial IVIG preparations are available and equivalent by a therapeutic point of view, an intrinsic variability may be present amongst different commercial products and different lots of the same products.

In this study, a set of bioanalytical methods have been used to characterize and comparatively analyse IVIG from different preparations to evaluate their application for the routine analysis of IVIG lots.

The experimental protocol for monitoring commercial IVIG preparations includes structural investigations carried out by circular dichroism (CD), protein denaturation studies, surface plasmon resonance (SPR) binding assays and two-dimensional electrophoresis (2DE).

The approach has proven to be very sensitive and reliable for the evaluation of full antibody, as well as of separate Fc and Fab, stability and integrity and for the monitoring of lot-to-lot consistency of different IVIG preparations. To demonstrate its applicability, we have analyzed in a comparative way, six different 10 % IVIG lots deriving from two distinct sets: one starting from cryosupernatant 1 and one from fraction II–III, both purified by chromatographic methods.

Materials and Methods

Circular Dichroism Analysis

The six lots of 10 % IVIG, comprising 3 lots prepared from cryosupernatant 1 (lots A1, A2, A3) and 3 lots prepared from fraction II + III (lots B1, B2, B3) are produced by Kedrion S.p.A. 10 % solutions were used as starting material and properly diluted in the indicated buffers prior analysis. All CD analyses were performed using a JASCO J-710 spectropolarimeter, equipped with a Peltier system for changing the temperature in a controlled way and quartz cuvettes 110-QS with 1.0 mm path length. Experiments were performed in 10 mM phosphate, pH = 8.0 at a concentration of 0.20 mg/mL [6]. Spectra were collected within the wavelength range 250–190 nm at a scan rate of 20 nm/min, with a data pitch of 0.2 nm, a band width of 1 nm and a response of 4 s. In order to compare the different protein lots, far UV CD spectra were recorded at 20, 55, 60, 65, 70, 75, and 85 °C and then again at 20 °C ('after cooling' condition). The 'after cooling' spectrum was required to assess whether proteins were able to recover original structures or had undergone irreversible aggregation. Thermal denaturation experiments were performed by monitoring changes in ellipticity at 209 nm by exposure to increasing temperatures between 40 and 90 °C, at a speed of 60 °C/h (1 °C/min). The melting point was determined by the method of the first derivative.

On every sample, five independent spectra were recorded, averaged and smoothed using the Spectra Manager software, version 1.53. Buffer scans were recorded under the same conditions and subtracted. The analysis of secondary structure content was performed using the online server named *Dichroweb* [7, 10].

2D-PAGE Analysis

IVIG preparations at 100 mg/mL (10 %) were used without any further manipulation except dilution. Immobilized pH gradient (IPG) buffers, IPG strips and electrophoresis apparatus were purchased from GE Healthcare (Italy). Electrophoresis reagents, including acrylamide, *N*,*N*,*N*,*N*-methylenebisacrylamide, *N*,*N*,*N*,*N*-tetramethylethylenediamine, ammonium persulfate and sodium dodecylsulfate (SDS), were from BioRad (Milano, Italy). Chemical reagents were from Sigma-Aldrich (Milano, Italy). Gels were scanned using a Molecular Dynamics densitometer, model 375–557, from Amersham Biosciences (USA). Image analysis was performed using the

ImageJ software (Image processing and analysis in Java), available on-line on the National Institutes of Health website (Bethesda, Maryland, USA, http://rsbweb.nih.gov/ij). All other reagents were of analytical grade.

An extensive reduction of IgG disulphide bonds was performed on aliquots of IgG samples (50 mg/mL) by adding DTT 2.3 % in aqueous solution containing SDS 10 % (final volume: 15 μL). Following an incubation of 5 min at 95 °C, samples were directly diluted in the rehydration solution to a final concentration of 2 mg/mL.

A total amount of 200 μg of IgG were loaded on each gel, reduced as reported above, was analyzed by 2D-PAGE. Samples to be processed by isoelectrofocusing (IEF) were diluted with the rehydration buffer (8 M urea, 0.5 % CHAPS, 0.2 % DTT, 0.5 % IPG ampholytes and 0.002 % bromophenol blue) to a final volume of 125 μL. The precast IPG strips (3–10 linear pH gradient, 7 cm long), used for the first dimension, were passively rehydrated and loaded with the sample at room temperature for 12 h under low-viscosity paraffin oil. IEF was then performed using an IPGphor isoelectric focusing cell, according to the following protocol: 50 V for 3 h, 100 V for 2 h, 500 V for 2 h, 1,000 V for 2 h, 3,000 V for 2 h, 4,000 V for 2 h, 5,000 V for 2 h, 6,000 V for 2 h, 8,000 V until about 25,000 V h total. Strips were then equilibrated twice for 15 min with gentle shaking in the equilibration solution (6 M urea, 50 mM Tris–Cl buffer pH 8.8, 30 % glycerol, 2 % SDS, 0.002 % bromophenol blue) containing 1 % DTT to reduce disulphide bonds, in the first equilibration step, and 2.5 % iodoacetamide to alkylate thiols, in the second. The second-dimension separation was performed in a 12 % polyacrylamide (7 × 8 cm). The strips were fixed with 0.5 % agarose and 0.002 % bromophenol blue dissolved in SDS/Tris running buffer. The run was carried out at constant power (10 mA/gel for 15 min; 20 mA/gel until the end of the run). At the end of the electrophoresis, the protein spots were visualized by Coomassie Blue R250 staining.

After staining, 2D-gels were scanned using a Molecular Dynamics densitometer. Gel images were then processed for background subtraction and analysed for spot identification and matching using image analysis Image J software (http://rsbweb.nih.gov/ij). Quantification of relative band intensities to determine IgG purity was performed using the same software.

SPR Analyses

All analyses were performed on a Biacore 3,000 instrument from GE Healthcare, using certified HBS buffer (20 mM Hepes, 0.15 M NaCl, pH 7.2, P20, 0.005 %), at 25 °C.

Protein A (Sigma-Aldrich, Milano) was dissolved in deionized water at a concentration of 1.0 mg/mL. Protein immobilization was efficiently performed on the flow cells (FC) of CM5 sensor chips at 5.0 μg/mL in sodium acetate 10 mM pH 4.5 following the canonical EDC/NHS (amine coupling) method, operating at 5 μL/min [8]. An underivatized surface was prepared and used as control blank. Analyses were carried out at a flow rate of 20 μL/min, injecting a constant volume of 60 μL of IVIG solutions at the following concentration: 1.0, 2.5, 5.0, 10.0, 50.0, 100, 250, 500, 1,000, 1,500, 2,500, 3,000 nM. Dissociations were monitored for at least 600 s, performing at the end a regeneration step by injecting 20 μL of a solution of 10 mM glycine, pH 2.7.

The immobilization of the anti-k-chain monoclonal antibody (mAb K4377, Sigma-Aldrich, Milano) was achieved in 10 mM sodium acetate pH 5, operating at a flow rate of 5 μL/min. In this case, three flow channels were derivatized with the mAb at different immobilization levels: low density on FC2, 613 RU; medium density on FC3, 1813 RU; high density on FC4, 4718 RU. On FC1, used as reference, no protein was immobilized. Experiments were performed at 20 μL/min with a total contact time of 180 s (60 μL injected for every run). Dissociations were monitored for at least 600 s, regenerating at the end with a 20 mM solution of HCl with added 0.005 % v/v of surfactant P20. The concentrations of IgGs used for the binding experiments were: 10, 25, 50, 100, 500, 1,000, 1,500 and 2,000 nM. For every single analysis, experimental sensorgrams were aligned, subtracted of blank signals and overlapped. All mathematical manipulations and fitting were performed using the BiaEvaluation software, version 4.1 from GE Healthcare. Analyses were carried out using the six samples opportunely diluted in the HBS running buffer.

Fragment Crystallizable (Fc) Function

Because most of the anti-inflammatory properties of IVIG are mediated by the Fc antibody portion, evaluation of the Fc functional integrity of IgG is an indirect way to measure their therapeutic potential. This has been determined by Fc function in accordance with Eu. Ph., 2.7.9, method A [9], using haemolytic complement-fixation assay. This test is based on the haemolysis of antigen-coated fresh human red blood cells in the presence of guinea pig complement. Rubella antigen is used in the reference method. Results are reported as a ratio to an IgG standard (biological reference preparation—BRP—batch 3). For experimental details see also: British Pharmacopoeia Volume IV, Appendix XIV J. Blood and Related Products.

Results and Discussion

Comparative Evaluation of the Structural Stability Properties of Different Lots of IgG Preparations by Circular Dichroism

The thermal stability of the different IVIG lots analysed in this study, was first evaluated by CD. In Fig. 1a–f, an overlay of the far UV–CD spectra recorded for the six different samples at increasing temperatures from 20 to 85 °C and then back at 20 °C ('after cooling' condition), is reported. As shown, CD spectra of IVIG analyzed at 20 °C exhibited the canonical positive band at 202 nm, the negative band at 216–218 nm and an intensity equal to zero at 208–210 nm, typical of proteins with a high β-sheet content. Although the occurrence of several other positive and negative bands in the near UV, at around 260–300 nm is reported [6], these bands have not been considered in our analysis, because they are much less intense and poorly diagnostic. During thermal denaturation, the canonical

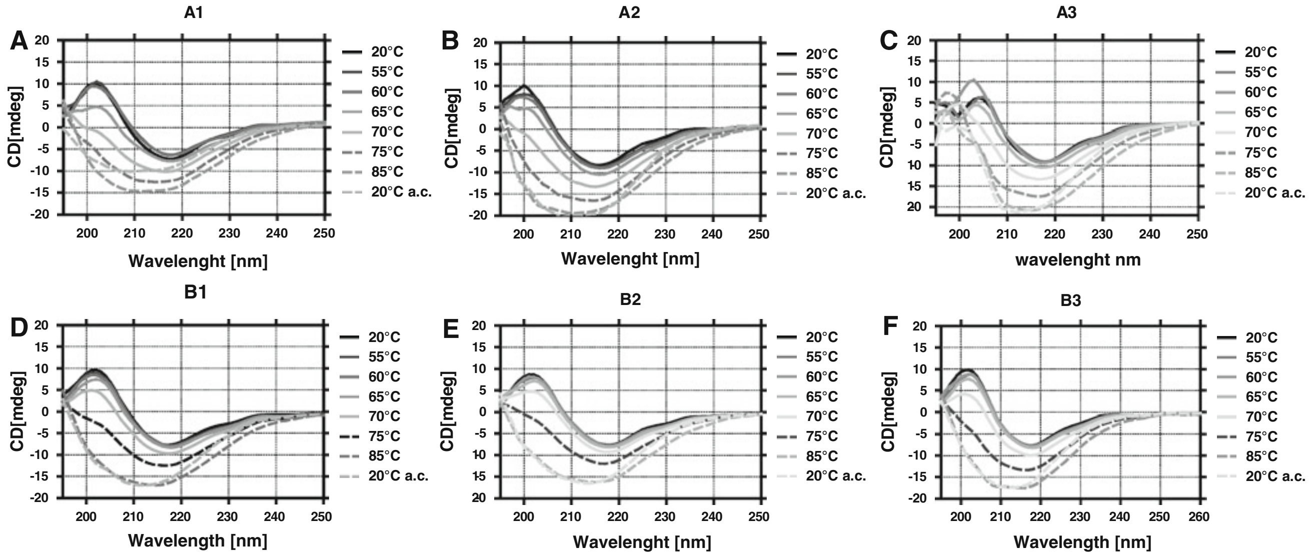

Fig. 1 **a–f** CD spectra of samples A1, A2, A3, B1, B2, B3 between 195 and 250 nm at the indicated temperatures

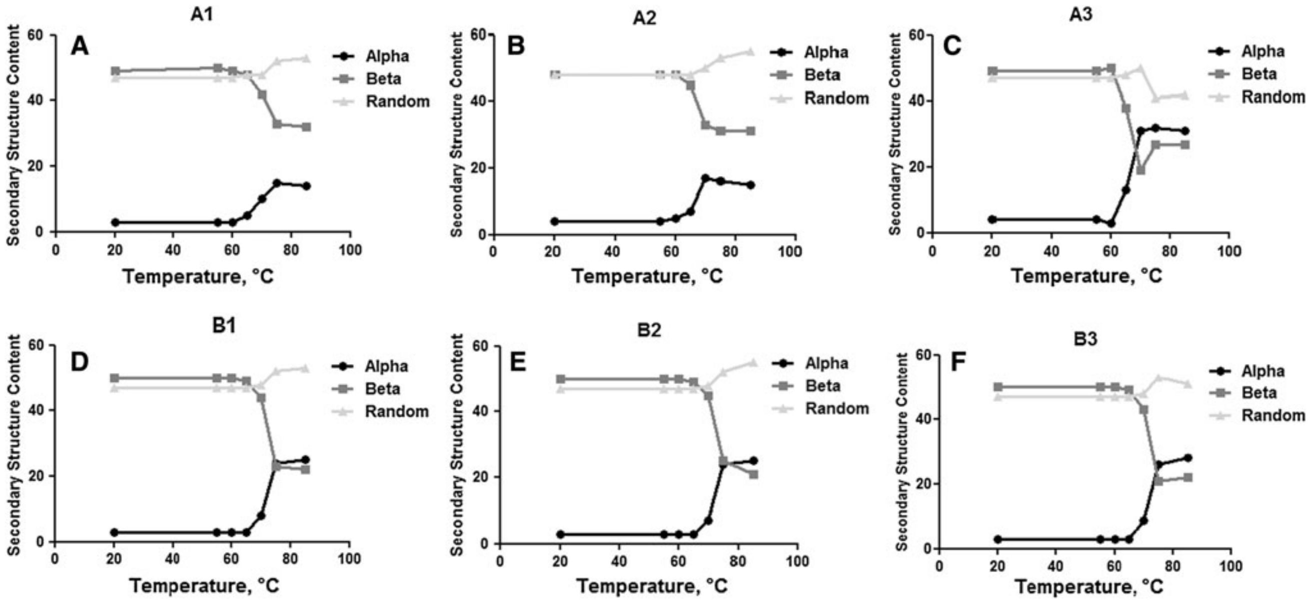

Fig. 2 **a–f** α-helix, β-sheet and random coil content determined for samples A1, A2, A3, B1, B2, B3 at the different temperatures using the Dichroweb server. Normalized root mean square deviation (NRMSD), expressed as percentage, have also been determined for all analyses (not shown)

β-sheet spectrum was maintained up to 60 °C for all samples, confirming the high stability of antibodies. For temperatures below this threshold, the minimum at 216–218 nm was maintained more or less at the same intensity, between about −6 and −8 mdegrees.

Afterwards, starting from 65 °C, spectra varied considerably, suggesting severe structural changes. As shown in Fig. 1c, sample A3 exhibited a different behavior at shorter wavelengths, with the maximum shifting from about 205 to 195 nm. Such changes are suggestive of a general reduced stability of proteins present in this preparation. By further temperature increase, a progressive denaturation was observed for all samples, witnessed by the large changes in the CD spectra. In particular, the band at 209 nm was progressively lost, leading to spectra resembling more those of proteins having a large content of α-helix (see for

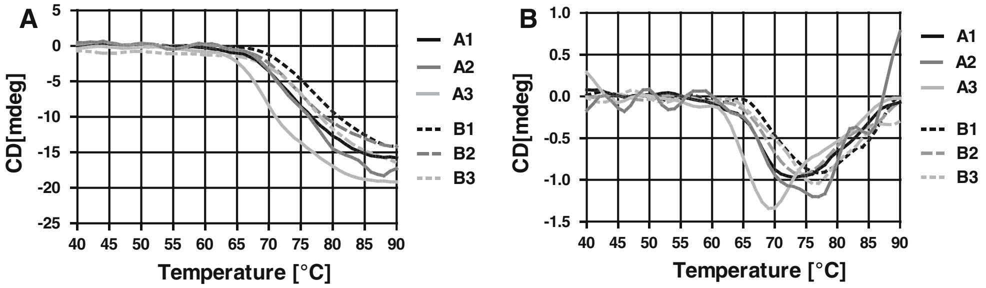

Fig. 3 **a** Curves of thermal denaturation between 40 and 95 °C for all samples analyzed in this study. **b** The corresponding first derivative for the curves are reported. Spectra were collected between 195 and 250 nm

Fig. 4 **a–f** 2D-PAGE analysis of immunoglobulin preparations on 7 cm strips (linear gradient pH 3–10). The basic isoelectric points are to the *right* and acidic to the *left*. *Red squares* three-dimensional magnifications are reported in 4g–n. **g–n** Three-dimensional profiles of 2D-maps of IgG preparations obtained using the 'interactive 3D-surface plot' application of ImageJ software. Magnifications of regions indicated by *red squares* in Fig. 1 are shown. *Red arrows* indicate streaks not detected in S220611, 270711 and S280911 2D-maps. (Color figure online)

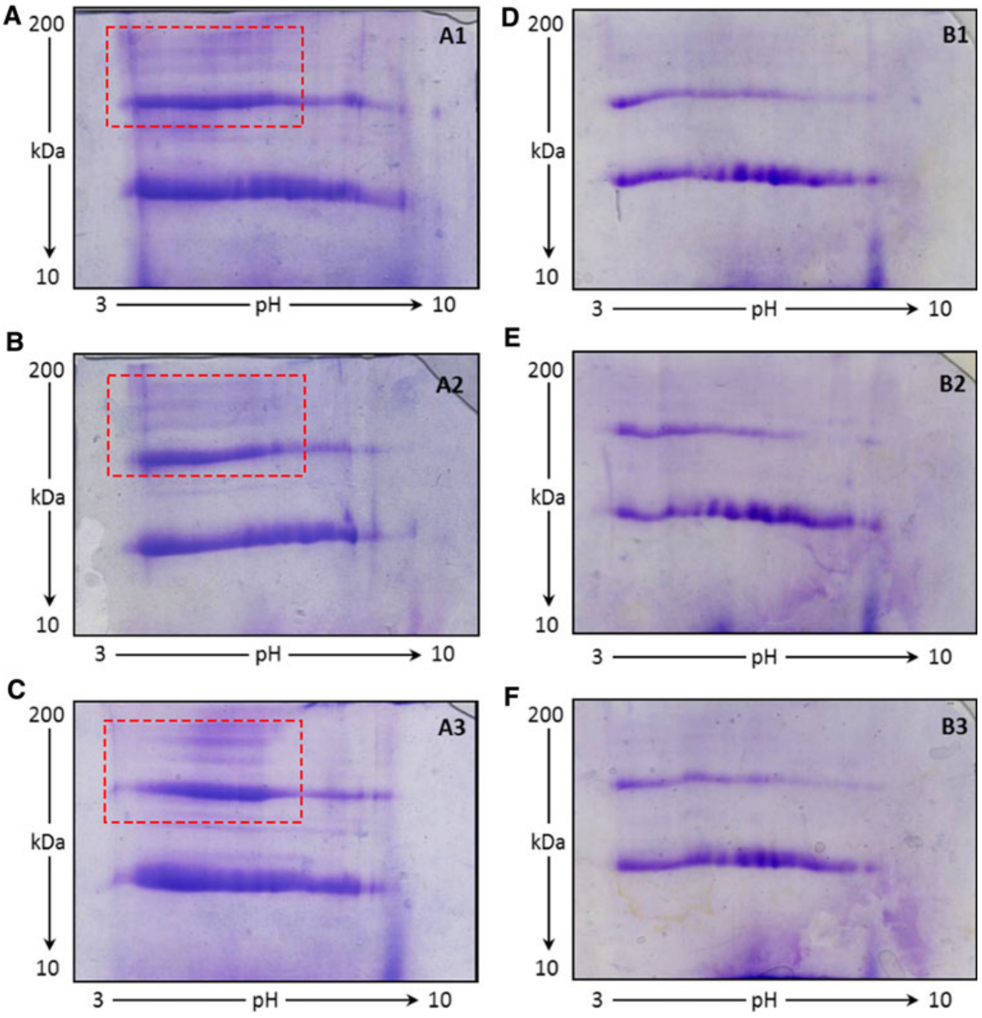

Fig. 4 continued

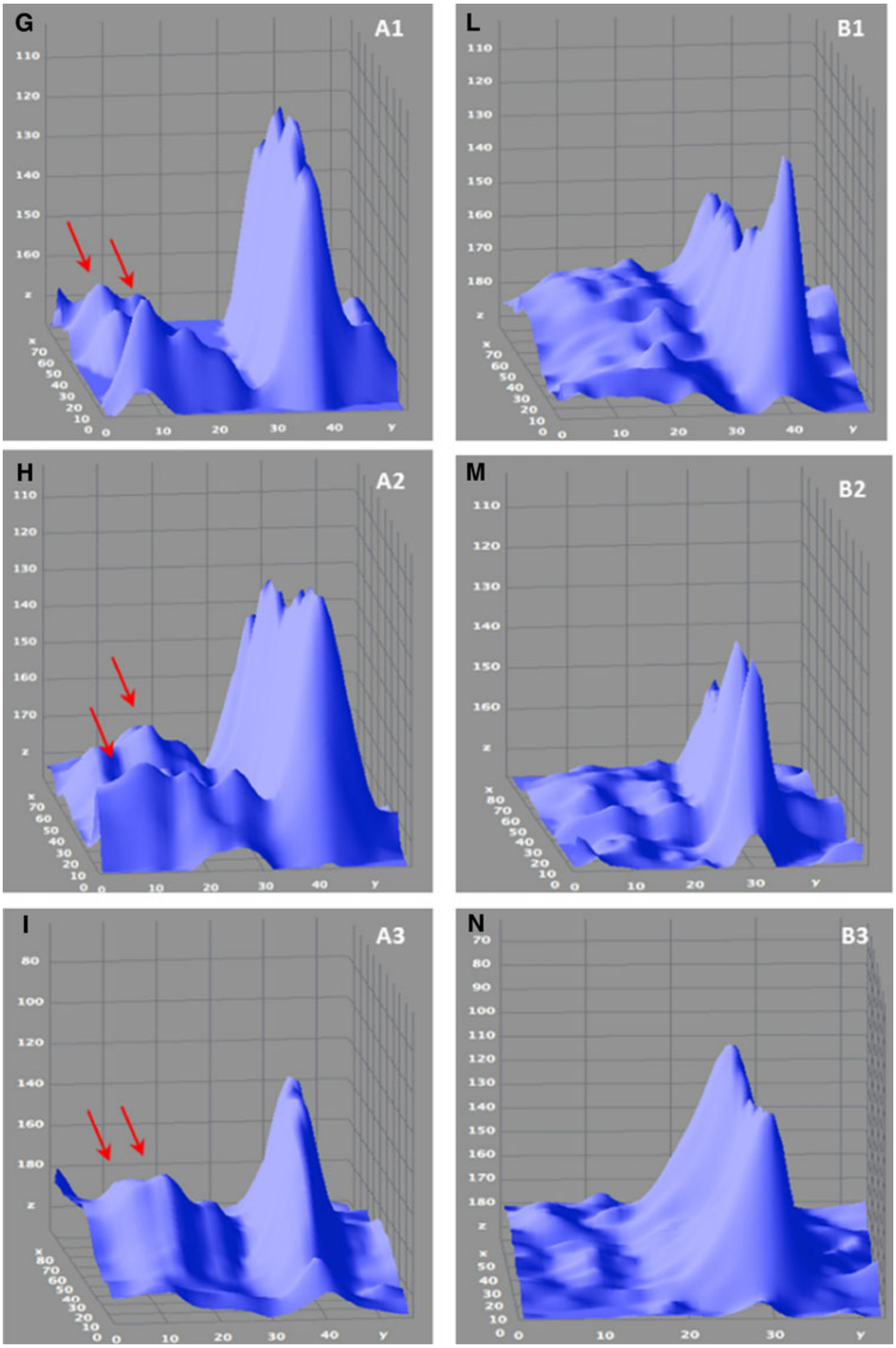

example spectra at 85 °C). For all samples, except A3, also a shift of the point at zero millidegrees was observed (from 208 up to about 197 nm). The shift observed by analyzing sample A3 was instead less intense, and the overall signal below 200 nm strongly changed with the temperature, certainly due to premature protein precipitation. After cooling to record again the spectra at 20 °C, original bands were not restored and white precipitates were observed in the cuvettes for all samples. In Fig. 2a–f, the global changes in α-helix, β-sheet and random coil contents, at all temperatures, obtained using the software Dichroweb, are reported [8, 9]. According to the changes observed in spectra, a progressive and remarkable reduction of the β-sheet content was noticed, paralleled by an increase in the α-helix character and a less intense increase of the random coil content. As shown, changes in the samples from cryosupernatant 1 were less intense; furthermore, one of the these samples, A3, exhibited a decrease of the random coil character and a more marked change of the α-helix and β-sheet contents, in agreement with the spectral changes below 200 nm described before.

To further unveil possible differences in stability, melting curves were recorded following signal change at 209 nm as a function of the temperature increase. Since proteins were essentially very stable up to about 60 °C, melting curves were recorded only between 40 and 95 °C. In Fig. 3a, an overlay of melting curves for all samples is shown, and as can be seen, except that referred to as sample A3, which yet declined at 65 °C, all exhibited a sudden drop of signal starting at about 70 °C. This difference is also reflected in the graph of Fig. 3b reporting the first derivatives of all spectra, where the minimum of sample A3 is clearly shifted some 5° towards lower temperatures compared to those of other samples. Altogether, data indicate that all IVIG samples behave in a similar way in terms of resistance to thermal denaturation, with a slightly higher stability exhibited by lots deriving from cryosupernatant 1 fraction. Amongst these, sample A3, more rapidly aggregated and precipitated upon heating, thus showing unique properties, presumably deriving by the occurrence of pre-existing random aggregates.

Analysis of IVIG Preparations by 2D-PAGE

Immunoglobulins (Igs) are a heterogeneous population of proteins (polyclonal immunoglobulins), whose basic structure consists of two identical halves connected by disulphide bonds. Each half is made up of a heavy chain of ∼55 kDa and a light chain of ∼25 kDa, joined together by a disulphide bond near the carboxyl terminus of the light chain. The heterogeneity of Igs is not detectable using monodimensional SDS-PAGE, which only resolves the most abundant protein bands at 55 and 25 kDa. An extensive bioanalytical characterization of all samples was thus performed by 2D-PAGE followed by densitometric analysis, in order to assess the occurrence of low-abundance impurities and a possible correlation with the different physico-chemical properties evidenced by the CD analysis. After extensive reduction, aliquots of proteins (200 µg) were separated by 2D-PAGE using, for the first dimension, IPG strips with a linear 3–10 pH gradient. The second dimension was carried out on 12 % polyacrylamide gel, following further reduction and alkylation steps. At the end of the run, 2D-gels were stained with Coomassie Blue R250 and the resulting gels are reported in Fig. 4a–f. As expected, multiple protein spots were visualized in the regions with molecular mass of about 25 and 55 kDa, corresponding to the light and heavy chains of IgG, respectively. These profiles attested the IgG polyclonal nature with many isoforms with the same molecular weight but differing in their isoelectric point. However, though all samples appeared highly homogeneous, 2D-maps corresponding to the A group, comprising A1, A2 and A3, showed a set of streaks having MW between about 70 and 150 kDa and pIs comprised between about 4 and 7; remarkably, the most intense streaks were visible on the gel corresponding to sample A3.

A more detailed comparison of the 2D-gels of the different IgG preparations was also performed following gel images acquisition and quantitative analysis. Three-dimensional profiles of the gel image sections boxed in Fig. 4a–f are reported in Fig. 4g–n and Fig. S1a–f in the supporting material, and provide a more quantitative view of the impurities (indicated by arrows). In Table 1, the level of purity of samples studied is reported and as shown, A lots contain detectable levels of impurities (1.12, 1.15 and 1.30 %, respectively), whereas B lots appear 100 % pure. Remarkably, lot A3 has the highest content of impurities, which could account for the difference in stability observed during the CD analysis.

Table 1 Impurities detected on the six samples of IVIGs. Both absolute and percentage values are reported

Intensity	IgG samples					
	A1	A2	A3	B1	B2	B3
IgG light chain	6,174.52	9,175.93	6,372.33	3,483.64	4,229.45	3,700.35
IgG heavy chain	17,293.27	19,822.25	18,559.78	12,689.34	12,496.99	11,052.83
IgG total	23,467.79	28,998.18	24,932.11	16,172.98	16,726.44	14,753.18
Impurities	262.85	334.38	324.01	0.00	0.00	
% impurities	1.12	1.15	1.30	0.00	0.00	0.00
% IgG	98.88	98.85	98.70	100.00	100.00	100.00

Fig. 5 **a–c** Envelope of sensorgrams for the IgG lots A1, A2 and A3. Concentrations are reported *below* each group of *curves*. **d–f** Envelope of sensorgrams for the IgG lots B1, B2 and B3. Concentrations are reported *below* each group of *curves*

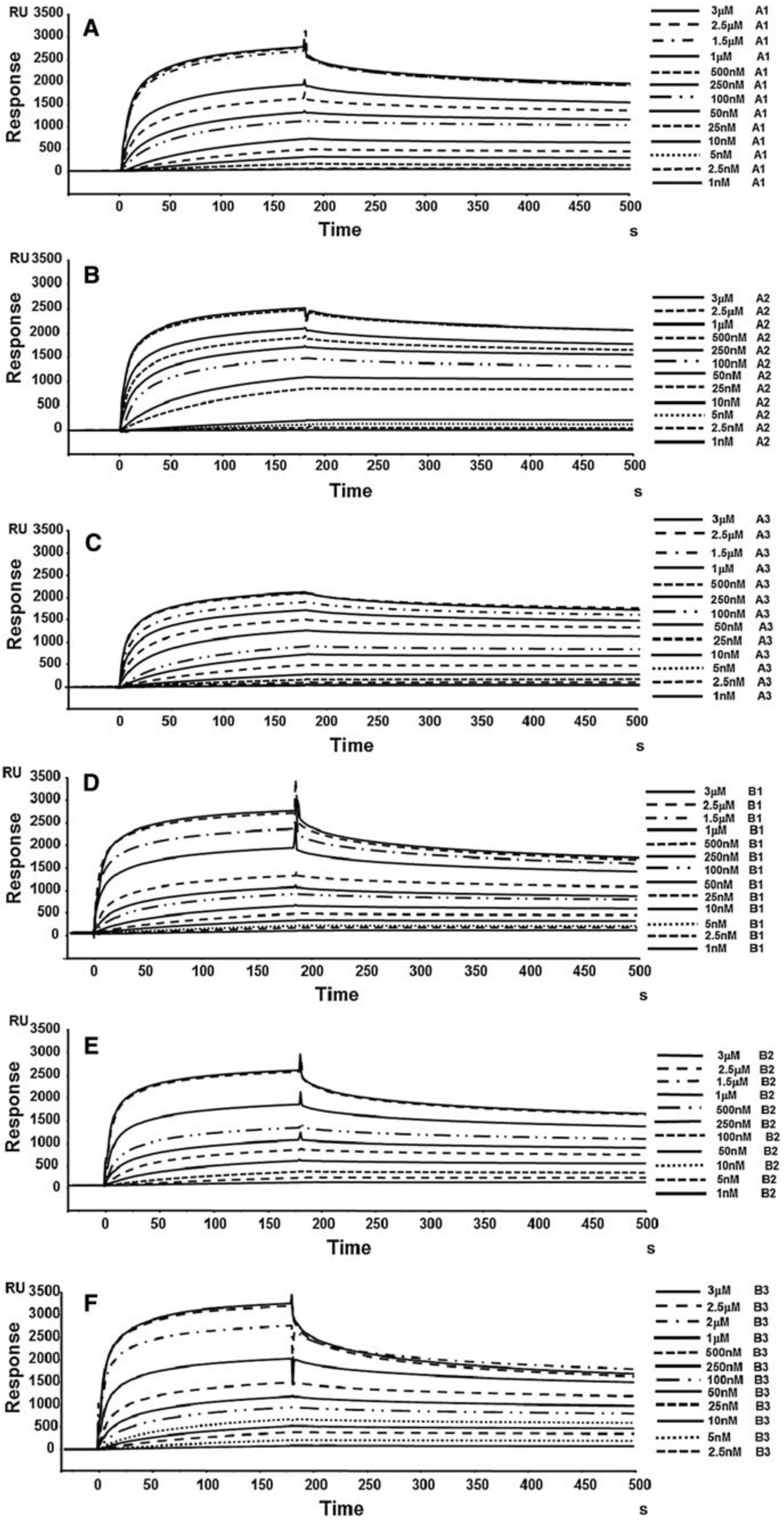

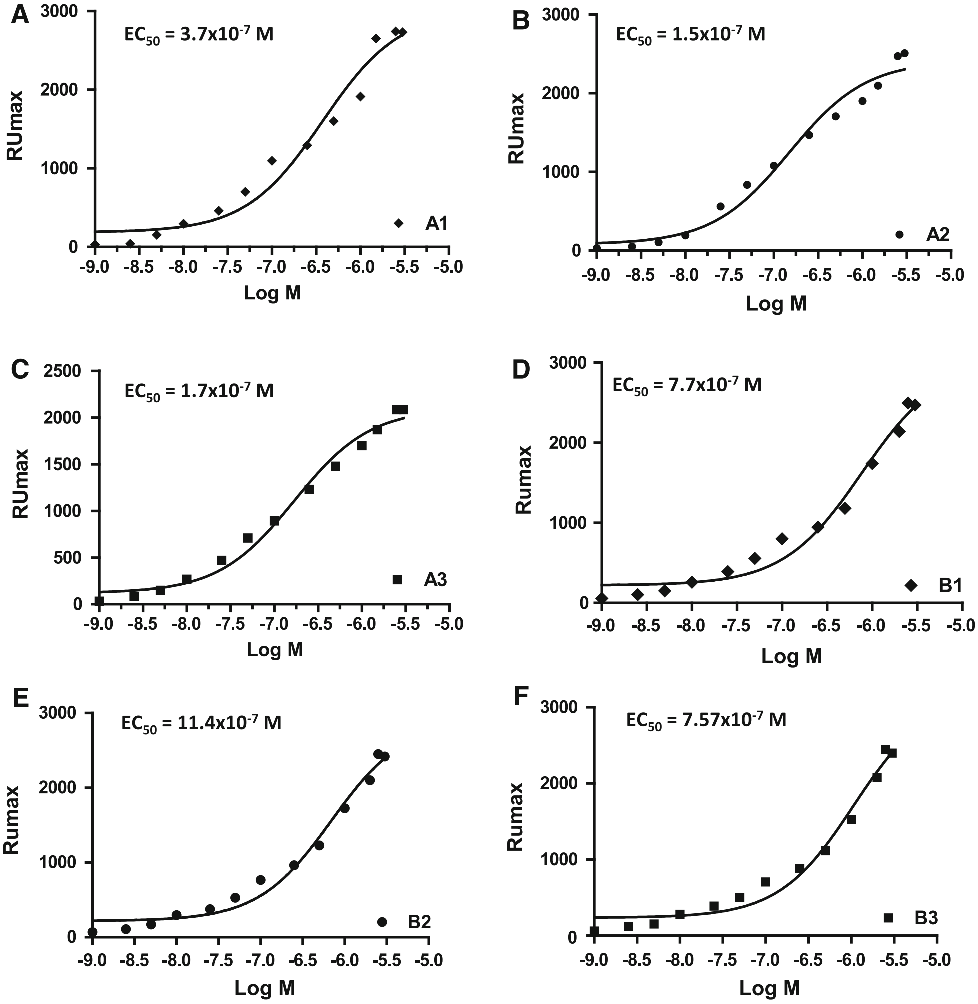

Fig. 6 a–f Correlation curves between RU_{max} values at each concentrations and concentrations itself for IgG lots A1, A2, A3 and B1, B2, B3 expressed as Log M. For each single plot the EC50 value calculated by this method is also reported. Correlation curves between RU_{max} values at each concentrations and concentrations itself for IgG lots A1, A2, A3 and B1, B2, B3 expressed as Log M. For each single plot the EC50 value calculated by this method is also reported

Table 2 Values of the EC50 values determined for all IgG lots and the relative standard errors

IgG samples	A1	A2	A3	B1	B2	B3
EC_{50} (M)	$3.7 \pm 2.0 \times 10^{-7}$	$1.5 \pm 0.8 \times 10^{-7}$	$1.7 \pm 0.7 \times 10^{-7}$	$7.7 \pm 1.0 \times 10^{-7}$	$11.4 \pm 0.7 \times 10^{-7}$	$7.5 \pm 0.7 \times 10^{-7}$

Comparative Binding Analysis of the Different Lots of IVIG to Protein A (pA) by SPR

To have a measure of the integrity of the Fc portion of IVIG, we performed binding analyses of the different IgG preparation to pA. pA is a bacterial protein largely used to purify Igs of different classes from complex matrices. It is known to bind on a region of the Fc portion that comprises residues from the Cγ2 and Cγ3, therefore comparative binding analyses can provide information on the relative integrity of this IgG region.

pA is a protein of 42 kDa which binds with high affinity and selectivity at least two distinct IgG molecules [11], however the exact stoichiometry is at present not known and generally is dependent on experimental conditions and technique used. In solution the stoichiometry can be higher than 2:1 and also binding sites on the IgGs are two, therefore the mathematical models for studying this interaction can be complex [11].

Analyses were carried out by SPR, using sensor chips with immobilized pA. Optimal concentrations for these analyses were between 1 and 2,500 nM.

The envelopes of sensorgrams referred to the six IVIG lots, reported in Fig. 5a–f, show as all curves have essentially the same shape and trend, reaching the saturation for concentrations higher than 2,500 nM. Since the binding stoichiometry between pA and IgGs is not well-defined, especially for interactions occurring on solid surfaces, to derive kinetic and thermodynamic binding parameters K_{on}s, K_{off}s and K_Ds, we tried with different mathematical

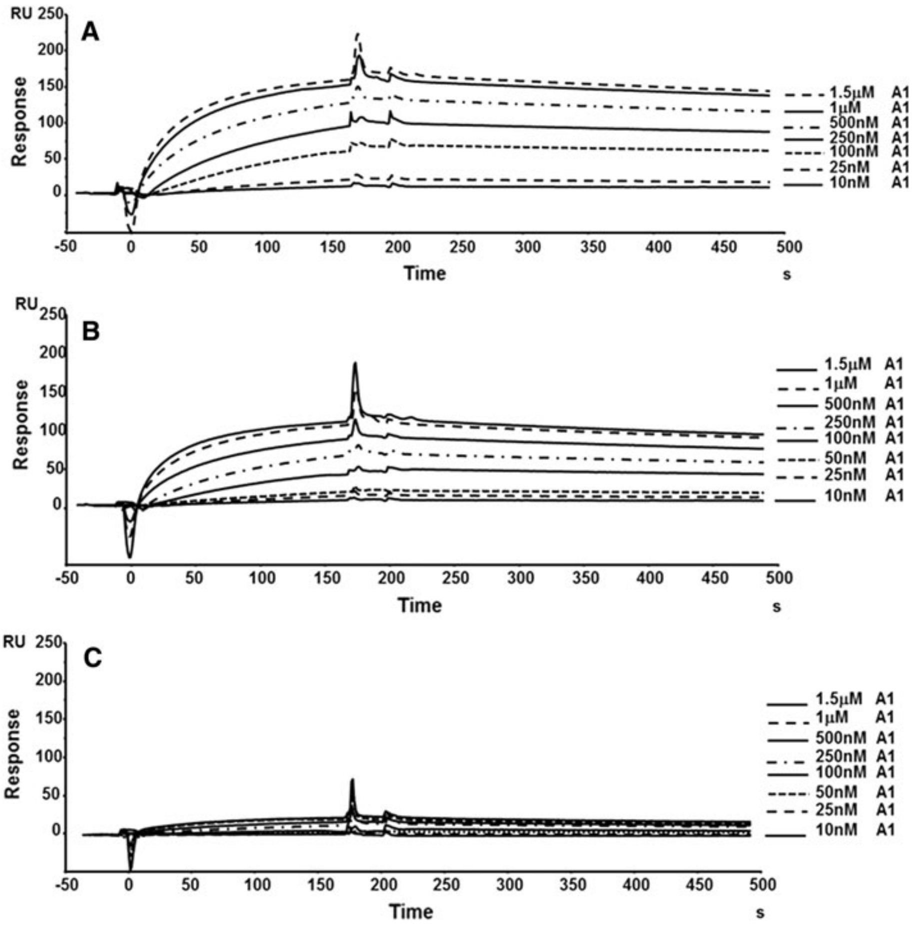

Fig. 7 **a–c** Sensorgrams obtained for the interaction between the immobilized Mab anti-k-chain and IgGs from the lot A1 on FC4 (high density, a), on FC3 (medium density, b) and on FC2 (low density, c)

models of interactions (including 1:1, 1:2 stoichiometries or even higher). However, all attempts to fit the curves failed or gave inaccurate results (see Fig. S2a, b in the supporting material as an example of failed fitting). Therefore, in order to compare the analyses, we built plots reporting RU_{max} values versus analyte concentration, as reported in Fig. 6a–f. Next, using an algorithm of nonlinear regression and assuming a 1:1 stoichiometry, we derived a measure of global affinities, expressed as EC_{50} which could be seen as the resultant of multiple interactions [12, 13]. EC_{50}s values determined by this method are summarized in Table 2. As expected, values are all very similar, being comprised between 1.5×10^{-7} and 3.9×10^{-7} M, however EC_{50}s for the B lots are slightly higher (about doubled), not only suggesting a higher consistency among lots within the same group, but also measurable differences among lots coming from different starting material.

A further comparison was performed by comparing RU_{max} values observed at a given concentration. Data are plotted in Fig. S3 in supporting material, whereby for each distinct lot, RU_{max} values at all concentrations are reported. It can be reasonably assumed that, the more similar are RU_{max} values, the more is expected that IgG samples are similar each other. By analyzing data, it emerged that the set of B samples comprising lots B1, B2 and B3, appears more homogeneous with almost identical values at the same concentrations. This holds not true for samples A1, A2 and A3 which indeed showed varying RU_{max} values at the same concentration. This effect, negligible at low concentrations, is more evident for concentrations higher than 10 nM. It should be also noticed that RU_{max} values are a little bit higher for IgGs lots from set A, as compared to those obtained with IgGs from the other one. This difference could be due to the presence of small amounts of aggregates in set A, which could form (or be retained after dilution) at higher concentrations and over time. Aggregates, being bigger than monomeric IgG, provide more intense SPR signals.

Comparative Analysis of Different Lots of IVIG to Anti-k-chain mAb by SPR

The study performed with pA was paralleled by another comparative study carried out using an anti-k-chain monoclonal antibody, in order to obtain a global evaluation of the Fab integrity.

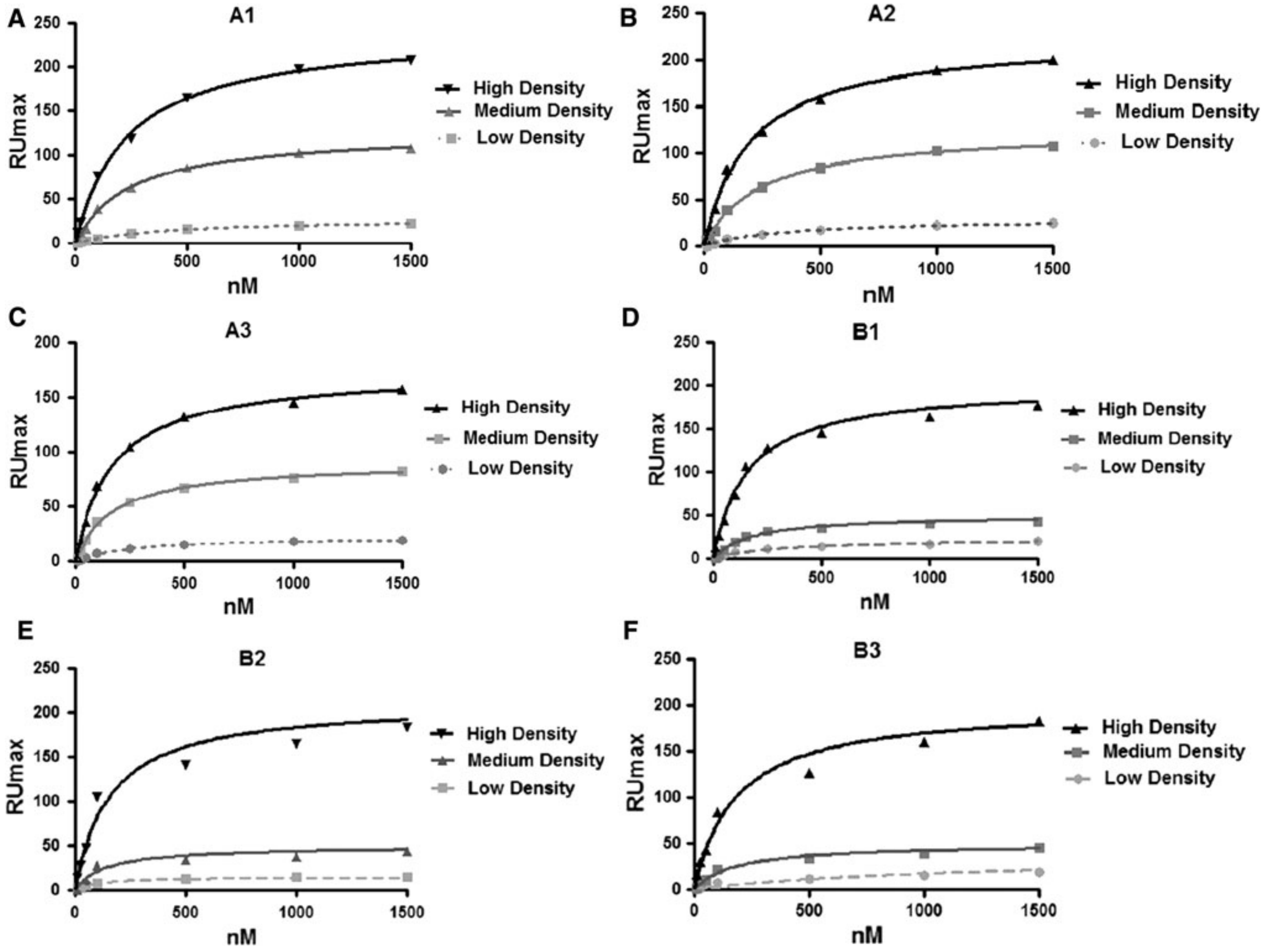

Fig. 8 **a–f** Plots reporting RU_{max} values versus IgGs concentration for all lots analyzed

Binding experiments were performed in parallel on three channels with different immobilization levels. In Fig. 7a–c, the envelopes of sensorgrams obtained for one of the six samples (sample A1) at three different immobilization levels, are reported. In the supporting material Fig. S4–S8, sensorgrams corresponding to the remaining five analyses are reported. In all plots, time and RU scales were kept at the same values to visualize at best differences in RUs achieved on the distinct channels by varying ligand density. As expected, lower bindings were recorded for lower ligand density and curves were all very similar. As with the pA, bindings were analyzed by determining the global KDs plotting the RU_{max} values derived from every single injection on distinct flow channels versus the concentration of Igs. Data were then best fitted by a nonlinear regression analysis and are reported in Fig. 8a–f. K_Ds determined by this method are instead reported in Table 3. As can be seen, values are very similar for the same IgG lot on channels at different immobilization levels, thus suggesting that the analyses are very reproducible and reliable. It should be pointed out that K_Ds are also very similar amongst different lots with values ranging between about 136 and 288 nM, suggesting that the population of Igs present in the different lots are highly comparable in terms of Fab homogeneity.

Fragment Crystallizable (Fc) Function

The functional integrity of the Fc fragment of all analysed lots was evaluated using a well-established method suggested by the European Pharmacopeia. Data for all six samples are presented in Table 4 and show that results are in compliance, therefore proving the full functionality of the analysed IgGs. Despite large differences in function are observed between the diverse IVIG lots, they do not correlate with the slight discrepancies emerged at the bioanalytical level.

Table 3 K_D values for the binding between IgGs and the immobilized anti-k-chain mAb K4377, as obtained by nonlinear regression analyses of curves reported in Fig. 8**a–f**

	Low density	Medium density	High density	Average	SD
A1					
KD (nM)	380.9	251.0	232.4	288.1	80.9
A2					
KD (nM)	347.1	254.2	203.8	264.4	73.7
A3					
KD (nM)	269.4	171.7	170.6	203.9	56.7
B1					
KD (nM)	303.2	176.3	159.5	213.0	78.5
B2					
KD (nM)	110.3	141.1	158.4	136.6	24.4
B3					
KD (nM)	1,149**	185.5	182.3	183.9	23**

SD standard deviation

** This value has not been considered for calculating the average KD, therefore the corresponding SD is also meaningless, being derived by only two values

Table 4 Fragment crystallizable function

	Limit	From cryosupernatant 1			From Fr II + III		
		Lot A1	Lot A2	Lot A3	Lot B1	Lot B2	Lot B3
Fragment crystallizable (Fc) function (%)	>60	82	116	90	79	87	85

Limits are defined in accordance with EU pharmacopoeia: the value is stated in the leaflet accompanying the reference preparation (BRP—batch 3)

Conclusions

We have undertaken a comparative evaluation of the macroscopic physico-chemical properties of six different lots of IVIG coming from two distinct preparations. Three lots, A1–A3, came out from a chromatographic purification from a cryosupernatant fraction, whereas three other lots were obtained from fraction II–III, using the same chromatographic purification procedure. The study has been carried out using different bioanalytical techniques to gain a global view of antibody properties, to assess lot-to-lot consistency and to point out possible differences arising from the different starting material. For this purpose we have conducted on all samples: (i) a macroscopic structural analysis by CD, also evaluating IgG resistance to thermal denaturation; (ii) an evaluation of purity by 2D-gel analyses and (iii) a macroscopic evaluation of Fc and Fab integrity by SPR, carrying out comparative binding studies to pA and to an anti-k chain monoclonal antibody.

As expected, samples displayed quite identical properties and it was difficult to unveil macroscopic dissimilarities, however subtle but measurable differences emerged amongst the different lots during the investigation, especially amongst lots coming from different starting material (lots A vs. lots B). Since the different lots have the same age and have been purified all by the same method, the presence of such impurities or degradation components demonstrates that side products occurring in these experimental IVIG lots can only arise from the diverse raw material. The reason for this has not been investigated here; we can however hypothesize that small impurities are either co-purified with the main component or generated during the purification steps or during storage. Irrespective of the way they are generated, these impurities can be detected and quantified by 2DE and, looking retrospectively at our CD data, could also be predicted to some extent by a CD analysis, which seems to be qualitatively affected by such low levels of contaminants.

Data show that IgGs purified from Fraction II-III are generally homogeneous compared to those obtained from cryosupernatant 1, but also that IgGs extracted from the same starting material have a higher lot-to-lot consistency, thus suggesting that also the very initial steps of plasma manipulation can affect final products. Furthermore, we have observed that one lot (lot A3), showed reduced resistance to thermal denaturation and, at the same time, also contained sensibly higher amounts of undetermined impurities (presumably immunoglobulin fragments), as detected by 2DE. Remarkably, lots A1 and A2, coming from the same raw material (cryosupernatant 1) also contained detectable levels of impurities (see Table 1; Fig. 4), but the resistance to thermal denaturation was comparable to that of the purer lots B1–B3. In order to further unravel differences between lots, an extensive characterization by SPR was also performed. In our experimental setting, the SPR approach would allow to dissect differences deriving from the Fab and/or the Fc antibody portions, however it proved generally less sensitive, being able to measure subtle differences only for the binding to pA and not to the anti-k-chain K4377 mAb. While confirming that samples coming from the same set of lots are more homogeneous, we also noticed that lots A are less comparable in terms of relative binding to pA in respect to B lots (see the supplementary Fig. S3).

Altogether, our results show that this set of bioanalytical techniques is useful and complementary to the analytical tests provided in the European Pharmacopeia for a better global view of IVIG purity, stability and integrity of full antibodies, as well as of separate Fc and Fab fragments.

References

1. Kaveri, S. V., Maddur, M. S., Hegde, P., Lacroix-Desmazes, S., & Bayry, (2011). Intravenous immunoglobulins in immunodeficiencies: More than mere replacement therapy. *Journal of Clinical and Experimental Immunology, 164*(Suppl 2), 2–5.
2. Navarro, R. P., Ballow, M., Fenrick, B., & Pezalla, E. J. (2012). Considerations for the optimal use of immunoglobulin. *American Journal of Managed Care, 18*(4 Suppl), S67–S78.
3. Baerenwaldt, A., Biburger, M., & Nimmerjahn, F. (2010). Mechanisms of action of intravenous immunoglobulins. *Expert Review of Clinical Immunology, 6*(3), 425–434.
4. Bayry, J., Fournier, E. M., Maddur, M. S., Vani, J., Wootla, B., Sibéril, S., et al. (2011). Intravenous immunoglobulin induces proliferation and immunoglobulin synthesis from B cells of patients with common variable immunodeficiency: A mechanism underlying the beneficial effect of IVIg in primary immunodeficiencies. *Journal of Autoimmunity, 36*(1), 9–15.
5. Radosevich, M., & Burnouf, T. (2010). Intravenous immunoglobulin G: Trends in production methods, quality control and quality assurance. *Vox Sanguinis, 98*(1), 12–28.
6. Vermeer, A. W., & Norde, W. (2000). The thermal stability of immunoglobulin: Unfolding and aggregation of a multi-domain protein. *Biophysical Journal, 78*(1), 394–404.
7. Whitmore, L., Wallace, B. A., & DICHROWEB. (2004). An online server for protein secondary structure analyses from circular dichroism spectroscopic data. *Nucleic Acids Research, 1*(32(web server issue)), W668–W673.
8. Johnsson, B., Lofas, S., & Lindquist, G. (1991). Immobilization of proteins to a carboxymethyldextran-modified gold surface for biospecific interaction analysis in surface plasmon resonance sensors. *Analytical Biochemistry, 198*, 268–277.
9. In accordance with EU pharmacopoeia: the values are stated in the leaflet accompanying the reference preparation (BRP—batch 3). See also: British pharmacopoeia volume IV, appendix XIV. *Journal of Blood and Related Products*.
10. Whitmore, L., & Wallace, B. A. (2008). Protein secondary structure analyses from circular dichroism spectroscopy: Methods and reference databases. *Biopolymers, 89*(5), 392–400.
11. Cohen, S., & Sweeney, H. M. (1979). Modulation of Protein A Formation in Staphylococcus aureus by Genetic Determinants for Methicillin Resistance. *Journal of Bacteriology, 140*(3), 1028–1035.
12. Velge-Roussel, F., Breton, P., Lescure, F., Guillon, X., Bout, D., & Hoebeke, J. (1995). Analysis of human CD4-antibody interaction using the BIAcore system. *Journal of Immunological Methods, 183*(1), 141–148.
13. Sandomenico, A., Monti, S. M., Marasco, D., Dathan, N., Palumbo, R., Saviano, M., et al. (2009). IgE-binding properties and selectivity of peptide mimics of the FcvarepsilonRI binding site. *Molecular Immunology, 46*(16), 3300–3309.